UNIVERSITÉ DU QUÉBEC À TROIS-RIVIÈRES

DÉVELOPPEMENT ET CARACTÉRISATION DE STRUCTURES AUXÉTIQUES INTELLIGENTES FABRIQUÉES PAR IMPRESSION 4D

THÈSE PRÉSENTÉE

COMME EXIGENCE PARTIELLE DU DOCTORAT EN INGÉNIERIE (CONC. GÉNIE MÉCANIQUE)

PAR

KARIMA BOUGUERMOUH

Avril 2026

DOCTORAT (Ph. D.)

Prof. Luc Laperrière
Prénom Nom — Directeur de recherche

Prof. Mohamed Habibi
Prénom Nom — Codirecteur de recherche

Jury d'évaluation

Prof. Éric Loranger, UQTR
Prénom Nom, Nom établissement — Président

Prof. Jihed Zghal, Université Paris Nanterre (UPN)
Prénom Nom, Nom établissement — Évaluateur externe

Prof. Mohammadali Shirinbayan, École nationale supérieure d'Arts et Métiers de Paris (ENSAM)
Prénom Nom, Nom établissement — Évaluateur externe

Prof. Luc Laperrière, UQTR
Prénom Nom, Nom établissement — Directeur de recherche

Prof. Mohamed Habibi, UQTR
Prénom Nom, Nom établissement — Codirecteur de recherche

REMERCIEMENTS

Au terme de cette thèse, il m'est particulièrement cher de remercier celles et ceux qui, de près ou de loin, ont accompagné cette aventure intellectuelle et humaine.

Je souhaite tout d'abord exprimer ma plus profonde reconnaissance à mon directeur de recherche, le Professeur Luc Laperrière, pour sa confiance, son encadrement rigoureux et bienveillant, ainsi que pour la richesse de ses conseils tout au long de ce parcours. Son expertise, sa vision scientifique et sa disponibilité ont été des repères précieux dans l'élaboration et l'aboutissement de ce travail.

Mes remerciements s'adressent également à mon codirecteur, le Professeur Mohamed Habibi, dont l'accompagnement attentif, les remarques constructives et l'implication constante ont fortement contribué à la qualité de cette recherche. Sa rigueur et sa méthodologie m'ont guidée dans les moments clés du projet.

Je remercie sincèrement les membres du jury, pour avoir accepté d'évaluer cette thèse et pour l'intérêt qu'ils ont porté à mon travail. Leurs observations et recommandations sont venues enrichir cette démarche et nourrir ma réflexion.

Un chaleureux merci à mes collègues et amis du laboratoire, Amal, Abdelhamid, Mohamed et Oussama, pour les échanges scientifiques inspirants, l'entraide quotidienne et les instants de convivialité partagés. Votre présence a donné à cette expérience une dimension humaine inestimable.

Je suis profondément reconnaissante envers ma famille, véritable socle de cette aventure. À mes parents, pour leur amour inépuisable, leur soutien indéfectible et leurs encouragements constants, qui m'ont portée dans les moments de doute comme dans les réussites. À mes frères et à ma sœur, merci pour votre confiance en moi et votre présence rassurante.

Je tiens aussi à exprimer toute ma gratitude à mon époux, pour sa patience, son soutien inconditionnel et sa présence rassurante dans les moments les plus exigeants. Un merci tout particulier à ma petite fille, dont l'amour, la tendresse et les sourires ont été ma plus belle source d'énergie et de motivation.

Enfin, je remercie de tout cœur mes amis, pour leur écoute, leur patience et leurs mots d'encouragement, qui ont fait de ce parcours exigeant un chemin empreint de chaleur, d'amitié et de réconfort.

À vous tous, merci infiniment.

RÉSUMÉ

Les polymères à mémoire de forme (PMF) sont une classe de matériaux intelligents qui ont la capacité de « se souvenir » d'une forme particulière et, lors de l'exposition à des stimuli externes, de revenir à cette forme originale. Cette propriété unique découle de la capacité du polymère à subir une transition de phase réversible entre une forme temporaire et une forme permanente. Les PMF font partie du domaine plus large des matériaux intelligents et sont souvent classés comme des matériaux sensibles aux stimuli. Les chercheurs explorent activement des moyens d'améliorer le rendement, les temps de réponse et les fonctionnalités des PMF. Le domaine est dynamique et la recherche en cours porte sur le développement de nouveaux matériaux et l'amélioration des techniques de conception et de traitement.

L'impression en quatre dimensions (4D) a récemment fait l'objet d'une grande attention dans le domaine des matériaux intelligents. Il s'agit d'utiliser la fabrication additive avec un PMF pour obtenir des géométries qui peuvent changer de forme sous l'effet de différents stimuli. Une telle technique permet la fabrication de pièces imprimées en 3D avec la fonctionnalité supplémentaire de formes de pièces évolutives, programmables et contrôlables au fil du temps.

Dans cette étude nous allons nous concentrer sur 2 aspects prometteurs de l'impression 4D. Le premier aspect concerne l'impression de structures auxétiques. La structure auxétique offre des prouesses mécaniques et une flexibilité exceptionnelle, tandis que le PMF peut mémoriser des formes modifiées, contribuant ainsi à une adaptabilité structurelle beaucoup plus étendue.

Le deuxième aspect concerne l'amélioration des propriétés mécaniques des pièces imprimées en 4D. La stratégie consiste à renforcer les filaments utilisés dans le procédé d'impression de dépôt de fils fondus (Fused Deposition Modeling ou FDM) avec des fibres naturelles et de nanocellulose. Les fibres naturelles de lin sont choisies en raison de leur disponibilité, leurs propriétés mécaniques et acoustiques intéressantes, et leur avantage environnemental comparativement aux fibres synthétiques traditionnelles (notamment le verre et le carbone). D'autre part, la nanocellulose est utilisée comme agent de renforcement en raison de ses excellentes propriétés mécaniques, notamment sa haute rigidité et sa grande résistance à la traction, permettant d'améliorer les performances des matériaux à faible taux de charge. Biodégradable, renouvelable et issue de ressources naturelles, elle répond aux exigences de durabilité des polymères modernes. De plus, elle améliore les propriétés barrières contre les gaz et l'humidité, favorise la cristallisation pour

renforcer la stabilité thermique et dimensionnelle. Son coût relativement faible constitue également un avantage pour le développement de matériaux durables et performants.

La méthodologie de recherche décrit l'approche pour étudier l'impression 4D de PMF renforcés de fibres naturelles et de nanocellulose. La sélection et la préparation des matières premières, y compris les mélanges PMF, les fibres naturelles et nanocellulose, sont discutées. L'étude porte sur le développement de mélanges optimaux de polymères, l'incorporation de fibres naturelles et de nanocellulose dans les matériaux composites. Le procédé comprend deux phases : l'extrusion de mélanges de polymères, composites et nanocomposites en filaments et l'impression 3D de ces derniers par FDM. La caractérisation thermique, structurale, mécanique et microstructurale des matériaux imprimés a été réalisée par DSC, FTIR, DRX, MEB et essais mémoire de forme.

L'étude se termine avec la conception, et la validation expérimentale de structures auxétiques chargées de fibres naturelles de lin et de nanocellulose pour exploiter les propriétés dynamiques et adaptatives de ces nouveaux matériaux.

Mots-clés : Impression 4D, mélanges de polymères, structure auxétique, renfort, propriétés mécaniques, mémoire de forme.

Table des matières

Liste des tableaux

Liste des figures

Liste des abréviations

ABS : Acrylonitrile Butadiène Styrène

CNC : Cellulose Nanocristalline

CNCs : Nanocristaux de Cellulose

CNRS : Centre National de la Recherche Scientifique

CPLA: PLA Cristallin

DMA: Dynamic Mechanical Analysis

DSC: Differential Scanning Calorimetry

FDM: Fused Deposition Modeling

HDPE: High-Density Polyethylene

IFSTTAR: Institut Français des Sciences et Technologies des Transports, de l'Aménagement et des Réseaux

MEB: Microscopie Électronique à Balayage

MF: Mémoire de Forme

PA: Polyamide

PC: Polycarbonate

PCL: Polycaprolactone

PEEK: Polyétheréthercétone

PETG: Polyéthylène Téréphtalate Glycol

PLA: Polylactic Acid / Acide Polylactique

PMMA: Polymethyl Methacrylate

PMF: Polymères à Mémoire de Forme

PP : Polypropylène

PS: Polystyrène

PVA: Polyvinyl Alcohol

PVAc: Poly(vinyl acetate)

SEM: Scanning Electron Microscopy

SME: Shape Memory Effect

SMP: Shape Memory Polymer

SMPs: Shape Memory Polymers

$\mathbf{T_g}$: Température de Transition Vitreuse

$\mathbf{T_m}$: Température de Fusion

TPU: Thermoplastic Polyurethane

XRD: X-ray Diffraction

Chapitre 1: Introduction

1.1 Contexte général

L'impression 4D représente une percée dans le domaine de la fabrication additive, dépassant les limites de l'impression 3D en introduisant une dimension supplémentaire : le temps. Cette méthodologie innovante permet de créer des objets imprimés qui ne sont pas seulement statiques mais dynamiques, capables de subir des transformations ou de modifier leur forme au fil du temps. Ces changements sont déclenchés en réponse à des stimuli externes, tels que les fluctuations de température, l'exposition à la lumière ou les variations d'humidité [1, 2]. Cet aspect de l'impression 4D annonce une nouvelle ère dans la fabrication, où les objets peuvent s'adapter, s'auto-assembler ou évoluer, ce qui ouvre des possibilités sans précédent dans divers domaines [3-6].

1.1.1 Amélioration des performances des PMF par l'utilisation de mélanges polymériques

Le nombre de polymères à mémoire de forme (PMF) capables de conserver plusieurs formes successives reste limité. Pour surmonter cette contrainte, le recours aux mélanges de polymères constitue une stratégie particulièrement prometteuse. En combinant différents polymères, il est possible de concevoir des matériaux présentant plusieurs températures de transition thermiques, permettant ainsi l'activation séquentielle de formes multiples [7]. Cette approche offre également la possibilité d'ajuster finement les propriétés mécaniques, d'améliorer la stabilité thermique et de développer des matériaux sensibles à divers stimuli [8]. Ainsi, les mélanges de polymères ouvrent la voie à la création de PMF avancés, adaptés aux besoins croissants dans les secteurs de la biomédecine, de l'aéronautique et de la robotique [9].

1.1.2 Vers des matériaux adaptatifs : Fusion des PMF et des géométries auxétiques

Les caractéristiques mécaniques des matériaux sont entre autres liées à leur structure géométrique. Il est maintenant possible de créer une structure intelligente dotée d'une capacité de morphing étendue et contrôlable en combinant le PMF avec une structure auxétique. Dans ce cas, la structure auxétique présente des prouesses mécaniques et une flexibilité exceptionnelle, tandis que le PMF peut se souvenir de sa forme modifiée, contribuant ainsi à une adaptabilité structurelle élargie [10].

Identifiés dès le début du XX^{e} siècle, les matériaux auxétiques n'ont suscité un intérêt marqué de la recherche scientifique que bien plus récemment, avec un regain d'attention notable à partir des années 1980 [10]. Depuis lors, les métamatériaux auxétiques ont été largement étudiés en raison de leurs performances mécaniques spécifiques, en particulier leur aptitude à dissiper et absorber efficacement l'énergie [11], les dilatations thermiques négatives [12], la résistance à l'indentation [13], le module de cisaillement [14] et le coefficient de Poisson négatif [15], par rapport aux matériaux conventionnels.

Les modèles micromécaniques qui visent à prévoir et à expliquer le comportement auxétique sont examinés par Xianglong Yu et al [16]. Sur la base de la conception structurelle entraînant des propriétés mécaniques différentes, quatre sous-classes de métamatériaux auxétiques ont été identifiées : (i) la structure rentrante originale, similaire aux cellules repliées fabriquées à partir de mousse de polyuréthane, y compris diverses microstructures rentrantes à cellules ouvertes, carrés ou triangles rotatifs ; (ii) le Ratio de Poisson Négatif (NPR) induit par une instabilité élastique, en particulier les modèles de nervures manquantes à la transformation du modèle ; (iii) NPR utilisant des blocs de construction chiraux, des treillis chiraux ou anti-chiraux ; (iv) une partie des métamatériaux origami, inspirés par la conception du casier à œufs.

1.1.3 Vers des structures intelligentes renforcées : Apport des fibres naturelles

D'autre part, les propriétés mécaniques des objets polymères imprimés en 3D peuvent être améliorées grâce au développement de composites renforcés par des fibres par le biais du procédé FDM [17].

Dans le domaine des matériaux composites, les fibres naturelles s'imposent progressivement comme une alternative crédible aux fibres synthétiques pour le renforcement. Cet intérêt s'explique par leurs performances intrinsèques, notamment sur le plan mécanique [18], acoustique [19] et en termes de capacités de morphing [20]. Par ailleurs, leur faible densité, leur impact environnemental limité ainsi que leurs modalités spécifiques de gestion en fin de vie constituent des avantages significatifs [21]. Aujourd'hui, diverses méthodes de traitement, telles que l'extrusion, l'empilage de films, le moulage par injection, le thermoformage et le moulage sous vide, peuvent être utilisées pour traiter les biocomposites à base de fibres naturelles thermoplastiques [21-23].

1.1.4 Nanocellulose : Un renfort biosourcé pour composites à haute performance

Par ailleurs, l'incorporation de nanocellulose dans les polymères constitue une approche prometteuse pour renforcer davantage les propriétés des matériaux. Issue de sources renouvelables,

la nanocellulose possède un module d'élasticité, une résistance et une surface spécifique élevés, la rendant particulièrement efficace pour améliorer à la fois le module et la résistance des composites au-delà des performances offertes par les microfibres traditionnelles [24]. De plus, elle optimise la dispersion, la stabilité thermique et la mouillabilité de surface des polymères, ce qui est essentiel pour des applications telles que l'emballage alimentaire et les dispositifs médicaux [25]. Sa légèreté, sa biocompatibilité et son caractère respectueux de l'environnement positionnent la nanocellulose comme un matériau clé pour le développement de composites polymères innovants [26].

1.2 Problématique

1.2.1 Complexité des réseaux polymères : Entre performance et faisabilité

Les PMF peuvent être classés en deux grandes catégories. L'un est celui des réseaux de polymères, y compris les copolymères amorphes ou cristallins réticulés de manière covalente et physiquement réticulée [27-30]. L'autre est le mélange de polymères (polymer blend en anglais) [31]. Le mécanisme de réseaux polymère offre un moyen simple de concevoir les réseaux polymères pour obtenir de bonnes propriétés de mémoire de forme. Mais en même temps, la synthèse et la caractérisation des réseaux conçus sont à la fois compliquées et peu pratiques.

Le mélange de polymères offre une façon beaucoup plus simple de fabriquer des PMF. Le type de mélanges décrits dans la littérature est généralement constitué d'un polymère amorphe et d'un polymère cristallin et les deux composants doivent être miscibles à l'état fondu, comme le PVDF/PMMA, le PVDF/PVAc et le PLA/PVAc, [31] etc. Le défi récent porte sur la recherche des rapports optimaux des différents polymères dans le mélange pour obtenir un effet synergique. Cela implique d'équilibrer les contributions de chaque polymère à la résistance mécanique, à la flexibilité et aux performances de mémoire de forme dans le domaine d'impression 4D.

1.2.2 Défi de l'équilibre propriétés mécaniques–fonction mémoire dans les PMF à renforts naturels

En réponse aux défis environnementaux et de durabilité, l'accent a été mis de plus en plus sur le développement de matériaux à haute performance utilisant les ressources naturelles [32]. Les polymères thermoplastiques renforcés de fibres naturelles, telles que le bois, le lin et le chanvre, ont démontré des qualités mécaniques spécifiques prometteuses et un impact environnemental plus faible, ce qui en fait une option attrayante pour l'impression 3D [10]. D'autre part, la fabrication de matériaux composites est une stratégie efficace pour surmonter les inconvénients des PMF pures

et élargir leur gamme d'applications. Dans les composites PMF classiques (CPMF), l'ajout de charges renforçantes augmente progressivement les propriétés mécaniques, tandis que la matrice PMF conserve l'effet de mémoire de forme [33]. Cependant, les composites plastiques renforcés de fibres naturelles présentent des défis importants notamment au cours du processus d'impression 3D en raison de leurs propriétés et caractéristiques diverses et le défi dans ce cas est de trouver le % de la charge en fibre qui assure l'équilibre entre les propriétés mécaniques et mémoire de forme.

1.2.3 Vers des composites fiables : Comment préserver l'effet mémoire sous sollicitations répétées et vieillissement thermohydrique ?

L'étude de l'effet de plusieurs cycles de programmation et de récupération est essentielle pour évaluer la durabilité des mélanges polymères et des composites à mémoire de forme. Après des sollicitations répétées, les performances de mémoire de forme peuvent être améliorées ou dégradées selon la stabilité des interfaces et la compatibilité des matériaux. En particulier, pour les composites renforcés de fibres naturelles ou de nanocellulose, il est crucial d'analyser la capacité à maintenir les propriétés mécaniques et la mémoire de forme sur le long terme. Cette approche est indispensable pour concevoir des matériaux fiables et performants pour des applications avancées en impression 4D.

En parallèle, un autre défi majeur reste peu exploré dans la littérature : l'impact du vieillissement en milieu humide, et en particulier dans l'eau chaude, sur les propriétés des composites polymères renforcés de fibres naturelles à mémoire de forme. Or, dans de nombreuses applications fonctionnelles (environnements biomédicaux, marins ou à forte humidité), ces matériaux sont exposés à des conditions thermohydriques prolongées susceptibles d'altérer leurs performances. L'absorption d'eau par les fibres naturelles peut entraîner un gonflement, une dégradation des interfaces fibre/matrice, une réduction de la cohésion mécanique et une perte d'efficacité de l'effet mémoire. Pourtant, les études expérimentales évaluant ces phénomènes restent rares et partielles, limitant la compréhension des mécanismes de dégradation et la capacité à concevoir des matériaux à la fois intelligents, durables et adaptés à des conditions d'usage réelles. Cette lacune constitue un obstacle important au déploiement à grande échelle des composites bio-inspirés en impression 4D.

1.2.4 Défi du renforcement nanoscopique : Comment exploiter la nanocellulose sans altérer la mémoire de forme ?

L'intégration de renforts nanométriques dans des polymères à mémoire de forme constitue un défi majeur. Comment exploiter le potentiel de la nanocellulose pour renforcer la matrice sans altérer la capacité de mémoire de forme du polymère ? En effet, la présence de charges rigides à l'échelle nanométrique peut perturber la mobilité des chaînes polymériques et modifier les transitions thermomécaniques critiques responsables du comportement mémoire. La question centrale est donc d'établir un équilibre entre renforcement mécanique et préservation de la fonction intelligente du matériau.

1.2.5 Fusionner géométrie et intelligence matérielle : Un défi pour la conception de structures auxétiques 4D

La faisabilité de l'impression 4D de structures auxétiques composites constitue un défi scientifique et technologique majeur. La complexité géométrique des motifs auxétiques, associée à la maîtrise des paramètres d'impression et à la compatibilité entre la matrice polymérique, les renforts naturels et les conditions thermomécaniques, rend difficile la production de structures stables et fonctionnelles. Ces contraintes influencent directement la programmation du mouvement, la réversibilité de forme et la durabilité des composites imprimés.

Pourtant, le potentiel de ces structures demeure considérable. Leur mécanisme de déformation unique, fondé sur un rapport de Poisson négatif, permet théoriquement d'obtenir une absorption d'énergie élevée, une résistance à l'indentation et une flexibilité remarquable [35].

L'impression 4D ouvre la possibilité de programmer ces comportements afin de provoquer des déformations contrôlées sous l'effet de stimuli externes tels que la chaleur, permettant ainsi des transformations séquentielles et adaptatives [36]. Ce comportement est notamment rendu possible grâce à l'utilisation de polymères à mémoire de forme, capables de répondre à des stimuli thermiques spécifiques et d'offrir un réglage précis de la température d'activation du mouvement [37].

1.3 Objectifs de la thèse

L'objectif général de cette thèse est d'améliorer la compréhension des phénomènes mis en cause dans l'impression 4D de matériaux composites à structures auxétiques. De cet objectif général découlent quatre objectifs spécifiques :

1.3.1 Développer de nouveaux mélanges optimaux de polymères à mémoire de forme (PMF)

L'objectif est de concevoir et formuler des mélanges de polymères capables de répondre à des exigences combinées de résistance mécanique et de performance mémoire de forme. Cela implique l'étude de différentes combinaisons de polymères (ex. PLA, ABS, PETG, PMMA) selon divers ratios de mélange. Un accent particulier sera mis sur l'analyse de l'effet des paramètres d'impression 3D, notamment l'orientation des couches déposées, sur les performances mécaniques (module de Young, résistance à la traction, déformation à la rupture). En effet, l'orientation des couches influe considérablement sur l'adhésion inter-couche, la répartition des contraintes et la déformation.

Un mélange binaire de polymères sera sélectionné en fonction de ses performances en mémoire de forme et de ses propriétés mécaniques, afin de permettre une étude approfondie de l'effet de la température et du nombre de cycles sur la stabilité fonctionnelle. Ce système sera également évalué pour sa capacité à être programmé avec plusieurs formes successives, ouvrant la voie à des applications potentielles en robotique souple.

1.3.2 Développer des matériaux composites à base de PMF renforcés par des fibres naturelles

L'objectif est d'intégrer des charges naturelles dans les mélanges de PMF définis à l'étape a), afin d'améliorer leurs propriétés mécaniques (rigidité, résistance à la traction) sans dégrader les performances de mémoire de forme. Il s'agira aussi d'évaluer l'impact de la nature et du taux de charge sur la compatibilité interfaciale et la dispersion des renforts, ainsi que leur influence sur la réponse aux stimuli thermiques.

Il faudra aussi analyser la durabilité des performances de mémoire de forme sous sollicitation cyclique qui vise à simuler des conditions d'utilisation réelles (répétitions de cycles de déformation-récupération) afin d'évaluer la stabilité fonctionnelle des composites développés. Les propriétés à surveiller incluent la stabilité dimensionnelle et la conservation des performances de mémoire de forme après plusieurs cycles.

De plus, cette partie propose une analyse approfondie de l'impact du vieillissement en eau chaude sur les propriétés mécaniques et le comportement à mémoire de forme de composites renforcés par des fibres de lin, fabriqués par impression 4D.

1.3.3 Intégrer la nanocellulose dans des PMF pour l'impression 4D de matériaux multifonctionnels

Ici le but est d'explorer l'intégration de la nanocellulose dans des matrices polymères à mémoire de forme afin d'optimiser les propriétés mécaniques des composites tout en préservant, voire en renforçant, l'effet mémoire, en vue du développement de matériaux durables, légers et multifonctionnels adaptés à l'impression 4D.

1.3.4 Évaluer la faisabilité technique de l'impression 4D de structures auxétiques avec les matériaux développés

L'objectif est de concevoir, simuler numériquement et imprimer des structures auxétiques programmables en 4D. Ces structures seront réalisées à partir des composites renforcés définis aux étapes précédentes et caractérisées en termes de comportement auxétique, d'efficacité mémoire de forme et de réponses mécaniques complexes (compression).

1.4 Structure de la thèse

Cette thèse est structurée en huit chapitres, conçus de manière progressive et interdépendante, afin de répondre aux objectifs spécifiques ci-dessus. Chaque chapitre constitue une étape méthodologique ou expérimentale contribuant directement à l'atteinte de l'un ou plusieurs de ces objectifs, avec un fil conducteur centré sur le développement de matériaux polymères intelligents destinés à l'impression 4D.

Le chapitre 1 introduit la problématique scientifique, en mettant en lumière les enjeux liés à la fabrication de structures intelligentes capables de changer de forme dans le temps, sous l'effet d'un stimulus externe. Il définit les objectifs généraux de la recherche ainsi que les quatre objectifs spécifiques, qui orienteront les développements expérimentaux présentés dans les chapitres suivants. Ce chapitre trace également les grandes lignes de l'approche adoptée, intégrant à la fois la formulation de matériaux, leur renforcement par des charges naturelles, leur évaluation fonctionnelle et leur application potentielle dans des géométries auxétiques.

Le chapitre 2 propose une revue de littérature complète sur les matériaux à mémoire de forme (PMF), les structures auxétiques, les fibres naturelles, les procédés de fabrication additive, notamment l'impression 4D. Il permet de situer la problématique dans le contexte scientifique

actuel, de justifier les choix de matériaux et d'orienter les stratégies expérimentales. Cette base théorique soutient la mise en œuvre des objectifs spécifiques en fournissant les fondements scientifiques nécessaires au développement des matériaux polymériques avancés.

Le chapitre 3 constitue la première étape expérimentale répondant à l'objectif spécifique a), qui vise à développer des mélanges polymériques à mémoire de forme ayant les meilleures propriétés mécaniques et fonctionnelles. Plusieurs formulations à base de polymères thermoplastiques sont explorées afin d'identifier celles présentant le meilleur compromis entre rigidité, capacité mémoire, imprimabilité et compatibilité avec l'impression 4D.

Le chapitre 4 prolonge ce travail par une étude approfondie des mélanges PLA/PETG, à travers un article scientifique qui détaille leur comportement thermo-mécanique, leur mémoire de forme, leur cristallinité et leur stabilité. Cette investigation expérimentale vient consolider l'objectif spécifique a), en validant un couple de polymères comme base solide pour les phases de renforcement ultérieures.

Le chapitre 5 répond à l'objectif spécifique b), en intégrant des fibres naturelles de lin dans les mélanges PMF afin d'améliorer leurs performances mécaniques sans compromettre leur effet mémoire. Ce chapitre analyse l'influence de la fibre de lin, la concentration du renfort et la compatibilité interfaciale sur les propriétés finales des composites obtenus, ouvrant la voie à des matériaux plus durables et biosourcés.

Le chapitre 6 approfondit cette approche en examinant la durabilité fonctionnelle des matériaux développés dans les chapitres précédents. À travers des essais de vieillissement accéléré en environnement humide. En effet, ce chapitre évalue la stabilité à long terme des propriétés mécaniques et mémoire de forme. Il permet de valider la fiabilité des composites renforcés, en lien avec l'objectif spécifique b), en garantissant leur bon fonctionnement dans des conditions d'usage réalistes.

Le chapitre 7 s'inscrit dans la continuité de l'objectif spécifique c), consacré à l'intégration de nanocristaux de cellulose (CNC) dans les matrices polymériques à mémoire de forme, et étend cette démarche vers la réalisation de structures auxétiques imprimées en 4D, conformément à l'objectif d).

L'incorporation des CNC vise à augmenter la performance mécanique et la stabilité thermique des composites tout en préservant leur effet mémoire de forme. Ces améliorations sont déterminantes

pour la mise en œuvre de géométries auxétiques actives, où la déformation réversible dépend à la fois des propriétés intrinsèques du matériau et de l'architecture de la structure**.**

Enfin, **le chapitre 8** conclut la thèse par une synthèse générale des résultats obtenus, une évaluation des contributions scientifiques du travail et une ouverture sur les perspectives. Ce chapitre met en relation l'ensemble des résultats avec les quatre objectifs spécifiques initiaux, en soulignant leur atteinte.

L'enchaînement des chapitres reflète une progression logique et structurée. Les deux premiers chapitres posent les bases théoriques et méthodologiques. Les chapitres 3 et 4 se concentrent sur l'élaboration de formulations PMF de base. Les chapitres 5 et 6 apportent des renforcements successifs : d'abord macroscopiques avec les fibres, puis à l'échelle nanométrique, tout en validant leur durabilité. Le dernier chapitre permet de replacer ces avancées dans un contexte d'application finale, fermant ainsi la boucle entre recherche fondamentale et innovation fonctionnelle. Cette structuration rigoureuse permet de répondre efficacement à l'ensemble des objectifs spécifiques et d'ouvrir vers des perspectives concrètes pour des matériaux programmables imprimés en 4D.

1.5 Références

1. Megdich, A., M. Habibi, and L. Laperriere, A review on 4D printing: Material structures, stimuli and additive manufacturing techniques. Materials Letters, 2023: p. 133977.
2. Park, J.Y., et al., Compatibility and physical properties of poly (lactic acid)/poly (ethylene terephthalate glycol) blends. Macromolecular Research, 2012. 20: p. 1300-1306.
3. Momeni, F., X. Liu, and J. Ni, A review of 4D printing. Materials & design, 2017. 122: p. 42-79.
4. Chu, H., et al., 4D printing: a review on recent progresses. Micromachines, 2020. 11(9): p. 796.
5. Sunte, J., A Review on 4D–Printing Design Materials. Int J Sci Res Mech Mater Eng, 2022. 6(3): p. 19.
6. Spiegel, C.A., et al., 4D printing at the microscale. Advanced Functional Materials, 2020. 30(26): p. 1907615.
7. Samuel, C., et al., Designing multiple-shape memory polymers with miscible polymer blends: evidence and origins of a triple-shape memory effect for miscible PLLA/PMMA blends. Macromolecules, 2014. 47(19): p. 6791-6803.
8. Meng, Q. and J. Hu, A review of shape memory polymer composites and blends. Composites Part A: Applied Science and Manufacturing, 2009. 40(11): p. 1661-1672.
9. Strzelec, K., N. Sienkiewicz, and T. Szmechtyk, Classification of shape-memory polymers, polymer blends, and composites. Shape Memory Polymers, Blends and Composites: Advances and Applications, 2020: p. 21-52.
10. Ahmed, H.I., et al., Development of 3D auxetic structures using para-aramid and ultra-high molecular weight polyethylene yarns. The Journal of the Textile Institute, 2021. 112(9): p. 1417-1427.
11. Chen, Y., et al., Lattice metamaterials with mechanically tunable Poisson's ratio for vibration control. Physical Review Applied, 2017. 7(2): p. 024012.
12. Wu, L., B. Li, and J. Zhou, Isotropic negative thermal expansion metamaterials. ACS applied materials & interfaces, 2016. 8(27): p. 17721-17727.
13. Alderson, K.L., A. Fitzgerald, and K.E. Evans, The strain dependent indentation resilience of auxetic microporous polyethylene. Journal of Materials Science, 2000. 35: p. 4039-4047.
14. Shan, S., et al., Design of planar isotropic negative Poisson's ratio structures. Extreme Mechanics Letters, 2015. 4: p. 96-102.
15. Ren, X., et al., Design and characterisation of a tuneable 3D buckling-induced auxetic metamaterial. Materials & Design, 2018. 139: p. 336-342.
16. Yu, X., et al., Mechanical metamaterials associated with stiffness, rigidity and compressibility: A brief review. Progress in Materials Science, 2018. 94: p. 114-173.
17. Parandoush, P. and D. Lin, A review on additive manufacturing of polymer-fiber composites. Composite Structures, 2017. 182: p. 36-53.
18. Boumaud, A., et al., Towards the design of high performance biocomposites. Prog Mater Sci, 2018. 97: p. 347-408.
19. Sekar, V., et al., Additive manufacturing: a novel method for developing an acoustic panel made of natural fiber-reinforced composites with enhanced mechanical and acoustical properties. Journal of Engineering, 2019. 2019.
20. Le Duigou, A., et al., Natural fibres actuators for smart bio-inspired hygromorph biocomposites. Smart Materials and Structures, 2017. 26(12): p. 125009.
21. Faruk, O., et al., Biocomposites reinforced with natural fibers: 2000–2010. Progress in

polymer science, 2012. 37(11): p. 1552-1596.
22. Mohanty, A.K., M. Misra, and L. Drzal, Sustainable bio-composites from renewable resources: opportunities and challenges in the green materials world. Journal of Polymers and the Environment, 2002. 10: p. 19-26.
23. Pickering, K.L., M.A. Efendy, and T.M. Le, A review of recent developments in natural fibre composites and their mechanical performance. Composites Part A: Applied Science and Manufacturing, 2016. 83: p. 98-112.
24. Aitomäki, Y. and K. Oksman, Reinforcing efficiency of nanocellulose in polymers. Reactive and Functional Polymers, 2014. 85: p. 151-156.
25. Arrieta, M., et al., Nanocellulose-based polymeric blends for food packaging applications. Multifunctional polymeric nanocomposites based on cellulosic reinforcements, 2016: p. 205-252.
26. Yuan Lu, A., et al., Nanocellulose in polymer composites and biomedical applications. TAPPI J, 2003. 13: p. 10-12.
27. Lendlein, A., A.M. Schmidt, and R. Langer, AB-polymer networks based on oligo (ε-caprolactone) segments showing shape-memory properties. Proceedings of the National Academy of Sciences, 2001. 98(3): p. 842-847.
28. Rousseau, I.A. and P.T. Mather, Shape memory effect exhibited by smectic-C liquid crystalline elastomers. Journal of the American Chemical Society, 2003. 125(50): p. 15300-15301.
29. Liu, C., et al., Chemically cross-linked polycyclooctene: synthesis, characterization, and shape memory behavior. Macromolecules, 2002. 35(27): p. 9868-9874.
30. Lee, B.S., et al., Structure and thermomechanical properties of polyurethane block copolymers with shape memory effect. Macromolecules, 2001. 34(18): p. 6431-6437.
31. Liu, C., H. Qin, and P. Mather, Review of progress in shape-memory polymers. Journal of materials chemistry, 2007. 17(16): p. 1543-1558.
32. Habibi, M., G. Lebrun, and L. Laperrière, Experimental characterization of short flax fiber mat composites: tensile and flexural properties and damage analysis using acoustic emission. Journal of materials science, 2017. 52: p. 6567-6580.
33. Lei, M., et al., Recent progress in shape memory polymer composites: methods, properties, applications and prospects. Nanotechnology reviews, 2019. 8(1): p. 327-351.
34. Shen, R., et al., Research progress and development demand of nanocellulose reinforced polymer composites. Polymers, 2020. 12(9): p. 2113.
35. Bouguermouh, K., M. Habibi, and L. Laperrière, 4D printing of fiber-reinforced auxetic structures: the building blocks: a review. Smart Materials and Structures, 2024.
36. Pandini, S., et al., Shape memory response and hierarchical motion capabilities of 4D printed auxetic structures. Mechanics Research Communications, 2020. 103: p. 103463.
37. Pasini, C., et al., Experimental investigation and modeling of the temperature memory effect in a 4D-printed auxetic structure. Smart Materials and Structures, 2022. 31(9): p. 095021.

Chapitre 2 : Revue de littérature sur les éléments constitutifs de l'impression 4D de structures auxétiques renforcées de fibres

Ce chapitre a fait l'objet d'une publication :

4D printing of fiber-reinforced auxetic structures: the building blocks: a review. Bouguermouh Karima, Habibi Mohamed, Laperrière Luc. Smart Materials and Structures, 2024, vol. 33, no 6, p. 063001.

Il peut être consulté en ligne à l'adresse suivante : DOI 10.1088/1361-665X/ad469d

Cet article propose une revue approfondie des avancées dans le domaine de l'impression 4D, en mettant en lumière les éléments constitutifs fondamentaux permettant de concevoir des structures intelligentes et morphables : les polymères à mémoire de forme (PMF), les structures auxétiques, les mélanges polymériques et les composites renforcés de fibres.

La première partie traite des polymères à mémoire de forme, capables de changer de forme en réponse à divers stimuli (chaleur, électricité, lumière, magnétisme). L'article distingue les PMF à transformation simple, double ou multiple, et explore les mécanismes de programmation/récupération. Il souligne l'intérêt croissant pour les mélanges polymériques (PLA/PCL, PLA/PMMA, etc.) comme alternative aux réseaux polymères réticulés. Ces mélanges permettent de moduler les températures de transition, d'élargir les gammes d'activation et d'améliorer la flexibilité, bien que leur miscibilité et leur comportement mécanique dépendent fortement de la formulation et des interactions interphases.

L'étude s'intéresse ensuite aux structures auxétiques, qui présentent un rapport de Poisson négatif, se dilatant latéralement lorsqu'elles sont étirées. Grâce à leur comportement mécanique singulier, ces structures offrent une excellente absorption d'énergie, une résistance accrue aux chocs et une grande flexibilité. Leur intégration à des PMF permet d'obtenir des systèmes capables de déformations programmées complexes, avec des applications en robotique souple, dispositifs biomédicaux et structures déployables.

La revue explore également le rôle du renforcement par fibres, qu'elles soient synthétiques (carbone, verre) ou naturelles (lin, chanvre, bambou), dans l'amélioration des propriétés mécaniques des PMF. Des études comparatives sont présentées entre fibres courtes et fibres continues, et l'effet de paramètres comme l'orientation, la porosité, la compatibilité interfaciale ou les procédés de dépôt (FDM, coextrusion).

Enfin, l'article met l'accent sur l'émergence des composites auxétiques imprimés en 4D, combinant géométries architecturées et matériaux actifs. L'impression 4D permet de fabriquer des structures capables de transformations séquentielles ou adaptatives sous stimuli. Plusieurs cas d'étude sont discutés (stents auxétiques, structures chirales à mémoire, composites bio-inspirés) illustrant l'intégration de fibres, de mélanges polymériques et de structures auxétiques dans un système imprimable, multifonctionnel et programmable.

La conclusion met en évidence les principaux défis scientifiques et technologiques actuels, notamment la compatibilité entre les constituants, le contrôle précis de l'effet mémoire de forme, la durabilité fonctionnelle à long terme, la stabilité thermique des systèmes, ainsi que l'intégration cohérente de ces matériaux dans les procédés de fabrication additive.

4D printing of fiber-reinforced auxetic structures: the building blocks: A review

Bouguermouh Karima[1], Mohamed Habibi[1*] and Luc Laperrière[1]

[1] *Department of Mechanical Engineering, Université du Québec à Trois-Rivières, Quebec, Canada.*

2.1 Abstract

Four-dimensional (4D) printing has recently received much attention in the field of smart materials. It concerns using additive manufacturing to obtain geometries that can change shape under the effect of different stimuli. Such a technique enables the fabrication of 3D printed parts with the additional functionality of scalable, programmable, and controllable part shapes over time.

This review provides a comprehensive examination of advances in the field of 4D printing, emphasizing the integration of fiber reinforcement and auxetic structures as crucial building blocks. The incorporation of fibers enhances structural integrity, while auxetic design principles contribute unique mechanical properties, such as negative Poisson's ratio and great potential for energy absorption due to their specific deformation mechanisms. Therefore, they present potential applications in aerospace, drones, and robotics.

The objective of this review article is first to describe the distinctive properties of shape memory polymers (SMPs), auxetic structures, and composite (fiber-reinforced) materials. A review of applications that use combinations of such materials is also presented when appropriate. The goal is to get a grip on the delicate balance between the different properties achievable in each case. The paper concludes by describing recent advances in 4D printing of fiber-reinforced auxetic structures.

Keywords: 4D printing, smart materials, SMPs, auxetic structures, fiber reinforcement.

2.2 Introduction

SMPs are a category of intelligent materials capable of transitioning between their original shape and a temporary shape in response to different external triggers [1], including heat [2], moisture [3], light [4], electricity [5], and magnetism [6]. SMPs have several advantages: being lightweight, simple to prepare, cost-effective, programmable, tunable (transformation temperature, modulus, stiffness, etc.), reversible, and recyclable techniques [7].

Due to their shape memory properties, smart materials have become a prominent class of engineering materials. When combined with 3D printing, these materials enable 4D printing, which

adds time as the fourth dimension and enhances the functionality of 3D-printed structures. Consequently, 4D printing has garnered substantial interest in various engineering applications, encompassing aerospace, automotive, civil infrastructure, electronics, robotics, biomimetics, biomedical fields, origami, and beyond [8].

Figure 2.1 shows that 4D printing is still relatively new but is expanding rapidly. Since 2014, a remarkable exponential increase in the volume of publications concerning this topic was noted [9]. For instance, between 2017 and 2022, sciencedirect.com published 173 and 983 articles, including review articles, research articles, and book chapters, covering various topics such as printing methods, shape memory material (SMM) development, and applications [10].

The mechanical characteristics of materials are essentially related to their structure, which can be managed by adjusting the material's structure. Therefore, it is possible to create a smart structure with a broad and controllable morphing capability by combining SMP with an auxetic structure. In this case, the auxetic structure shows exceptional mechanical prowess and flexibility, while the Shape Memory Polymer (SMP) can remember its altered shape, contributing to expanded structural adaptability [11].

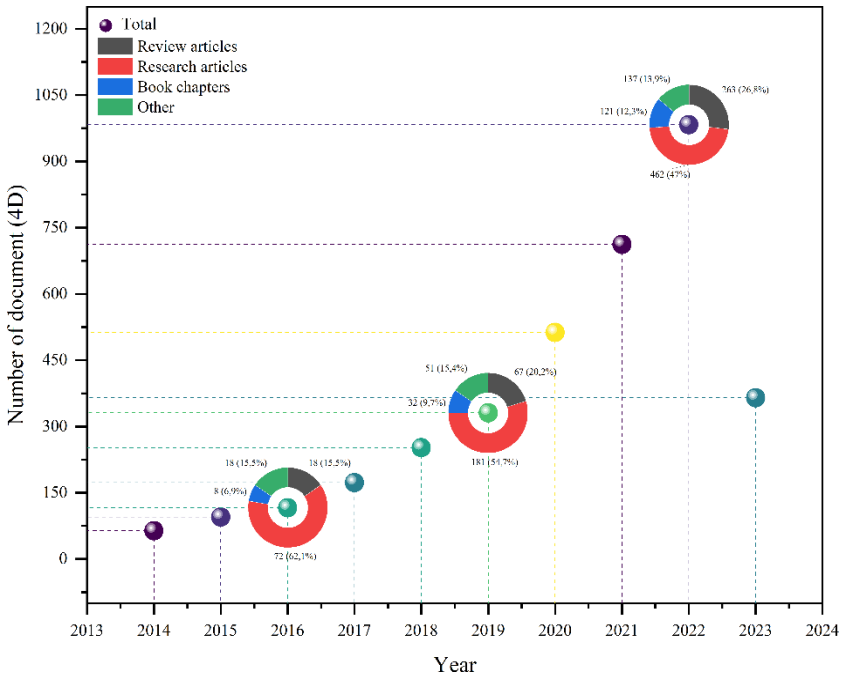

Figure 2.1:The progression of scientific publications on 4D printing according to sciencedirect.com.

Auxetic materials have been known for more than a century, but only in the past four decades (from the late 1980s to the present) have they attracted new attention [12]. Auxetic metamaterials exhibit superior mechanical properties, such as energy absorption [13], negative thermal expansions [14], resistance to indentation [15], shear modulus [16], and negative Poisson's ratio [17], compared to conventional materials.

Currently, the micromechanical models that aim to forecast and explain auxetic behavior are reviewed by Xianglong Yu et al. [18]. Indeed, based on the structural design resulting in the different mechanical properties, four subclasses of auxetic metamaterials have been identified: (i) the original re-entrant structure, similar to the folded-in cells fabricated from polyurethane foam, including various re-entrant open-cell microstructures, rotating squares or triangles; (ii) NPR induced by an elastic instability, particularly the missing rib models to pattern transformation; (iii) NPR using chiral building blocks, chiral or anti-chiral lattices; (iv) a portion of origami metamaterials, inspired by the design of the egg rack.

A hybrid auxetic structure, named re-entrant chiral auxetic structure (RCA), was recently developed by Amer Alomarah et al. [19] based on topological features of both re-entrant and chiral auxetic honeycombs fabricated from polyamide12 (PA12) and using an additive manufacturing process, Multi Jet Fusion (MJF). The findings indicate that specimens crushed quasistatically absorb more energy than those compressed dynamically. Moreover, differences in the deformation modes cause variations in Poison's ratio curves under quasistatic and dynamic tests. The findings indicate that specimens crushed quasistatically absorb more energy than those compressed dynamically. Moreover, differences in the deformation modes cause variations in Poison's ratio curves under quasistatic and dynamic tests.

The mechanical properties of 3D-printed polymeric objects can be improved thanks to the development of fiber-reinforced composites through Fused Filament Fabrication (FFF) [20]. Natural fibers are increasingly being used as a replacement for synthetic fibers in composite reinforcement due to their mechanical [21], acoustic [22], or even morphing properties [23], besides their low density, little effect on the environment, and different end-of-life handling [24]. Today, various processing methods, such as extrusion, film stacking, injection molding, thermoforming, and vacuum bag molding, can be used to process thermoplastic-based natural fiber biocomposites [24-26].

This paper demonstrates the potential advantages of combining auxetic structures, SMPs, and biocomposites into 4D printed structures. A thorough review of the literature in these distinctive but complementary fields highlights the benefits of such combinations.

2.3 SMPs

2.3.1 Types of SMPs

2.3.1.1 One-way and two-way SMPs

One-way SMPs always return to their original shape after deformation and can change to a new, temporary shape under the influence of an external stimulus, which is maintained over time. The original shape is recovered when the same stimulus is applied again. Two-way SMPs can gradually change shape in response to a stimulus (Figure 2.2. However, as soon as the stimulus is removed, the polymer immediately returns to its original shape. Therefore, unlike the single-way SMPs, two-way SMPs do not have a temporarily stable shape [27].

2.3.1.2 Multiple-way SMPs

Liu et al. [28] described a double dual-shape memory effect using a new type of semi-IPN (poly(methyl methacrylate)-poly(ethylene glycol) (PMMA-PEG)) that they developed through radical homopolymerization and cross-linking, in the presence of linear PEG. This semi-IPN exhibited two independent shape memory effects after melting PEG crystals and the T_g of semi-IPN. Later, a triple-SMP (t-SMP) was developed [29], which could change from its initial temporary shape (A) to a second temporary shape (B) and then to a third shape (C) triggered by a subsequent temperature rise.

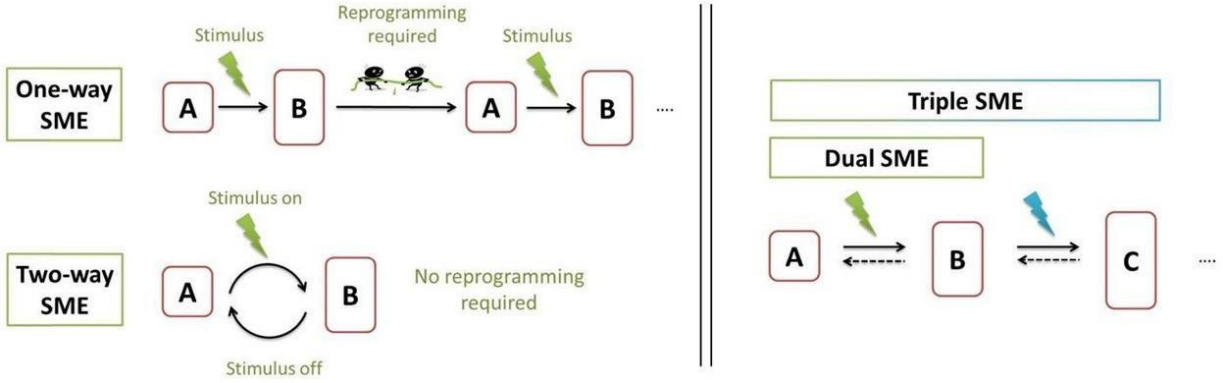

Figure 2.2: Basic definitions of shape memory effect (SME). Left: One-way and two-way SME. Right: Dual and triple SME. Each transition can represent a one-way or two-way SME, respectively. In case more than three shapes are achievable, the nomenclature is applied in accordance with that (quadruple, etc.) [30].

Bellin et al. [29] studied polymer networks comprising at least two distinctive domains. The first domain is a MACL network consisting of poly(cyclohexyl methacrylate) (PCHMA) main-chain cross-linked with difunctional PCL, which is characterized by two T_{trans} (T_m of the polymers). The second domain is a CLEG network consisting of grafted short PEG side chains on the PCL main chains.

While a quadruple SMP (q-SMP) showed good recovery, its fixation in the first two temporary shapes was relatively low. On the other hand, the literature describes the Quintuple- and multi-shape memory effect observed in electrospun membranes made from the thermoplastic polymer Nafion®, which has a broad transition temperature and potential applications in smart textiles, artificial intelligence robots, and biomedical engineering [31, 32].

2.3.2 Interesting properties of SMPs

The shape memory effect refers to the remarkable ability of a certain material to be deformed from a stable shape within a specific temperature range and, when exposed to an outside stimulus, revert to its initial form [33]. This stimulus can be direct thermal (temperature), indirect thermal (light, electric and magnetic fields), or of chemical origin (pH, specific ions and enzymes, etc.) [34, 35].

Many types of SMP systems are available, making it challenging to categorize them. Most SMPs are thermally induced, and their deformation must be above the transition temperature (T_{trans}). This temperature can be glass transition temperature (T_g) for amorphous SMPs, melting temperature (T_m) for semi-crystalline SMPs, or liquid crystal-isotropic phase transition (T_{ni}) for liquid crystal SMPs [36-38].

Figure 2.3 shows the shape memory effect of a polymer in response to a thermal stimulus. Firstly, the "programming" of the material which consists of deforming it using mechanical force after heating ($T > T_g$) to the needed secondary shape. The material is cooled in the second step while the applied force is kept constant. The stresses are subsequently relieved, leading to minimal elastic rebound of the material. At this step, the secondary shape is maintained without heat treatment. Lastly, the initial or permanent form is rendered when the material is reheated without external forces. The temperature required to fix the secondary shape and regain the initial shape is included in the glass transition area of the material [27, 39-41].

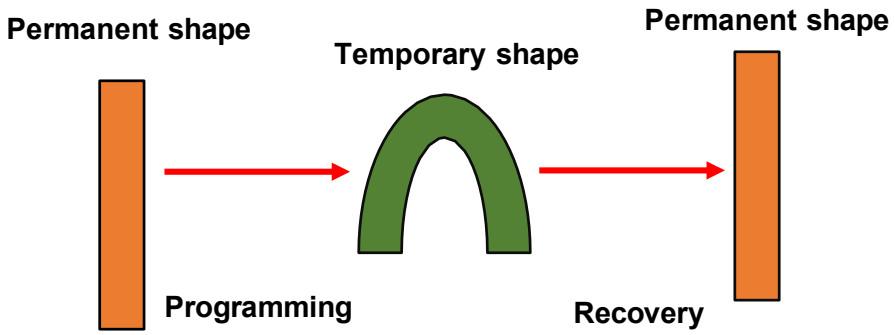

Figure 2.3: Schematic representation of the thermally induced one-way shape-memory effect.

2.3.3 Stimulus

2.3.3.1 Electro active SMPs

Conductive fillers, such as carbon particles, carbon nanotubes (CNTs), carbon fibers (CFs), carbon black (CB) and Nickel (Ni) powders, can be introduced into SMPs to create conductive pathways within the matrix. This results in electrical conductivity in the composite, and when an electric current is passed through it, the SMPs can be activated by the Joule heating effect.

In 2004, Koerner et al. [42] achieved electro-stimuli shape recovery by incorporating CNT into a PU network. The CNT network improved the polymer composite mechanical properties and shape recovery stress. In another study, Cho et al. [43] added conductive carbon fillers, such as carbon black and CNT, to SMPs. However, this strategy was ineffective as these particles did not increase the strength or toughness of the polymer matrix. Conversely, using CNTs proved to be a better approach as it required less substance and strengthened the materials. In fact, polymers containing 5% CNT had a conductivity of roughly 10^{-3} s cm^{-1}.

Liu et al. [44] introduced CNTs into PLA (polylactic acid) and observed a dependence of the volume resistivity on the raster angle and temperature, particularly above 70°C (Figure 2.4). The resistive heating resulted in different time dependencies of the temperatures reached in the samples. Authors achieved shape recovery values close to 100% during 100–350 s, depending on the voltage and the printing parameters. CNT-reinforced PLA filaments were used to prepare various braid-mimicking printed shapes [45]. Recovery was carried out at a temperature of 90°C, reached with a heat rate of 5 K/min, and was found to start earlier for CNT/PLA specimens than pure PLA, depending on the printed shapes. Furthermore, specimens infused with a silicone elastomer matrix were tested, showing higher shape recovery values of approximately 97% [46]. Moreover, recent research has demonstrated that carbon nanofiber and graphene can effectively enhance polymer composites' mechanical performance and conductivity [47].

Qian et al. [48] have reported a novel approach in which vapor-produced carbon nanofiber was incorporated into poly(ethylene-co-vinyl acetate). Indeed, Vapor-grown carbon nanofibers were inserted into poly(ethylene-co-vinyl acetate) through a solution mix. The resulting nanocomposite made of 15% vapor-grown carbon nanofibers exhibited rapid and uniform electrical heating, thanks to the high conductivity of the nanofibers and their homogeneous dispersion in the matrix. This led to successfully realizing an electrical-active two-way shape memory effect.

Furthermore, Leng et al. [49] developed an SMP/CB/Ni system by adding Ni particles and carbon black powders into a polyurethane (PU) SMP matrix. The CB powders were uniformly distributed within the PU matrix, while Ni powders were aligned into chains within the polymer matrix via a magnetic field during the preparation step. This alignment of Ni particles served as conductive channels to bridge CB aggregates together. To compare induction heating and shape recovery behavior under an electric field, referencing systems such as SMP/CB/Ni randomly distributed Ni particles and SMP/CB without Ni particles were also prepared to compare induction heating and shape recovery behaviour under an electric field. The Results showed that the system with aligned Ni particles exhibited significantly reduced resistivity and higher resistant heating than the reference systems, resulting in a complete shape recovery within 120 seconds under an electric field.

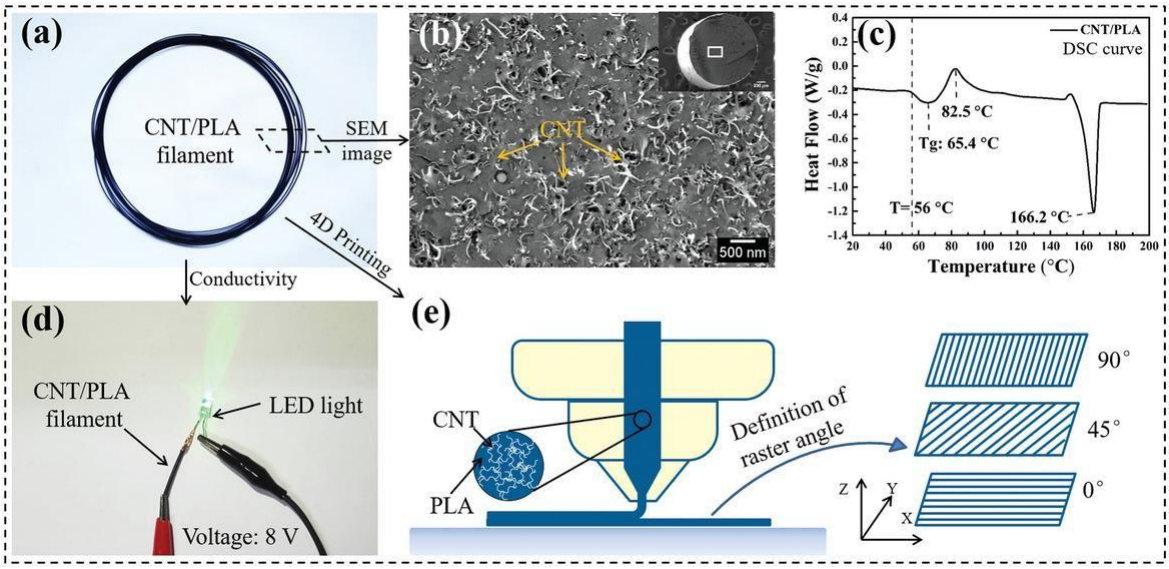

Figure 2.4: Shape-memory CNT/PLA filament for 4D printing. a) As-fabricated CNT/PLA filament. b) SEM cross- sectional image of the CNT/PLA filament. c) DSC curve of the CNT/PLA filament. d) Demonstration of the CNT/PLA filament as a conductor. e) Description of the fused deposition modeling technique and raster angle illustration [44].

In a recent study, Wang and co-workers [50] developed a novel 3D conductive network structure by incorporating silver nanowire/melamine foams/epoxy SMPCs. In another study, Shao et al. [51] utilized silver nanowires (Ag-NWs) and polylactic acid (PLA) to create an innovative electrically driven 4D printing composite. The Ag-NWs networks demonstrated outstanding electrical conductivity, even following repeated tensile and bending deformations. Researchers used a bio-inspired flower model to illustrate how each petal could be controlled separately.

Luo et al. [52] reported findings on using an Ag nanowire substrate with epoxy polymer and PCL layer, demonstrating remarkable self-healing and electro-active properties. However, the incompatibility between metal fillers and polymers poses a significant challenge as they exhibit entirely distinct interfacial characteristics [53].

2.3.3.2 Magnetic active SMPs

Magnetic SMPs offer numerous advantages. Firstly, the risk of overheating can be eliminated by carefully selecting particle materials with a specific ferromagnetic Curie temperature. Secondly, the self-generated heat allows for the activation of complex-shaped devices. Finally, the technique can be applied to embedded devices, including medical devices within the human body, as actuation can be triggered wirelessly and remotely [54, 55].

Incorporating magnetic particles, like Fe_2O_3 and Fe_2O_3, into SMPs can facilitate magnetically controlled shape memory behaviors. Electromagnetic energy can be converted into heat by subjecting these particles to a high-frequency alternating magnetic field. In a previous study 2006, Lendlein et al. [56] extruded Fe_3O_4 particles, with an average diameter of around 25 nm, into a polyether urethane (PEU)-based thermoplastic SMP matrix. The addition of magnetic fillers did not affect the switch temperature of the poly(tetramethylene glycol) (PTMG, soft segment of PEU), which acts as switch temperature (74 °C) in the shape memory process. Under a magnetic field (f = 258 kHz, H = 30 kA*m^{-1}), the composite rapidly increased in temperature (from 20 °C to around 90 °C within 150 seconds), and its shape recovery behavior under a magnetic field was similar to that obtained with direct heating.

Zhang et al. [32] reported on a composite membrane made from Nafion/Fe_3O_4 with a controlled magnetic trigger and shape memory effect. They observed surface temperatures of 38 to 40 °C, which are close to typical body temperature. To improve the distribution of ferrite oxide and its incorporation into the polymer, surface modification was necessary since the Fe_3O_4 particles created visible boundaries with the polymer matrix.

The introduction of magneto-responsive shape memory polymers (SMPs) into 4D printing has opened up new possibilities for developing intelligent items that can be controlled without the use of physical contact. Liu et al. [57] fabricated promising SMPs using 3D printing technology based on polylactic acid (PLA), thermoplastic polyurethane (TPU), and Fe_3O_4 particles with good mechanical properties and magneto-responsive behavior. The results demonstrated that the 3D-printed PLA/TPU/Fe_3O_4 possessed enhanced tensile strength and modulus with a homogeneous distribution of magnetic particles in polymer blends. Additionally, PLA/TPU/Fe_3O_4 showed excellent shape fix ratio (~100%), recovery ratio (>91%) and rapid magnetic response within as short as 40 seconds, which implies the high efficiency of heat generation by magnetic particles (Figure 2.5). To achieve stability and usefulness, magneto-active composites, like electro-active materials, require a homogeneous dispersion of sensitive components. A low addition of nanoparticles will not cause activation, while an excessive quantity will lead to aggregation [58]. Lee et al. [59] 3D printed shape memory materials in two-way adaptable size with two-way size adaptability could offer a useful volume change.

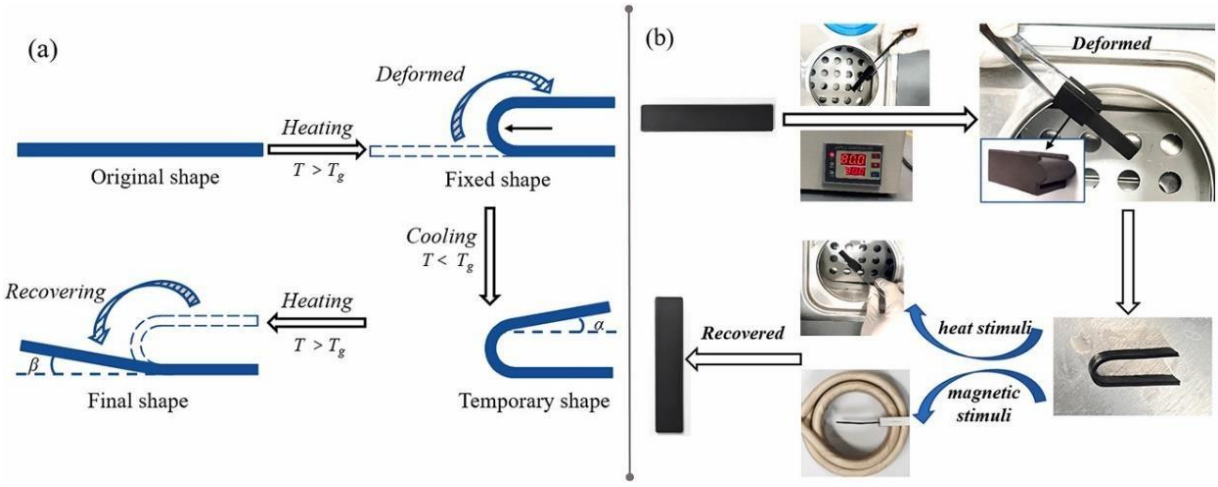

Figure 2.5: (a) Schematic representation and (b) experimental procedure of the shape memory programming technique [57].

Akshay et al. [60] used gelatin and an amino acid-based surfactant to create sensitive magnetic material suitable for active scaffolds, demonstrating the significant potential for long-term use, recoverable product parts and low production costs [58].

2.3.3.3 Light active SMPs

Various photo-reactive species such as organic dyes, ligands, carbon nanotubes, graphene, black ink, gold nanoparticles (AuNP), and gold nanorods have been employed for inductive heating for the shape recovery process of SMPs. Indeed, these species absorb light energy and convert it into heat through non-irradiative energy dissipation of electrons from excited state to ground state.

To achieve good light-activated shape recovery performance, the driving light's wavelength must be carefully selected [61]. Optical fibers can be embedded in SMPs to transmit infrared light to the SMPs. Appropriate optical fibers that work within the suitable frequency range for the SMPs' absorption peaks should be selected [61]. For example, Vaia et al. [42] prepared a polyurethane/carbon nanotube composite that exhibited shape memory behavior controllable by infrared light. The elongated deformation is preserved by strain-induced soft segment crystallization with a melting temperature of about 48°C.

Photoactive shape memory polymers can be developed through reversible photochemical crosslinking. This involves the formation of photo-induced reversible covalent cross-links using photochemically reactive groups found in polymers. Photodimerization moieties such as cinnamic acid, cinamylidene acetic acid, and coumarin and their derivatives have been introduced into polymer macromolecules to create photoactive shape memory switches [62-64].

Lendlein et al. [64, 65] developed two photo-responsive polymers with cinnamic acid and cinamylidene acetic acid terminal as the photoreversible switch. On the other hand, Wu et al. [66] synthesized a biodegradable SMP composed of N,N-bis(2-hydroxyethyl) cinnamamide, poly-(L-lactic acid), and polycaprolactone, where the photoactive cinnamamide was included into the block copolymer.

Gold nanoparticles and nanorods have also been applied as functional fillers for light control and shape memory behavior. These particles exhibit photothermal properties because of localized surface plasmon resonance (SPR) attributes. Zhang and coworkers [67] developed SMPCs with light-triggered shape memory effect and self-healing characteristics by crosslinking a small quantity of gold particles with a poly(ethylene oxide) (PEO) network. By adjusting the temperature in relation to the T_m of the crystalline phase, the photothermal effect regulates the shape memory process and enables damage repair within crystal melting and recrystallization (Figure 2. 6).

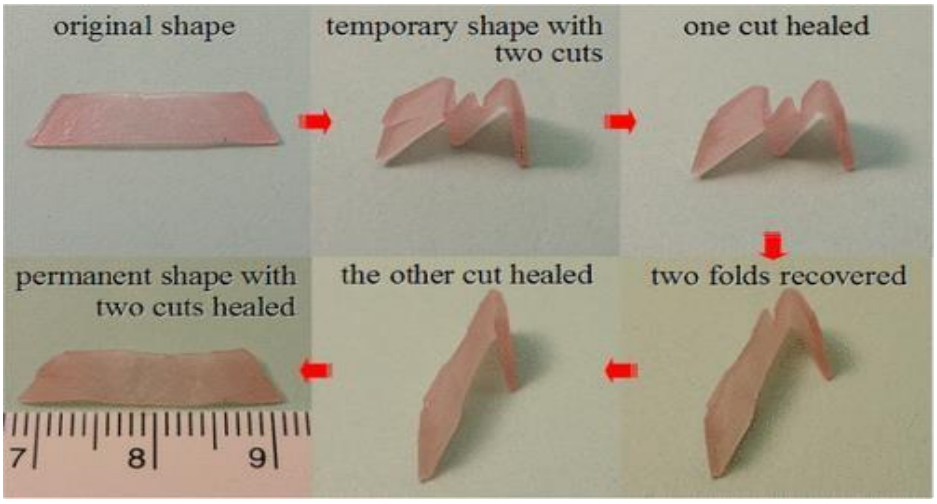

Figure 2. 6: SMPCs with light-triggered shape memory and self-healing properties [67].

In 2019, A new 4D printable photosensitive resin based on acrylate for digital light processing was developed by Wu et al. [68]. Additionally, they looked into how the amount of cross-linkers affected the mechanical and shape memory qualities. The findings demonstrate that the designed SMP with a 10 wt% crosslinker can endure 16 consecutive cycles and maintain an incredibly high shape recovery ratio of 100% even after 14 cycles. The storage modulus may reach up to 1.48 × 103 MPa with 50 wt% crosslinker, while the one with 20 wt% crosslinker has the best shape fixity ratio of over 96%. The 4D printed SMPs have a good shape recovery rate because they only need 7–13 seconds to restore their 180° shape.

Zhao et al. [69] used photopolymers to 4D-print SMPs via stereolithography. The fold-deploy test and shape-memory cycle measurements demonstrated a high shape recovery rate, shape fixity, and recovery of the printed samples. On the other hand, by using several 4D-printed patterns and some layers, Zolfagharian et al. [70] achieved controlled bending in a commercial prestrained SMP film. Differential shrinkage through the thickness of the actuator hinge was induced using photothermal stimulation.

2.4 Miscibility of Shape Memory polymer blends

2.4.1 PLA based SMPs blends

There are various methods to enhance the properties of PLA, including mixing it with different materials [71]. It has been found that in PLA/poly(ε-caprolactone) (PCL) blends, the homogeneous distribution of components in the composite indicates the microphase separation phenomena,

indicating that PLA and PCL are immiscible [72]. The PCL was the reversible phase and PLA the fixed phase [46]. By varying the PCL content between 10% and 60%, shape recovery ratios of 59% and 84% were achieved, while shape fixity exceeded 95%.

Recently, Poly(lactic acid) (PLA) and poly(vinyl acetate) (PVAc), a miscible model of pair polymer, were electrospun simultaneously using the dual-electrospinning approach. Indeed, using dynamic mechanical analysis revealed possibility to create an interwoven polymer composite with two clearly thermal transitions. Consequently, triple-SM behavior was found in the electrospun PLA/PVAc composites based on the results of SM studies [73].

To address the issue of brittleness in PLA at room temperature, Carlson and Li [74] blended it with thermoplastic polyurethane (TPU) in weight ratios ranging from 9:1 to 6:4, which resulted in reduced cracking and improved shape memory characteristics. Mohan et al. [75] reported that the PU/PLA (90/10) polymer blend system is thermodynamically miscible, which inhibits the production of distinct crystalline phases, in contrast to previous observations.

Additionally, Sun et al. [75] used Poly(ethylene glycol) (PEG) melt-blending to modify PLA filament, which enabled them to adjust the actuation temperatures of different parties of a sample. Compared to pure PLA with a recovery temperature above 60°C, PEG-blended samples had recovery temperatures of 55°C and below.

The PLA and PVDF systems exhibit semi-crystalline characteristics, with a crystallinity degree of approximately 50%. The T_g of the amorphous phase serves as a transition temperature and can be adjusted between the T_g of the two homopolymers.

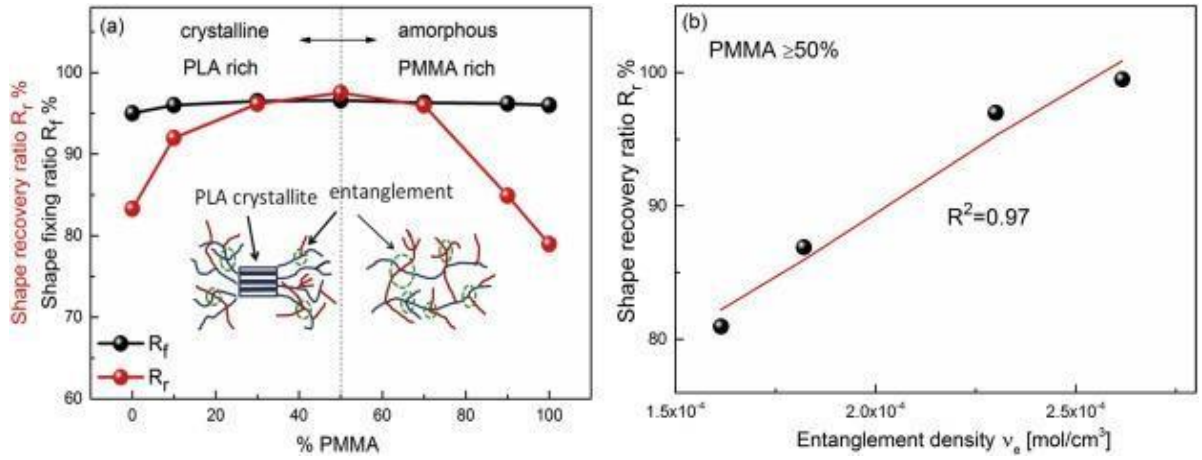

Figure 2.7: (a) The shape fixing ratio (Rf) and shape recovery ratio (Rr) of PLA/PMMA blends in relation with PMMA content, as well as the shape memory mechanism under various conditions, (b) The linear regression analysis between the shape recovery ratio (Rr) and the entanglement density (v_e) for blends containing more than 50% of PMMA [76].

Furthermore, Hao et al. [76] carried out research on the thermo-mechanical and rheological approaches of the miscible amorphous PMMA/semi-crystalline PLA blends shape memory. The results showed that by adding PMMA into PLA, a broad and increased glass transition temperature T_g was noticed by differential scanning calorimetry (DSC). Their findings demonstrated that 100% shape recovery was achieved when the PMMA content was up to 50%, as illustrated in Figure 2.7 Zhang et al. [77] prepared PAE/PLA blends by melt blending, improving mechanical properties. DMA experiments revealed that the PAE/PLA blends were partially miscible systems, and SEM images demonstrated that the PAE was uniformly dispersed in the PLA matrix.

Compared to plain PLA, the PAE/PLA considerably revealed greater elongation at break and exhibited impressive shape-memory effects. The PAE acting as concentrators facilitated the stress release and energy dissipation process, which prevented the PLA from breaking under extreme deformation.

Additionally, Min [78] and Zheng [79] developed a multiblock copolymer, PLA-co-poly(glycolide-cocaprolactone), and PLA–HA composites that exhibit desirable shape-memory properties.

2.4.2 TPU based SMPs blends

Previous research has shown that several types of aliphatic polyesters are miscible with (polyvinyl chloride) (PVC), poly (styrene-co-acrylonitrile) (SAN), and phenoxy resin. With segmented thermoplastic polyurethanes (TPUs) that contain aliphatic polyester soft segment, PVC and aliphatic polyester segments were found to be miscible, with the glass transition temperature (T_g) of the PVC/aliphatic polyester segment domain varying smoothly with composition. The hard segment domain of the blend acted as a physical cross-linker. However, the aliphatic polyester segment and SAN were not miscible in TPUs containing aliphatic polyester with SAN or acrylonitrile butadiene styrene (ABS) resin. In this case, when the aliphatic polyester segment content in TPU is 20±75 wt:%, the blend exhibited two distinct T_{gs} for the SAN domains and aliphatic polyester segment [80].

Jeong et al. [81] conducted research to investigate the compatibility and the shape memory properties of PVC blends when combined with segmented thermoplastic polyurethanes (TPUs) synthesized from diol-terminated polycaprolactone (PCL), hexamethylene diisocyanate, and 4,4-dihydroxy biphenyl. Their findings revealed that PVC exhibited miscibility with the PCL segment

within the TPU, and the glass transition temperature (T_g) of this miscible amorphous region exhibited a gradual change as a function of composition. The hysteresis in repeated cyclic tensile tests was decreased in PVC/TPU blends with a weight ratio of 8/2, but unrecoverable permanent deformation increased in 6/4 blends.

2.4.3 Other SMPs blends

In a recent study, Eken et al. [82] utilized Atom transfer radical polymerization (ATRP) to prepare P(VDF-co-CTFE)-g-PEGMA copolymers. They used poly(vinylidene fluoride-co-chlorotrifluoroethylene) P(VDF-co-CTFE) as macroinitiator and poly(ethylene glycol) methyl ether methacrylate (PEGMA) as the building block of side chains. The resultant hydrophilic SMPs (SMPs) had adjustable mechanical and thermal properties. By altering the soft segment ratio, the soft segments' melting temperature (T_m) was adjusted to range from 35.3 to 40.9°C, close to human body temperature. The copolymers exhibited remarkable shape memory capabilities comparable to the T_m of the soft segments, with full recovery achieved in just 10 seconds.

Mather et al. [83] described miscible amorphous/semicrystalline SMP blend, namely amorphous PMMA/semicrystalline polyvinylidene fluoride (PVDF). It was found that the crystals acted as physical crosslinks, and the critical temperature for triggering shape recovery was T_g of the amorphous phase [84]. You et al. [85] reported shape memory characteristics of (PVDF)/acrylic copolymer blends in various compositions and found that blends containing 40 to 50 % PVDF had the best shape memory recovery qualities.

Acrylic bone cement commonly uses a prepolymer of PMMA, PMMA-co-PS, or their mixtures [86]. The compatibility and miscibility of polymer blends comprising PS, PMMA, or both have been studied [87, 88], with some reports suggesting the immiscibility of PS/PMMA blends [89, 90].

Liu et al. [91] prepared PMMA/PEG semi-interpenetrating network (PMMA-PEG semi-IPN) using radical polymerization and crosslinking of methyl methacrylate (MMA) in the presence of 2,2′-azoisobutyronitrile (AIBN) initiator, ethylene glycol dimethacrylate (EGDMA) cross-linker, and linear PEG. The study demonstrated that PMMA-PEG semi-IPN exhibited two shape memory effects based on the T_m of the PEG crystals and the T_g of the semi-IPN, with a high recovery ratio of 99%.

2.5 Auxetic structures

Auxetic materials, also referred to as materials exhibiting a negative Poisson's ratio (NPR) effect, possess the distinctive characteristic of expanding in width when stretching and narrowing when subjected to compression [92].

As Figure 2.8 (a) illustrates, conventional materials exhibit a positive Poisson's ratio (ν). However, by changing the geometry to an auxetic structure, as shown in Figure 2.8 (b), subjecting it to the same loading through hinging of the ribs leads to elongation/compression along both axes, thereby resulting in a negative Poisson's ratio (ν) [11].

Classical elasticity theory indicates that many material characteristics depend on its Poisson ratio. A widely recognized example is the shear modulus, denoted as G, which can be mathematically represented as:

$$G = \frac{E}{2*(1+\nu)}$$

E is Young's modulus. It is evident that when ν gets closer to -1, the limit for an isotropic material, the shear modulus will tend toward infinity.

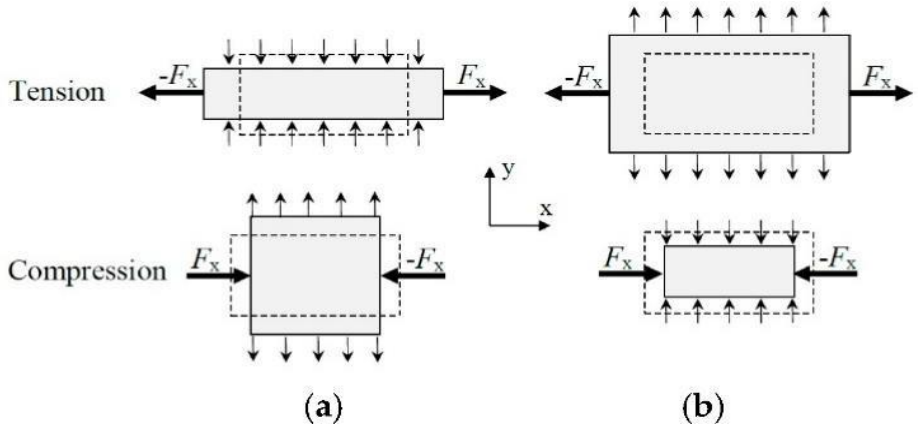

Figure 2.8: (a) Non-auxetic (b) Auxetic behavior under loading [93]. Initial state before loading in dotted lines.

Auxetic materials and structures can be found at various levels, ranging from the macroscopic to the molecular levels. Auxetic metamaterials are essentially categorized as cellular, natural, metallic, or multi-material composites [21] based on their base material and internal structure. Among these, auxetic polymeric materials have received significant attention and have been extensively researched.

Recently, numerous developments in the field of auxetic polymeric materials, including foam, fiber, and even composite, have taken place. Examples of such materials include polytetrafluoroethylene (PTFE) [94], polyester urethane (PU) [95], ultra-high molecular weight polyethylene (UHMWPE) [96], polypropylene foam (PP) [97], polyester [98], nylon [99], liquid crystalline polymers [100] and other synthetic molecular auxetic polymer [101]. In addition to polymeric materials, different varieties of auxetic materials based on metal, ceramic, and other inorganic materials have also been synthesized [102-104].

Cellular auxetic meta-materials can be classified into re-entrant structures, chiral structures, rotational (semi-) rigid structures, crumpled and perforated sheet models, and other miscellaneous structures as Figure 2.9 illustrates [105].

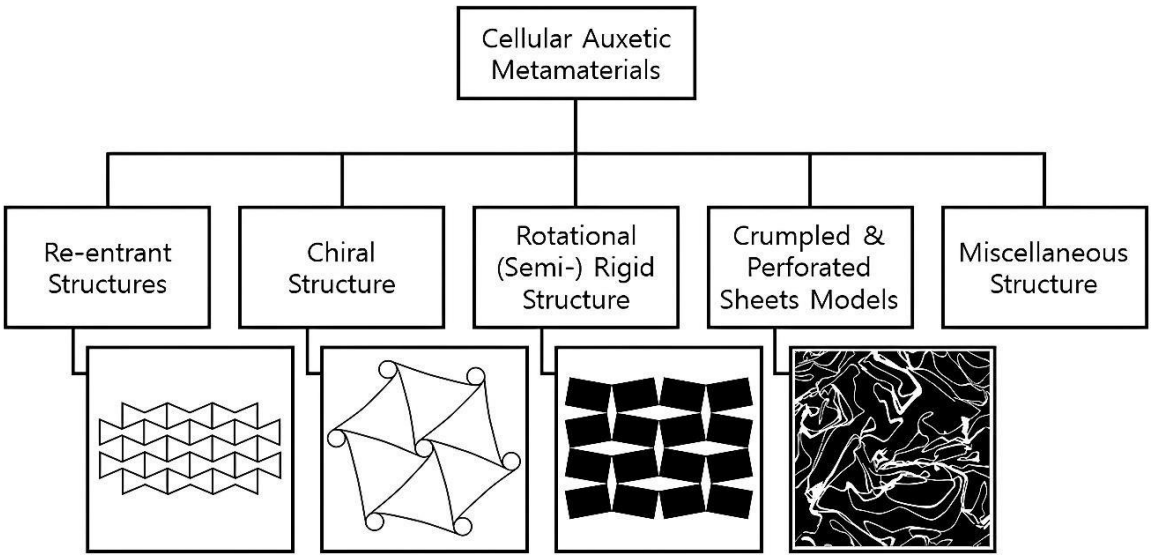

Figure 2.9: Classification of cellular auxetic metamaterials [105].

Recently, a novel 3D printed auxetic structure, called re-entrant chiral auxetic (RCA) structure, has been introduced. This structure has been designed by integrating chiral characteristics into a re-entrant honeycomb, as proposed in previous studies [106, 107]. The experimental results have demonstrated that the RCA structure outperformed the re-entrant honeycomb in terms of both stress and auxetic behavior, particularly in the X direction. These promising have prompted further investigations into the compressive properties of the RCA structure, including stress-strain curves, energy absorption, and auxetic behavior.

Choudhry et al. [108] conducted a study on modified re-entrant auxetic honeycombs using fused filament fabrication (FFF) along with parametric analysis and geometry optimization to investigate their in-plane energy absorption characteristics. The results showed that the modified structure exhibited a 36% increase in specific energy absorption capacity compared to the original design. The increase in energy absorption capacity was attributed to the introduction of more nodes with low rotational stiffness, which also resulted in a higher failure strain. Overall, these findings indicate that the modified re-entrant structure has an improved capacity to absorb energy.

Grima and Evans [109] developed auxetic structures with rotating units that connect rigid rectangular and triangular cells using hinges at specific vertices. These structures exhibit a negative Poisson's ratio, which can be adjusted by changing the rotational 3D lattice of auxetic material. This flexibility in design allows for a wide range of applications [110]. In addition, semirigid rotating units were developed [111], and both experimental testing and numerical simulations were conducted to analyze real structures with similar behavior to the rotating units, such as a square array with elliptical voids) [112]. Recently, Sorrentino et al. [113] studied an innovative variable arc fillet solution at the interconnection regions between the rotating units to improve the structural response of a 3D-printed titanium alloy-based rotating squares metamaterial. Through digital image correlation, the experimental displacement field of the specimen measurements showed excellent agreement with the finite element predictions. The material exhibited a Poisson Ratio equal to approximately -1 up to a 3% overall strain.

2.5.1 Interesting properties of Auxetic Structures

Auxetic materials possess several unique features when compared to conventional materials. These materials exhibit unusual behavior during deformation, and their negative Poisson's ratio can lead to improved properties such as indentation resistance, thermal shock resistance, and fracture toughness. Research has demonstrated the improvements in these properties as Poisson's ratio approaches infinite negative extremes as $\nu \rightarrow -1$ [104].

The Poisson's ratio is also linked to the curvature of a beam or plate exposed to an out-of-plane moment. When a beam or plate experiences an out-of-plane moment, its curvature is influenced by Poisson's ratio. Sheets with a positive Poisson's ratio will result in a saddled shape anticlastic curvature, Figure 2.10 (a), while sheets with a negative Poisson's ratio will result in a synclastic

curvature (Figure 2.10 (b). The combination of lateral expansion on the upper surface, matched by equal contractions on the lower surface and axial loading, leads to a phenomenon known as "doming" due to the effects of Poisson's ratio [114].

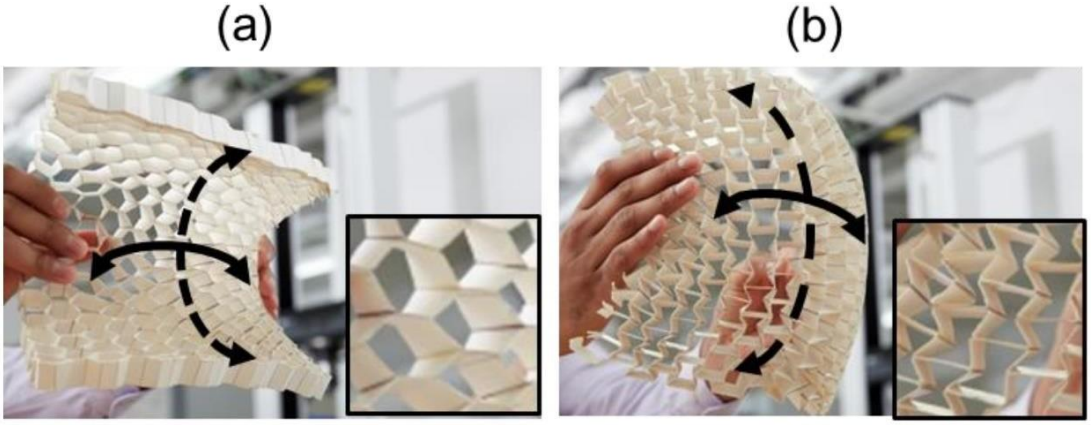

Figure 2.10: (a) Traditional honeycomb with saddled curvature; (b) Re-entrant auxetic honeycomb [114].

Energy absorption is a crucial mechanical characteristic for energy-absorbing materials and structures. This feature involves converting initial kinetic energy into an alternative energy form, including heat, through plastic deformation, viscosity, viscoelasticity, or friction [115].

When a load is applied to an auxetic material, significant energy is absorbed due to their unique deformation mechanism as they densify under the compressive loading, leading to high load bearing.

Ross and Zafer [116] investigated the behaviour of PLA-nylon and PLA-thermoplastic polyurethane (TPU) under quasi-static compressive load using both single and dual materials (auxetic and non-auxetic), and FEA modelling was used to confirm the result. Their study revealed that PLA–TPU exhibited excellent energy absorption characteristics when subjected to a single cycling load. At the same time, the dual-material system displayed superior absorption performance under multiple loading cycles.

Similarly, Najafi et al. [117] examined the energy absorption capabilities of three distinct structural types (re-entrant, arrowhead, and anti-tetra chiral) in both quasi-static and low-velocity impact scenarios. Their results suggested that auxetic structures could serve as highly efficient energy absorbers.

In a comparable investigation, Linforth et al. [118] conducted research on the energy absorption potential of an oval auxetic structure through a combination of dynamic and quasi-static

experimental tests. In another work, Rad et al. [119] examined the energy absorption response of auxetic structures with various unit cells using experimental tests and numerical analyses. Their findings indicated that auxetic structures could be effectively used as energy absorbers.

Recently, Alomarah et al. [120] developed a novel auxetic metamaterial based on Polyamide11 specimens namely, butterfly-shaped auxetic metamaterial **(**BSAM) inspired by the geometry of a butterfly by 3D printing method using Multi Jet Fusion (MJF). Indeed, NPRs were observed during the compression along X and Y directions. In addition, the specific energy absorption per unit mass (SEA) were 2.4 and 3.2 times that of the re-entrant honeycomb when they were compressed along the X and Y directions, respectively.

Research has also demonstrated that auxetic materials possess intriguing acoustic properties compared to standard materials. In particular, auxetic polymeric and metallic foams exhibit superior acoustic absorption at frequencies up to 1600 Hz. Eghbali et al. [121] found that 3D printing of a polylactic acid (PLA) auxetic resonator could remarkably improve the performance of the acoustic energy harvesting system. In an optimal scenario, it could achieve a magnification factor of around 10.5 for a 100 dB sound pressure level at low frequencies (138 Hz).

2.5.2 4D Printing of Auxetic Structures

Complex patterns found in auxetic structures lend themselves to being obtained using additive manufacturing. But a whole new spectrum of applications becomes possible when SMPs are used as the 3D printed material (i.e. 4D printing) to generate auxetic structures [122]. For instance, Li et al. [123] utilized shape memory effects to preserve the buckling state of holed membranes, which can alter the diffraction color to a transparent film. Liu and Zhang [124, 125] have reprogrammed cylindrical shells using various zigzag patterns with shape memory characteristics.

Zheng et al. [126] introduced an innovative auxetic shape-memory PLA metamaterial, allowing for customizable buckling responses achieved through thermomechanical coupled in-plane instability. They also studied the impact of viscoelasticity on in-plane moduli and Poisson's ratios, with experimental results showing promising potential.

Pandini et al. [127] reported on a 4D-printed SMP-based auxetic structure. Their design exhibited a negative Poisson's ratio of approximately 0.18 due to the linear correlation between axial and transverse strain. Furthermore, their experiments demonstrated the typical auxetic response in the material's mechanical behavior, as well as an intriguing shape memory behavior with high fixity values and nearly complete recovery of the original shape for high cell elongation.

Xin et al. [128] have developed four types of chiral materials that process memory effects using arc-shaped and crescent-shaped ligament microstructures. The potential applications of customized chiral metamaterials include flexible electronics and tissue engineering.

Zhao et al. [129] have used 4D printing to create two bioinspired scaffolds that match the trachea's geometry to the shape memory potential. This innovation shows promise in the field of tissue engineering.

Liu and Zhang [124] have successfully designed network materials with precisely tuned geometries. The materials produce appropriate Poisson's ratio values and utilize zigzag microstructures to achieve this.

Yang et al. [130] have introduced 4D printing mechanical metamaterials that are lightweight and possess shape memory effects. The effective stiffness of these materials can be significantly altered using additive manufacturing techniques.

Wu et al. [131] introduced an innovative stent design, depicted in Figure 2.11, which has been previously reported in diverse 3D printing applications [132]. Multiple geometries were evaluated for the development of vascular stents, which underwent compression and subsequent recovery in a water bath maintained at 65°C [131]. Recovery rates for diameter and length were found to range between 95% and 98%, demonstrating that such auxetic structures may be excellent candidates for stent preparation.

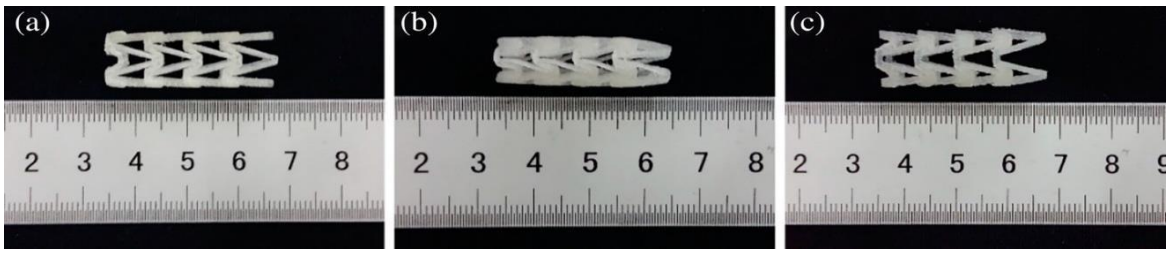

Figure 2.11: Transformation of a 3D-printed stent featuring an arrowhead structure: (a) post-printing, (b) following crimping; (c) after recovery [46, 131].

Liu et al. [133] have developed a multi-component layered metamaterial that can provide a customizable strain energy release rate for optimizing auxetic and form recovery behaviors. The material incorporated viscoelastic and elastic SMPs (SMPs) and was experimentally tested for auxetic, yielding, and shape recovery behaviors, which agreed with finite element method results.

Li et al. [134] utilized a multi-material jet printing technique to 4D print a multi-stable structure with automatic stiffness and deformation recovery effects. The smart multi-stable metamaterial's geometric parameters and external temperature were managed to achieve the desired outcomes.

Mechanical metamaterials exhibiting negative Poisson's ratio and auxetic behavior show significant promise for aerospace and flexible electronics applications. Nevertheless, the low-temperature phase transition of typical SMPs severely limits the advancement of 4D-printed mechanical metamaterials in the high-temperature and high-strength designation. To overcome this challenge, Ren et al. [135] used high-performance polymer polyetheretherketone (PEEK) as the printing material and fused deposition molding technology (FDM) to create a new mechanical metamaterial.

2.6 Composite materials

Composite materials combine two or more materials to create an end product with enhanced properties than each component material [136]. Nowadays, composite materials are made up of reinforcement arrangements (also known as fillers), embedded in a matrix [137]. The characteristics of a composite material can be affected by various factors, such as the type of matrix and charge, the form and amount of charge, the quality of the interface, and the production process [138, 139].

Shape memory polymer composites are particularly attractive due to their ability to retain and recover deformation for use in deployable and morphing structures [140]. Researchers have discovered that manufacturing composite materials is an effective strategy for overcoming the drawbacks of pure SMPs and expanding their range of applications. In conventional shape memory polymer composites (SMPCs), the addition of reinforcing fillers gradually increases the mechanical properties, while the SMP matrix maintains the shape memory effect. What's more interesting is that fillers may also allow SMPCs to perform several functions during shape recovery. Fillers can perform multiple functions during shape recovery, such as functioning as energy converters to activate an SMP matrix with thermal responsiveness, such as Joule heat producers, radiofrequency, or infrared radiation absorbers [141]. Pure 3D-printed polymers are not commonly used as fully functional and load-bearing elements due to their lack of strength and functionality, making them more suitable for conceptual prototypes than functional components. This has limited the industrial application of 3D-printed polymers [142]. To address this issue, composite-

compatible 3D printers have been developed to incorporate fillers such as nanoparticles, carbon nanotubes, fibers, and graphene to resolve this problem. Fiber reinforcement, in particular, has shown promise in enhancing the characteristics of polymers [143].

To create fiber-reinforced filaments in FDM, polymer pellets and fibers are first blended and then transferred for extrusion operation to ensure the uniform distribution of fibers. In contrast, a direct writing process involves mixing polymer paste and fibers before extruding them. Powder-based technologies are unsuitable for producing fiber-reinforced composites due to the difficulty of forming a smooth layer of the powder-fiber mixture [140].

The limited material characteristics of many 4D printing techniques have restricted their applications. For instance, while 4D printing can create artificial muscles, existing materials lack the required mechanical to replicate the desired performance and functions of real biological muscles [144]. As a result, developing sophisticated smart materials that possess desirable features and are compatible with printers is crucial to expanding the use of 4D printing. Programmable materials composite materials reinforced with carbon fiber, wood, and textiles have the potential to significantly impact various industries, including aerospace, automotive, construction, clothing, healthcare, and utility [144]. By utilizing these materials, researchers can explore novel applications of 4D printing and create functional products that meet specific needs.

2.6.1 3D printing with synthetic fibers

In 3D printing, short synthetic fibers like carbon and glass are commonly used as reinforcements to increase the mechanical characteristics of polymer composites. The void fraction and fiber orientation significantly affect the characteristics of the final composite parts [140].

Studies have been carried out to learn more about the impact of short fiber reinforcements on the FDM processing of acrylonitrile–butadiene–styrene (ABS) resin. Zhong et al. [145] found that adding plasticizer and compatibilizer enhanced the feedstock processibility. Meanwhile, Shofner et al. [146] examined the impact of vapor-grown carbon fibers on the ABS FDM feedstock and observed a 39% improvement in tensile strength at a 10 wt% of nanofiber loading.

Tekinalp et al. [147] examined the processability, microstructure, and mechanical performance of ABS composites reinforced with short fibers (0.2-0.4 mm) used in 3D printing, comparing them to conventionally compression molded composites. The results indicate that the tensile strength and modulus of the 3D-printed samples increased by approximately 115% and 700%, respectively.

In a separate study, Ning et al. [148] investigated the influence of fiber content on the mechanical features of FDM-printed ABS/carbon fiber composites. They found that the maximum efficiency was achieved at a 5 wt% fiber loading, and higher fiber content led to reduced performance due to increased porosity in the printed items.

Lin et al. [47] employed an electric mixing and melting technique to evenly disperse short carbon fibers (SCF) within polyvinyl alcohol (PVA) and developed an SMP with an electrical and thermal response. The study showed that PVA/SCF10wt.% could return to its original shape in 31 seconds after using a voltage of 50 V, and the electrically stimulated sample had a better recovery rate than the thermally activated PVA composite. The composite material made of CF exhibited optimal electro-activated SME and excellent mechanical qualities, making it highly promising for creating deployable devices for aerospace applications.

For use in the FDM procedure, Gray et al. [149, 150] produced polypropylene (PP) strands reinforced with thermotropic liquid crystalline polymer (TLCP) fibers. They studied how short TLCP fiber-reinforced items respond to different printing parameters. The addition of short fiber into the plastic samples only resulted in a small rise in mechanical efficiency, with a maximum of 20% increase in tensile strength because of short fibers limits reinforcement.

Recently, researchers have been exploring continuous synthetic fiber composites like glass, carbon (Figure 2.12), or aramid fibers, more frequently due to their superior performance compared to their discontinuous counterparts. Using pre-impregnated filaments or simultaneously impregnating polymer and fibers are two methods for 3D printing continuous fiber composites. The former demonstrates greater potential for use in structural applications with high mechanical properties [151].

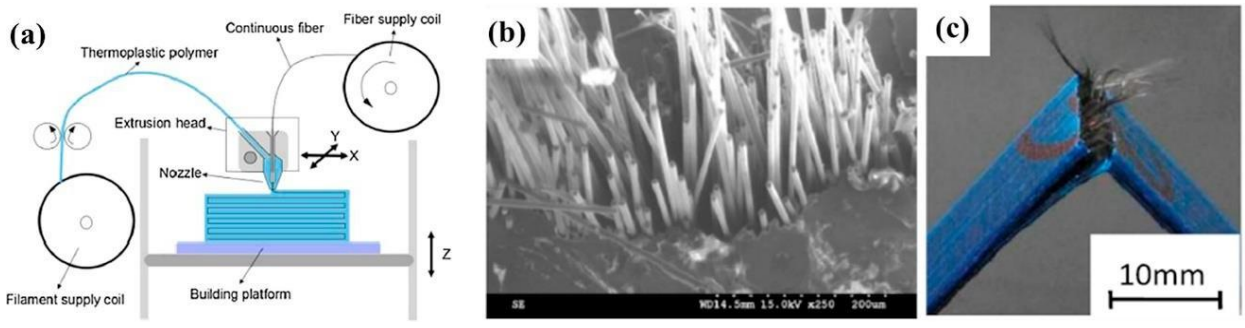

Figure 2.12: (a) The arrangement for 3D printing continuous fiber-reinforced polymer composites. (b) Interface microstructures (c) Fracture pattern observed in a broken cross-section of carbon fiber-reinforced PLA composites [140].

A recent study investigated the mechanical properties of thermoplastic composites reinforced with continuous carbon fibers, printed using the Mark One printer [152]. As shown in Figure 2.12, continuous carbon fibers and PLA filaments were provided separately and co-extruded to create the composites. Various printing parameters such as deposition layer thickness, liquefier temperature, hatch spacing, and printing speed were evaluated for their influence on the mechanical characteristic of the resulting items.

The study found that these printing parameters substantially influenced the composites' characteristics, as it was proved by another research [153, 154]. In their study, Matsuzaki et al. [115] find that the tensile modulus and strength of 3D-printed continuous carbon fiber-reinforced PLA composites reached 19.5 (±2.08) GPa and 185.2 (±24.6) MPa, respectively. These values were found to be 599 % and 435 % greater than those of pure PLA samples. This represents a much more significant increase in mechanical properties compared to PLA composites reinforced with short fibers. Overall, these findings highlight the potential of 3D printing as a method for creating high-performance composites with tailored properties.

Zeng et al. [155] employed a custom FDM printer to add continuous carbon fibers to a unique PLA filament with exceptional shape memory characteristics during 3D printing. The printer allowed simultaneous feeding of the PLA and carbon filaments through a single nozzle [156, 157]. The addition of conductive carbon filaments enabled electrical actuation through resistive heating, resulting in a remarkable recovery rate of over 95% in just 75 seconds (Figure 2.13) [155]. These findings demonstrate the potential of combining 3D printing with advanced materials, such as conductive carbon fibers, to create functional and responsive devices with unique properties.

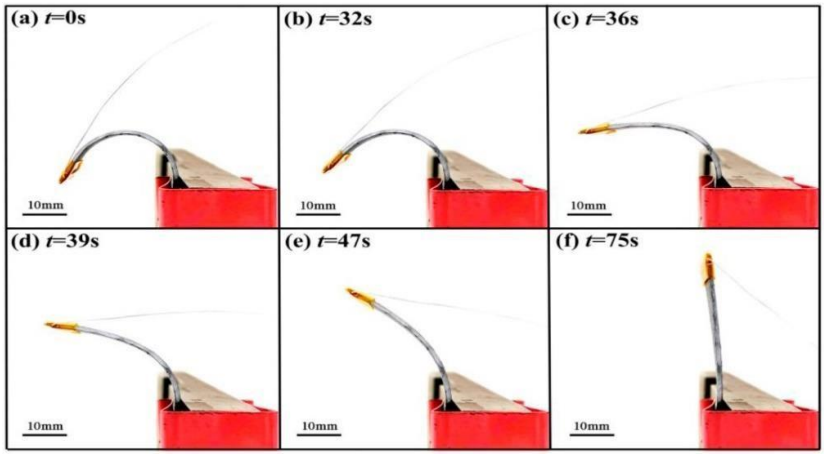

Figure 2.13: Capture of the shape recovery induced by Joule heating in 4D-printed CFRSMPC [155].

2.6.2 3D printing with natural fibers

In response to environmental and sustainability challenges, there has been an increasing focus on developing high-performance materials using natural resources [158]. However, natural fiber-reinforced plastic composites provide important challenges due to their diverse properties and characteristics [158-160].

Six categories exist for natural fibers, including bast fibers (jute, flax, hemp, ramie, and kenaf), leaf fibers (abaca, sisal, and pineapple), core fibers (hemp, kenaf, and jute), seed fibers (cotton, coir, and kapok), grass and reed fibers (corn, wheat, and rice) plus all other kinds (wood and roots) [24]. Thermoplastic polymers reinforced with natural fibers, such as wood, flax, and hemp, demonstrated promising specific mechanical qualities and smaller environmental impact, making them an attractive option for 3D printing [161].

Depuydt et al. [162] and Duigou et al. [151] have successfully printed bamboo and flax fiber-reinforced PLA, continuous flax fiber and poly-lactic acid (cFF/PLA) blends, respectively, with minimal modifications in an FFF printer. Nevertheless, as illustrated in Figure 2.14 (b, c and d), the use of the FFF process can result in higher porosity in cFF printed samples, which can be reduced by increasing extrusion and cooling rates.

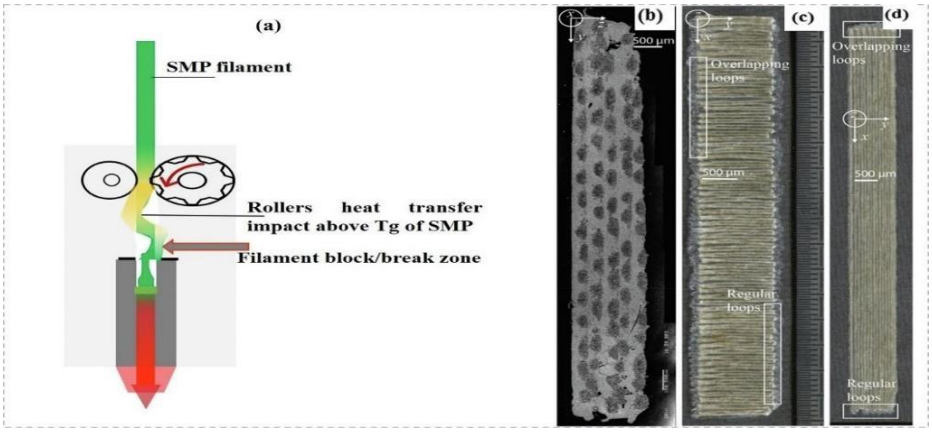

Figure 2.14: FFF process examples (a) The problem of filament blockage in contemporary 3D printers (b) Microphotographic depiction of the cFF/PLA specimen (c) cFF / PLA printed sample transversally (90°) exhibiting regular and overlapping loops (d) longitudinally (0°) printed sample showing overlapping and regular loops [151].

Low transition point SMP printing presented difficulties for Yang et al. [163] due to heat transfer effects from feeding filament rollers, causing filament bending, breaking, or blocking (Figure 2.14 (a)). Matsuzaki et al. [164] examined the mechanical performance of 3D printing continuous jute

yarn reinforcing PLA matrix through a simultaneous impregnation method. The obtained results show a longitudinal stiffness of 5.11 ± 0.41 GPa, a strength of 57.1 ± 5.3 MPa and a strain at failure of 1.81 ± 0.44%. Although the properties of jute fiber are limited instead of other natural fibers [165], The fiber content was small (vf = 6.1%), but the linear density of jute yarn was substantial (500 Tex). [151, 164, 166]. Duigou et al. [151] proposed an innovative approach to enhance continuous flax fiber/PLA (cFF/PLA) composite filaments produced via a personalized coextrusion method and printed using Fused Deposition Modeling (FDM). As evidenced, the cFF/PLA biocomposite's microstructure displayed a uniform dispersion of yarn throughout the cross-section. The presence of twisted flax yarn led to areas rich in fibers at the mesoscale. The CFF/PLA exhibited tensile modulus and strength values exceeding those reported for other printed composites utilizing continuous natural fibers more than 4.5 times. The tensile properties of the cFF/PLA were similar to those of printed continuous glass fiber/polyamide (PA) composites, suggesting that biocomposites could be used for structural applications.

Research efforts have focused on developing hygromorph biocomposites (HBC) comprised of wood, spores, and natural fibers like flax, jute, coir, and kenaf [167]. These materials belong to the category of intelligent material, a topic often explored in contemporary literature on 4D printing [168-171].

2.6.3 4D printing of composites

Recent studies have shown that combining or blending two or more polymeric material composites can significantly increase their recovery ratio. Such composites have been extensively utilized in the production of intelligent devices and 4D printing for practical purposes [172, 173]. These composites often employ multi-material structures to achieve the desired shape after recovery [172]. Their applications are numerous, including but not limited to mechanical actuators, sensors, the biomedical industry, and textile manufacturing [173-176].

A recent study conducted by Lalegani Dezaki and Bodagh [177], involved the development of a 4D-printed composite actuator using iron-filled magnetic polylactic acid (MPLA) and carbon black-filled conductive PLA (CPLA) materials. The research demonstrated that the Shape Memory Polymer Composite (SMPC) can rapidly revert to its original shape when energized by a 120 V power supply. Furthermore, the composite actuator achieved a remarkable maximum bending angle of 59° in response to low external magnetic fields.

Siqueira et al. [178] introduced modified cellulose nanocrystals (CNC) into a polymer matrix consisting of photoreactive cinnamate derivatives. They employed a DIW alignment process and localized photopatterning techniques to craft distinct soft and hard regions within a single material. In their study, Zeng et al. [179] conducted experiments on 4D-printed continuous fiber-reinforced composite horseshoe lattice structures. They explored the temperature-dependent nature of the structural mechanical properties, revealing that the material exhibits temperature-dependent equivalent stiffness and peak loads, with shape recovery influenced by the geometric configuration. Duigou et al. [166] investigated the potential of 4D printing for hygromorphic biocomposites (HBCs), which could produce a new generation of environmentally friendly metamaterials with shape-changing function. The HBCs made of continuous flax fibers exhibit hygromorphism, making them suitable for actuation and 4D printing.

Figure 2.15 (a-d) presents the cross-sectional and in-plane microstructure of cFF/PLA HBC after printing, as well as cFF/PLA and cFF/PBS HBC before and after water immersion. Microscopic analysis of the HBC's microstructure indicates that both interlaminar and matrix porosities play a role in shaping the microstructure (Figure 15 (a)). Additionally, local misalignment of the yarn and variations in the interfilament distance were observed (Figure 2.15 (b)).

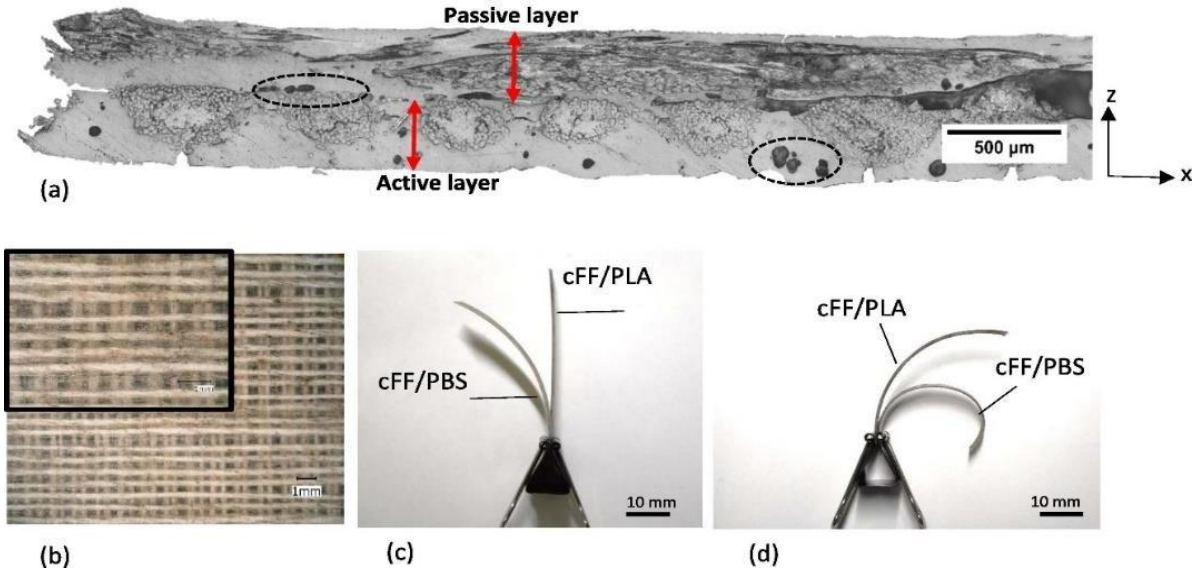

Figure 2.15: Microscopic observation of a cFF/PLA cross section showing bilayer microstructure and interlaminar defects (a), in-plane microstructure with a higher magnification insert showing local misalignment and variation of interfilament distance (b), comparison of the initial state of the hygromorphic biocomposites cFF/PLA and cFF/PBS taken after printing (c) and after water immersion (d) [180].

In contrast to HBCs charged with short natural fibers, hygromorph biocomposites reinforced with continuous flax fibers and a bilayer architecture produced by 4D printing have substantially superior actuation performance. Indeed, short-wood-fibers/PLA-PHA hygromorph biocomposites achieved a maximal curvature of 0.012 ± 0.003 mm. The enhanced performance of hygromorph biocomposites with continuous flax fibers can be attributed to several factors, including the higher fiber content, distinct fiber biochemistry and architecture (including lignin content and reduced MFA), and improved precision in controlling fiber orientation during the printing process [181]. The morphing performance of HBCs can be improved by choosing the adequate matrix. In comparison to the Poly Lactic Acid (PLA)/Flax HBC matrix, the soft Poly Buthylene Succinate (PBS) matrix demonstrated a 500% and 92% increase in reactivity and recovery, respectively [180].

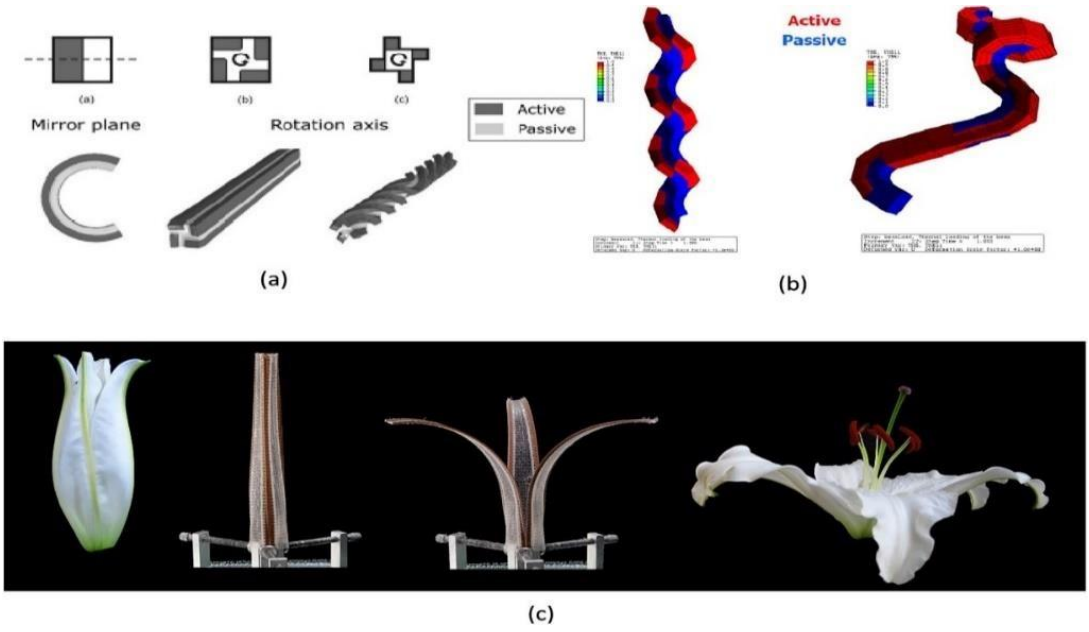

Figure 2.16: (a) Simulated actuation patterns for several cross-sections with a passive/active area ratio of 50:50. (b) Helical bending obtained by rotating the bending plane along the rod due to the distribution of passive (green) and active (white) regions. (c) The mechanism of flower opening in Lilium casa Blanca is driven by edge expansion creating a strain gradient. A 4D printed mechanism with a wood-based hygromorph composite edge is based on this idea [167].

For instance, wood-based hygromorph biocomposites have been utilized to craft bio-inspired systems, including a multi-stage double curvature structure resembling a pine cone [167], The lily flower's petal expansion as depicted in Figure 2.16 (c), the snap-through elastic instability akin to the Venus flytrap and the curved-folding kinematic amplification, inspired by the carnivorous waterwheel plant, are achieved through origami-style structures [161].

2.6.4 4D printing of auxetic composites

Progress in additive manufacturing technology have greatly facilitated the development of 3D structures with auxetic behavior. This has allowed for increased design freedom and shortened production times and enhanced characteristics like flexural strength, modulus, and impact strength. Wang et al. [183] have made further progress in this area by introducing composite 3D re-entrant auxetic structures based on carbon fiber-reinforced polymer laminates, utilizing an interlocking assembly technique as illustrated in Figure 2.17.

The auxetic characteristics of the composite structure have been validated through both experimental testing and finite element simulations. A comparative study has been carried out between Poisson's ratio and specific stiffness of the carbon fiber reinforced polymer composite with auxetic structure and previously published 3D printed polymer and metal auxetic structures. The findings suggest that the composite 3D re-entrant auxetic structure has the capacity to exhibit increased specific stiffness.

Poisson's ratio and specific stiffness of the carbon fiber reinforced polymer composite with auxetic structure and previously published 3D printed polymer and metal auxetic structures. The findings suggest that the composite 3D re-entrant auxetic structure has the capacity to exhibit increased specific stiffness.

Poisson's ratio ν_{ZX} of the composite and steel 3D re-entrant auxetic structure are parabolically dependent on re-entrant angle θ. When the re-entrant angle of the composite structure is approximately 40°, Poisson's ratio ν_{ZX} achieves its maximum value; in the case of the steel structure, it is approximately 45°.In addition, when the re-entrant angle is minimal, the composite structure's auxetic character becomes more relevant than the steel structure's, as shown in Figure 2.18 (a).

It is evident from Figure 2.18 (b) that when the re-entrant angle θ decreases, the effective compression modulus E_Z of the steel and composite 3D re-entrant auxetic structures increases monotonically. Furthermore, the steel 3D re-entrant auxetic structure's effective compression modulus (E_Z) is significantly larger than that of the composite structure because the modulus ES of steel is significantly higher than the modulus E11 of the CFRP. Additionally, composite only one-third of the fibers are oriented along the struts' axis.

On the other hand, Figure 2.18 (c) illustrates that the specific stiffness $E_Z/E_{Z\rho S\rho S}$ of the composite 3D auxetic re-entrant structure is either higher than the steel structure when the re-entrant angle is relatively small or comparable when it is relatively large because of the steel structure's density (ρ_S) is substantially higher in the composite structure, and only one-third of the fibers are aligned along the axis of the struts.

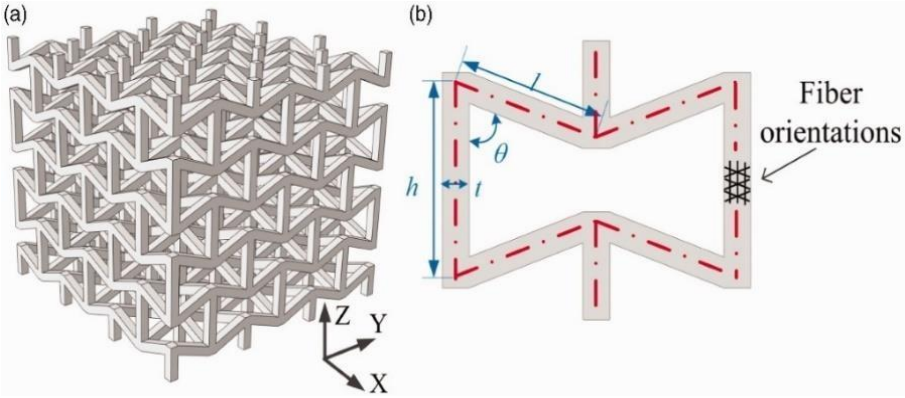

Figure 2.17: (a) 3D re-entrant auxetic structure. (b) Geometry parameters, and schematic of fiber orientations on the struts [183].

In recent studies, researchers have also investigated the potential of 3D printing technology to fabricate advanced composites with enhanced mechanical properties. Quan et al. [184] demonstrated the effectiveness of continuous fibre-reinforced thermoplastic PLA composite (CFRTPC) auxetic honeycomb structures, which exhibited a significant rise in compressive stiffness and energy absorption compared to pure polylactic acid (PLA) honeycombs.

The addition of continuous fibers caused a 6% increase in mass, leading to 86.3% enhancement in compressive stiffness, 100% increase in energy absorption and reduced Poisson ratios.

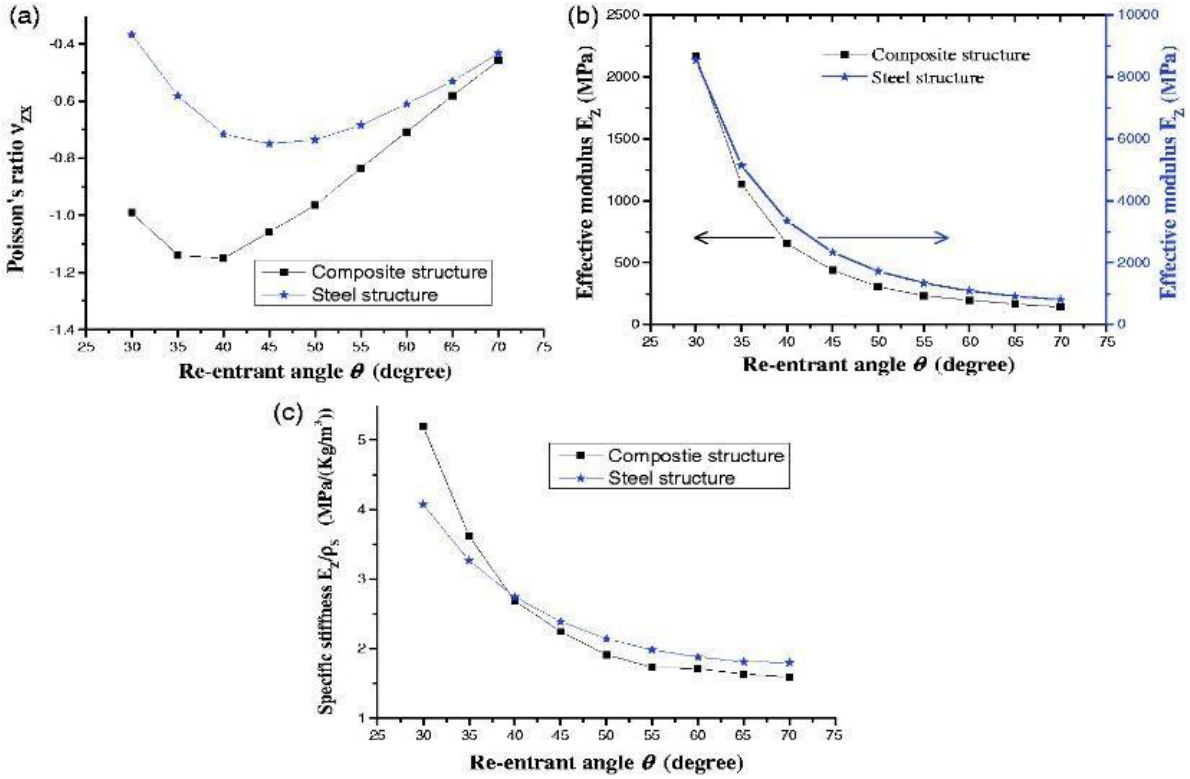

Figure 2.18: (a) Poisson's ratio vZX plotted against re-entrant angle θ; (b) effective Young's modulus EZ plotted against re-entrant angle θ; (c) specific stiffness EZ/EZρSρS plotted against re-entrant angle θ [183].

Another study by Hu et al. [185] showed the potential of integrating various polynomial curves to create a new class of chiral structures. These materials were then used to produce high-performance composites, with the addition of chopped carbon fiber (CF) reinforcement. These novel chiral composites have promising applications in developing advanced metamaterials with high mechanical performance characteristics.

The integration of SMPs with 3D printing (namely 4D printing) [186, 187] has been shown to overcome the limitation of fixed material configurations and mechanical properties. 4D printing technology also offers the advantage of creating complex structures with highly ordered geometry, which was previously unachievable. [125, 188-190]. Recent advancements in SMP-based metamaterials have resulted in programmable and reversible structures, such as continuously tunable gradient/digital patterns and cylinder shells [191, 192]. Lei [122] illustrated the potential to customize Poisson's ratios and moduli by adjusting the printed curvature of the mesh.

On the other hand, the emergence of 3D printing technology for continuous fiber- reinforced thermoplastic composites paves the way for fresh opportunities in crafting 4D printed active materials characterized by exceptional mechanical properties. Dong et al. [193] prepared continuous fiber-reinforced electro-induced shape memory auxetic composites (CFRSMCs) through the integration of conductive filaments derived from a blend nanocomposite of Polylactic acid/Thermoplastic-urethane/Carbon-nanotube (PLA/TPU/CNT) and continuous carbon fiber, employing 4D printing technology. In contrast to 3D printed samples without fibers, the resulting CFRSMCs displayed exceptional mechanical characteristics, as well as speed electro-induced shape memory effects achieving a recovery ratio of 94% in just 25 seconds with a 10 V input.

Dong et al. [194] employed a 3D printing technique to create cellular continuous fiber-reinforced composites (CFRCs) with various geometries featuring uniform fiber distribution, interlacement, and shape memory effect (as shown in Figure 2.19 (a). According to the experimental findings increasing the fiber content by a mere 3.8% can considerably enhance the tensile strength by more than 300%. For a specific structure, raising the fiber content to 16.32% resulted in an 87.36 MPa improvement in breaking strength. However, composites containing fiber inclusions exhibit poor performance in terms of shape memory.

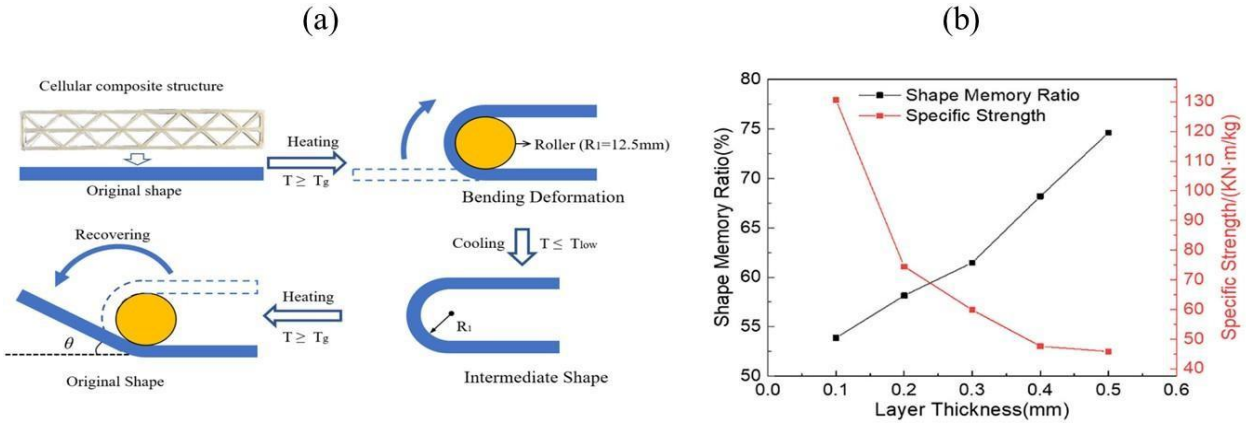

Figure 2.19: Diagram of (a) the shape memory process, (b) Shape recovery ratio of printed cellular structures and the specific strength with a different printed layer thickness [194].

The shape memory functionality of printed cellular CFRCs can be influenced by their geometric parameters, which can impact their stiffness. However, increasing the stiffness of cellular structures requires more pre-force during shape deformation, resulting in a lower shape recovery ratio.

In order to establish a satisfactory equilibrium between specific strength and the Shape Memory Effect (SME), the printed structures underwent an augmentation in layer thickness, transitioning

from 0.2 to 0.3 mm, along with an increase in fiber content from 6.18% to 8.5%. Thus, the mechanical characteristics and SME of the lightweight structures can be designed and optimised by adjusting relevant printing parameters, as shown in Figure 2.19 (b), and fiber content.

2.7 Conclusions

4D printing is an advanced technology that builds upon 3D printing by incorporating active materials, enabling structures to transform their shape over time. With 4D printing, structures can be created with greater complexity and precision, and their shapes to be programmed to modify configurations, characteristics, and functions.

Improved properties including indentation resistance, thermal shock resistance, and fracture toughness can result from auxetic structures, which have a negative Poisson's ratio and display unique behavior during deformation.

Additive manufacturing has facilitated the development of structures with 3D auxetic behavior. This is because this technology has significantly reduced the time between design and production and has increased design flexibility.

Advances in composite 3D printers have led to the development of pre-blended materials containing fillers such as nanoparticles, carbon nanotubes, fibers, and graphene. The use of fiber-reinforced composites, in particular, has enabled the creation of complex active structures with novel actuation performance, possessing specific mechanical properties and higher energy absorption capabilities. As a result, the combination of SMPs and fiber-reinforced composites in 3D printed auxetic structures has opened up new possibilities for the creation of functional materials with tunable shapes and adaptable mechanical properties.

2.8 Outlooks

The development of 4D printing of fiber-reinforced auxetic structures could go in different possible paths, considering general advances in materials science and technology. In the field of smart materials, research and development may lead to the creation of new smart composites with enhanced responsiveness and adaptability, allowing for more precise control over shape changes. The adaptability inherent in the customization capabilities of 4D printing can be employed to fabricate implantable structures featuring auxetic properties tailored for medical use. These structures have the potential to adjust dynamically to the body's movements, serving both as

supportive elements and contributing to advancements in tissue engineering. Furthermore, the development of materials with tailored mechanical properties could find applications in robotics and wearable technologies.

On the other hand, increased understanding and optimization of auxetic composites may lead to their wider adoption in engineering applications, such as lightweight and adaptive structures for aerospace or automotive industries.

The ability to tailor the mechanical properties of composites on a microscopic level through 4D printing allows for customized solutions. This can be especially valuable in industries where specific material properties are required for different applications.

Continued research and development in materials science will likely lead to the creation of advanced fibers and matrices with improved strength, flexibility, and auxetic properties. Indeed, integrating novel materials, such as nanofibers or nanocomposites, could enhance the overall performance and functionality of auxetic 4D printing composites. Additionally, advances in multi-material 4D printing could enable the integration of different types of fibers and materials within a single structure, providing enhanced mechanical properties and functionalities. Additionally, improvements in printing technologies and process repeatability may lead to higher precision in the fabrication of auxetic structures, allowing for intricate designs and fine-tuned control over the mechanical behavior.

Finally, developing sustainable materials for 4D printing may also receive more attention, in line with international initiatives to lessen environmental effects. Indeed, exploration of recyclable and biodegradable materials could become a priority in the development of 4D printed auxetic structures.

2.9 Acknowledgment

The authors acknowledge the funding provided by the Natural Sciences and Engineering Research Council (NSERC) of Canada (grant number: CRSNG – RGPIN -2021-02846).

2.10 References

1. Dayyoub, T., et al., Shape memory polymers as smart materials: A review. Polymers, 2022. 14(17): p. 3511.
2. Li, W., Y. Liu, and J. Leng, Harnessing Wrinkling Patterns Using Shape Memory Polymer Microparticles. ACS Applied Materials & Interfaces, 2021. 13(19): p. 23074-23080.
3. Wu, S., et al., Salt-mediated triple shape-memory ionic conductive polyampholyte hydrogel for wearable flexible electronics. Journal of Materials Chemistry A, 2021. 9(2): p. 1048-1061.
4. Bi, H., et al., Near infrared-induced shape memory polymer composites with dopamine-modified multiwall carbon nanotubes via 3D-printing. European Polymer Journal, 2020. 136: p. 109920.
5. Wei, W., et al., Ultrathin flexible electrospun EVA nanofiber composite with electrothermally-driven shape memory effect for electromagnetic interference shielding. Chemical Engineering Journal, 2022: p. 137135.
6. Ze, Q., et al., Magnetic shape memory polymers with integrated multifunctional shape manipulation. Advanced Materials, 2020. 32(4): p. 1906657.
7. Wei, W., et al., Recent advances and perspectives of shape memory polymer fibers. European Polymer Journal, 2022: p. 111385.
8. Li, Z. and X.J. Loh, Four-dimensional (4D) printing: Applying soft adaptive materials to additive manufacturing. Journal of Molecular and Engineering Materials, 2017. 5(02): p. 1740003.
9. Alshebly, Y.S., et al., Review on recent advances in 4D printing of shape memory polymers. European Polymer Journal, 2021. 159: p. 110708.
10. Kouka, M.A., et al., 4D Printing of Shape Memory Polymers, Blends, and Composites and Their Advanced Applications: A Comprehensive Literature Review. Advanced Engineering Materials: p. 2200650.
11. Ikram, H., A. Al Rashid, and M. Koç, Additive manufacturing of smart polymeric composites: Literature review and future perspectives. Polymer Composites, 2022. 43(9): p. 6355-6380.
12. Bhullar, S.K., Three decades of auxetic polymers: a review. e-Polymers, 2015. 15(4): p. 205-215.
13. Chen, Y., et al., Lattice metamaterials with mechanically tunable Poisson's ratio for vibration control. Physical Review Applied, 2017. 7(2): p. 024012.
14. Wu, L., B. Li, and J. Zhou, Isotropic negative thermal expansion metamaterials. ACS applied materials & interfaces, 2016. 8(27): p. 17721-17727.
15. Alderson, K.L., A. Fitzgerald, and K.E. Evans, The strain dependent indentation resilience of auxetic microporous polyethylene. Journal of Materials Science, 2000. 35(16): p. 4039-4047.
16. Shan, S., et al., Design of planar isotropic negative Poisson's ratio structures. Extreme Mechanics Letters, 2015. 4: p. 96-102.
17. Ren, X., et al., Design and characterisation of a tuneable 3D buckling-induced auxetic metamaterial. Materials & Design, 2018. 139: p. 336-342.
18. Yu, X., et al., Mechanical metamaterials associated with stiffness, rigidity and compressibility: A brief review. Progress in Materials Science, 2018. 94: p. 114-173.
19. Alomarah, A., S.H. Masood, and D. Ruan, Dynamic and quasistatic properties of an auxetic structure: a comparative study. Advanced Engineering Materials, 2022. 24(9): p. 2101811.

20. Parandoush, P. and D. Lin, A review on additive manufacturing of polymer-fiber composites. Composite Structures, 2017. 182: p. 36-53.
21. Boumaud, A., et al., Towards the design of high performance biocomposites. Prog Mater Sci, 2018. 97: p. 347-408.
22. Sekar, V., et al., Additive manufacturing: a novel method for developing an acoustic panel made of natural fiber-reinforced composites with enhanced mechanical and acoustical properties. Journal of Engineering, 2019. 2019.
23. Le Duigou, A., et al., Natural fibres actuators for smart bio-inspired hygromorph biocomposites. Smart Materials and Structures, 2017. 26(12): p. 125009.
24. Faruk, O., et al., Biocomposites reinforced with natural fibers: 2000–2010. Progress in polymer science, 2012. 37(11): p. 1552-1596.
25. Mohanty, A.K., M. Misra, and L. Drzal, Sustainable bio-composites from renewable resources: opportunities and challenges in the green materials world. Journal of Polymers and the Environment, 2002. 10(1): p. 19-26.
26. Pickering, K.L., M.A. Efendy, and T.M. Le, A review of recent developments in natural fibre composites and their mechanical performance. Composites Part A: Applied Science and Manufacturing, 2016. 83: p. 98-112.
27. Lendlein, A. and S. Kelch, Shape-memory polymers. Angewandte Chemie International Edition, 2002. 41(12): p. 2034-2057.
28. Liu, W. and D. Zuckerbrod, In situ detection of hydrogen peroxide in PEM fuel cells. Journal of The Electrochemical Society, 2005. 152(6): p. A1165.
29. Bellin, I., S. Kelch, and A. Lendlein, Dual-shape properties of triple-shape polymer networks with crystallizable network segments and grafted side chains. Journal of Materials Chemistry, 2007. 17(28): p. 2885-2891.
30. Hager, M.D., et al., Shape memory polymers: Past, present and future developments. Progress in Polymer Science, 2015. 49: p. 3-33.
31. Zhang, F., et al., The quintuple-shape memory effect in electrospun nanofiber membranes. Smart materials and structures, 2013. 22(8): p. 085020.
32. Zhang, F., et al., Remote, fast actuation of programmable multiple shape memory composites by magnetic fields. Journal of Materials Chemistry C, 2015. 3(43): p. 11290-11293.
33. Sillion, B., Les polymères à mémoire de forme. Actualite Chimique, 2002(3): p. 182-188.
34. Behl, M. and A. Lendlein, Shape-memory polymers. Materials today, 2007. 10(4): p. 20-28.
35. Ratna, D. and J. Karger-Kocsis, Recent advances in shape memory polymers and composites: a review. Journal of Materials Science, 2008. 43(1): p. 254-269.
36. Roy, D., J.N. Cambre, and B.S. Sumerlin, Future perspectives and recent advances in stimuli-responsive materials. Progress in Polymer Science, 2010. 35(1-2): p. 278-301.
37. Yan, X., et al., Stimuli-responsive supramolecular polymeric materials. Chemical Society Reviews, 2012. 41(18): p. 6042-6065.
38. Xie, T., Recent advances in polymer shape memory. Polymer, 2011. 52(22): p. 4985-5000.
39. Zende, R., V. Ghase, and V. Jamdar, A review on shape memory polymers. Polymer-Plastics Technology and Materials, 2023. 62(4): p. 467-485.
40. Idumah, C.I., et al., Construction, characterization, properties and multifunctional applications of stimuli-responsive shape memory polymeric nanoarchitectures: a review. Polymer-Plastics Technology and Materials, 2023. 62(10): p. 1247-1272.

41. Megdich, A., M. Habibi, and L. Laperriere, A review on 4D printing: Material structures, stimuli and additive manufacturing techniques. Materials Letters, 2023: p. 133977.
42. Koerner, H., et al., Remotely actuated polymer nanocomposites—stress-recovery of carbon-nanotube-filled thermoplastic elastomers. Nature materials, 2004. 3(2): p. 115-120.
43. Cho, J.W., et al., Electroactive shape-memory polyurethane composites incorporating carbon nanotubes. Macromolecular Rapid Communications, 2005. 26(5): p. 412-416.
44. Liu, Y., et al., Remotely and sequentially controlled actuation of electroactivated carbon nanotube/shape memory polymer composites. Advanced Materials Technologies, 2019. 4(12): p. 1900600.
45. Liu, Y., et al., Microstructural design for enhanced shape memory behavior of 4D printed composites based on carbon nanotube/polylactic acid filament. Composites Science and Technology, 2019. 181: p. 107692.
46. Ehrmann, G. and A. Ehrmann, 3D printing of shape memory polymers. Journal of Applied Polymer Science, 2021. 138(34): p. 50847.
47. Lin, L., Q. Zhou, and M. Li, A thermally and electrically shape memory polymer prepared by a novel electro-mixed fusion preparation method. Materials Letters, 2019. 256: p. 126574.
48. Qian, C., et al., Vapor-grown carbon nanofiber/poly (ethylene-co-vinyl acetate) composites with electrical-active two-way shape memory behavior. Journal of Intelligent Material Systems and Structures, 2017. 28(19): p. 2749-2756.
49. Leng, J., et al., Significantly reducing electrical resistivity by forming conductive Ni chains in a polyurethane shape-memory polymer/carbon-black composite. Applied Physics Letters, 2008. 92(20): p. 204101.
50. Wang, P., et al., Low voltage driven electro-active shape memory composites with 3D AgNWs conductive networks. Materials Letters, 2018. 220: p. 297-300.
51. Shao, L.-H., et al., 4D printing composite with electrically controlled local deformation. Extreme Mechanics Letters, 2020. 39: p. 100793.
52. Luo, H., et al., Multi-stimuli triggered self-healing of the conductive shape memory polymer composites. Pigment & Resin Technology, 2018.
53. Xia, Y., et al., A review of shape memory polymers and composites: mechanisms, materials, and applications. Advanced materials, 2021. 33(6): p. 2000713.
54. Varga, Z., G. Filipcsei, and M. Zrínyi, Magnetic field sensitive functional elastomers with tuneable elastic modulus. Polymer, 2006. 47(1): p. 227-233.
55. Razzaq, M.Y., et al., Mechanical spectroscopy of magnetite filled polyurethane shape memory polymers. Materials Science and Engineering: A, 2007. 471(1-2): p. 57-62.
56. Mohr, R., et al., Initiation of shape-memory effect by inductive heating of magnetic nanoparticles in thermoplastic polymers. Proceedings of the National Academy of Sciences, 2006. 103(10): p. 3540-3545.
57. Liu, H., et al., 4D printing of mechanically robust PLA/TPU/Fe3O4 magneto-responsive shape memory polymers for smart structures. Composites Part B: Engineering, 2023. 248: p. 110382.
58. Tee, Y.L. and P. Tran, On bioinspired 4d printing: materials, design and potential applications. Australian Journal of Mechanical Engineering, 2021. 19(5): p. 642-652.
59. Lee, Y.-W., et al., 3D-printed multi-stimuli-responsive mobile micromachines. ACS applied materials & interfaces, 2020. 13(11): p. 12759-12766.
60. Kulshrestha, A., et al., Magnetoresponsive biocomposite hydrogels comprising gelatin and valine based magnetic ionic liquid surfactant as controlled release nanocarrier for drug

delivery. Materials Advances, 2022. 3(1): p. 484-492.
61. Leng, J., et al., Study on the activation of styrene-based shape memory polymer by medium-infrared laser light. Applied Physics Letters, 2010. 96(11): p. 111905.
62. Rajani, T. and A. Bhogi, Meso, Micro, and Nano Particulate Filled Shape-Memory Polymers, in Shape Memory Composites Based on Polymers and Metals for 4D Printing. 2022, Springer. p. 253-266.
63. Jiang, H., S. Kelch, and A. Lendlein, Polymers move in response to light. Advanced Materials, 2006. 18(11): p. 1471-1475.
64. Wells, L.A., et al., Responding to Change: Thermo-and Photoresponsive Polymers as Unique Biomaterials. Critical Reviews™ in Biomedical Engineering, 2010. 38(6).
65. Lendlein, A., et al., Light-induced shape-memory polymers. Nature, 2005. 434(7035): p. 879-882.
66. Wu, L., C. Jin, and X. Sun, Synthesis, properties, and light-induced shape memory effect of multiblock polyesterurethanes containing biodegradable segments and pendant cinnamamide groups. Biomacromolecules, 2011. 12(1): p. 235-241.
67. Zhang, H. and Y. Zhao, Polymers with dual light-triggered functions of shape memory and healing using gold nanoparticles. ACS applied materials & interfaces, 2013. 5(24): p. 13069-13075.
68. Wu, H., et al., Four-dimensional printing of a novel acrylate-based shape memory polymer using digital light processing. Materials & Design, 2019. 171: p. 107704.
69. Zhao, T., et al., 4D printing of shape memory polyurethane via stereolithography. European Polymer Journal, 2018. 101: p. 120-126.
70. Zolfagharian, A., et al., Pattern-driven 4D printing. Sensors and Actuators A: Physical, 2018. 274: p. 231-243.
71. Mehrpouya, M., et al., 4D printing of shape memory polylactic acid (PLA). Polymer, 2021. 230: p. 124080.
72. Wang, Y., et al., Effects of the composition ratio on the properties of PCL/PLA blends: A kind of thermo-sensitive shape memory polymer composites. Journal of Polymer Research, 2021. 28(12): p. 451.
73. Sabzi, M., et al., Designing triple-shape memory polymers from a miscible polymer pair through dual-electrospinning technique. Journal of Applied Polymer Science, 2019. 136(19): p. 47471.
74. Carlson, M. and Y. Li, Development and kinetic evaluation of a low-cost temperature-sensitive shape memory polymer for 4-dimensional printing. The International Journal of Advanced Manufacturing Technology, 2020. 106(9): p. 4263-4279.
75. Sun, Y.-C., et al., 4D-printed hybrids with localized shape memory behaviour: Implementation in a functionally graded structure. Scientific reports, 2019. 9(1): p. 1-13.
76. Hao, X., et al., Entanglement network formed in miscible PLA/PMMA blends and its role in rheological and thermo-mechanical properties of the blends. Polymer, 2015. 80: p. 38-45.
77. Zhang, W., L. Chen, and Y. Zhang, Surprising shape-memory effect of polylactide resulted from toughening by polyamide elastomer. Polymer, 2009. 50(5): p. 1311-1315.
78. Min, C., et al., Biodegradable shape-memory polymer—polylactide-co-poly (glycolide-co-caprolactone) multiblock copolymer. Polymers for advanced technologies, 2005. 16(8): p. 608-615.
79. Zheng, X., et al., Shape memory properties of poly (D, L-lactide)/hydroxyapatite composites. Biomaterials, 2006. 27(24): p. 4288-4295.

80. Jeong, H.M., B.K. Ahn, and B.K. Kim, Miscibility and shape memory effect of thermoplastic polyurethane blends with phenoxy resin. European Polymer Journal, 2001. 37(11): p. 2245-2252.
81. Jeong, H.M., et al., Miscibility and shape memory property of poly (vinyl chloride)/thermoplastic polyurethane blends. Journal of materials science, 2001. 36(22): p. 5457-5463.
82. Eken, G.A. and M.H. Acar, PVDF-based shape memory polymers. European Polymer Journal, 2019. 114: p. 249-254.
83. Mather, P.T., C. Liu, and C.J. Campo, Blends of amorphous and semicrystalline polymers having shape memory properties. 2007, Google Patents.
84. Liu, C., H. Qin, and P. Mather, Review of progress in shape-memory polymers. Journal of materials chemistry, 2007. 17(16): p. 1543-1558.
85. You, J., et al., Crystal orientation behavior and shape-memory performance of poly (vinylidene fluoride)/acrylic copolymer blends. The Journal of Physical Chemistry B, 2012. 116(4): p. 1256-1264.
86. He, Z., et al., Bone cements for percutaneous vertebroplasty and balloon kyphoplasty: current status and future developments. Journal of orthopaedic translation, 2015. 3(1): p. 1-11.
87. Chuai, C., K. Almdal, and J. Lyngaae-Jørgensen, Phase continuity and inversion in polystyrene/poly (methyl methacrylate) blends. Polymer, 2003. 44(2): p. 481-493.
88. Bouzid, L., et al., Molecular dynamics simulation studies of the miscibility and thermal properties of PMMA/PS polymer blend. Chinese Journal of Physics, 2018. 56(6): p. 3012-3019.
89. Tüzüner, Ş. and M.M. Demir, Dispersion of organophilic Ag nanoparticles in PS-PMMA blends. Materials Chemistry and Physics, 2015. 162: p. 692-699.
90. Yun, M., et al., Nanomechanical thermal analysis of the effects of physical aging on glass transitions in PS/PMMA blend and PS-PMMA diblock copolymers. Polymer, 2011. 52(18): p. 4136-4140.
91. Liu, G., et al., Novel shape-memory polymer with two transition temperatures. Macromolecular Rapid Communications, 2005. 26(8): p. 649-652.
92. Yanping, L. and H. Hong, A review on auxetic structures and polymeric materials. Scientific Research and Essays, 2010. 5(10): p. 1052-1063.
93. Dobnik Dubrovski, P., et al., In-plane behavior of auxetic non-woven fabric based on rotating square unit geometry under tensile load. Polymers, 2019. 11(6): p. 1040.
94. Xu, C., et al., Expanded polytetrafluoroethylene as an auxetic material: effect of extension ratio on its structure and properties. Iranian Polymer Journal, 2018. 27(1): p. 49-56.
95. Zhai, X., et al., Mechanical behaviors of auxetic polyurethane foam at quasi-static, intermediate and high strain rates. International Journal of Impact Engineering, 2019. 129: p. 112-118.
96. Ahmed, H.I., et al., Development of 3D auxetic structures using para-aramid and ultra-high molecular weight polyethylene yarns. The Journal of The Textile Institute, 2021. 112(9): p. 1417-1427.
97. Li, N., et al., Preparing Polypropylene Auxetic Foam by a One-Pot CO2 Foaming Process. Advanced Engineering Materials, 2022. 24(3): p. 2100859.
98. Magalhaes, R., et al., Development, characterization and analysis of auxetic structures from braided composites and study the influence of material and structural parameters. Composites Part A: Applied Science and Manufacturing, 2016. 87: p. 86-97.

99. Günaydın, K., C. Rea, and Z. Kazancı, Energy absorption enhancement of additively manufactured hexagonal and re-entrant (auxetic) lattice structures by using multi-material reinforcements. Additive Manufacturing, 2022. 59: p. 103076.
100. Verma, P., C. He, and A.C. Griffin, Implications for Auxetic Response in Liquid Crystalline Polymers: X-Ray Scattering and Space-Filling Molecular Modeling. physica status solidi (b), 2020. 257(10): p. 2000261.
101. Mistry, D., et al., Coincident molecular auxeticity and negative order parameter in a liquid crystal elastomer. Nature communications, 2018. 9(1): p. 1-9.
102. Ren, X., et al., Auxetic metamaterials and structures: a review. Smart materials and structures, 2018. 27(2): p. 023001.
103. Tang, H., et al., Highly tailorable electromechanical properties of auxetic piezoelectric ceramics with ultra-low porosity. Journal of the American Ceramic Society, 2020. 103(11): p. 6330-6347.
104. Alderson, A. and K. Alderson, Auxetic materials. Proceedings of the Institution of Mechanical Engineers, Part G: Journal of Aerospace Engineering, 2007. 221(4): p. 565-575.
105. Kelkar, P.U., et al., Cellular auxetic structures for mechanical metamaterials: A review. Sensors, 2020. 20(11): p. 3132.
106. Alomarah, A., D. Ruan, and S. Masood, Tensile properties of an auxetic structure with re-entrant and chiral features—a finite element study. The International Journal of Advanced Manufacturing Technology, 2018. 99(9): p. 2425-2440.
107. Alomarah, A., et al., An investigation of in-plane tensile properties of re-entrant chiral auxetic structure. The International Journal of Advanced Manufacturing Technology, 2018. 96(5): p. 2013-2029.
108. Choudhry, N.K., B. Panda, and S. Kumar, In-plane energy absorption characteristics of a modified re-entrant auxetic structure fabricated via 3D printing. Composites Part B: Engineering, 2022. 228: p. 109437.
109. Grima, J.N. and K.E. Evans, Auxetic behavior from rotating squares. 2000.
110. Gao, Y., et al., Novel 3D auxetic lattice structures developed based on the rotating rigid mechanism. International Journal of Solids and Structures, 2021. 233: p. 111232.
111. Grima, J.N., et al., Auxetic behaviour from rotating semi-rigid units. physica status solidi (b), 2007. 244(3): p. 866-882.
112. Taylor, M., et al., Low porosity metallic periodic structures with negative Poisson's ratio. Advanced Materials, 2014. 26(15): p. 2365-2370.
113. Sorrentino, A., et al., Rotating squares auxetic metamaterials with improved strain tolerance. Smart Materials and Structures, 2021. 30(3): p. 035015.
114. Duncan, O., et al., Review of auxetic materials for sports applications: Expanding options in comfort and protection. Applied Sciences, 2018. 8(6): p. 941.
115. Zhang, J., G. Lu, and Z. You, Large deformation and energy absorption of additively manufactured auxetic materials and structures: A review. Composites Part B: Engineering, 2020. 201: p. 108340.
116. Johnston, R. and Z. Kazancı, Analysis of additively manufactured (3D printed) dual-material auxetic structures under compression. Additive Manufacturing, 2021. 38: p. 101783.
117. Najafi, M., H. Ahmadi, and G. Liaghat, Experimental investigation on energy absorption of auxetic structures. Materials today: proceedings, 2021. 34: p. 350-355.
118. Linforth, S., et al., Investigation of the auxetic oval structure for energy absorption through

quasi-static and dynamic experiments. International Journal of Impact Engineering, 2021. 147: p. 103741.
119. Rad, M.S., et al., Determination of energy absorption in different cellular auxetic structures. Mechanics & Industry, 2019. 20(3): p. 302.
120. Alomarah, A., Y. Yuan, and D. Ruan, A bio-inspired auxetic metamaterial with two plateau regimes: Compressive properties and energy absorption. Thin-Walled Structures, 2023. 192: p. 111175.
121. Eghbali, P., D. Younesian, and S. Farhangdoust, Enhancement of the low-frequency acoustic energy harvesting with auxetic resonators. Applied Energy, 2020. 270: p. 115217.
122. Lei, M., et al., 3D printing of auxetic metamaterials with digitally reprogrammable shape. ACS applied materials & interfaces, 2019. 11(25): p. 22768-22776.
123. Li, J., et al., Switching periodic membranes via pattern transformation and shape memory effect. Soft Matter, 2012. 8(40): p. 10322-10328.
124. Liu, J. and Y. Zhang, Soft network materials with isotropic negative Poisson's ratios over large strains. Soft Matter, 2018. 14(5): p. 693-703.
125. Liu, J. and Y. Zhang, A mechanics model of soft network materials with periodic lattices of arbitrarily shaped filamentary microstructures for tunable poisson's ratios. Journal of Applied Mechanics, 2018. 85(5): p. 051003.
126. Li, Z., et al., 3D printing of auxetic shape-memory metamaterial towards designable buckling. International Journal of Applied Mechanics, 2021. 13(01): p. 2150011.
127. Pandini, S., et al., Shape memory response and hierarchical motion capabilities of 4D printed auxetic structures. Mechanics Research Communications, 2020. 103: p. 103463.
128. Xin, X., et al., 4D printing auxetic metamaterials with tunable, programmable, and reconfigurable mechanical properties. Advanced Functional Materials, 2020. 30(43): p. 2004226.
129. Zhao, W., et al., Personalized 4D printing of bioinspired tracheal scaffold concept based on magnetic stimulated shape memory composites. Composites Science and Technology, 2019. 184: p. 107866.
130. Yang, C., et al., 4D printing reconfigurable, deployable and mechanically tunable metamaterials. Materials Horizons, 2019. 6(6): p. 1244-1250.
131. Wu, Z., et al., Radial compressive property and the proof-of-concept study for realizing self-expansion of 3D printing polylactic acid vascular stents with negative Poisson’s ratio structure. Materials, 2018. 11(8): p. 1357.
132. Grimmelsmann, N., H. Meissner, and A. Ehrmann. 3D printed auxetic forms on knitted fabrics for adjustable permeability and mechanical properties. in IOP conference series: materials science and engineering. 2016. IOP Publishing.
133. Liu, Y., D.-W. Shu, and H. Lu, 3D printing shape memory polymer of laminated multi-component metamaterial towards optimization of auxetic and shape recovery behaviors. Smart Materials and Structures, 2023.
134. Tao, R., et al., 4D printed multi-stable metamaterials with mechanically tunable performance. Composite Structures, 2020. 252: p. 112663.
135. Ren, L., et al., 3D Printing of Auxetic Metamaterials with High-Temperature and Programmable Mechanical Properties. Advanced Materials Technologies, 2022. 7(9): p. 2101546.
136. Hsissou, R., et al., Synthesis and anticorrosive properties of epoxy polymer for CS in [1 M] HCl solution: Electrochemical, AFM, DFT and MD simulations. Construction and Building Materials, 2021. 270: p. 121454.

137. Van de Werken, N., et al., Additively manufactured carbon fiber-reinforced composites: State of the art and perspective. Additive Manufacturing, 2020. 31: p. 100962.

138. Nagarajan, B., et al., Additive manufacturing ferromagnetic polymers using stereolithography–Materials and process development. Manufacturing Letters, 2019. 21: p. 12-16.
139. Hsissou, R., et al., Polymer composite materials: A comprehensive review. Composite structures, 2021. 262: p. 113640.
140. Wang, X., et al., 3D printing of polymer matrix composites: A review and prospective. Composites Part B: Engineering, 2017. 110: p. 442-458.
141. Lei, M., et al., Recent progress in shape memory polymer composites: methods, properties, applications and prospects. Nanotechnology reviews, 2019. 8(1): p. 327-351.
142. Malhotra, S.K., K. Goda, and M.S. Sreekala, Part one introduction to polymer composites. Polymer composites, 2012. 1: p. 1-2.
143. Singh, S., S. Ramakrishna, and F. Berto, 3D Printing of polymer composites: A short review. Material Design & Processing Communications, 2020. 2(2): p. e97.
144. Loh, X.J., Four-Dimensional (4D) Printing in Consumer Applications, in Polymers for Personal Care Products and Cosmetics, X.J. Loh, Editor. 2016, The Royal Society of Chemistry. p. 0.
145. Zhong, W., et al., Short fiber reinforced composites for fused deposition modeling. Materials Science and Engineering: A, 2001. 301(2): p. 125-130.
146. Shofner, M., et al., Single wall nanotube and vapor grown carbon fiber reinforced polymers processed by extrusion freeform fabrication. Composites Part A: Applied Science and Manufacturing, 2003. 34(12): p. 1207-1217.
147. Tekinalp, H.L., et al., Highly oriented carbon fiber–polymer composites via additive manufacturing. Composites Science and Technology, 2014. 105: p. 144-150.
148. Ning, F., et al., Additive manufacturing of carbon fiber-reinforced plastic composites using fused deposition modeling: Effects of process parameters on tensile properties. Journal of composite materials, 2017. 51(4): p. 451-462.
149. Gray IV, R., D. Baird, and J. Bøhn, Thermoplastic composites reinforced with long fiber thermotropic liquid crystalline polymers for fused deposition modeling. Polymer composites, 1998. 19(4): p. 383-394.
150. Gray IV, R.W., D.G. Baird, and J. Helge Bøhn, Effects of processing conditions on short TLCP fiber reinforced FDM parts. Rapid Prototyping Journal, 1998. 4(1): p. 14-25.
151. Le Duigou, A., et al., 3D printing of continuous flax fibre reinforced biocomposites for structural applications. Materials & Design, 2019. 180: p. 107884.
152. Van Der Klift, F., et al., 3D printing of continuous carbon fibre reinforced thermo-plastic (CFRTP) tensile test specimens. Open Journal of Composite Materials, 2016. 6(01): p. 18.
153. Tian, X., et al., Interface and performance of 3D printed continuous carbon fiber reinforced PLA composites. Composites Part A: Applied Science and Manufacturing, 2016. 88: p. 198-205.
154. Ziadia, A., M. Habibi, and S. Kelouwani, Machine Learning Study of the Effect of Process Parameters on Tensile Strength of FFF PLA and PLA-CF. Eng, 2023. 4(4): p. 2741-2763.
155. Zeng, C., et al., 4D printed electro-induced continuous carbon fiber reinforced shape memory polymer composites with excellent bending resistance. Composites Part B: Engineering, 2020. 194: p. 108034.
156. Liu, T., et al., 4D printed anisotropic structures with tailored mechanical behaviors and

shape memory effects. Composites Science and Technology, 2020. 186: p. 107935.
157. Zhang, W., et al., Shape memory behavior and recovery force of 4D printed textile functional composites. Composites Science and Technology, 2018. 160: p. 224-230.
158. Habibi, M., G. Lebrun, and L. Laperrière, Experimental characterization of short flax fiber mat composites: tensile and flexural properties and damage analysis using acoustic emission. Journal of Materials Science, 2017. 52: p. 6567-6580.
159. Habibi, M., et al., Combining short flax fiber mats and unidirectional flax yarns for composite applications: Effect of short flax fibers on biaxial mechanical properties and damage behaviour. Composites Part B: Engineering, 2017. 123: p. 165-178.
160. Tao, Y., et al., A review of fused filament fabrication of continuous natural fiber reinforced thermoplastic composites: Techniques and materials. Polymer Composites.
161. Poppinga, S., et al., Plant movements as concept generators for the development of biomimetic compliant mechanisms. Integrative and Comparative Biology, 2020. 60(4): p. 886-895.
162. Depuydt, D., et al., Production and characterization of bamboo and flax fiber reinforced polylactic acid filaments for fused deposition modeling (FDM). Polymer composites, 2019. 40(5): p. 1951-1963.
163. Yang, Y., et al., 3D printing of shape memory polymer for functional part fabrication. The International Journal of Advanced Manufacturing Technology, 2016. 84: p. 2079-2095.
164. Matsuzaki, R., et al., Three-dimensional printing of continuous-fiber composites by in-nozzle impregnation. Scientific reports, 2016. 6(1): p. 1-7.
165. Baley, C., et al., Compressive and tensile behaviour of unidirectional composites reinforced by natural fibres: Influence of fibres (flax and jute), matrix and fibre volume fraction. Materials Today Communications, 2018. 16: p. 300-306.
166. Le Duigou, A., et al., Bioinspired electro-thermo-hygro reversible shape-changing materials by 4D printing. Advanced Functional Materials, 2019. 29(40): p. 1903280.
167. Le Duigou, A., et al., A review of 3D and 4D printing of natural fibre biocomposites. Materials & Design, 2020. 194: p. 108911.
168. Mitchell, A., et al., Additive manufacturing—A review of 4D printing and future applications. Additive Manufacturing, 2018. 24: p. 606-626.
169. Momeni, F., X. Liu, and J. Ni, A review of 4D printing. Materials & design, 2017. 122: p. 42-79.
170. Wang, Q., et al., Programmable morphing composites with embedded continuous fibers by 4D printing. Materials & Design, 2018. 155: p. 404-413.
171. Rayate, A. and P.K. Jain, A review on 4D printing material composites and their applications. Materials Today: Proceedings, 2018. 5(9): p. 20474-20484.
172. Dogan, S., et al., Thermally induced shape memory behavior, enzymatic degradation and biocompatibility of PLA/TPU blends:“Effects of compatibilization”. Journal of the mechanical behavior of biomedical materials, 2017. 71: p. 349-361.
173. Pilate, F., et al., Shape-memory polymers for multiple applications in the materials world. European Polymer Journal, 2016. 80: p. 268-294.
174. Li, X., J. Shang, and Z. Wang, Intelligent materials: a review of applications in 4D printing. Assembly Automation, 2017. 37(2): p. 170-185.
175. Lee, J., et al., A review on 3D printed smart devices for 4D printing. International Journal of Precision Engineering and Manufacturing-Green Technology, 2017. 4: p. 373-383.
176. Gao, B., et al., 4D bioprinting for biomedical applications. Trends in biotechnology, 2016. 34(9): p. 746-756.

177. Lalegani Dezaki, M. and M. Bodaghi, Sustainable 4D printing of magneto-electroactive shape memory polymer composites. The International Journal of Advanced Manufacturing Technology, 2023. 126(1-2): p. 35-48.
178. Müller, L.A., et al., Mechanical properties tailoring of 3D printed photoresponsive nanocellulose composites. Advanced functional materials, 2020. 30(35): p. 2002914.
179. Zeng, C., et al., Temperature-dependent mechanical response of 4D printed composite lattice structures reinforced by continuous fiber. Composite Structures, 2022. 280: p. 114952.
180. Le Duigou, A., et al., 4D printing of continuous flax-fibre based shape-changing hygromorph biocomposites: Towards sustainable metamaterials. Materials & Design, 2021. 211: p. 110158.
181. Le Duigou, A., et al., 3D printing of wood fibre biocomposites: From mechanical to actuation functionality. Materials & Design, 2016. 96: p. 106-114.
182. Turcaud, S., et al., An excursion into the design space of biomimetic architectured biphasic actuators. International Journal of Materials Research, 2011. 102(6): p. 607-612.
183. Wang, X.-T., Y.-L. Chen, and L. Ma, The manufacture and characterization of composite three-dimensional re-entrant auxetic cellular structures made from carbon fiber reinforced polymer. Journal of Composite Materials, 2018. 52(23): p. 3265-3273.
184. Quan, C., et al., 3d printed continuous fiber reinforced composite auxetic honeycomb structures. Composites Part B: Engineering, 2020. 187: p. 107858.
185. Hu, C., et al., 3D printing of chiral carbon fiber reinforced polylactic acid composites with negative Poisson's ratios. Composites Part B: Engineering, 2020. 201: p. 108400.
186. Kuang, X., et al., Advances in 4D printing: materials and applications. Advanced Functional Materials, 2019. 29(2): p. 1805290.
187. Nuzzo, R., Biomimetic 4D Printing. 2015.
188. Clausen, A., et al., Topology optimized architectures with programmable Poisson's ratio over large deformations. Adv. Mater, 2015. 27(37): p. 5523-5527.
189. Ma, Q., et al., A nonlinear mechanics model of bio-inspired hierarchical lattice materials consisting of horseshoe microstructures. Journal of the Mechanics and Physics of Solids, 2016. 90: p. 179-202.
190. Yuan, S., C.K. Chua, and K. Zhou, 3D-printed mechanical metamaterials with high energy absorption. Advanced Materials Technologies, 2019. 4(3): p. 1800419.
191. Yuan, C., et al., Thermomechanically triggered two-stage pattern switching of 2D lattices for adaptive structures. Advanced Functional Materials, 2018. 28(18): p. 1705727.
192. Zhao, Z., et al., Three-dimensionally printed mechanical metamaterials with thermally tunable auxetic behavior. Physical Review Applied, 2019. 11(4): p. 044074.
193. Dong, K., et al., Electro-induced shape memory effect of 4D printed auxetic composite using PLA/TPU/CNT filament embedded synergistically with continuous carbon fiber: A theoretical & experimental analysis. Composites Part B: Engineering, 2021. 220: p. 108994.
194. Dong, K., et al., Mechanical properties and shape memory effect of 4D printed cellular structure composite with a novel continuous fiber-reinforced printing path. Materials & Design, 2021. 198: p. 109303.

Chapitre 3 : Conception de mélanges polymères thermo-sensibles à mémoire de forme pour l'impression 4D

Ce chapitre a fait l'objet d'une publication :

Designing advanced 4D printing thermo-sensitive shape memory polymer blends for enhanced mechanical and shape memory performances. Bouguermouh Karima, Habibi Mohamed, Laperrière Luc, Zeshi Li and Abdin Yasmine. Progress in Additive Manufacturing, 2025, p. 1-20.

Il peut être consulté en ligne à l'adresse suivante : https://doi.org/10.1007/s40964-025-00989-7

En répondant à l'objectif spécifique a), cet article explore le développement de mélanges avancés de polymères à mémoire de forme (SMPs) thermo-sensibles, destinés à l'impression 4D via la technologie Fused Deposition Modeling (FDM). L'objectif principal est d'améliorer les propriétés mécaniques et les performances de mémoire de forme des structures imprimées. Les polymères étudiés incluent le polylactide (PLA), l'acrylonitrile butadiène styrène (ABS), le polyéthylène téréphtalate glycol (PETG) et le polyméthacrylate de méthyle (PMMA), combinés en diverses proportions pour former des mélanges binaires.

Les résultats montrent que le mélange PLA/PMMA contenant 75 % de PMMA offre la meilleure résistance à la traction avec une valeur de 54,19 MPa à une orientation d'impression de 0°. En parallèle, le mélange PLA/PETG dans un ratio 50/50 présente la plus grande déformation à la rupture, atteignant 10,32 % à une orientation de 90°. En termes de performance mémoire, le mélange PLA/PMMA avec 75 % de PLA atteint un taux de fixation de forme de 93,33 % et une récupération totale (100 %) en seulement 7 secondes. Le mélange PLA/PETG affiche également une excellente récupération (100 %) avec un taux de fixation de 98,33 %.

L'étude révèle aussi que la compatibilité entre polymères joue un rôle crucial. Les analyses thermiques (DSC) et spectroscopiques (FTIR) montrent une bonne miscibilité entre PLA/PMMA, PLA/ABS et PETG/PMMA, ce qui contribue directement à de meilleures propriétés mécaniques et de mémoire de forme.

Les observations au microscope électronique à balayage (SEM) confirment que les mélanges bien miscibles présentent une microstructure plus homogène, avec moins de porosité, ce qui améliore l'adhésion inter-couche et la solidité des pièces imprimées. Par ailleurs, la durabilité des matériaux

est influencée par leur composition : les mélanges riches en PLA sont plus biodégradables, tandis que ceux contenant davantage de PETG sont plus facilement recyclables.

En conclusion, ce travail démontre que les mélanges de polymères bien conçus permettent d'améliorer à la fois les propriétés mécaniques et les effets de mémoire de forme des structures imprimées en 4D. Cela ouvre de nombreuses possibilités pour des applications avancées, notamment en robotique douce, dans les dispositifs médicaux intelligents et les systèmes adaptatifs.

Designing advanced 4D printing thermo-sensitive shape memory polymer blends for enhanced mechanical and shape memory performances

Karima Bouguermouh[1], Mohamed Habibi[1*], Luc Laperrière[1], Zeshi Li[2], and Yasmine Abdin[2]

[1] *Department of mechanical engineering, Université du Québec à Trois-Rivières, Quebec, Canada.*
[2]*Department of Materials Engineering, The University of British Columbia, Vancouver, BC, Canada V6T 1Z4*

3.1 Abstract

This study explores the development of advanced thermo-sensitive shape memory polymer (SMP) blends for 4D printing using Fused Deposition Modeling (FDM). The investigation explores the thermal, mechanical, and shape memory properties of various polymer blends, including polylactic acid (PLA), acrylonitrile butadiene styrene (ABS), polyethylene terephthalate glycol (PETG), and polymethyl methacrylate (PMMA). By employing Differential Scanning Calorimetry (DSC), mechanical testing, and shape memory evaluation, the study assesses the miscibility, tensile strength, and shape recovery performance of different blend compositions. Results reveal that PLA/PMMA blend with 75 wt% PMMA exhibited the highest tensile strength at 54.19 MPa in the 0° orientation, while the PLA/PETG blend demonstrated the best tensile strain of 10,32% in the 90° orientation. In terms of shape memory performance, the PLA/PMMA blend with 75 wt% PLA achieved optimal shape fixity of 93.33% and shape recovery of 100%, with a rapid recovery time of 7 seconds**.** The PLA/PETG blend also performed well, with a shape fixity of 98.33% and a full recovery of 100%, though with a slower recovery time of 28 seconds. These findings highlight the potential of these polymer blends to enhance the mechanical performance and responsiveness of 4D printed structures, making them ideal for applications in soft robotics, biomedical devices, and adaptive systems.

Keywords

Shape memory polymers (SMPs), 4D printing, Fused Deposition Modeling (FDM), Polymer blends, Mechanical properties.

3.2 Introduction

4D printing represents an advancement over traditional 3D printing by introducing the dimension of time, allowing objects to change their shape or geometry in response to external stimuli [1-4].

This innovation is made possible through the use of shape memory polymers (SMPs), which enable printed structures to dynamically adapt and revert to to predetermined shapes upon activation under different types of stimuli such as temperature, light, electric field, magnetic field, pH, specific ions, or enzymes [5-7]. Among these, thermally sensitive SMPs are the most popular [8]. It has attracted the attention of scientists and engineers for its unique ability to be manipulated into the desired shape and subsequently recover to another predetermined shape as the temperature shifts from below to above the transition temperature. This capability offers substantial potential for applications in sensors, actuators, packaging, medical materials, and more [9-11].

Existing studies on 4D Printing have largely focused on individual polymers like polylactic acid (PLA) [12, 13] or polyethylene terephthalate glycol (PETG) [14-17], and while their shape memory properties are well-documented, the exploration of blends of multiple polymers remains limited. The blending approach holds promise for enhancing mechanical robustness and fine-tuning shape memory performance. In this context, using polymer blends based on PLA, acrylonitrile butadiene styrene (ABS), PETG, and polymethyl methacrylate (PMMA) can significantly enhance the mechanical and shape memory performances of 4D printed structures. PLA is widely used in 4D printing due to its biocompatibility, biodegradability, and superior shape memory properties [18]. PLA-based SMPs efficiently revert to their original shape upon exposure to suitable thermal stimuli [12, 13, 19]. PETG has also emerged as a valuable material in SMP blends for 4D printing due to its excellent printability, chemical resistance, and robust mechanical properties. SMPs incorporating PETG exhibit notable improvements in shape fixity and recovery, facilitating the development of functional, responsive structures for diverse applications [14, 20, 21]. Additionally, ABS is known for its strength and toughness [22] and can further enhance these properties when integrated into polymer blends for 4D printing. By incorporating ABS into SMP blends, the durability and mechanical performance of printed structures are significantly improved, making these blends suitable for applications requiring high-impact resistance and structural integrity.

The polymer blending process is recognized as a viable method to develop new SMPs or to improve the shape memory properties of existing ones. Combining SMPs with miscible polymers makes it possible to tailor mechanical properties and modify the programming temperature [23]. For example, PMMA-based shape memory polymer blends offer significant advantages in terms of enhanced mechanical strength, thermal stability, and shape memory capabilities. These attributes make them highly appropriate for applications in biomedical devices, flexible electronics, and

adaptive structures [24]. Hao et al.[25] reported that the shape memory mechanism in miscible PMMA/PLA blends is affected by the degree of molecular entanglement and the nanoscale heterogeneity within the blend responsible for glass transition broadening related to the self-concentration of the components. These properties lead to enhanced shape recovery and fixity ratios. Indeed, higher entanglement density leads to better shape recovery, reaching up to 100% with optimal PMMA content.

Another study by Ma et al. [26] showed that PLA/PCL (polycaprolactone) blends exhibit enhanced shape memory properties, making them suitable for applications in biomedicine and soft robotics. Furthermore, results show that the glass transition temperature (T_g) of 4D-printed PLA/PCL composites decreases as PCL content increases, from 67.2°C for pure PLA to 55.2°C for a 50/50 PLA/PCL blend. On the other hand, adding a small amount of PCL (≤10%) increases the maximum strain of PLA, making the material softer and more flexible. In addition, the shape recovery time shortens with higher PCL content. Recently, da Cunha et al. [27] explored the 4D printing of PETG/TPU blends, which exhibited more balanced shape memory effects (SME) compared to the individual polymers. Notably, the PETG/TPU (50/50) blend achieved a fixity ratio of approximately 97% and a recovery ratio of around 93% in bending mode. In torsion mode, the blend demonstrated an even higher fixity ratio of nearly 100%, with a recovery ratio of about 87%. Rahmatabadi et al. [28] explores blending PLA with Polybutylene Adipate Terephthalate (PBAT) to create eco-friendly, biodegradable materials with enhanced properties. PBAT percentages of 15%, 30%, and 45% were used for softening PLA, resulting in successfully 4D-printed composites. Blends with 45% PBAT showed excellent elongation (220%) and high shape recovery (93%), while 15% PBAT retained high strength (40 MPa) and rapid shape recovery (8 s). Scanning electron microscopy confirmed high printability, with the 30% PBAT blend showing the best layer interfaces and minimal porosity.

The combination of PLA, ABS, PETG, and PMMA in SMP blends for 4D printing holds immense potential for creating highly functional and mechanically robust structures with excellent shape memory capabilities. This integration not only enhances the performance of the printed objects but also expands the range of applications for 4D printing technology [21, 29, 30]. By leveraging the unique properties of each polymer, these blends can achieve superior mechanical strength, thermal

stability, and shape memory functionality, making them suitable for a wide array of advanced applications.

This study is significant as it explores not only the material composition but also the interactions between different polymers that influence the overall functionality of 4D-printed structures. In addition, it aims to evaluate the thermal, mechanical, and shape memory properties of various polymers and their blends using Differential Scanning Calorimetry (DSC), Fourier Transform Infrared Spectroscopy (FTIR), and mechanical testing. It investigates the T_g, melting temperatures, and miscibility of PLA, ABS, PETG, and PMMA polymers, as well as their blends. The study also examines the effect of printing orientation and blend composition on mechanical properties. Additionally, it evaluates the shape memory properties, focusing on shape fixity and shape recovery across different polymer blends, aiming to enhance material performance for 4D printing applications.

3.3 Materials and methods

PLA, ABS, PMMA, and PETG resin pellets, with densities of 1.24 g/cm^3, 1.03 g/cm^3, 1.18 g/cm^3, and dried in a vacuum dryer oven at 60 °C for 24 h before melt-blending. The materials were mixed in the required ratio for the desired blends, as detailed in Table 1.

3.3.1 Filament preparation for 3D printing

Six binary combinations of polymers in three weight ratios (25/75, 50/50, and 75/25) were prepared, as reported in Table 3.1. A single screw extruder operating at 60 rpm was used to produce 1.75 mm diameter 3D printing filaments which was cooled with a 4 CFM fan, as illustrated in Figure 3.1. The extrusion temperatures were carefully adjusted within a range of 180°C to 205°C, as detailed in Table 3.1 to accommodate the distinct thermal and flow properties of each polymer in the blend, ensuring a smooth extrusion process and the desired quality of the filament. The filaments were wound onto spools and prepared for use in printing. These polymers and blends were printed using a Fused Deposition Modeling (FDM) process. Printing parameters, including layer height (0.20 mm), infill density (100%), infill line distance (0.4 mm), printing speed (60 mm/s), and nozzle size (0.4 mm) [31], were consistently maintained across all samples. The specific nozzle and bed temperatures, which varied among the samples, are comprehensively listed in Table 3.1.

Table 3.1: Compositions, extrusion temperatures, and 3D printing parameters of raw materials and blends.

Raw materials and Blends	Polymers ratios	Extrusion temperature (°C)	Nozzle temperature (°C)	Bed temperature (°C)
PLA	100/0	180	215	80
ABS	100/0	197	255	100
PMMA	100/0	200	255	100
PETG	100/0	205	255	100
PLA-25/ABS-75	25/75	197	250	100
PLA-50/ABS-50	50/50	197	245	100
PLA-75/ABS-25	75/25	197	230	90
PLA-25/PMMA-75	25/75	200	255	100
PLA-50/PMMA-50	50/50	200	255	100
PLA-75/PMMA-25	75/25	210	255	100
PLA-25/PETG-75	25/75	197	255	100
PLA-50/PETG-50	50/50	197	255	100
PLA-75/PETG-25	7525	197	255	100
ABS-25/PMMA-75	25/75	220	255	100
ABS-50/PMMA50	50/50	220	255	100
ABS-75/PMMA-75	75/25	220	255	100
ABS-25/PETG-75	25/75	205	255	100
ABS-50/PETG-50	50/50	205	255	100
ABS-25/PETG-75	7525	205	255	100
PETG-25/PMMA-75	25/75	197	250	100
PETG-50/PMMA-50	50/50	197	245	100
PETG-75/PMMA-25	75/25	197	245	100

3.3.2 Characterization

3.3.2.1 Tensile test

The mechanical testing was conducted using an MTS instrument machine equipped with a 20 KN load cell under standard ambient conditions, following ASTM D 638 guidelines. Three Type IV specimens were 3D printed in three distinct orientations (0°, ±45°, and 90°) for each composition to analyze their mechanical behavior.

3.3.2.2 Differential Scanning Calorimeter (DSC)

The thermal analyses were performed using the DSC Q 800 (TA instruments). The heating process ranged from 30°C to 200°C for PLA, PMMA, ABS and their mixtures, and from 30 to 290°C for PETG and its mixtures. Conversely, the cooling process ranged from 200°C to 30°C for the polymers and mixtures based on PLA, PMMA, and ABS and from 290°C to 30°C for PETG and its mixtures. Both heating and cooling were conducted at a rate of 10 °C/min, with a holding time of 5 minutes.

3.3.2.3 Infrared Spectroscopy (FTIR)

The chemical composition and the interactions between the functional groups of different polymer blends were analyzed using Fourier Transform Infrared Spectroscopy (FTIR) with a resolution of 4 cm^{-1}. The Attenuated Total Reflectance (ATR) mode was employed to examine representative bands over a 4000-400 cm-1 spectral range.

3.3.2.4 Scanning Electron Microscopy (SEM)

Samples were sputter-coated with gold using argon to generate plasma at approximately 20mv for ~3.5 minutes. Images were captured under a low vacuum (50Pa) with water in the chamber. The imaging was performed with a spot size of 5 μm at an accelerating voltage of 20kv.

3.3.2.5 Shape Memory Test

To evaluate shape memory characteristics, as shown in Figure 3.1, three 3D-printed samples of each composition, measuring 100 mm x 20 mm x 1 mm and oriented in the 0° direction, were heated to a designated programming temperature (T_p). The samples were then deformed by applying a force sufficient to conform to a mold 20 mm thick.

After applying the external force, the reconfigured samples were allowed to cool to room temperature while still under force. Once the sample achieved a stable shape, the mold and the force were removed, and the sample was left at room temperature until fully set. The angle of the set shape is referred to as θ_{fixed}. Subsequently, the sample was subjected to a constant temperature condition, during which the bending angle (θ_i) was meticulously recorded. More in depth detail about the tests can be found in our previous study [21]. The shape fixity and shape recovery ratios were then calculated based on these observed angles as follows:

$$Shape\ fixity\ (Sf) = \frac{\theta fixed}{\theta max}\ X\ 100 \qquad \text{(eq. 1)}$$

$$Shape\ recovery\ (Sr) = \frac{\theta \text{max} - \theta i}{\theta \text{max}}\ X\ 100 \qquad \text{(eq. 2)}$$

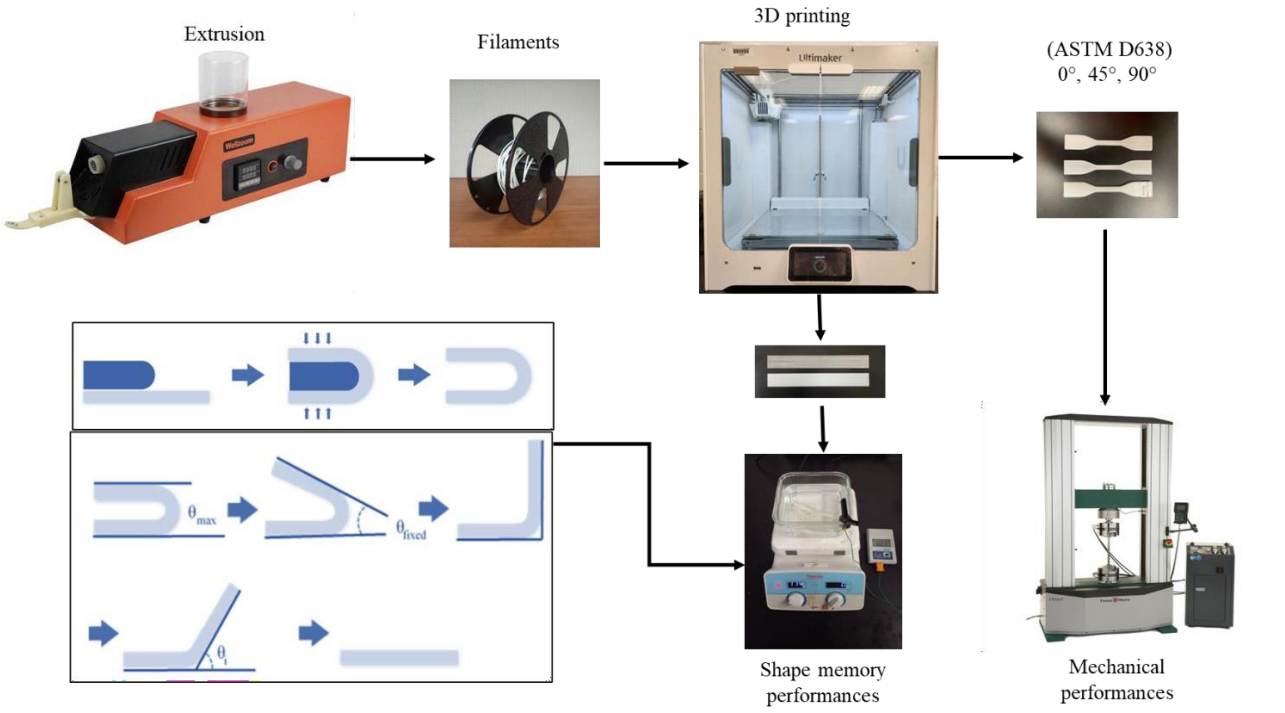

Figure 3.1: Steps involved in examining the mechanical and shape memory performances of 4D printing polymers and polymer blends.

3.4 Results and discussions

3.4.1 Differential scanning calorimeter (DSC)

As summarized in Table 3.2, and as illustrated in Figure 3.2, differential scanning calorimeter (DSC) analysis of the polymers indicates the following T_g: 58.85°C for PLA, 106.76°C for ABS, 78.30°C for PETG, and 117.07°C for PMMA. These temperatures represent the transition from the glassy phase to the rubbery phase. Additionally, the DSC curve for PLA shows a melting temperature of 143°C, confirming its semi-crystalline structure.

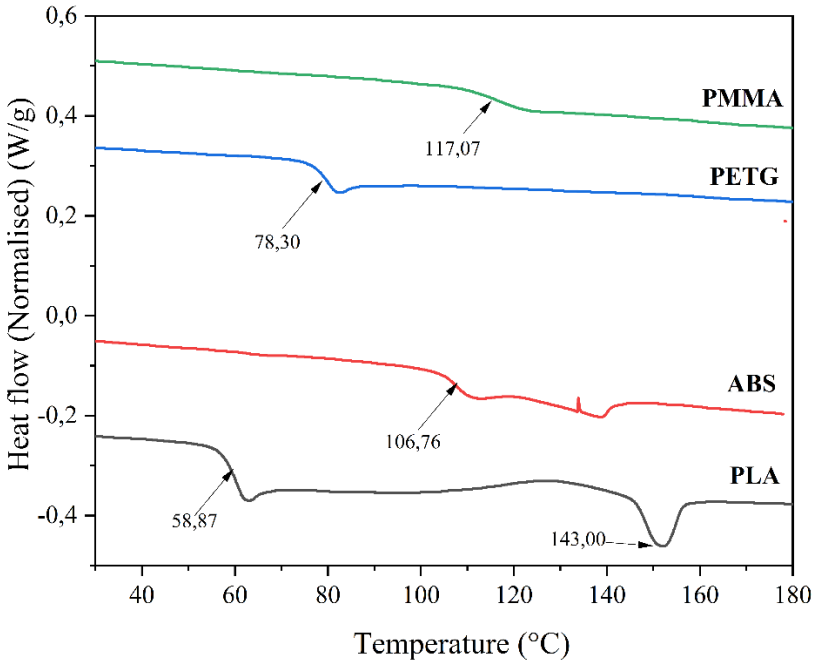

Figure 3.2: DSC curves of raw materials.

As ABS is amorphous, it does not exhibit a specific melting temperature. Instead, the endothermic peak around 140 °C observed in the DSC curve is attributed to the melting of processed materials used in blending styrene acrylonitrile (SAN) and butadiene copolymer, as confirmed by Reed et al. [32]. They also noted that the mold lubricant used during ABS production remains embedded within the ABS matrix. Furthermore, the manufacturer incorporates certain undisclosed chemicals to reduce viscosity and optimize extrusion and compression parameters. Therefore, the observed melting temperature at 140 °C is likely due to the melting of these auxiliary processing materials.

The T_g of different blends, as determined by DSC analysis, are summarized in Table 3.2. The results reveal six miscible blends, each displaying a single T_g, as illustrated in Figure 3.3. These blends include PLA-75/ABS-25, ABS-25/PMMA-75, ABS-50/PMMA-50, ABS-75/PMMA-25, PLA-75/PMMA-25 and PETG- 75/PMMA-25.

According to previous studies, the behavior of T_g in polymer blends serves as a crucial indicator of their miscibility. A single T_g observed between the T_g values of the pure components suggests molecular homogeneity, whereas multiple T_g values indicate phase separation among the blend's components [33].

Additionally, the blend ABS-25/PETG-75 shows partial miscibility, as its T_g values are closer compared to the other two polymer mixtures. Furthermore, the T_g values of these polymer blends fall within the range expected based on the neat polymers, aligning perfectly with the findings of Charasseangpaisarn et al. [34].

In the PLA blends, the results indicate that the difference in glass transition temperatures (ΔT_g) decreases with a reduction in the percentage of ABS. Complete miscibility was observed when 25% of ABS or PMMA was incorporated. Conversely, PLA/PETG and ABS/PETG blends displayed two distinct T_g, indicating their non-miscibility. In contrast, a single T_g value was recorded when 25% of PMMA was added to PETG, suggesting enhanced compatibility and miscibility at this specific blend ratio.

The ABS/PMMA blend exhibits miscibility at all concentrations, with the T_g decreasing as the percentage of PMMA decreases.

Interestingly, the endothermic peak commonly associated with PLA crystallinity could not be detected in some PLA polymer blend groups, such as PLA-25/PMMA-75, PLA-50/PMMA-50, and all levels of PLA/PETG, as shown in the heating curves presented in Figure 3.3. A potential explanation for this is that the presence of amorphous PMMA and PETG may disrupt the polymer chain arrangement in PLA, thus inhibiting the formation of crystalline structures in PLA. This observation is consistent with findings from earlier research conducted by Zhang et al. [35], which indicated that the endothermic peak associated with PLA's melting temperature only occurred when the PLA composition exceeded 90%. Similarly, Gonzalez-Garzon et al. [36] reported that the crystallization of PLA within a polymer blend was significantly hindered when the PMMA content exceeded 30%.

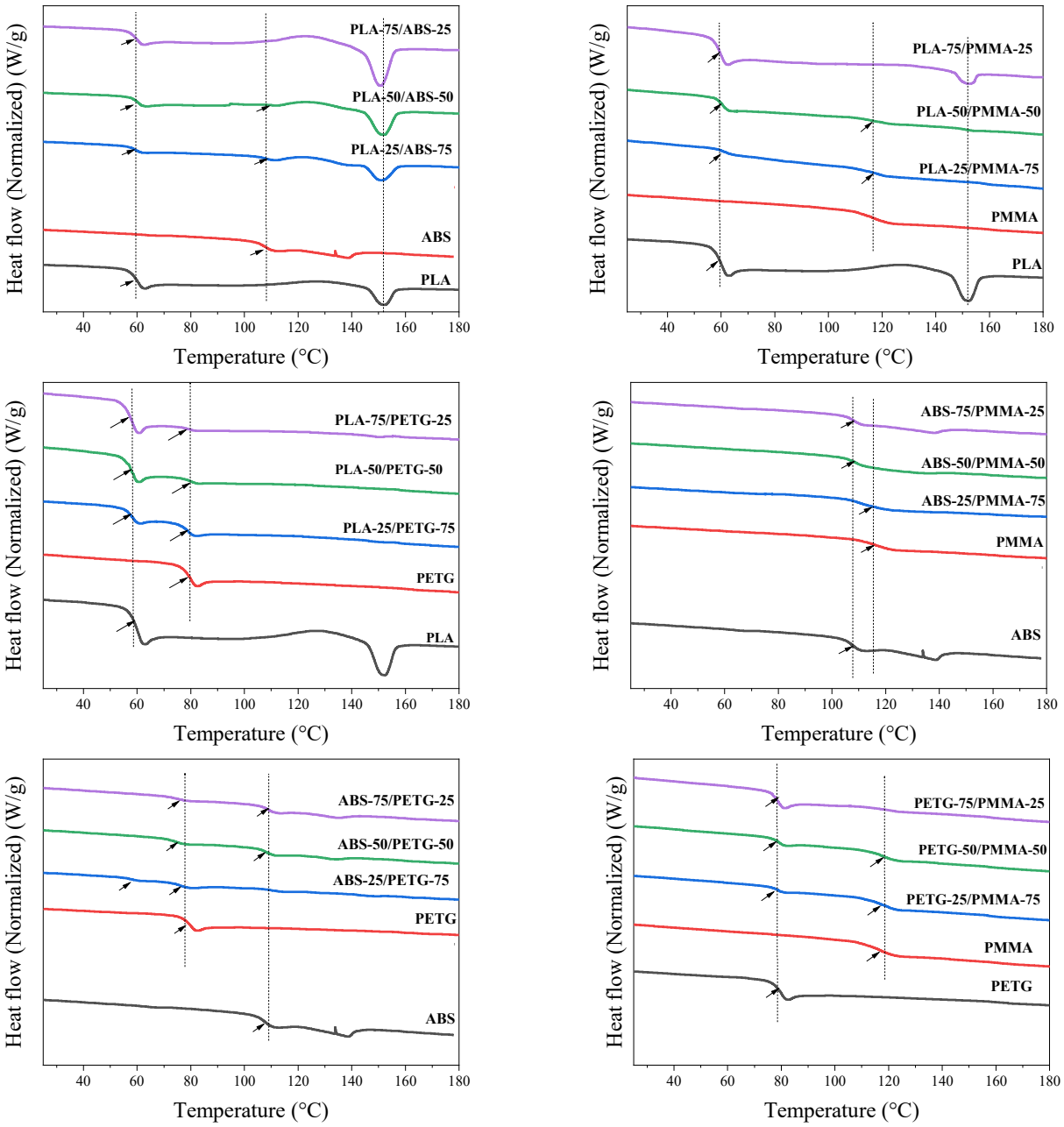

Figure 3.3: DSC curves of the different binary blends. The DSC curve of PLA, PETG and PLA/PETG polymer blends was also reported in [21].

Table 3.2: Thermal properties of polymers and blends.

Polymers and blends	Glass transition temperature (T_g) (°C)		ΔTg (°C)	Melting temperature (T_f)(°C)	Enthalpy of fusion (ΔH_f) (J/g)	Taux de cristalinité X_c (%)
	Tg_1	Tg_2				
PLA	58,870	-	-	143,000	6,319	6,795
ABS	106,760	-	-	-	-	-
PMMA	117,070	-	-	-	-	-
PETG	78,300	-	-	-	-	-
PLA-25/ABS-75	58,890	106,590	47,700	151,240	3,879	16,685
PLA-50/ABS-50	59,450	102,560	43,110	151,860	6,191	13,314
PLA-75/ABS-25	58,880	-	-	150,790	9,830	14,094
PLA-25/PMMA-75	60,940	117,180	56,240	-	-	-
PLA-50/PMMA-50	60,610	117,040	56,430	-	-	-
PLA-75/PMMA-25	59,090	-	-	152,150	-	-
PLA-25/PETG-75	57,200	78,380	21,180	150,49	2,3412	10,070
PLA-50/PETG-50	57,340	79,770	22,430	151,9	3,4345	7,390
PLA-75/PETG-25	57,000	78,950	21,950	152,36	3,3999	4,870
ABS-25/PMMA-75	112,610	-	-	-	-	-
ABS-50/PMMA-50	108,360	-	-	-	-	-
ABS-75/PMMA-25	107,450	-	-	-	-	-
ABS-25/PETG-75	57,710	76,540	18,830	-	-	-
ABS-50/PETG-50	74,330	108,020	33,690	-	-	-
ABS-25/PETG-75	74,170	109,230	35,060	-	-	-
PETG-25/PMMA-75	78,150	118,000	39,850	-	-	-
PETG-50/PMMA-50	79,140	119,360	40,220	-	-	-
PETG-75/PMMA-25	78,680	-	-	-	-	-

3.4.2 Infrared Spectroscopy (FTIR)

3.4.2.1 Polymers

The FTIR analysis was conducted to explore the distribution of functional groups at the molecular level in the different filaments resulting from the blending and extrusion process. Figure 3.4 illustrates that the main bonds identified in the FTIR spectra of PLA include the carbonyl (C=O) stretching at around 1750 cm^{-1}[37], C-H stretching between 2855-3000 cm^{-1}[38], C-O-C stretching from 1182-1266 cm^{-1} [39], O-H stretching around 3500-3200 cm^{-1}, and CH_3 bending at around 1450 cm^{-1}[40]. These characteristic bands are crucial for identifying and analyzing the structural and compositional aspects of PLA. Conversely, the main bonds observed in the FTIR spectrum of

ABS include the nitrile (C≡N) group from the acrylonitrile component, exhibiting an absorption band around 2236 cm^{-1}. The carbonyl (C=O) group, indicative of oxidative degradation, shows bands around 1749 cm^{-1}. The vinyl group (C=C Stretching) in the butadiene component results in absorption bands around 1603 cm^{-1}. Aliphatic C-H stretching vibrations are noted around 2850-2950 cm^{-1}, with C-H bending vibrations observed near 1450 cm^{-1} and 1380 cm^{-1}. Additionally, aromatic C-H stretching vibrations in the styrene component appear around 3029 cm^{-1}, and aromatic ring stretching vibrations near 1600 cm^{-1} and 1500 cm^{-1} [41]. The band at 967 cm^{-1} is associated with the carbon-hydrogen bonds in 1,4-butadiene, further defining the structural complexity of ABS.

The FTIR spectra of PETG reveal distinct peaks that delineate its molecular structure. The C=O stretching is prominently observed at approximately ~1713 cm^{-1}. C–H stretching vibrations in the aliphatic polymeric chain, characteristic of the alkanes present in PETG, are evident between 2850-3000 cm^{-1}. A peak at 1407 cm^{-1} corresponds to a slight aromatic rotation of C–H bends. Symmetrical C=O bends contribute to peaks observed at 1245 and 1092 cm^{-1}, enhancing the understanding of its molecular interactions. Additionally, the peak at 1017 cm^{-1} is attributed to C–H bends in PETG, while the stretch associated with these bends stretch is marked at 872 cm^{-1}. Another significant peak was observed at 724 cm^{-1}, which is indicative of the out-of-plane C–H bending vibration of the benzene ring, further confirming the aromatic components within the PETG structure [42].

The main bonds observed in the FTIR spectra of PMMA include the carbonyl (C=O) stretching around 1729 cm^{-1} [43], C–O stretching in the region 1140-1270 cm^{-1}[44], C–H stretching between 2800-3022 cm^{-1}, and C–H bending in the region of 1400-1500 cm^{-1}. Additionally, the peak at 699 cm^{-1} is attributed to the C-H out-of-plane bending vibrations, a characteristic bond associated with the methylene and methyl groups in the PMMA structure [43].

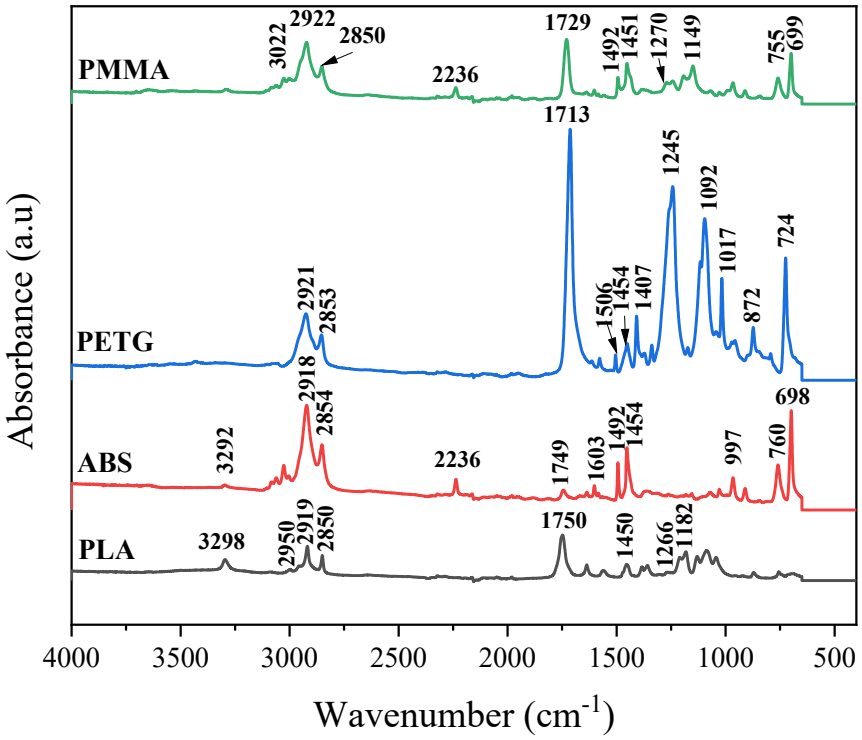

Figure 3.4: FTIR of PLA, ABS, PETG, and PMMA.

3.4.2.2 Polymer blends

The Fourier Transform Infrared (FTIR) spectroscopy analysis of polymer blends, as shown in Figure 3.5, offers valuable insights into the interactions and miscibility between different polymer components.

FTIR spectra of PLA/ABS blends often reveal changes in the intensity and position of peaks associated with the carbonyl group (around 1750 cm^{-1}) as a function of composition, indicating interactions between PLA and ABS components [41]. Specifically, the blends PLA-50/ABS-50 and PLA-75/ABS-25 exhibit a decrease in intensity of the (C=O) stretching compared to PLA-25/PETG-75. This observation corroborates the DSC results illustrated in Figure 3.3, which reported the miscibility of PLA-75/ABS-25. Moreover, the disappearance of ABS-specific peaks at 756 cm^{-1}, 697 cm^{-1}, and 2238 cm^{-1} is noted across all polymer blends. Additionally, ABS peaks at 3001 cm-1, 3026 cm-1, 3084 cm-1, and 3062 cm-1 are absent in the PLA-75/ABS-25 spectra, further confirming significant molecular interactions between the PLA and ABS components.

FTIR spectra of PLA/PMMA blends exhibit notable changes due to molecular interactions between the components. Specifically, there is a decrease in intensity in the C=O stretching region (around 1720-1750 cm^{-1}) and C–O–C stretching region (around 1140-1270 cm^{-1}), particularly in PLA-75/PMMA-25. Additionally, C–H stretching at around 2850 cm^{-1}disappear and C-H out-of-plane bending vibrations shifted from 699 $cm^{-1}$to 726 cm^{-1} in PMMA, PLA-25/PLA-75 and PLA-50/PLA-50 blends, respectively, and disappear entirely in PLA-75/PMMA-25 blend. These spectral changes signify alterations in the bonding environment, reflective of the miscibility between PLA and PMMA when the blend composition is 75wt% PLA and 25wt% PMMA [45].

The FTIR spectra of PLA-25/PETG-75 and PLA-50/PETG-50 blends reveal that they exhibit the same peaks as those of pure PLA and PETG without any changes in intensity or position. This observation suggests minimal interaction between the PLA and PETG components in these blends. Conversely, the spectra of the PLA-75/PETG-25 25 blend show increased peak intensities, which align with those of pure PLA, indicating a dominant PLA characteristic in the material properties.

Significant changes have been observed in the FTIR spectra of ABS/PMMA polymer blends. Notably, the ABS peaks at 1494 cm^{-1} ,1557 cm^{-1}, 1583 cm^{-1}, 1602 cm^{-1}, 1636 cm^{-1} ,2239 cm^{-1} and 3030 cm^{-1} have disappeared. In addition, there is a noticeable shift in the peak around 1730 cm^{-1} related to C=O stretching vibration in PMMA, which is influenced by interactions with ABS components [46]. Variations in the intensities of absorption bands were also noted. These spectroscopic observations–confirm the interaction between PMMA and ABS, indicating the miscibility of these two polymers.

In the ABS-25/PETG-75 polymer blend spectra, new peaks appear at1183 cm^{-1} and 1040 cm^{-1}, alongside the disappearance of peaks located at 760 cm^{-1}, 698 cm^{-1}, 3005 cm^{-1}, 3085 cm^{-1} in ABS, suggesting probable interaction between ABS and PETG. This observation supports the partial miscibility of these components as reported in section 3.4.1. Conversely, no changes are observed in the spectra of ABS-50/PETG-50 and ABS-75/PETG-25 spectra, indicating a lack of significant interaction or miscibility changes in these specific blend ratios.

Several changes in the FTIR spectra of PETG/PMMA polymer blends indicate interactions between the two polymers. Notably, peaks at 699 cm^{-1}, 757 cm^{-1}, 2240 cm^{-1}, and 3028 cm^{-1}, typically present in PMMA spectra, have disappeared. Additionally, a noticeable decrease in peak intensity is

observed in the PETG-25/PMMA-75 curve. These spectroscopic changes suggest significant molecular interaction between PETG and PMMA.

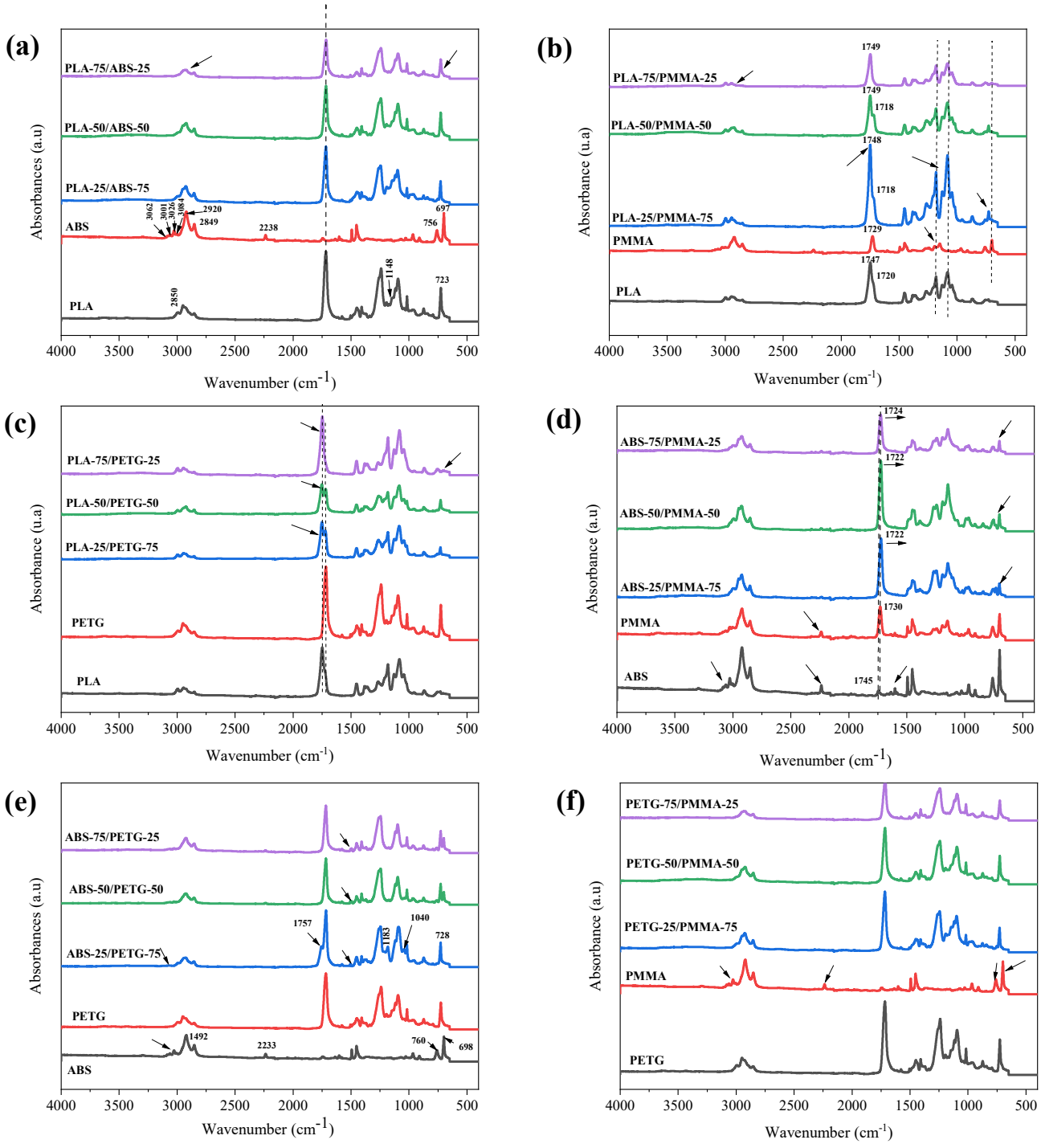

Figure 3.5: FTIR spectra of different polymer blends with (a): PLA/ABS polymer blend, (b): PLA/PMMA polymer blend, (c): PLA/PETG polymer blend, (d): ABS/PMMA polymer blend, (e): ABS/PETG polymer blend, (f): PETG/PMMA polymer blend.

3.4.3 Mechanical performances

3.4.3.1 Mechanical behavior of 3D printing polymers

As shown in Figure 3.6 (A), the mechanical behavior of the polymers varies significantly depending on the printing orientation, which is crucial for optimizing the mechanical performance of printed parts [47]. Specifically, PLA exhibits a brittle elastic behavior when printed in the 0° and 90° orientations. In contrast, an elastic ductile behavior is observed in samples printed at a ±45° orientation, as depicted in Figure 3.6 (a). On the other hand, ABS consistently shows an elastic ductile behavior (Figure 3.6 (b)). PMMA, however, shows a brittle elastic behavior in different printing orientations, as shown in Figure 3.6 (c). Furthermore, PETG demonstrates an elastic ductile behavior in 0° and ±45° orientations, while a brittle elastic behavior is observed in 90°, as detailed in Figure 3.6 (d).

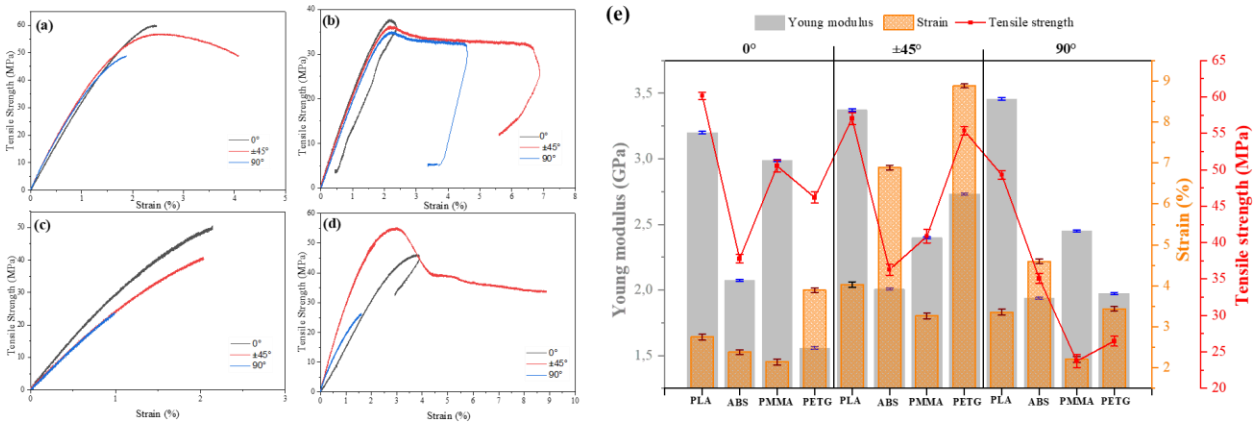

Figure 3.6: (a-d) Tensile curves of PLA, ABS, PMMA and PETG respectively in 0, ±45° and 90 printing orientation and (e) summary of mechanical performance of the PLA, ABS, PMMA and PETG. The tensile curves of PLA and PETG polymers were also reported in [21].

3.4.3.2 Effect of printing orientation on mechanical properties of polymers

As detailed in Figure 3.6 (B), the highest tensile strengths observed are 60 MPa, 37,8 MPa for ABS, and 50.5 MPa for PMMA when printed in the 0° orientation. This enhanced strength is attributed to better layer adhesion and alignment along the tensile load direction [21, 48, 49]. Conversely, samples printed at a ±45° orientation exhibit a slight decrease in tensile strength compared to the 0° orientation but offer a balance between strength and other mechanical properties like tensile strain. Specifically, PLA, ABS, PMMA, and PETG show increased tensile strain at this orientation,

recording values of 4,032 %, 6,884%, 3,268%, and 8,878%, respectively. This improvement is due to balanced stress distribution, increased flexibility, improved layer adhesion, and favorable anisotropic behavior. Collectively, these factors contribute to enhanced mechanical performance and greater deformation capacity before failure [50-52].

Samples printed in a 90° orientation tend to exhibit the lowest tensile strength due to weaker interlayer bonding. This decrease in strength arises because the layers are stacked perpendicular to the applied load, creating stress concentrators at the layer interfaces, which impede force distribution [53].

Despite variations in orientation, the Young modulus of PLA and ABS remains nearly constant. The intrinsic properties of these materials contribute to their homogeneous behavior, indicating their stiffness is largely isotropic. This uniformity ensures that the material's response to stress is consistent, regardless of the load direction [54].

In the case of PMMA and PETG, the highest elastic modulus values of 2,988 GPa and 2,731GPa, respectively, are recorded in the 0° and ±45° orientations. Specifically, when PMMA is printed at 0° orientation, the polymer chains align parallel to the direction of the applied load, enhancing intermolecular forces along the load direction, which results in increased stiffness and higher elastic modulus [55]. Conversely, in ±45° orientation, PETG layers are interlocked in a manner that significantly enhances the interlayer bonding strength. This improved bonding not only contributes to higher overall stiffness but also increases the elastic modulus, optimizing the material for applications requiring robust mechanical properties [56].

3.4.3.3 Mechanical behavior of 3D printing blends

According to Appendix 1, which displays the mechanical behavior of polymer blends in 0° printing orientation, the curves for the polymer blends are positioned between the neat polymers. Specifically, the PLA/ABS and PLA/PMMA blends demonstrate an elastic brittle behavior.

Conversely, the PLA/PETG and PETG/PMMA blends exhibit an elastic ductile behavior, except for compositions at a 25:75 weight ratio, which show different mechanical characteristics. Furthermore, the ABS/PMMA polymer blend predominantly exhibits elastic ductile behavior, especially in the ABS-75/PMMA-25 composition. Similarly, ABS/PETG blends generally present elastic ductile behavior, except for the ABS-75/PETG-25 blend.

Samples printed in the 90° orientation, as documented in Appendix 2, predominantly display elastic brittle behavior for PLA/ABS, PLA/PMMA, PLA/PETG (except for PLA-50/PETG-50), and PETG/PMMA polymer blends. In contrast, the ABS/PMMA and ABS/PETG blends exhibit elastic ductile behavior in this orientation.

Regarding the ±45° printing orientation, as detailed in Appendix 3, the polymer blends generally show elastic ductile behavior. However, exceptions include the PLA/PMMA blend and specific PETG/PMMA compositions, namely PETG-25/PMMA-75 and PETG-50/PMMA-50, which do not adhere to this trend.

3.4.3.4 Effect of composition and printing orientation on mechanical properties of polymer blends

The composition and printing orientation significantly affect the mechanical performances of polymer blends during 3D printing, as illustrated in Figure 3.7. For the PLA/ABS polymer blend shown in Figure 3.7 (a), the Young's modulus increases as the weight percentage (wt%) of ABS decreases, while the tensile strain decreases regardless of the printing orientation. On the other hand, tensile strength increases with a decrease of ABS wt% when printed in the 0° orientation. The highest tensile strength, recorded at 43,20 MPa, was observed when 75wt% ABS was blended with PLA. This enhancement is attributed to the improved properties resulting from the miscibility of PLA and ABS, as discussed in section 3.4.1. In the case of ±45° and 90° orientations, the optimal tensile strength of 35 MPa and 22,75 MPa, respectively, were recorded for the blend with 25wt% PLA and 75wt% ABS.

In the case of the PLA/PMMA (Figure 3.7 (b), the optimal Young's modulus and tensile strain values were recorded when the blend incorporated 75wt% of PMMA, independently of printing orientations. In addition, the highest tensile strength of 54,19 MPa, 62,08 MPa, and 47,54 MPa were recorded at 0°, ±45° and 90° orientations, respectively. The enhanced mechanical properties of this composition are attributed to the compatibility of PLA and PMMA, as previously suggested by Gonzalez-Garzon et al. [36]. This compatibility is confirmed by the DSC and FTIR analyses reported in sections 3.4.1 and 3.4.2. PMMA effectively acts as a compatibilizer, improving interfacial interactions and thereby enhancing the mechanical profile of the blend [57].

The Young's modulus of the PLA/PETG blend, as depicted in Figure 3.7 (c), exhibits an increase with the decrease of wt% PETG in 0° and ±45° printing orientations. In contrast, the Young's

modulus decreases as the wt% of PETG decreases when printed at a 90° orientation. On the other hand, the highest tensile strain of 10,32% was recorded for the PLA-50/PETG-50 blend in the 90° orientation. This finding result aligns with the findings of Vinyas et al.[58], which reported that the PLA/PETG blend achieves an optimal balance of mechanical strength and thermal properties, making it particularly suitable for applications where both characteristics are critical.

In the case of the ABS/PMMA polymer blend, as illustrated in Figure 3.7 (d), the elastic modulus decreases with the reduction in wt% PMMA across all printing orientations. This trend can be attributed to the inherently higher stiffness of PMMA compared to ABS, as detailed in section 3.3.2. Conversely, the tensile strain increases with the decrease as the wt% of PMMA in the 0° and ±45° printing orientation. However, an opposite trend is observed in the 90° printing orientation, where the tensile strain decreases with a reduction in PMMA content.

The tensile strength of the ABS/PMMA polymer blend varies significantly depending on the composition and printing orientation. The highest tensile strength values for the blend with 25% ABS and 75% PMMA were recorded at 42.38 MPa in the 0° orientation and 45.23 MPa in the 90° orientation. Conversely, the blend with 75% ABS and 25% PMMA exhibited its best tensile strength of 44.48 MPa in the ±45° printing orientation.

The mechanical performance of the ABS/PETG blend, as presented in Figure 3.7 (e), indicates that the Young's modulus increases with a decrease in wt% PETG in the 0° orientation. Conversely, the Young's modulus appears almost stable in the ±45° and 90° orientations.

The tensile strain increases of the ABS/PETG blend with the increases of PETG content at 0°. Notably, the highest tensile strain values of 13,31% and 5,92% are recorded for ABS-50/PETG-50 printed at ±45° and 90°, respectively. Additionally, this blend configuration also exhibits the best tensile strength of 38.36 MPa in the 0° orientation.

On the other hand, the ABS-25/PETG-75 demonstrates even higher tensile strengths of 44,48 MPa and 39,04 MPa at ±45° and 90°, respectively. This agrees with results from DSC, which suggest partial miscibility between ABS and PETG in this specific composition, contributing to enhanced tensile strength compared to other blend ratios. This indicates a direct correlation between polymer miscibility and the resulting mechanical properties, emphasizing the importance of blend composition in achieving optimal performance.

Figure 3.7 (f) illustrates that the elastic modulus of PETG/PMMA polymer blend in 0° printing orientation decreases as the PETG content increases. Conversely, the tensile strain increases with a higher PETG content in the blend. Additionally, the optimal elastic modulus values are observed for blends with varying ratios: PETG-50/PMMA-50 and PETG-25/PMMA-75, which exhibit elastic moduli of 2.12 GPa and 2.50 GPa at ±45° and 90° printing orientations, respectively. This trend highlights the influence of PETG concentration on the mechanical properties, with increased PETG leading to greater flexibility but reduced stiffness, affecting the performance characteristics depending on the printing orientation.

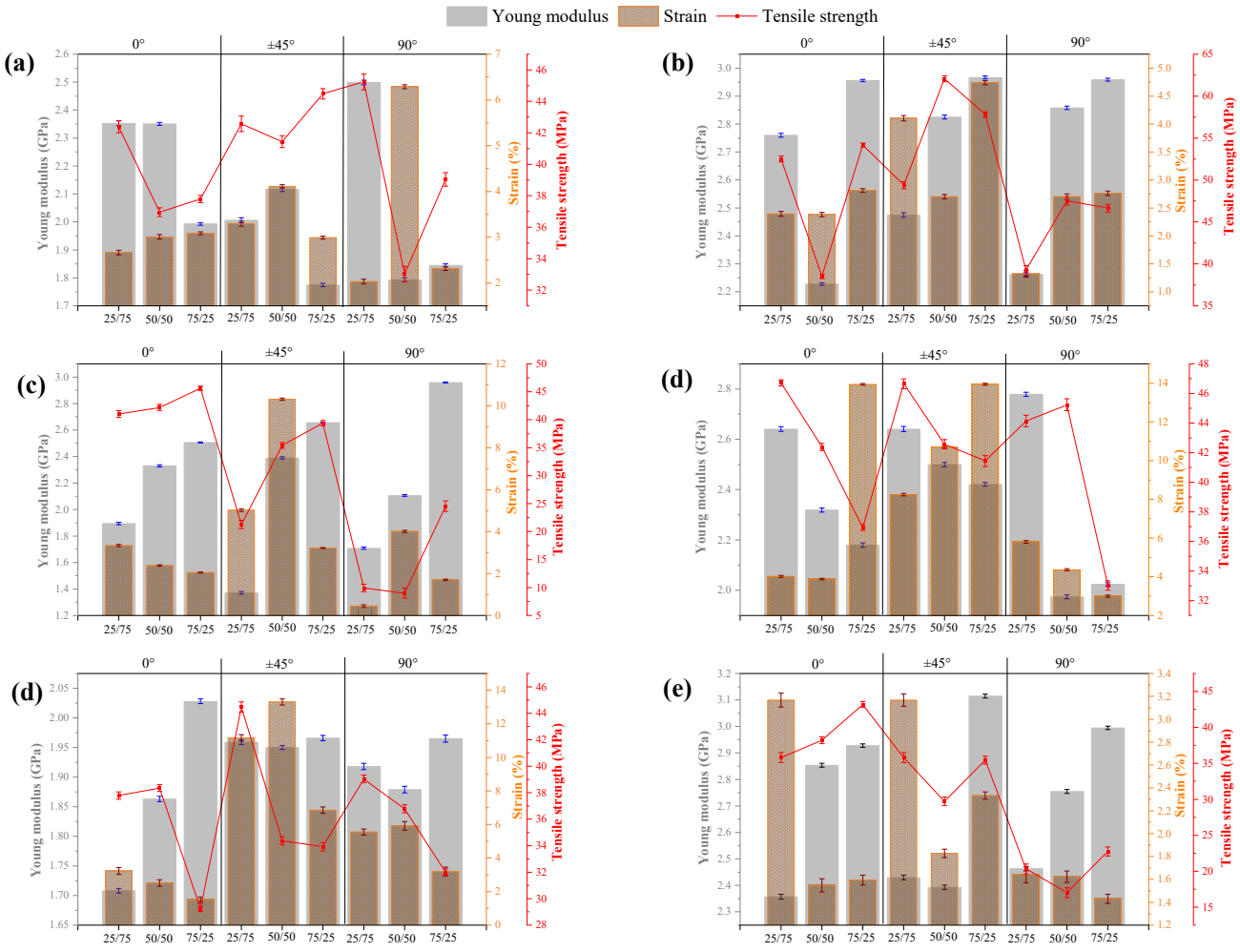

Figure 3.7: Mechanical performances of different polymer blends as a function of composition and orientation with (a) PLA/ABS, (b) PLA/PMMA, (c) PLA/PETG, (d) ABS/PMMA, (e) ABS/PETG, and (f) PETG/PMMA.

Furthermore, the highest tensile strength values for the PETG/PMMA polymer blend demonstrate how printing orientation further influences mechanical properties. Specifically, the PETG-

50/PMMA-50 blend exhibited the greatest tensile strength of 48.51 MPa in the 0° orientation and 39.70 MPa in the ±45° orientation. Meanwhile, the best tensile strength at the 90° orientation, 24.45 MPa, was observed in the PETG-25/PMMA-75 blend. These findings highlight the critical role of both blend ratio and orientation in optimizing the mechanical performance of 3D printed materials.

3.4.4 Scanning Electron Microscopy (SEM)

The study of polymer blend compositions is instrumental in examining the compositions of polymer blends, providing critical insights into how different polymer ratios in the blend affect their morphology and mechanical properties. It allows a detailed view of the materials' microstructures, facilitating a deeper understanding of the relationship between polymer blend composition, morphology, and mechanical properties under various conditions.

Figure 3.8 (a-c) illustrates how the composition of the polymer blends impacts morphology and the adhesion of deposited filaments. Notably, the images reveal the presence of pores in the PLA-25/PMMA-75 and PLA-50/PMMA-50 blends, with a noticeable reduction in pores in the PLA-75/PMMA-25 blend. This variation suggests that the ratio of PLA to PMMA significantly affects both morphology and porosity. Higher concentrations of PMMA lead to more pronounced phase separation, leading to larger pores. Conversely, a blend with a higher proportion of PLA exhibits smaller, more uniformly distributed pores, enhancing the material's overall structural integrity. [59]. This result correlates with the thermal analysis by DSC, which indicated good miscibility at 25wt% PMMA in PLA. Moreover, improved adhesion between deposited filaments in this composition was noted, contributing to the enhanced mechanical properties.

Furthermore, the interfacial adhesion between PETG and PMMA improves with increased PETG content, leading to better mechanical properties and reduced interfacial cavities, as shown in Figure 3.8 (f). This enhancement is attributed to increased miscibility and interaction between the two polymers, a finding supported by the thermal characterization discussed earlier. These interactions lead to a more cohesive blend, effectively minimizing the formation of cavities at the interface and thereby strengthening the overall material structure.

Zhang et al. [60] reported that the strength of interlayer adhesion in 3D-printed polymers is largely determined by the diffusion of polymer chains between the layers. As each layer is deposited, the surface of the molten polymer from the previous layer stays sufficiently warm, allowing for molecular diffusion and interlocking with the newly added material. The extent of diffusion and

the width of the wetted interface play key roles in determining the bonding strength. Research indicates that increased filling densities and optimized cooling rates enhance adhesion strength by promoting improved molecular diffusion.

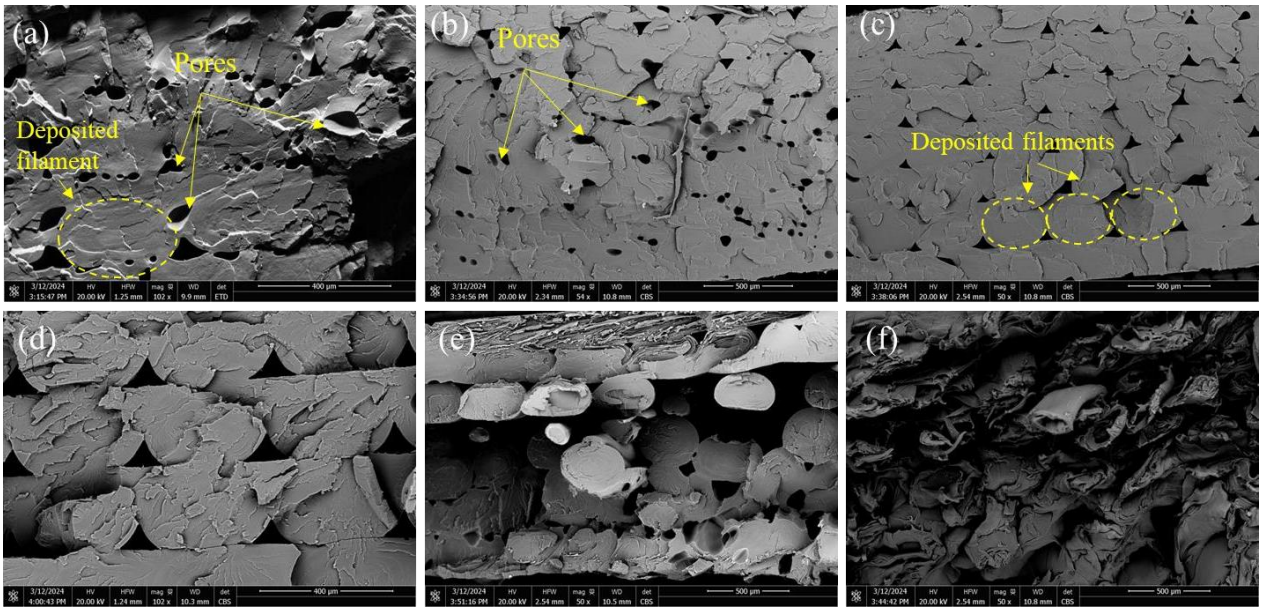

Figure 3.8: SEM micrographs of PLA/PMMA and PETG/PMMA polymer blends with (a) PLA-25/PMMA-75, (b) PLA-50/PMMA-50, (c) PLA-75/PMMA-25, (d) PETG-25/PMMA-75, PETG-50/PMMA-50, PETG-75/PMMA-25.

3.4.5 Shape memory performance

3.4.5.1 Shape memory performance of polymers

According to Figure 3.9, PLA and PETG exhibit optimal U-shape fixity and shape recovery, achieving 100% when programmed at 70°C and 90°C, respectively, and recovered at 90°C. The shortest recovery time values recorded were 3 seconds for PLA and 5 seconds for PETG. The shape memory effect (SME) in PLA is significantly influenced by its crystallinity. The crystal regions within PLA act as network nodes that help maintain the deformed shape. When heated above the T_g, PLA returns to its original shape due to the release of stored elastic energy [61]. Conversely, the shape memory properties of PETG are primarily attributed to its amorphous structure, which allows molecular entanglements to act as network points. This structural characteristic makes PETG highly responsive to temperature changes, facilitating its shape memory capabilities [14].

Figure 3.10 reveals that the lowest shape fixity values, 63,89 % for ABS and 47.78% for PMMA, indicate challenges in achieving optimal shape memory performance. ABS, a thermoplastic polymer consisting of three distinct monomers (acrylonitrile, butadiene, and styrene), exhibits a phase-separated structure that complicates the formation of a cohesive network essential for effective shape memory behavior [62]. Furthermore, the mechanical properties disparities among the three phases in ABS impact its capacity to efficiently store and release elastic energy efficiently, which is crucial for shape memory functionality [63]. This underscores the complexity of achieving consistent shape memory effects in polymers with heterogeneous structures.

PMMA, as an amorphous polymer, lacks a crystalline phase that would provide physical cross-links essential for effective shape memory performance [64]. Because of its stiff polymer chains and limited molecular mobility, PMMA's inherent brittleness compromises its ability to exhibit significant elastic recovery. This structural limitation restricts the polymer's capacity to revert to its original form, impeding the shape recovery process crucial for shape memory functionality [65].

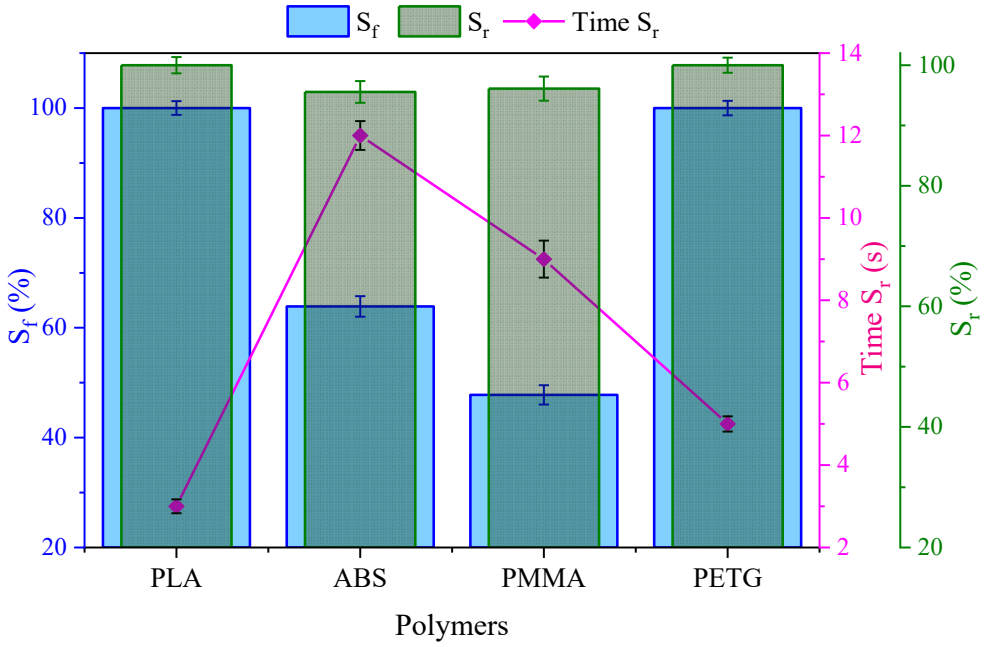

Figure 3.9: Shape fixity, shape recovery, and time of shape recovery of polymers.

Shape memory polymer blends that combine PLA, ABS, PMMA, and PETG capitalize on the distinct advantages of each constituent polymer. By carefully adjusting the ratios and processing conditions, it is possible to tailor specific properties to meet the needs of targeted applications. This strategic customization facilitates the development of innovative materials that offer broad

application potential in industries demanding durability, flexibility, and environmental friendliness. These blends represent a versatile approach in material science, enabling the creation of products that are not only effective in their functionality but also align with sustainability goals.

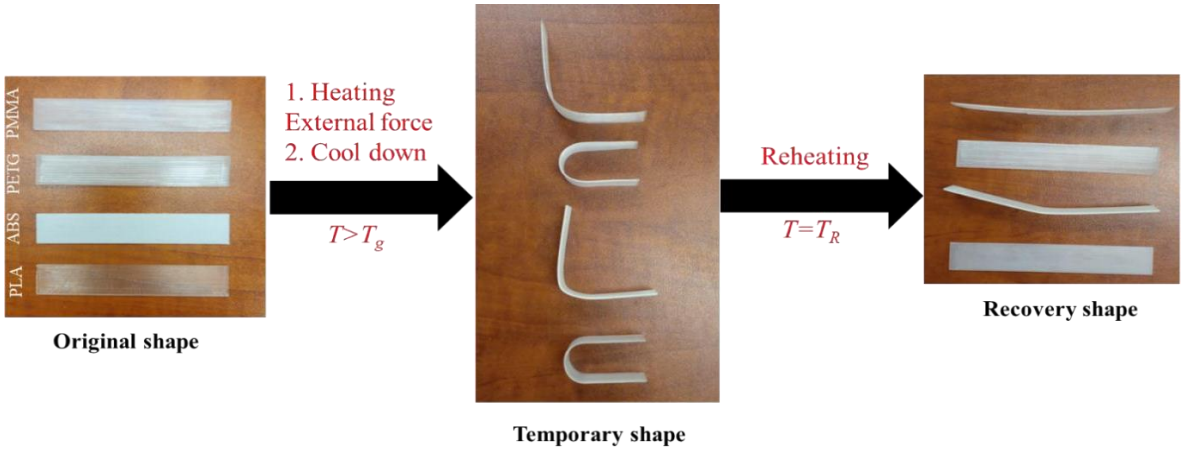

Figure 3.10: U-Shape memory of 4D printed PLA, ABS, PETG, and PMMA.

3.4.5.2 Shape memory performances of polymer blends

Shape memory polymer blends are cutting-edge materials designed to return to their original shape after deformation when exposed to an external stimulus, such as heat. These blends synergistically combine the beneficial properties of various polymers to fine-tune mechanical, thermal, and shape memory characteristics [27, 66, 67]. This section specifically examines blends that incorporate PLA, ABS, PMMA, and PETG.

First, the shape fixity and recovery of the 3D printing PLA/ABS polymer blend increase as the PLA content in the blend increases (Table 3.3). The highest shape fixity and recovery values, 90% and 97,22%, respectively, were observed for the PLA-75/ABS-25 blend at 100°C, as shown in Figure 3.11. Additionally, this composition also demonstrated the quickest shape recovery time, recorded at just 8 seconds. This indicates that increasing the PLA proportion enhances the blend's ability to retain and revert to its original form efficiently under thermal stimulus.

In the case of the PLA/PMMA blend, as depicted in Figure 3.11 (b), shape fixity and recovery improve with increased PLA content within the blend. The optimal shape fixity (S_f) and shape recovery (S_R) of 93,33 % and 100%, respectively, were observed in the blend containing 75wt%

PLA (PLA-75/PMM-75). The lowest shape recovery time of 7 seconds was observed when 75wt% of PLA was blended with PMMA.

The incorporation of PMMA into PLA enhances the degree of molecular entanglement, which is critical for shape memory performance. This increased entanglement facilitates better miscibility at the nanoscale, as evidenced by the broadening of the T_g in the DSC results. This enhancement in miscibility directly contributes to the improved shape memory properties of the blend [25].

Hight shape memory performance was demonstrated in the PLA/PETG blend (Figure 3.11 (c)), particularly with the PLA-75/PETG-25 blend, which exhibits a shape fixity of 98,33% and a shape recovery of 100% at 79°C, as reported in and illustrated in Figure 3.12. In contrast, the shape recovery time increases as the PETG content in the blend decreases, with the longest recovery time of 28 seconds observed for the PLA-25/PETG-75 blend. This is due to the effect of PETG on the entanglement and interaction between polymer chains; higher PETG content enhances chain mobility and reduces the energy required for shape recovery. As PETG content decreases, these interactions diminish, resulting in slower shape recovery times [14]. Furthermore, the ABS/PETG blend also shows an increase in recovery time as PETG content decreases. However, the highest recovery, at 86,67 %, was observed in the ABS-25/PETG-75 blend. This pattern highlights the crucial role of PETG in enhancing the flexibility and inter-chain interactions necessary for efficient shape recovery in these polymer blends.

The ABS/PMMA blend shows relatively low shape fixity and recovery, as indicated previously. The limited shape memory performance of this blend can be attributed to the lack of sufficient crosslinking and crystallinity, as detailed in Table 3.2. Polymers with higher degrees of crosslinking or crystallinity generally show enhanced shape memory properties. This is because crosslinking and crystalline structures provide stable networks within the polymer matrix that effectively retain and revert to their original shape under the appropriate stimuli [64]. Therefore, the absence of these critical network structures in the ABS/PMMA blends hampers their ability to efficiently store and recover mechanical energy, reflecting their suboptimal shape memory capabilities.

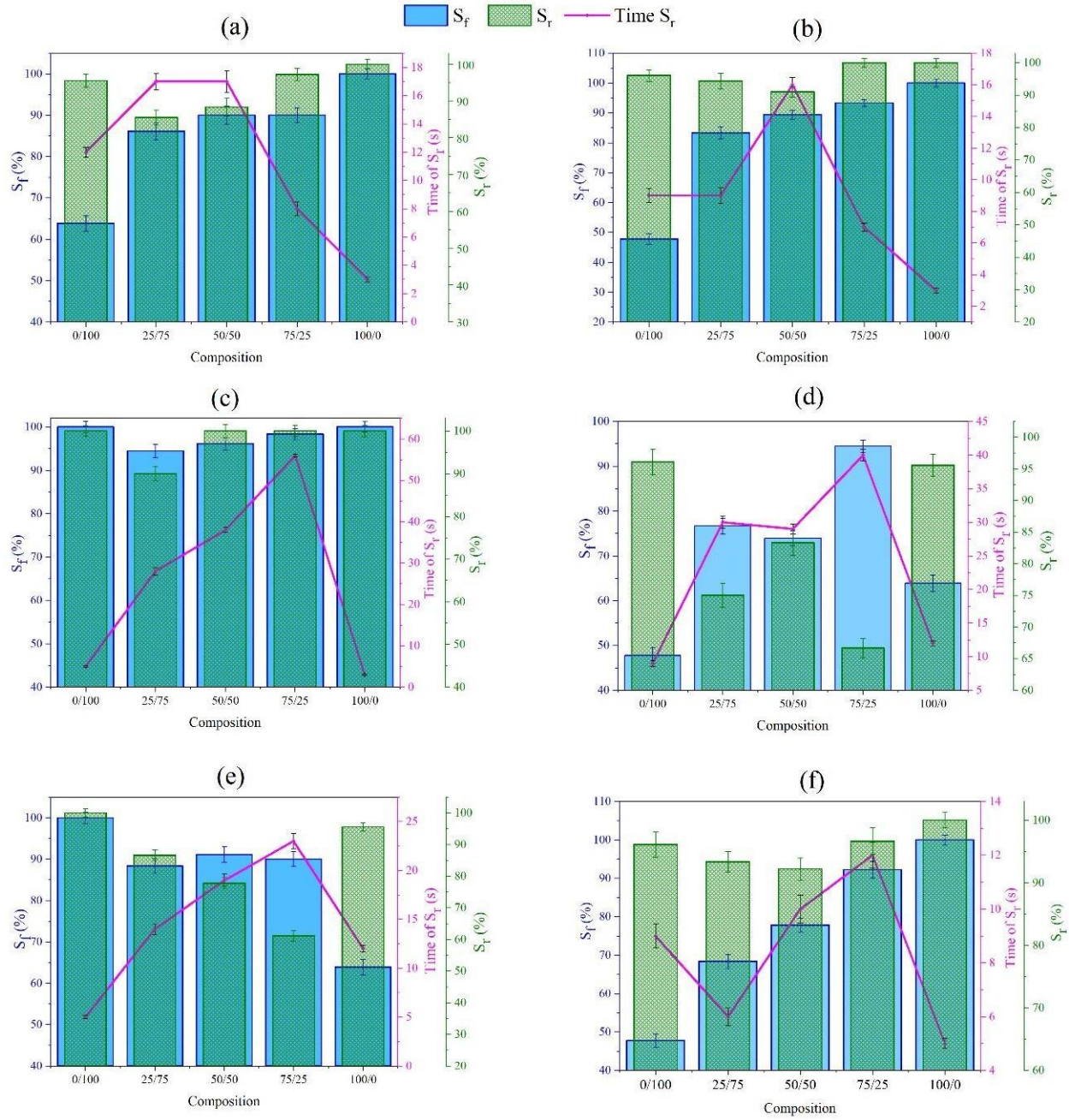

Figure 3.11: Shape fixity, shape recovery, and time of shape recovery of (a) PLA/ABS, (b) PLA/PMMA, (c) PLA/PETG, (d) ABS/PMMA, (e) ABS/PETG, and (f) PETG/PMMA.

The PETG/PMMA blend shows enhanced shape fixity, shape recovery, and recovery time with increased PETG content. Notably, the highest S_f and S_r values of 92,22 % and 96,67 %, respectively, were observed for the miscible PETG-75/PMMA-25 blend. Research on similar

polymer blends indicates that higher content of flexible components, such as PETG in this case, can lead to improved shape memory properties due to the formation of a more effective entanglement network. This network enhances the material's capability to recover its original shape efficiently [68]. Conversely, the improved shape recovery time is attributed to a lower PMMA content, which affects the viscoelastic properties of the blend. PMMA is known to contribute to viscoelastic relaxation processes that facilitate quick shape recovery. With decreased PMMA content, these processes become less effective, resulting in longer recovery times due to the diminished ability of the polymer to promptly return to its original configuration [69].

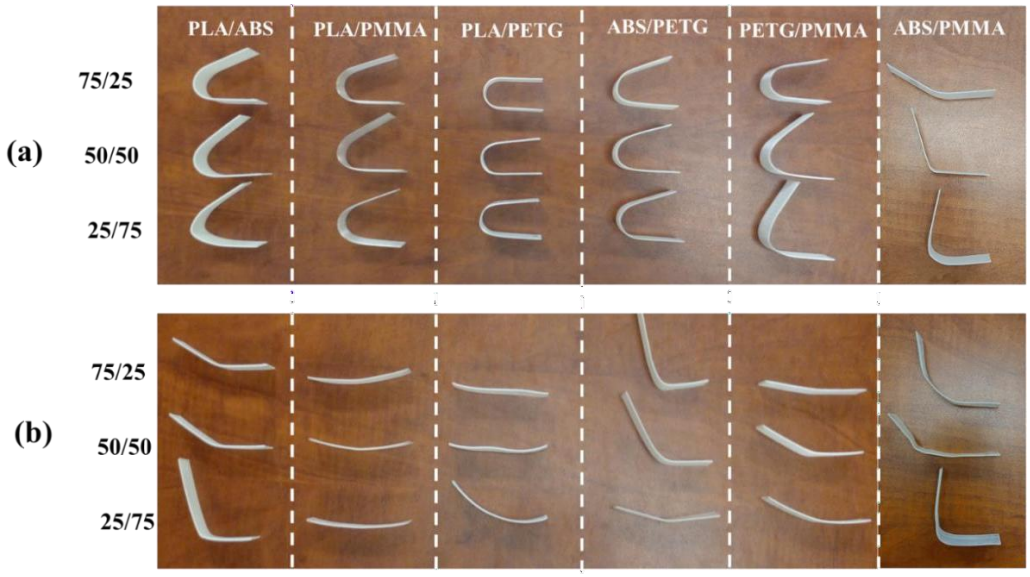

Figure 3.12: U-Shape memory performance of different polymer blends with (a) Shape fixity, and (b) Shape recovery.

This highlights the delicate balance between the components of a polymer blend in determining its overall performance in terms of shape memory and recovery speed.

An essential consideration in the development of these blends is the balance between biodegradability and recyclability. Indeed, the biodegradability and recyclability of PLA blends with ABS, PMMA, and PETG are strongly influenced by their composition. Blends with high PLA content, such as PLA-75/ABS-25, PLA-75/PMMA-25, and PLA-75/PETG-25, retain significant biodegradability, as PLA is inherently biodegradable [70]. However, increasing the proportion of ABS or PMMA reduces this property due to their non-biodegradable nature [71]. PETG, while non-biodegradable, enhances recyclability, making blends with higher PETG content more suitable for recycling applications [72, 73]. Miscibility plays a crucial role, with blends like PLA-

75/PMMA-25 and PETG-75/PMMA-25 exhibiting better recyclability due to their homogeneity [74]. To achieve specific sustainability goals, high PLA content is ideal for biodegradable solutions, while increasing PETG content supports recyclability. Balancing these components allows for tailoring blends to meet diverse environmental and functional requirements.

Table 3.3: Shape memory performances of polymers and polymer blends.

Raw materials and Blends	Extrusion temperatures (°C)	Programmation temperatures (T_p) (°C)	Recovery temperatures (T_R)(°C)	Shape fixity (S_f) (%)	Shape recovery (S_r) (%)	Time (s)
PLA	180	70	90	100,00±1,25	100,00±1,35	3±0,17
ABS	197	100	100	63,89±1,87	95,56±1,80	12±0,35
PMMA	200	100	100	47,78±1,76	96,11±2,00	9±0,45
PETG	205	90	90	100,00±1,32	100,00±1,25	5±0,18
PLA-25/ABS-75	197	105	100	86,11±2,10	85,56±2,00	17±0,56
PLA-50/ABS-50	197	100	100	90,00±2,24	88,33±2,44	17±0,78
PLA-75/ABS-25	197	100	100	90,00±1,72	97,22±1,60	8±0,48
PLA-25/PMMA-75	200	90	100	83,33±2,00	94,44±2,40	9±0,50
PLA-50/PMMA-50	200	100	100	89,44±1,50	91,11±1,60	16±0,48
PLA-75/PMMA-25	210	90	100	93,33±1,24	100,00±1,34	7±0,26
PLA-25/PETG-75	197	77	77	94,44±1,56	90,00±1,66	28±0,90
PLA-50/PETG-50	197	77	78	96,11±1,45	100,00±1,55	38±0,67
PLA-75/PETG-25	197	79	79	98,33±1,28	100,00±1,27	56±0,33
ABS-25/PMMA-75	220	120	100	76,66±1,77	75,00±1,93	30±0,88
ABS-50/PMMA50	220	120	100	73,88±1,66	83,33±1,97	29±0,73
ABS-75/PMMA-75	220	120	100	94,44±1,32	66,66±1,55	40±0,85
ABS-25/PETG-75	205	90	95	88,33±1,78	86,67±1,65	14±0,55
ABS-50/PETG-50	205	105	100	91,11±1,85	77,78±1,83	19±0,63
ABS-75/PETG-25	205	105	100	90,00±1,76	61,11±1,74	23±0,77
PETG-25/PMMA-75	197	100	100	68,33±1,87	93,33±1,67	6±0,33
PETG-50/PMMA-50	197	100	100	77,78±1,89	92,22±1,79	10±0,52
PETG-75/PMMA-25	197	100	100	92,22±2,20	96,67±2,12	12±0,47

3.5 Conclusions

The mechanical properties of polymer blends are significantly influenced by both the composition and the 3D printing orientation. Compatible blends that exhibit proper phase morphology and are optimized in orientation during processing tend to display enhanced mechanical performance. Improved interfacial interactions and controlled orientation contribute notably to properties such

as tensile strength and tensile strain, fostering the development of high-performance polymer materials.

Miscible polymer blends provide the capability to finely tune shape memory effects (SMEs) through adjustments in composition. This design flexibility allows for manipulating mechanical properties and stimuli-responsiveness, which are essential for tailored applications. For example, the miscibility of specific polymer blends facilitates the creation of multiple-SMEs characterized by variable glass transition temperatures and transition zones, thereby broadening their functional range.

For PLA/ABS blends, the PLA-75/ABS-25 configuration demonstrated the highest shape fixity (90%) and recovery (97.22%) at 100°C, with a recovery time of 8 seconds. These blends also achieved a tensile strength of 43.20 MPa in the 0° orientation, showcasing improved miscibility and mechanical performance.

In PLA/PMMA blends, the PLA-75/PMMA-25 composition exhibited the best overall performance, with a shape fixity of 93.33%, a recovery of 100%, and the shortest recovery time of 7 seconds at 90°C. The tensile strength reached 54.19 MPa in the 0° orientation, benefiting from enhanced molecular entanglement and nanoscale miscibility.

For PLA/PETG blends, the PLA-75/PETG-25 composition achieved optimal shape memory properties, with a shape fixity of 98.33%, a recovery of 100%, and a recovery time of 28 seconds at 79°C. The tensile strain peaked at 10.32% in the 90° orientation for the PLA-50/PETG-50 blend, highlighting its balance of strength and flexibility.

The ABS/PMMA blends demonstrated relatively lower shape memory performance, with the ABS-75/PMMA-25 configuration achieving a tensile strength of 44.48 MPa in the ±45° orientation. The limited crosslinking and crystallinity in these blends restricted their shape memory capabilities.

In PETG/PMMA blends, the PETG-75/PMMA-25 composition showed the highest shape fixity (92.22%) and recovery (96.67%) at 100°C, with a tensile strength of 48.51 MPa in the 0° orientation. The improved miscibility and entanglement network contributed to superior mechanical and shape memory performance.

Overall, these findings demonstrate the potential of polymer blends to enhance biodegradability and recyclability through tailored compositions. High PLA content prioritizes biodegradability,

while increased PETG content enhances recyclability. These results emphasize the versatility of polymer blends for achieving specific performance and sustainability objectives in advanced 4D printing applications.

3.6 Acknowledgement

The authors acknowledge the funding provided by the Natural Sciences and Engineering Research Council (NSERC) of Canada (grant number: CRSNG – RGPIN -2021-02846).

3.7 References

1. Rahmatabadi, D., et al., 4D printing thermo-magneto-responsive PETG-Fe3O4 nanocomposites with enhanced shape memory effects. Applied Materials Today, 2024. 40: p. 102361.
2. Rahmatabadi, D., et al., Poly (ethylene terephthalate) glycol/carbon black composites for 4D printing. Materials Chemistry and Physics, 2024. 325: p. 129737.
3. Zhang, J., et al., Advances in 4D printed shape memory polymers: from 3D printing, smart excitation, and response to applications. Advanced Materials Technologies, 2022. 7(9): p. 2101568.
4. Wang, J., et al., Biomimetic shape–color double-responsive 4D printing. Advanced Materials Technologies, 2019. 4(9): p. 1900293.
5. Hatami, H., et al., Exploring the potential of 3D and 4D printing in advancing stent manufacturing for cardiovascular diseases. European Polymer Journal, 2024: p. 113035.
6. Megdich, A., M. Habibi, and L. Laperrière, A review on 4D printing: Material structures, stimuli and additive manufacturing techniques. Materials Letters, 2023. 337: p. 133977.
7. Karima, B., M. Habibi, and L. Laperrière, 4D printing of fiber-reinforced auxetic structures: the building blocks: a review. Smart Material Structures, 2024. 33(6): p. 063001.
8. Meng, Q. and J. Hu, A review of shape memory polymer composites and blends. Composites Part A: Applied Science and Manufacturing, 2009. 40(11): p. 1661-1672.
9. Zhang, H., et al., A novel type of shape memory polymer blend and the shape memory mechanism. Polymer, 2009. 50(6): p. 1596-1601.
10. Wan, X., et al., Recent Advances in 4D Printing of Advanced Materials and Structures for Functional Applications. Advanced Materials, 2024: p. 2312263.
11. Haleem, A., et al., Significant roles of 4D printing using smart materials in the field of manufacturing. Advanced Industrial and Engineering Polymer Research, 2021. 4(4): p. 301-311.
12. Mehrpouya, M., et al., 4D printing of shape memory polylactic acid (PLA). Polymer, 2021. 230: p. 124080.
13. Barletta, M., A. Gisario, and M. Mehrpouya, 4D printing of shape memory polylactic acid (PLA) components: Investigating the role of the operational parameters in fused deposition Soleyman, E., et al., Shape memory performance of PETG 4D printed parts under compression in cold, warm, and hot programming. Smart Materials and Structures, 2022. 31(8): p. 085002.
14. Hassan, M.H., et al. Preliminary studies on the suitability of PETG for 4D printing applications. in MATEC Web of Conferences. 2020. EDP Sciences.
15. Fallah, A., Q. Saleem, and B. Koc, Assessment of mechanical properties and shape memory behavior of 4D printed continuous fiber-reinforced PETG composites. Composites Part A: Applied Science and Manufacturing, 2024. 181: p. 108165.
16. Rahmatabadi, D., et al., 4D printing and annealing of PETG composites reinforced with short carbon fibers. Physica Scripta, 2024. 99(5): p. 055957.
17. Muthe, L.P., K. Pickering, and C. Gauss, A review of 3D/4D printing of poly-lactic acid composites with bio-derived reinforcements. Composites Part C: Open Access, 2022. 8: p. 100271.
18. Hosseinzadeh, M., M. Ghoreishi, and K. Narooei, 4D printing of shape memory polylactic acid beams: an experimental investigation into FDM additive manufacturing process parameters, mathematical modeling, and optimization. Journal of Manufacturing Processes,

2023. 85: p. 774-782.
19. Soleyman, E., et al., 4D printing of PET-G via FDM including tailormade excess third shape. Manufacturing Letters, 2022. 33: p. 1-4.
20. Bouguermouh, K., et al., 4D-printed PLA-PETG polymer blends: comprehensive analysis of thermal, mechanical, and shape memory performances. Journal of Materials Science, 2024: p. 1-18.
21. Memarian, F., A. Fereidoon, and M. Ghorbanzadeh Ahangari, Effect of acrylonitrile butadiene styrene on the shape memory, mechanical, and thermal properties of thermoplastic polyurethane. Journal of Vinyl and Additive Technology, 2018. 24: p. E96-E104.
22. Booth, C.J., et al., Copolyterephthalates containing tetramethylcyclobutane with impact and ballistic properties greater than bisphenol A polycarbonate. Polymer, 2006. 47(18): p. 6398-6405.
23. Ge, Q., et al., Multimaterial 4D printing with tailorable shape memory polymers. Scientific reports, 2016. 6(1): p. 31110.
24. Hao, X., et al., Entanglement network formed in miscible PLA/PMMA blends and its role in rheological and thermo-mechanical properties of the blends. Polymer, 2015. 80: p. 38-45.
25. Ma, S., et al., 4D printing of PLA/PCL shape memory composites with controllable sequential deformation. Bio-Design and Manufacturing, 2021. 4: p. 867-878.
26. da Cunha, R.B., et al., 4D printing of shape memory polyethylene terephthalate glycol/thermoplastic polyurethane (PETG/TPU) blends. Journal of Manufacturing Processes, 2024. 119: p. 596-608.
27. Rahmatabadi, D., et al., Advancing sustainable shape memory polymers through 4D printing of polylactic acid-polybutylene adipate terephthalate blends. European Polymer Journal, 2024. 216: p. 113289.
28. Mirasadi, K., et al., Investigating the Effect of ABS on the Mechanical Properties, Morphology, Printability, and 4D Printing of PETG-ABS Blends. Macromolecular Materials and Engineering, 2024. 309(6): p. 2400038.
29. Doostmohammadi, H., et al., 4D Printing of Magneto-Thermo-Responsive PLA/PMMA/Fe3O4 Nanocomposites with Superior Shape Memory and Remote Actuation. Macromolecular Materials and Engineering: p. 2400090.
30. Bayas, E., P. Kumar, and M. Harne, Impact of process parameters on mechanical properties of FDM 3D-printed parts: A comprehensive review. European Chemical Bulletin, 2023. 12: p. 708-725.
31. Reed, T., H. Bair, and R. Vadimsky, The causes of pitting and haze on molded ABS plastic surfaces, in Recent advances in polymer blends, grafts, and blocks. 1974, Springer. p. 359-373.
32. Ibrahim, B.A. and K.M. Kadum, Influence of polymer blending on mechanical and thermal properties. Modern Applied Science, 2010. 4(9): p. 157.
33. Charasseangpaisarn, T., et al., Development of poly (methyl methacrylate)/poly (lactic acid) blend as sustainable biomaterial for dental applications. Scientific Reports, 2023. 13(1): p. 16904.
34. Zhang, G., et al., Miscibility and phase structure of binary blends of polylactide and poly (methyl methacrylate). Journal of polymer science part B: Polymer physics, 2003. 41(1): p. 23-30.
35. Gonzalez-Garzon, M., S. Shahbikian, and M.A. Huneault, Properties and phase structure

of melt-processed PLA/PMMA blends. Journal of Polymer Research, 2018. 25: p. 1-13.
36. Pan, P., et al., Temperature-variable FTIR and solid-state 13C NMR investigations on crystalline structure and molecular dynamics of polymorphic poly (L-lactide) and poly (L-lactide)/poly (D-lactide) stereocomplex. Macromolecules, 2012. 45(1): p. 189-197.
37. Tabasi, R.Y. and A. Ajji, Selective degradation of biodegradable blends in simulated laboratory composting. Polymer Degradation and Stability, 2015. 120: p. 435-442.
38. Luo, Y.-B., et al., Preparation and characterization of poly (lactic acid)-grafted TiO2 nanoparticles with improved dispersions. Applied Surface Science, 2009. 255(15): p. 6795-6801.
39. Jing, N., et al., Attenuated total reflectance/Fourier transform infrared (ATR/FTIR) mapping coupled with principal component analysis for the study of in vitro degradation of porous polylactide/hydroxyapatite composite material. Analytical methods, 2014. 6(15): p. 5590-5595.
40. Li, J., et al., FTIR analysis on aging characteristics of ABS/PC blend under UV-irradiation in air. Spectrochimica Acta Part A: Molecular and Biomolecular Spectroscopy, 2017. 184: p. 361-367.
41. Kumar, J. and S. Negi, Development of 3D printable cenosphere-reinforced polyethylene terephthalate glycol (PETG) filaments for lightweight structural applications. Polymer Composites, 2023. 44(10): p. 7030-7039.
42. Tripathi, S., et al. FTIR and XRD study of PMMA/PCTFE blend films. in AIP Conference Proceedings. 2014. American Institute of Physics.
43. Tretinnikov, O.N. and K. Ohta, Conformation-sensitive infrared bands and conformational characteristics of stereoregular poly (methyl methacrylate) s by variable-temperature FTIR spectroscopy. Macromolecules, 2002. 35(19): p. 7343-7353.
44. Tripathi, J., et al., Modifications in optical and structural properties of PMMA/PCTFE blend films as a function of PCTFE concentration. Materials Chemistry and Physics, 2017. 194: p. 172-181.
45. Al-hydary, I., L. Manocha, and P. George, Preparation and characterization of PMMA-ABS Blend. The Iraqi Journal of mechanical and material engineering, 2012. 12(4): p. 709-722.
46. Abdelhamid, Z., H. Mohamed, and S. Kelouwani, The use of machine learning in process–structure–property modeling for material extrusion additive manufacturing: a state-of-the-art review. Journal of the Brazilian Society of Mechanical Sciences and Engineering, 2024. 46(2): p. 70.
47. Syaefudin, E., et al. The effect of orientation on tensile strength 3D printing with ABS and PLA materials. in Journal of Physics: Conference Series. 2023. IOP Publishing.
48. Ziadia, A., M. Habibi, and S. Kelouwani, Machine learning study of the effect of process parameters on tensile strength of FFF PLA and PLA-CF. Eng, 2023. 4(4): p. 2741-2763.
49. Cantrell, J.T., et al., Experimental characterization of the mechanical properties of 3D-printed ABS and polycarbonate parts. Rapid Prototyping Journal, 2017. 23(4): p. 811-824.
50. Guessasma, S., H. Nouri, and S. Belhabib, Digital image correlation and finite element computation to reveal mechanical anisotropy in 3D printing of polymers. Materials, 2022. 15(23): p. 8382.
51. Ya'akub, S., N. Ibrahim, and R. Singh. Effect of 3D-printing parameters on the tensile strength of acrylonitrile butadiene styrene (ABS) polymer. in IOP Conference Series: Materials Science and Engineering. 2021. IOP Publishing.
52. Keleş, Ö., C.W. Blevins, and K.J. Bowman, Effect of build orientation on the mechanical reliability of 3D printed ABS. Rapid Prototyping Journal, 2017. 23(2): p. 320-328.

53. Pszczółkowski, B., et al., A comparative analysis of selected methods for determining young's modulus in polylactic acid samples manufactured with the FDM method. Materials, 2021. 15(1): p. 149.
54. Letcher, T., B. Rankouhi, and S. Javadpour. Experimental study of mechanical properties of additively manufactured ABS plastic as a function of layer parameters. in ASME international mechanical engineering congress and exposition. 2015. American Society of Mechanical Engineers.
55. Tian, W., et al., Numerical simulation on elastic properties of short-fiber-reinforced metal matrix composites: Effect of fiber orientation. Composite Structures, 2016. 152: p. 408-417.
56. Mehrabi Mazidi, M., et al., Highly-toughened polylactide-(PLA-) based ternary blends with significantly enhanced glass transition and melt strength: tailoring the interfacial interactions, phase morphology, and performance. Macromolecules, 2018. 51(11): p. 4298-4314.
57. Vinyas, M., et al., Experimental evaluation of the mechanical and thermal properties of 3D printed PLA and its composites. Materials Research Express, 2019. 6(11): p. 115301.
58. Marin, N. and B.D. Favis, Co-continuous morphology development in partially miscible PMMA/PC blends. Polymer, 2002. 43(17): p. 4723-4731.
59. Zhang, X. and J. Wang, Controllable interfacial adhesion behaviors of polymer-on-polymer surfaces during fused deposition modeling 3D printing process. Chemical Physics Letters, 2020. 739: p. 136959.
60. Nie, D., et al., Effect of crystallization on shape memory effect of poly (lactic acid). Polymers, 2022. 14(8): p. 1569.
61. Memarian, F., et al., Shape memory and mechanical properties of TPU/ABS blends: The role of pristine versus organo-modified carbon nanotubes. Polymer Composites, 2018. 39(S2): p. E984-E995.
62. Sohrabia, Z., A. Fereidoona, and F. Memarianb, Effect of Alumina Nanoparticles on the Enhancement of Shape Memory, Mechanical and Impact Properties of TPU/ABS blend. Journal of Nanoanalysis, 2016. 3(3): p. 96-109.
63. Ratna, D. and J. Karger-Kocsis, Shape memory polymer system of semi-interpenetrating network structure composed of crosslinked poly (methyl methacrylate) and poly (ethylene oxide). Polymer, 2011. 52(4): p. 1063-1070.
64. Inomata, K., et al., Shape memory behavior of poly (methyl methacrylate)-graft-poly (ethylene glycol) copolymers. Polymer, 2010. 51(3): p. 793-798.
65. Xia, Y., et al., A review of shape memory polymers and composites: mechanisms, materials, and applications. Advanced materials, 2021. 33(6): p. 2000713.
66. Carrillo, L.E.L., et al., Development of binary and ternary polyester shape memory blends for additive manufacturing. Journal of Materials Science, 2024. 59(18): p. 8040-8057.
67. Samuel, C., et al., Designing multiple-shape memory polymers with miscible polymer blends: evidence and origins of a triple-shape memory effect for miscible PLLA/PMMA blends. Macromolecules, 2014. 47(19): p. 6791-6803.
68. Aihara, T., et al., Dielectric studies of specific interaction and molecular motion in single-phase mixture of poly (methyl methacrylate) and poly (vinylidene fluoride). Polymer, 1998. 39(1): p. 129-134.
69. Farah, S., D.G. Anderson, and R. Langer, Physical and mechanical properties of PLA, and their functions in widespread applications—A comprehensive review. Advanced drug delivery reviews, 2016. 107: p. 367-392.

70. Chaikeaw, C. and K. Srikulkit, Preparation and properties of poly (lactic acid)/PLA-g-ABS blends. Fibers and Polymers, 2018. 19: p. 2016-2022.
71. Bremer, M., et al., Influence of plastic recycling—a feasibility study for additive manufacturing using glycol modified polyethylene terephthalate (PETG). SN Applied Sciences, 2022. 4(5): p. 156.
72. Seno Flores, J.D., et al., Sustainable polymer reclamation: recycling poly (ethylene terephthalate) glycol (PETG) for 3D printing applications. Journal of Materials Science: Materials in Engineering, 2024. 19(1): p. 16.
73. Raj, A., et al., Morphologies, Compatibilization and Properties of Immiscible PLA-Based Blends with Engineering Polymers: An Overview of Recent Works. Polymers, 2024. 16(13): p. 1776.
74. modelling (FDM). Journal of Manufacturing Processes, 2021. 61: p. 473-480.

Chapitre 4 : Comportement thermo-mécanique et mémoire de forme des mélanges PLA/PETG imprimés en 4D

Ce chapitre a fait l'objet d'une publication :

4D-printed PLA-PETG polymer blends: comprehensive analysis of thermal, mechanical, and shape memory performances. Bouguermouh Karima, Habibi Mohamed, Laperrière Luc, Zeshi Li and Abdin Yasmine. Journal of Materials Science, 2024, vol. 59, no 25, p. 11596-11613.

Il peut être consulté en ligne à l'adresse suivante : https://doi.org/10.1007/s10853-024-09862-4

Dans la continuité de l'étude précédente ayant mis en évidence que le mélange binaire PLA/PETG présente les meilleures performances en termes de mémoire de forme parmi diverses combinaisons polymériques, cette recherche approfondit les propriétés de ce système à travers une analyse complète des performances thermiques, mécaniques et fonctionnelles des mélanges PLA-PETG imprimés en 4D. L'objectif de cette étude est de déterminer la composition la plus performante et d'adapter les paramètres d'impression de ces matériaux afin de concevoir des structures intelligentes capables de transformations complexes sous stimulation thermique, en vue d'applications dans des systèmes adaptatifs, notamment en robotique souple.

Trois formulations PLA/PETG ont été élaborées par extrusion (25/75, 50/50 et 75/25) et testées selon des orientations d'impression variées. Parmi elles, le mélange PLA-75/PETG-25 s'est révélé être le plus performant. Il présente une excellente rigidité avec une contrainte maximale de 46,62 MPa, associée à une bonne élasticité, rendue possible grâce à l'effet plastifiant du PETG. Sur le plan fonctionnel, cette composition affiche des performances exceptionnelles en mémoire de forme avec une fixité et une récupération atteignant 97 % sur 15 cycles consécutifs, démontrant une stabilité cyclique rare pour des polymères imprimés en 3D. De plus, des essais qualitatifs ont validé la capacité de cette formulation à fonctionner comme polymère à mémoire triple forme : elle est capable d'adopter et de restituer successivement deux états intermédiaires avant de retrouver sa forme initiale sous différents paliers de température. Cette caractéristique ouvre la voie à la conception de composants intelligents à comportements programmables complexes.

Les propriétés observées, combinées à une réponse rapide au stimulus thermique, font de PLA-75/PETG-25 un excellent candidat pour les applications en robotique souple, notamment pour la fabrication d'actionneurs thermiquement activés, de structures auto-déployantes ou de dispositifs biomimétiques. Sa capacité à restituer des formes avec précision après plusieurs cycles, permet d'envisager des systèmes souples, légers, réversibles et fiables, adaptés aux environnements changeants ou aux exigences biomécaniques. En somme, cette étude confirme non seulement l'intérêt du PLA/PETG en tant que matériau 4D à mémoire de forme, mais met également en évidence son potentiel dans les technologies de fabrication avancée et les systèmes robotiques adaptatifs.

4D-Printed PLA-PETG Polymer Blends: Comprehensive analysis of thermal, mechanical, and shape memory performances

Karima Bouguermouh[1], Mohamed Habibi[1*], Luc Laperrière[1], Zeshi Li[2], and Yasmine Abdin[2]

[1] *Department of mechanical engineering, Université du Québec à Trois-Rivières, Quebec, Canada.*
[2]*Department of Materials Engineering, The University of British Columbia, Vancouver, BC, Canada V6T 1Z4*

4.1 Abstract

This article investigates the thermal, mechanical, and shape memory performances of 3D-printed polylactic acid (PLA), polyethylene terephthalate glycol (PETG), and their blends for potential applications in 4D printing. Differential Scanning Calorimetry (DSC) reveals distinct glass transition temperatures for PLA-PETG blends, confirming their immiscibility. The integration of PETG alters the crystalline structure of PLA, shifting its behavior from brittle to ductile. This confirms PETG's function as an effective plasticizer.

The tensile strength and Young's modulus influenced by material composition and printing orientation. The results show that 75% PLA and 25% PETG blend demonstrated enhanced mechanical properties compared to other polymer blends. Shape memory experiments demonstrate exceptional fixity and recovery rates, reaching 100%, with the 75% PLA blend exhibiting outstanding performance across 15 cycles. These findings, coupled with insights into the impact of programming temperature, offer valuable perspectives for designing 4D-printed structures with shape memory attributes, unlocking innovative applications across diverse fields.

Keywords: 3D printing, polymer blends, shape memory, differential scanning calorimetry, mechanical properties, 4D printing.

4.2 Introduction

4D printing represents a breakthrough in additive manufacturing, extending beyond the realms of 3D printing by introducing an additional dimension: time. This innovative methodology enables the creation of printed objects that are not only static but dynamic, capable of undergoing transformations or altering their shapes over time. These changes are triggered in response to external stimuli, including temperature fluctuations, light exposure, or variations in humidity [1,

2]. This aspect of 4D printing heralds a new era in manufacturing, where objects can adapt, self-assemble, or evolve, opening up unprecedented possibilities in various fields [3-6].

One of the most promising areas in the field of 4D printing is the utilization of shape memory polymers (SMPs), which have gained considerable popularity, especially in fused deposition modeling (FDM) [7]. The shape memory effect (SME) is not a natural characteristic of most thermoplastics, such as PLA, polyurethane, and polyvinyl acetate (PVA), exhibiting inherent shape memory properties [8, 9]. This limitation in FDM has led to a growing interest in polymer blending as opposed to polymerization. Polymer blending is favored due to its cost-effectiveness and more straightforward approach to the design and manufacturing of SMPs [10, 11].

Polylactic acid (PLA), a bio-based polymer, has increasingly become the focus of attention in recent years, primarily due to its advantageous properties and environmentally friendly profile [12]. Moreover, PLA is highly compatible with additive manufacturing techniques, making it an ideal candidate for 3D printing [13-18].

Song et al. [19] developed a unique shape memory blend using varied weight ratios of Thermoplastic Polyurethane (TPU) and PLA polymers. Their research involved an extensive investigation into a range of weight fraction combinations of these polymers. Although the initial assessment suggested compatibility and isotropic properties in the mixed polymers, subsequent analysis revealed immiscibility at the microstructural level. Intriguingly, despite this immiscibility, these blends exhibited shape memory behavior when exposed to heat.

Previous studies have demonstrated that incorporating TPU into the Poly-L-lactic acid (PLLA) matrix effectively reduces brittleness, owing to the inherent elasticity of TPU. This combination enables enhanced deformation capabilities that are essential for the shape memory process. Conversely, PLLA gains increased flexibility from this integration. In this blend, TPU acts as the 'switching phase' within the PLLA matrix, providing the crucial additional recovery force necessary for reverting to its original shape [20, 21].

Recently, Braga da Cunha et al. [22] explored the potential of binary polylactide/ethylene-glycidyl methacrylate (PLA/E-GMA) blends for 4D printing by preparing them through melt blending. Their findings revealed that these materials exhibit favorable processability and printability, as indicated by their rheological properties. Dynamic Mechanical Thermal Analysis (DMTA) further highlighted enhanced mechanical properties and notable shape memory behavior in the PLA/E-

GMA samples. In another study, Cunha et al. [23] successfully produced filaments and 4D printed structures, showcasing the impressive shape memory behavior of PLA/EBA-MAH blends.

Arabiyat et al. [24] developed a scaffold by blending poly(ϵ-caprolactone)-diacrylate (PCL-DA) with PLLA, aiming to introduce shape memory properties into the material. The resulting scaffold, characterized by a semi-interpenetrating network of PLLA, exhibited biocompatibility and a pronounced shape memory effect.

Polycaprolactone (PCL), a semi-crystalline thermoplastic, was combined with polystyrene-*block*-poly(ethylene-*co*-butylene)-*block*-polystyrene (SEBS), a highly extensible thermoplastic elastomer known for its shape memory and self-healing properties, in a recent 4D printing endeavor using cost-effective Fused Deposition Modeling (FDM). The study results show that by controlling the orientation of the printed fibers, the material could achieve an exceptional strain at break, exceeding 1200. This performance significantly surpasses that of previously reported flexible 4D- printed materials, marking a substantial advancement in the field of 4D printing technologies. [9]. Recently, efforts have been made to augment the inherent limitations of PLA by incorporating Poly(ethylene terephthalate glycol) (PETG) through melt blending, especially targeting improvements for packaging industry applications. In this context, Park et al. [25] produced blends of PLA and PETG with different compositions through melt compounding. Their research focused on examining the compatibility and physical properties of these blends. Notably, their findings indicated that PLA and PETG are miscible up to a PETG content of 22 wt%, in alignment with the Flory–Huggins theory predictions. This result opens new possibilities for using PLA-PETG blends in various applications, particularly where specific material characteristics are essential.

This study investigates the 4D printing and characterization of an innovative shape memory polymer blend formulated by combining PLA and PETG in three distinct weight ratios: 25/75, 50/50, and 75/25. The investigation encompasses an in-depth analysis of the thermal, mechanical, and shape memory properties of these blends. A comparative assessment was conducted against the baseline properties of neat PLA and PETG. Additionally, the research explored the impact of programming temperature and the time required for shape recovery. The study also evaluated the endurance of these properties over 15 cycles, aiming to identify polymers and blends that offer an optimal balance between mechanical robustness and shape memory capabilities.

4.3 Materials and methods

Resin pellets of polylactic acid (PLA) and polyethylene terephthalate glycol-modified (PETG), with respective densities of 1.24 g/cm³ and 1.27 g/cm³, were thoroughly mixed in precise ratios to form the various extruded blends outlined in Table 4.1. This preparatory step ensured uniformity and consistency in the composition of the blends for subsequent analysis.

Table 4.1: Compositions and extrusion temperatures of raw materials and blends-based filaments.

Raw materials and Blends	Polymers ratios	Extrusion temperature (°C)
PLA	100 :0	180
PETG	100 :0	205
PLA-25/PETG-75	25 :75	200
PLA-50/PETG-50	50 :50	200
PLA-75/PETG-25	75 :25	200

4.3.1 Filament preparation for 3D printing

To produce the 3D printing filaments, PLA and PETG resin pellets were initially subjected to a drying process at 60°C in a dryer for 24 hours. This step was crucial to remove any moisture that could affect the extrusion quality. Following this, a single-screw extruder was employed to produce the filaments. Filaments were produced with a target diameter of 1.75 mm to ensure optimal quality and aimed for minimal surface roughness. PLA, PETG and PLA-PETG blends filaments, comprising 25%, 50%, and 75% PLA by weight, were prepared and designated by the following nomenclature PLAwt%/PETGwt% as shown in Figure 4.1. The extrusion temperatures were carefully adjusted within a range of 180°C to 205°C, as detailed in Table 4.1.

Table 4.2: 3D printing parameters of raw materials and polymer blends.

Raw materials and Blends	Flow (%)	Nozzle temperature (°C)	Bed temperature (°C)
PLA	95	215	80
PETG	100	255	100
PLA-25/PETG-75	95	255	100
PLA-50/PETG-50	95	255	100
PLA-75/PETG-25	95	255	100

The filaments were wound onto spools and readied for use in 3D printing. The obtained 3D printing in 3 orientations (0°, 90° and ±45°) of these polymers and blends shown in Figure 4.2 was carried out using a Fused Deposition Modeling (FDM) 3D printer. Printing parameters, including layer height (0.20 mm), infill density (100%), infill line distance (0.4 mm), printing speed (60 mm/s), and nozzle size (0.4 mm), were consistently maintained across all samples. The specific nozzle, bed temperatures and flow, which varied among the samples, are comprehensively listed in Table 4.2.

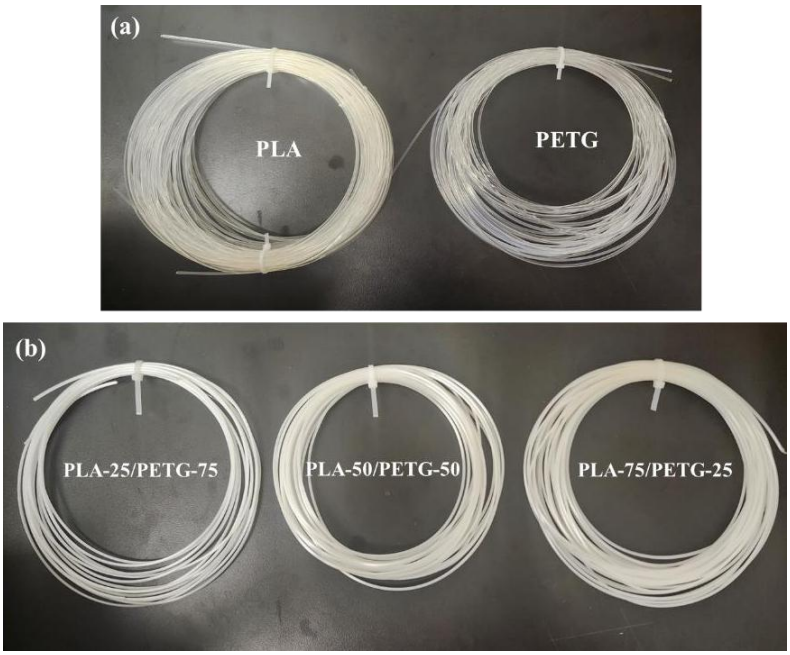

Figure 4.1: Extruded filament illustrations of a: PLA and PETG, b: polymer blends.

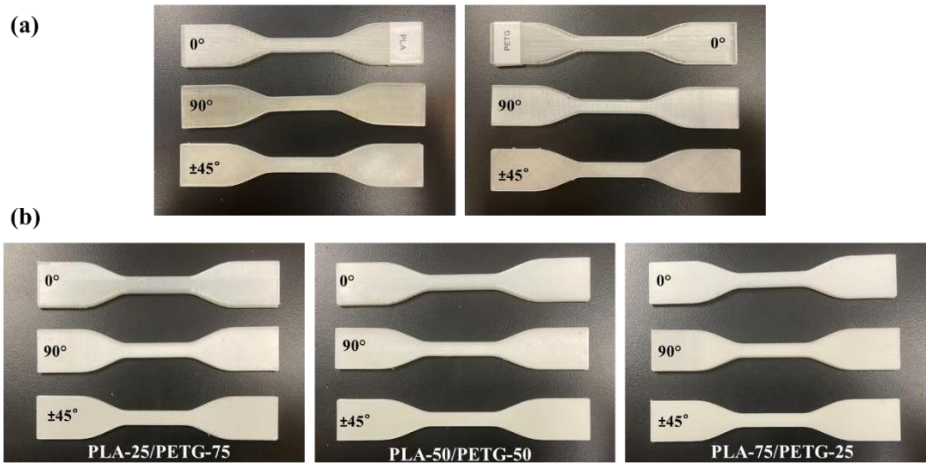

Figure 4.2: 3D printing of a: PLA and PETG, b: polymer blends, in 3 orientations (0°, 90° and ±45°).

4.3.2 Characterization

4.3.2.1 Tensile test

The mechanical testing was conducted using an MTS instrument machine (equipped with a 20 KN load cell) in standard ambient conditions in accordance with ASTM D 638 guidelines. For this purpose, Type IV specimens were 3D printed in three distinct orientations (0°, ±45°, and 90°) to analyze their mechanical behavior.

4.3.2.2 Differential scanning calorimeter (DSC)

Thermal properties were evaluated using a Q 800 Differential scanning calorimeter (DSC) from TA instruments. The heating range was set from 30°C to 200 °C for PLA and from 30 to 290°C for PETG and their blends. The cooling started from 200°C and 290°C to 30 °C for PLA, PETG and polymer blends, respectively, at a controlled rate of 10 °C/min, with a 5-minute holding time at each temperature.

4.3.2.3 Shape Memory Test

To evaluate shape memory characteristics, 3D printed samples measuring 100 mm x 20 mm x 1 mm, oriented in the 0° direction, were heated to a specific programming temperature (T_p). They were then deformed by applying a force sufficient to conform to a mold 20 mm thick. The maximum bending angle achieved was recorded as θ_{max}.

Figure 1 (a) illustrates the fixed mold, while Figure 4.3 (b) depicts the shape fixation process. After applying the external force, the reconfigured sample was allowed to cool to room temperature while still under force. Once the sample achieved a stable shape, the mold and the force were removed, and the sample was left at room temperature until it was fully set. The angle of the set shape is referred to as θ_{fixed}. Subsequently, the sample was subjected to a constant temperature condition, during which the bending angle (θ_i) was meticulously recorded. The shape fixation and recovery ratios were then calculated based on these observed angles as follows:

$$Shape\ fixity\ (S_f) = \frac{\theta_{fixed}}{\theta_{max}}\ X\ 100 \qquad \text{(eq. 1)}$$

$$Shape\ recovery\ (S_r) = \frac{\theta_{max} - \theta_i}{\theta_{max}} X\ 100 \qquad \text{(eq. 2)}$$

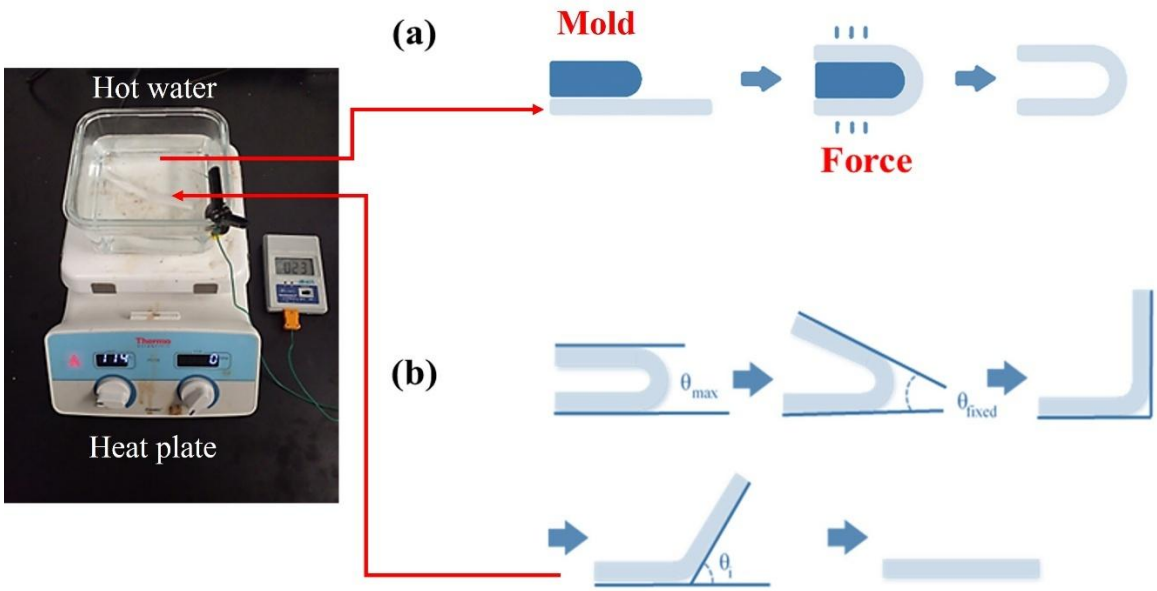

Figure 4.3: Shape Fixation Process, (b): Process for testing the shape fixation method and properties: maximum and fixed bending angles.

4.4 Results and discussions

4.4.1 Differential scanning calorimeter (DSC)

4.4.1.1 Raw materials

The glass transition temperatures for PLA and PETG are 58.85°C and 78.30°C, respectively, as depicted in Figure 4.4. These transitions signify the change from a glassy to a rubbery phase.

Additionally, an endothermic peak at 128.71°C was observed in the PLA curve, indicative of cold crystallization. This process occurs due to the ordering of molecular chains within the crystalline lamellae of PLA, which is facilitated by increased mobility during heating. Furthermore, the PLA exhibited another endothermic peak at 143°C, corresponding to the melting of its crystalline phase.

On the other hand, PETG did not exhibit any crystallization peaks during cooling, which can be attributed to its slow crystallization rate. This observation aligns with the findings of Park et al. [25]. Consistent with these results, none of the blends displayed crystallization peaks during the cooling process.

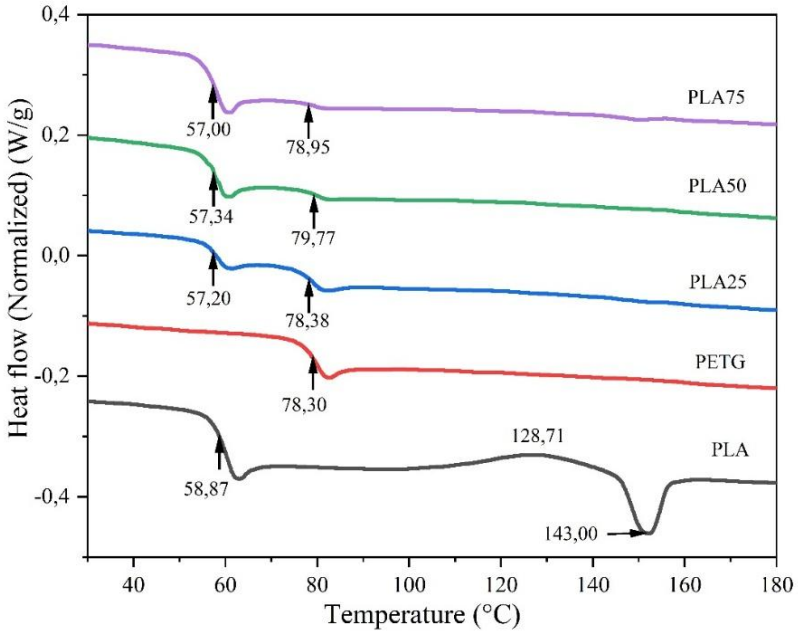

Figure 4.4: DSC of raw materials and blends.

.

4.4.1.2 Blends

The glass transition temperatures (T_g) of the various PLA/PETG blends are collated in Table 4.3. As illustrated in Figure 4.4, two distinct T_g values were recorded for the PLA/PETG blends, suggesting the non-miscibility of these polymers. In line with previous studies, the behavior of T_g in polymer blends is often indicative of their miscibility. A single T_g observed at an intermediate temperature between the T_g values of the individual components typically implies molecular homogeneity and miscibility. Conversely, the presence of multiple T_g values is indicative of phase separation, reflecting the distinct phases of the blend's components [26].

Furthermore, the glass transition temperatures (T_g's) of the polymer blends fell within the range between the T_g's of the neat polymers. This observation is in perfect accordance with the findings reported by Charasseangpaisarn et al. [27], reinforcing the consistency of these results with established research in the field.

Table 4.3: Thermal properties of PLA, PETG and blends.

Raw materials and Blends	Glass transition temperatures (°C)		T_c (°C)	ΔH_c (J/g)	T_m (°C)	ΔH_m (J/g)	ΔX_c (J/g)
	T_{g1}	T_{g2}					
PLA	58,87	-	128,71	*6,32*	143,00	*5,83*	6,27
PETG	78,30	-	-	-	-	-	-
PLA-25/PETG-25	57,20	78,38	86,7	0,73	150,49	2,34	10,07
PLA-50/PETG-50	57,34	79,77	81,85	0,39	151,90	3,43	7,39
PLA-75/PETG-25	57,00	78,95	84,32	0,16	152,36	3,40	4,87

During cooling, the PLA/PETG blends did not exhibit any endothermic peaks at any composition level. A plausible explanation for this is that the amorphous nature of PETG may have interfered with the arrangement of PLA polymer chains, thereby inhibiting the formation of crystalline structures in PLA. This finding agrees with the research conducted by Park et al. [25].

The melting temperatures (T_m) of the blends showed a decreasing trend with an increase in PETG content. In systems where polymers are miscible or suitably mixed, it is often observed that the melting temperature of the blend is lower than that of the pure polymer, as noted in previous studies [28].

In our research, the melting peaks for all blends were distinctly divided into two separate peaks, an effect primarily attributed to crystalline PLA. The crystallization rate of PLA is notably faster compared to that of PETG. Kattan et al. [29] found that PETG can crystallize after 48 hours of isothermal crystallization at 120°C, with the melting temperature of this crystalline phase at 163°C. As neat PETG did not exhibit any crystallization and melting peaks in our measurements, the heat of fusion is predominantly influenced by PLA. Consequently, the degree of crystallinity (X_c) of PLA and the blends were calculated using the following equation:

$$Xc = \frac{\Delta Hf}{\omega_{PLA} \, \mathrm{X} \, \Delta Hf^{\circ}} X100 \qquad \text{(eq. 3)}$$

where ΔHf represents the heat of fusion of the blends PLA/PETG, and ω_{PLA} is the weight fraction of PLA in the blends. Further, ΔHf° denotes the heat of fusion for 100% crystalline PLA, which is 93.0 J/g.

As illustrated in Table 4.3, an increase in PETG content led to a rise in X_c, indicating that blending with PETG enhances the crystallization ability of PLA. This improvement in crystallization is

likely due to PETG acting as a nucleating agent in the blends, aligning with the findings reported in [25].

4.4.2 Mechanical properties

4.4.2.1 Mechanical behavior of 3D printing polymers and blends

Figure 4.5 demonstrates that PLA exhibits a brittle elastic behavior when printed in the 0° and 90° orientations. Conversely, an elastic ductile behavior is observed in samples printed with a ±45° orientation. On the other hand, PETG exhibits an elastic ductile behavior in both 0° and ±45° 3D printing orientations. In addition, an elastic brittle behavior is observed in the 90° orientation.

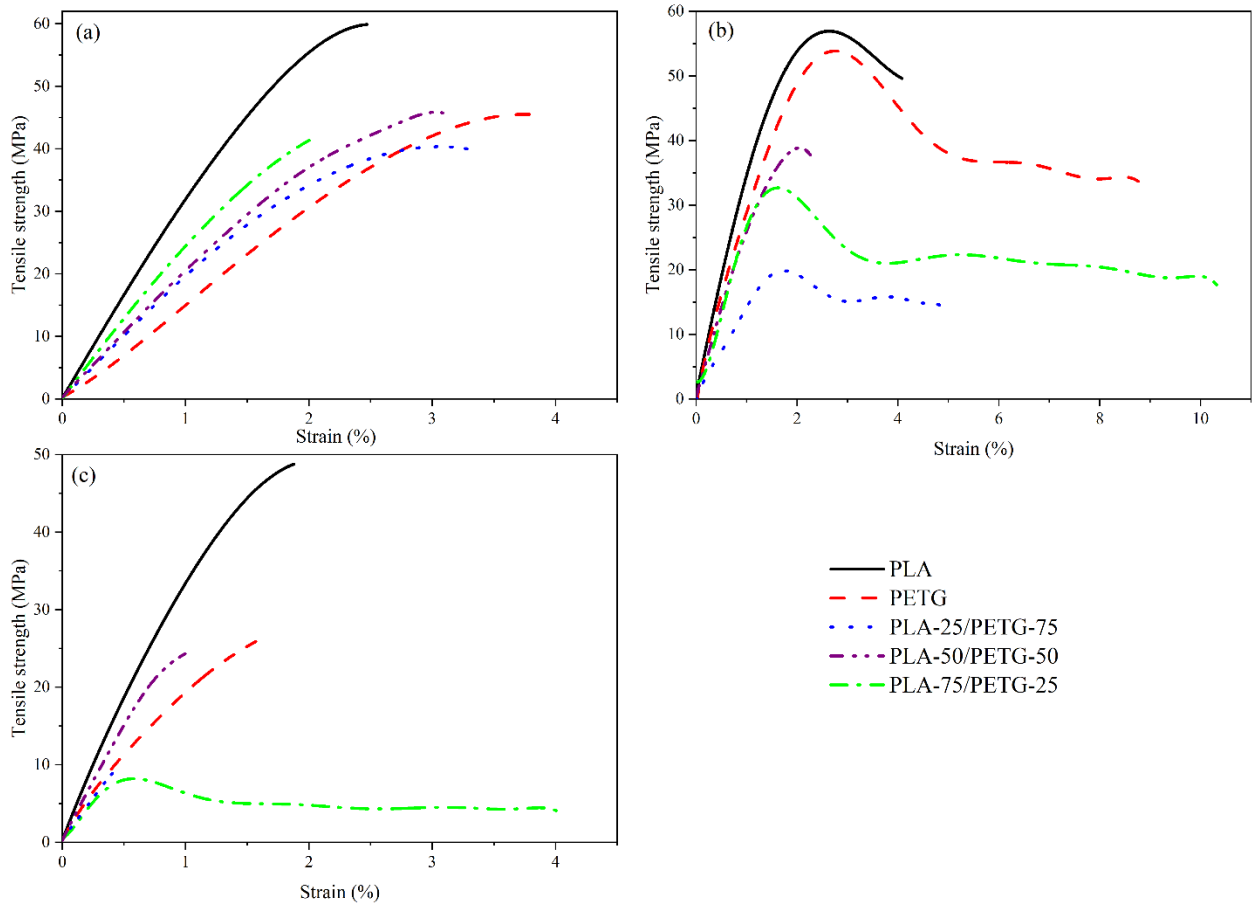

Figure 4.5: Tensile strength of different 3D printing polymers and blends in three printing orientations: (a): 0°, (b): ±45° and (c): 90°.

For the blends, PLA-25/PETG-75 and PLA-75/PETG-25 consistently show elastic ductile behavior, irrespective of the printing direction. However, PLA-50/PETG-50 displays a brittle elastic response when printed at a 0° orientation.

The printing orientation significantly influences the mechanical behavior of the 3D printed specimens. The ductility of PLA, PETG, and their blends is notably improved, especially in the ±45° orientation. The angled structure of the ±45° pattern provides better resistance against crack propagation.

Despite initial compatibility considerations, the toughness of PLA is enhanced with the incorporation of PETG. This suggests that PETG acts as a plasticizer for PLA, transitioning the fracture behavior from the brittle nature characteristic of pure PLA to a more ductile fracture in blends that include PETG.

4.4.2.2 Effect of printing direction and composition on mechanical properties

Figure 37 illustrates that mechanical properties are influenced by both composition and printing orientation. Specifically, the tensile strength of PLA decreases as the printing orientation increases, with the highest value being 60.13 MPa observed in the 0° direction. This trend aligns with the findings of Es-Said OS et al. [30], who investigated the mechanical properties of ABS models produced via FDM in various printing orientations. Their study, which included assessments of tensile strength, modulus of rupture, and impact resistance, found that models printed at a 0° angle exhibited the highest strength and impact resistance. This is attributed to the fact that in a 0° orientation, the axial members align with the tensile load during testing, offering optimal support and strength in the axial direction.

The high tensile strength observed in 3D printed PLA parts, compared to those manufactured via injection molding, was attributed to their increased crystallinity, as suggested by Song et al. [31] and Wang et al. [32]. Specifically, Song et al. [31] conducted a comparative analysis of parts fabricated with PLLA using both 3D printing and injection molding techniques. The initial crystallinity of the filament – both as received from the supplier and after being extruded by the Fused Deposition Modeling (FDM) process – was measured using Differential Scanning Calorimetry (DSC) during the first heating cycle. They reported that the FDM process did not significantly alter the filament's initial crystallinity, which remained around 8% before and after extrusion. However, a notable difference was observed in the initial crystallinity of parts made by

3D printing (37%) compared to injection molding (30%). This discrepancy in crystallization rates was attributed to the slower cooling process in 3D printing, where parts are constructed layer by layer on a heated bed, as opposed to the quicker cooling in injection molding.

The Young's modulus was found to increase with the printing orientation, reaching a peak of 3.45 GPa at a 90° orientation. This observation is supported by recent research from Khosravani et al. [33], which explored the impact of printing parameters on the mechanical properties of PLA-based 3D printed objects. Their study confirmed that printing orientation significantly influences both the strength and the elastic modulus of the samples.

Furthermore, the highest tensile strength and Young's modulus for PETG were recorded at 55.32 MPa and 2.73 GPa, respectively. In the case of PLA-25/PETG-75, PLA-50/PETG-50, and PLA-75/PETG-25 polymer blends, both the tensile strength and Young's modulus were observed to increase as the proportion of PETG in the blend decreased. This is attributed to the increased content of PLA, which possesses superior mechanical properties compared to PETG.

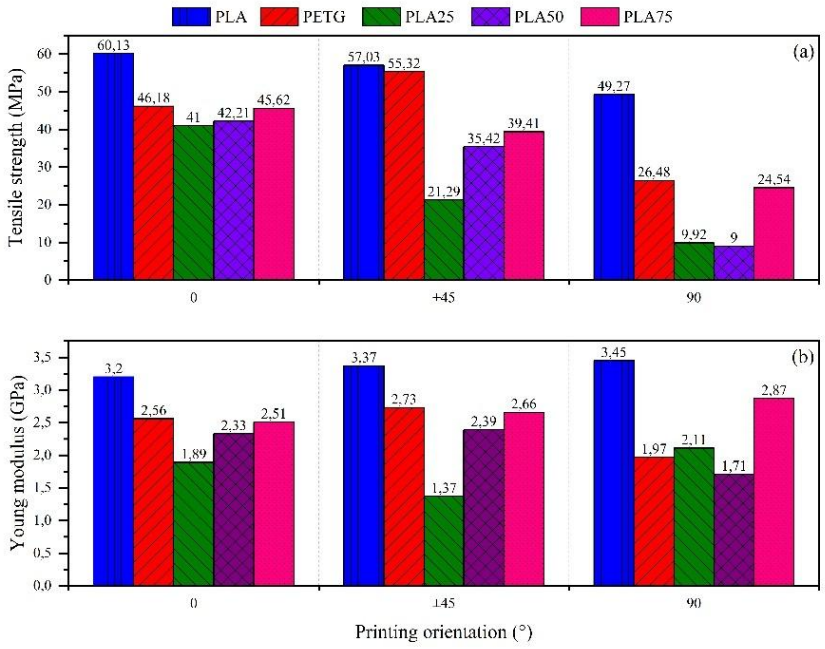

Figure 4.6: (a): Tensile strength and (b): Young modulus of polymers and blends.

The tensile strength of polymer blends was observed to decrease with an increase in printing orientation. The highest tensile strength, 46.62 MPa, was recorded for PLA-75/PETG-25 in the 0°

direction, as shown in Figure 4.6 **(**a). This finding aligns perfectly with previous research, which consistently indicates that the strongest printing orientation is along the pull direction [34-39].

The strength of a part is significantly enhanced when a longitudinal raster angle is used, aligning the raster parallel to the load direction or when a 0° raster orientation is used. This improvement is primarily attributed to the prevalence of trans-raster failure in such specimens, as the interlayer bonding becomes the weakest area in parts with a 0° raster orientation [40]. Furthermore, specific raster orientations can lead to stress concentration under particular loading conditions like bending and torsion [41].

Additionally, the most notable values of Young's modulus for PLA-75/PETG-25, as depicted in Figure 4.6 (b), were 2.51 GPa, 2.66 GPa, and 2.87 GPa at 0°, ±45°, and 90° orientations, respectively.

4.5 Shape memory performance

4.5.1 4D printing of PLA and PETG shape memory polymers

In this section, the U-shape memory performances of the 3D printed parts are evaluated, as illustrated in Figure 4.7 (a, b and c). Practically, controlling the shape-memory effects in thermoplastics often involves leveraging either the glass transition temperature (T_g) or the melting temperature (T_m) of the polymer's ordered phases [42]. At the macromolecular level, the shape-memory behavior is closely linked to the presence of netpoints and switchable segments within the polymer structure [43]. Netpoints are rigid domains that facilitate permanent shape fixation and can manifest as microscopic phases, crosslinking points, or entanglements [44]. In contrast, switchable segments are more malleable domains, typically represented by the amorphous phase of the polymer.

In our study, polylactic acid (PLA) was selected as the polymer with shape-memory properties attributed to shape-switching domains within its structure. These domains enable PLA to perform elastic recoiling when activated [43]. On the other hand, semi-crystalline polymers, unlike their amorphous thermoplastic counterparts, typically remain solid until they rapidly transform into a low-viscosity liquid when upon exceeding their melting point T_m. To address this characteristic, semi-crystalline materials are often combined with amorphous materials, such as glasses or

polymers, to facilitate their integration into extended structures and overcome their intrinsic limitations [45].

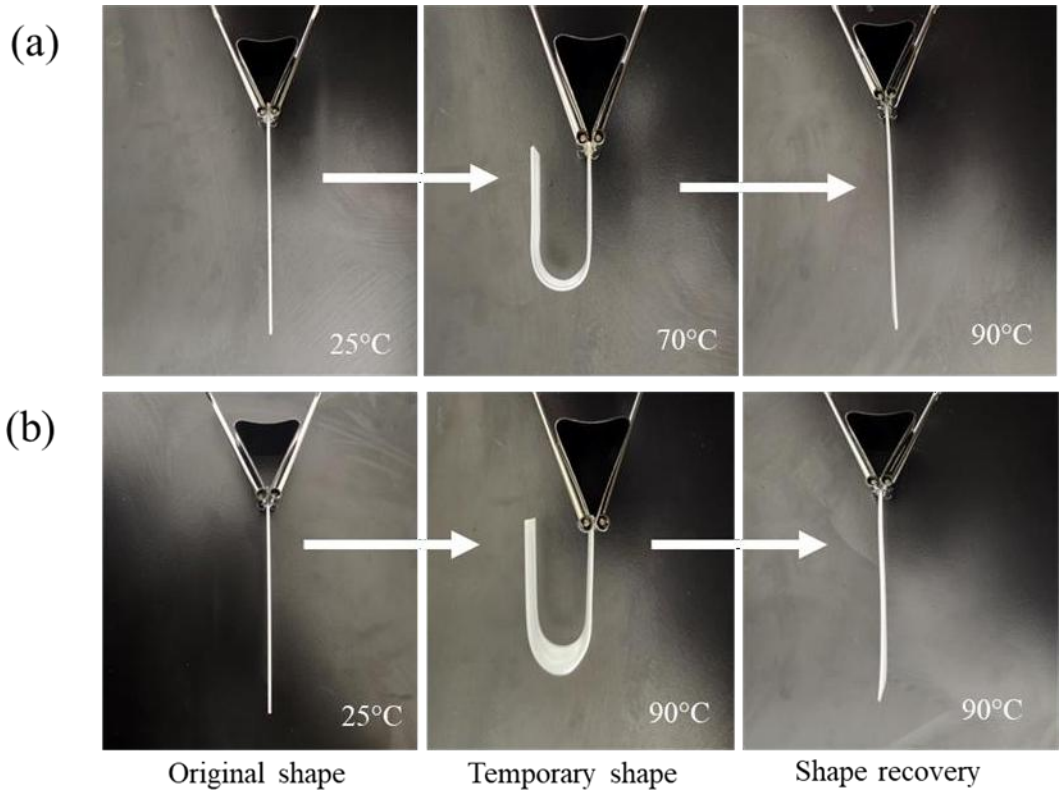

Figure 4.7: Illustration of U-shape memory mechanism of (a): PLA, (b): PETG.

PETG was chosen as the amorphous thermoplastic for its printing temperature, which is higher than the melting temperature of PLA – a critical factor for the printing process. Additionally, PETG's glass transition temperature is relatively close to PLA's. This facilitates the completion of shape recovery cycles of the blends. The characteristic temperatures of both PETG and PLA, as derived from the DSC analysis, are illustrated in Figure 4.3 and summarized in Table 4.3.

The programming temperatures for the temporary shape and the recovery temperatures for the permanent shape in this study are set higher than the T_g, as reported in Table 4.2. The results demonstrate that both PLA and PETG exhibit exceptional shape fixity and recovery, each achieving 100%. Furthermore, the permanent shape was recovered in 3 seconds for PLA and 5 seconds for PETG.

4.5.2 4D printing of PLA/PETG shape memory polymer blends

In the case of polymer blends, an increase in shape fixity was observed alongside an increase in PLA content. The highest shape fixity, at 98.33%, was achieved by the PLA-75/PETG-25 samples when programmed at 79°C. This is primarily due to the crystalline segments of PLA acting as netpoints, which are crucial for restoring the original shape. A higher PLA content results in more rigid constraints [11]. In terms of shape recovery, PLA-25/PETG-75 exhibited 90% recovery, while both PLA-50/PETG-50 and PLA-75/PETG-25 achieved 95% and complete shape recovery (100%) respectively as illustrated in Figure 4.8. These findings indicate that PLA-75/PETG-25 is the most effective shape memory polymer blend. Furthermore, as demonstrated in Section 4.4.2 and illustrated in Table 4.4**,** the PLA-75/PETG-25 blend also possesses the best mechanical properties. Based on these criteria, this composition was selected for further investigation in this study.

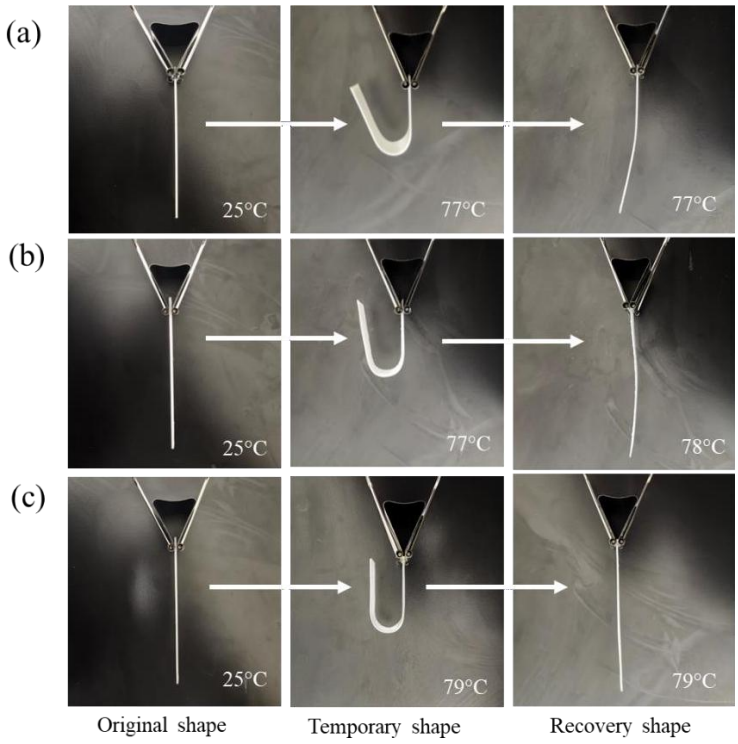

Figure 4.8: U-shape memory mechanism of a: PLA-25/PETG-75, b: PLA-50/PETG-50 and c: PLA-75/PETG-25.

Figure 4.9 (a) demonstrates that the shape fixity of PLA75 is significantly influenced by the programming temperature (T_p) used for setting the temporary U-shape. Notably, shape fixity improves as the programming temperature increases, particularly when it falls between the glass

transition temperatures (T_g's) of neat PLA and PETG. Shape fixity values of 96% and 98% were observed at T_p's of 70°C and 79°C, respectively.

Table 4.4: Shape memory properties of polymers and blends.

Raw materials and Blends	Programmation Temperature (T_p)(°C)	Recovery Temperature (T_r) (°C)	Shape fixity (S_f) (%)	Shape recovery (S_r) (%)	Time (s)	Tensile strength (MPa)	Young modulus (GPa)
PLA	70	90	100,00	100,00	*3,00*	*60,13*	*3,20*
PETG	90	90	100,00	100,00	5,00	46,18	2,56
PLA-25/PLA-75	77	77	94,44	90,00	28,00	41,00	1,90
PLA-50/PETG-50	77	78	96,11	95,00	38,00	42,21	2,33
PLA-75/PETG-75	79	79	98,33	100,00	56,00	46,62	2,51

A perfect shape fixity of 100% was achieved when the programming temperature exceeded 80°C, which is below the T_g of neat PETG. At such temperatures, temporary shape programming occurs within the rubbery region. Here, the elastic modulus of the soft segments decreases markedly, resulting in an increased free volume and enhanced mobility of the polymer chains [46-48]. Consequently, when an external force is applied, the polymer chains encounter reduced resistance, stretch in the direction of the force, and undergo a significant reduction in entropy [49].

Conversely, an outstanding shape recovery of 100% was recorded at temperatures ranging from 70°C to 95°C. However, bending phenomena were observed when samples were immersed in hot water at 90°C, a temperature exceeding the T_g's of both PLA and PETG polymers. It's important to note that 3D printing processes, particularly Fused Deposition Modeling (FDM), can induce residual stresses in the printed parts. In the case of amorphous PETG, its tightly knitted molecular entanglements, acting as net points, contribute to stress relaxation, a characteristic of the viscoelastic nature of PETG. This stress relaxation kinetics, accelerated by chain slippage due to the opening of molecular entanglements, is more pronounced at higher stretching temperatures and longer load-holding times [7].

Therefore, immersing the printed object in hot water allows the material to relax and relieve some of these internal stresses, resulting in bending [50].

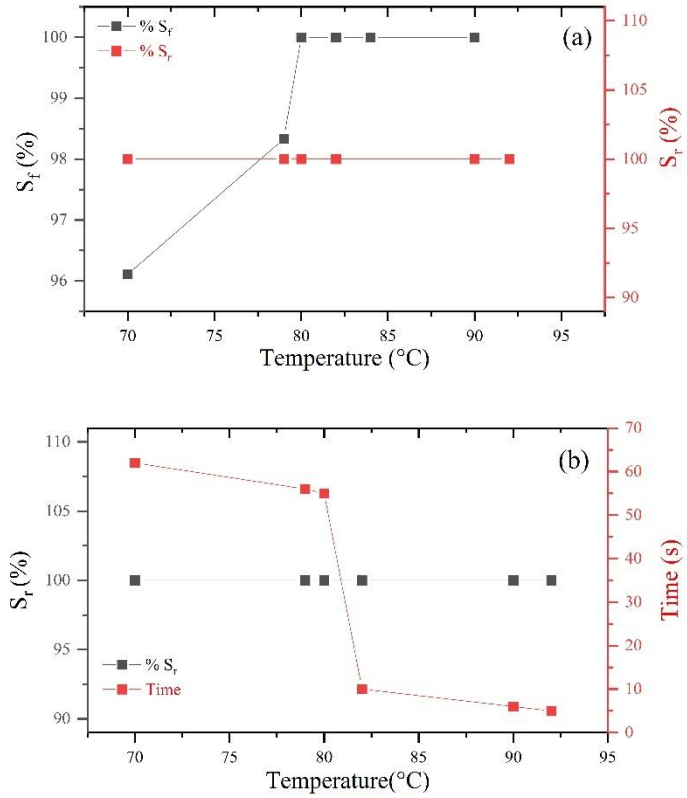

Figure 4.9: Effect of temperature on (a): the shape fixity and shape recovery, (b): time for shape recovery.

Additionally, the effect of temperature on the time of shape recovery was studied. The results show that the recovery time decreases as the temperature increases, with the fastest recovery time for 100% permanent shape, taking only 5 seconds, recorded at 92°C, as illustrated in Figure 4.9 (b). A related study by Zhang et al. [51] focused on temperature programming in PLA reinforced with PAE. They discovered that the recovery rate was quicker at a higher recovery temperature (90°C), while the extent of shape recovery was greater at a lower temperature (80°C). Additionally, they observed a recovery time of just 3 seconds at 90°C. During such a short period of rapid shrinkage, there is insufficient time for the original shape to be fully regained through intermolecular slippage.

Triple-shape memory performances were also tested qualitatively (Figure 4.10). The original shape was successfully bended at 90°C and at 50 °C. The recoveries observed at 60°C and 90 °C demonstrated again that the original and the intermediate shape could be efficiently recovered. Consequently, PLA-75/PETG-25 blend could be used as a triple-SMP for practical issues.

Figure 4.10: 7 petals flower configuration of triple-shape memory based on 4D printing of PLA-75/PETG-25 polymer blend: (a) original shape 1; (b) shape 2, blended at 90 °C and cooled to 50 °C; (c) shape 3, blended at 50°C and cooled to 25 °C; (d) recovered shape 2 after heating at 60 °C; (e) recovered shape 1 after heating to 90 °C.

4.5.3 Cycling effects

Although polymers exhibit shape fixity and recovery properties, their durability in terms of shape memory cycle life has rarely been investigated. This factor is crucial in determining whether these polymers can meet the demands of industrial applications, where robust shape memory performance over multiple cycles is essential. Choong et al. [52] demonstrated a photopolymer suitable for stereolithography (SLA) printing, utilizing a *tert*-Butyl acrylate-co-di(ethylene glycol) diacrylate (DEGDA) crosslinker tBA-co-DEGDA network based on a dual-component phase switching mechanism. This approach enabled the creation of complex geometries with shape memory behavior. Shape memory tests revealed excellent performance, with the material enduring over 20 shape memory cycles, surpassing the durability of current 4D printed parts.

Bashandeh et al. [53] designed, fabricated, and investigated a 3D shape memory polymer (SMP) structure using a kirigami design approach. The sample successfully underwent 15 cycles of repetitive shape transformation and recovery without any fractures.

In the case of our study Figure 4.11 (a) reveals that programming 15 successive cycles on PLA at 90°C maintained a 100% shape fixity up to the 10th cycle. Beyond this point, a slight decrease was noted, with a fixity of 98% reported after 15 cycles. In comparison, PETG maintained a consistent shape fixity of 100% across all 15 cycles. For the PLA-75/PETG-25 blend, shape fixity increased with the number of cycles, peaking at 100% between the 5th and 7th cycles. However, it then diminished slightly, registering 97% after 15 cycles at 95°C.

According to Figure 4.11 (b), the shape recovery of PLA at 90°C remained at 100% up to the 9th cycle, then gradually declined to 98% after 15 cycles. PETG, on the other hand, consistently showed 100% shape recovery at 90°C regardless of the cycle number. In the case of PLA-75/PETG-25, a full 100% shape recovery at 79°C was observed during the initial two cycles, followed by a

decrease to 95% by the 11th cycle. A minor increase in shape recovery was noted up to the 13th cycle, reaching 97%.

Investigation of the impact of programming cycles on the time required for shape recovery for PLA, PETG, and PLA-75/PETG-25 is presented in Figure 4.11 (c). PLA exhibited the shortest recovery time, ranging from 3 seconds at the 3rd cycle to 9 seconds at the 15th cycle, with a slight increase over the cycles. Conversely, for PETG, the time required for shape recovery decreased as the number of cycles increased. The quickest recovery time for PETG, just 8 seconds, was observed at the 12th cycle. A similar trend was noted for the PLA-75/PETG-25 4D printed parts. Notably, the recovery time for PLA-75/PETG-25 was found to lie between those of the neat PLA and PETG shape memory polymers, illustrating a balance in the properties of the blended material.

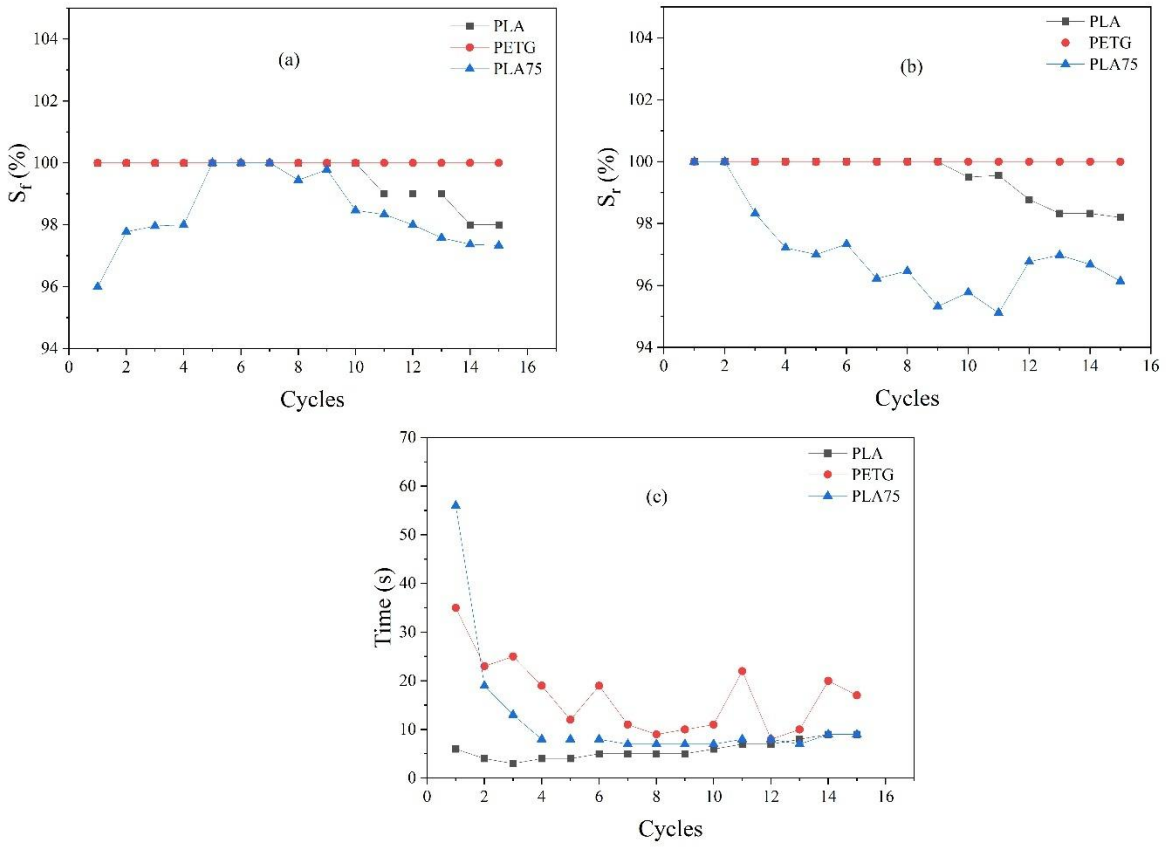

Figure 4.11: Influence of number of cycles on (a): Shape fixity, (b): Shape recovery and (c): Recovery time.

4.6 Conclusion

DSC analysis of various PLA/PETG blends revealed multiple glass transition temperatures (T_g), indicating non-miscibility and suggesting phase separation among the components of the blends.

The analysis of mechanical behavior showed that printing orientation significantly affects the properties of 3D-printed polymers and their blends. Notably, the ductility of PLA, PETG, and their blends was significantly enhanced, particularly at the ±45° printing orientation. Despite initial compatibility concerns, introducing PETG to PLA improved its toughness, altering its fracture behavior from brittle to more ductile. Additionally, the PLA-75/PETG-25 blend exhibited the highest tensile strength of 46.62 MPa among the tested compositions.

Shape memory performance for individual polymers and blends revealed outstanding shape fixity and recovery. The shape fixity of PLA-75/PETG-25 was especially remarkable at higher programming temperatures. Bending phenomena observed in hot water were attributed to residual stresses and the viscoelastic nature of amorphous PETG. Notably, the recovery time decreased with an increase in temperature.

Furthermore, the impact of repeated cycling on shape memory properties was investigated. PLA and PETG consistently maintained 100% shape fixity, while PLA-75/PETG-25 achieved 100% fixity up to the 7th cycle at 79°C, with a gradual decline in shape recovery to 97% after 15 cycles. PLA's shape recovery time showed slight variations across cycles, whereas PETG and PLA-75/PETG-25 displayed decreasing recovery times with an increasing number of cycles.

Overall, this comprehensive analysis of DSC, mechanical properties, and shape memory performance offers valuable insights into the behavior of 4D-printed PLA-PETG shape memory polymer blends, opening avenues for potential applications across various sectors.

4.7 Acknowledgement

The authors acknowledge the funding provided by the Natural Sciences and Engineering Research Council (NSERC) of Canada (grant number: CRSNG – RGPIN -2021-02846).

4.8 Author contributions

Karima Bouguermouh: Conceived and designed the study, collected and analyzed data, drafted the

manuscript.

Mohamed Habibi: Supervised the research process, revised the manuscript critically for important intellectual content, and provided final approval for publication.

Luc Laperrière: Supervised the research process, revised the manuscript critically for important intellectual content, and provided final approval for publication.

Zeshi Li: Experimental design, carrying out measurements and formal result analysis.

Yasmine Abdin: Supervised the experimental design and carrying out measurement, revised the manuscript.

4.9 References

1. Megdich, A., M. Habibi, and L. Laperriere, A review on 4D printing: Material structures, stimuli and additive manufacturing techniques. Materials Letters, 2023: p. 133977. https://doi.org/10.1016/j.matlet.2023.133977
2. Kouka, M.A., et al., 4D Printing of Shape Memory Polymers, Blends, and Composites and Their Advanced Applications: A Comprehensive Literature Review. Advanced Engineering Materials, 2023. 25(4): p. 2200650. https://doi.org/10.1002/adem.202200650
3. Momeni, F., X. Liu, and J. Ni, A review of 4D printing. Materials & design, 2017. 122: p. 42-79. https://doi.org/10.1016/j.matdes.2017.02.068
4. Chu, H., et al., 4D printing: a review on recent progresses. Micromachines, 2020. 11(9): p. 796. https://doi.org/10.3390/mi11090796
5. Sunte, J., A Review on 4D–Printing Design Materials. Int J Sci Res Mech Mater Eng, 2022. 6(3): p. 19.
6. Spiegel, C.A., et al., 4D printing at the microscale. Advanced Functional Materials, 2020. 30(26): p. 1907615. https://doi.org/10.1002/adfm.201907615
7. Soleyman, E., et al., Assessment of controllable shape transformation, potential applications, and tensile shape memory properties of 3D printed PETG. Journal of Materials Research and Technology, 2022. 18: p. 4201-4215. https://doi.org/10.1016/j.jmrt.2022.04.076
8. Miao, S., et al., 4D anisotropic skeletal muscle tissue constructs fabricated by staircase effect strategy. Biofabrication, 2019. 11(3): p. 035030. DOI 10.1088/1758-5090/ab1d07
9. Peng, B., et al., Fused filament fabrication 4D printing of a highly extensible, self-healing, shape memory elastomer based on thermoplastic polymer blends. ACS applied materials & interfaces, 2020. 13(11): p. 12777-12788. https://doi.org/10.1021/acsami.0c18618
10. Lin, C., et al., 4D printing of shape memory polybutylene succinate/polylactic acid (PBS/PLA) and its potential applications. Composite Structures, 2022. 279: p. 114729. https://doi.org/10.1016/j.compstruct.2021.114729
11. Rahmatabadi, D., et al., 4D printing of PLA-TPU blends: effect of PLA concentration, loading mode, and programming temperature on the shape memory effect. Journal of Materials Science, 2023: p. 1-17. https://doi.org/10.1007/s10853-023-08460-0
12. Nagarajan, V., A.K. Mohanty, and M. Misra, Perspective on polylactic acid (PLA) based sustainable materials for durable applications: Focus on toughness and heat resistance. ACS
13. Nishi, T. and T. Wang, Melting point depression and kinetic effects of cooling on crystallization in poly (vinylidene fluoride)-poly (methyl methacrylate) mixtures. Macromolecules, 1975. 8(6): p. 909-915. https://doi.org/10.1021/ma60048a040
14. Kattan, M., et al., Strain-induced crystallization in uniaxially drawn PETG plates. Journal of applied polymer science, 2001. 81(14): p. 3405-3412. https://doi.org/10.1002/app.1797
15. Es-Said, O.S., et al., Effect of layer orientation on mechanical properties of rapid prototyped samples. Materials and Manufacturing Processes, 2000. 15(1): p. 107-122. https://doi.org/10.1080/10426910008912976
16. Song, Y., et al., Measurements of the mechanical response of unidirectional 3D-printed PLA. Materials & Design, 2017. 123: p. 154-164. https://doi.org/10.1016/j.matdes.2017.03.051
17. Wang, L., W.M. Gramlich, and D.J. Gardner, Improving the impact strength of Poly (lactic acid)(PLA) in fused layer modeling (FLM). Polymer, 2017. 114: p. 242-248. https://doi.org/10.1016/j.polymer.2017.03.011

18. Khosravani, M.R., et al., Characterization of 3D-printed PLA parts with different raster orientations and printing speeds. Scientific Reports, 2022. 12(1): p. 1016. https://doi.org/10.1038/s41598-022-05005-4
19. Letcher, T., B. Rankouhi, and S. Javadpour. Experimental study of mechanical properties of additively manufactured ABS plastic as a function of layer parameters. in ASME International Mechanical Engineering Congress and Exposition. 2015. American Society of Mechanical Engineers. https://doi.org/10.1115/IMECE2015-52634
20. Tymrak, B., M. Kreiger, and J.M. Pearce, Mechanical properties of components fabricated with open-source 3-D printers under realistic environmental conditions. Materials & Design, 2014. 58: p. 242-246. https://doi.org/10.1016/j.matdes.2014.02.038
21. Bellini, A. and S. Güçeri, Mechanical characterization of parts fabricated using fused deposition modeling. Rapid Prototyping Journal, 2003. 9(4): p. 252-264. https://doi.org/10.1108/13552540310489631
22. Ahn, S.H., et al., Anisotropic material properties of fused deposition modeling ABS. Rapid prototyping journal, 2002. 8(4): p. 248-257. DOI 10.1108/13552540210441166
23. Rankouhi, B., et al., Failure analysis and mechanical characterization of 3D printed ABS with respect to layer thickness and orientation. Journal of Failure Analysis and Prevention, 2016. 16: p. 467-481. DOI 10.1007/s11668-016-0113-3
24. Sepahi, M.T., et al., Mechanical properties of 3D-printed parts made of polyethylene terephthalate glycol. Journal of Materials Engineering and Performance, 2021. 30: p. 6851-6861. https://doi.org/10.1007/s11665-021-06032-4
25. Akhoundi, B. and A.H. Behravesh, Effect of filling pattern on the tensile and flexural mechanical properties of FDM 3D printed products. Experimental Mechanics, 2019. 59: p. 883-897. https://doi.org/10.1007/s11340-018-00467-y
26. Kuznetsov, V.E., et al., Increasing strength of FFF three-dimensional printed parts by influencing on temperature-related parameters of the process. Rapid Prototyping Journal, 2020. 26(1): p. 107-121. https://doi.org/10.1108/RPJ-01-2019-0017
27. Yakacki, C.M., et al., Strong, tailored, biocompatible shape-memory polymer networks. Advanced functional materials, 2008. 18(16): p. 2428-2435. https://doi.org/10.1002/adfm.200701049
28. Xu, J. and J. Song, Polylactic acid (PLA)-based shape-memory materials for biomedical applications. Shape memory polymers for biomedical applications, 2015: p. 197-217. https://doi.org/10.1016/B978-0-85709-698-2.00010-6
29. Xia, Y., et al., A review of shape memory polymers and composites: mechanisms, materials, and applications. Advanced materials, 2021. 33(6): p. 2000713. https://doi.org/10.1002/adma.202000713
30. Strutynski, C., et al., 4D Optical fibers based on shape-memory polymers. Nature Communications, 2023. 14(1): p. 6561. https://doi.org/10.1038/s41467-023-42355-7
31. Li, G. and A. Wang, Cold, warm, and hot programming of shape memory polymers. Journal of Polymer Science Part B: Polymer Physics, 2016. 54(14): p. 1319-1339. https://doi.org/10.1002/polb.24041
32. Rolińska, K., Bakhshi, H., Balk, M., Blocki, A., Panwar, A., Puchalski, M., ... & Mazurek-Budzyńska, M. (2023). Electrospun Poly (carbonate-urea-urethane) s Nonwovens with Shape-Memory Properties as a Potential Biomaterial. ACS Biomaterials Science & Engineering, 9(12), 6683-6697. https://doi.org/10.1021/acsbiomaterials.3c01214
33. Wang, A. and G. Li, Stress memory of a thermoset shape memory polymer. Journal of Applied Polymer Science, 2015. 132(24). https://doi.org/10.1002/app.42112

34. Soleyman, E., et al., Shape memory performance of PETG 4D printed parts under compression in cold, warm, and hot programming. Smart Materials and Structures, 2022. 31(8): p. 085002. DOI 10.1088/1361-665X/ac77cb
35. Wu, J., et al., Multi-shape active composites by 3D printing of digital shape memory polymers. Scientific reports, 2016. 6(1): p. 24224. DOI: 10.1038/srep24224
36. Ahmed, H.I., et al., Development of 3D auxetic structures using para-aramid and ultra-high molecular weight polyethylene yarns. The Journal of The Textile Institute, 2021. 112(9): p. 1417-1427. https://doi.org/10.1080/00405000.2020.1819007
37. Choong, Y.Y.C., et al., 4D printing of high performance shape memory polymer using stereolithography. Materials & Design, 2017. 126: p. 219-225. https://doi.org/10.1016/j.matdes.2017.04.04
38. Bashandeh, K., et al., Mechanics and deformation of shape memory polymer kirigami microstructures. Extreme Mechanics Letters, 2020. 39: p. 100831. https://doi.org/10.1016/j.eml.2020.100831.

Chapitre 5: Impression 4D avancée de composites PLA/PETG renforcés par fibres de lin: amélioration des propriétés mécaniques, thermiques et de mémoire de forme

Ce chapitre a fait l'objet d'une publication :

Advanced 4D Printing of Flax Fiber-Reinforced PLA/PETG Blends for Enhanced Mechanical, Thermal, and Shape Memory Properties. Bouguermouh Karima, Habibi Mohamed, Laperrière Luc, Zeshi Li, Abdin Yasmine and Daniel Monplaisir. Polymer, 2025, p. 128587.

Il peut être consulté en ligne à l'adresse suivante : https://doi.org/10.1016/j.polymer.2025.128587

Dans la continuité des travaux antérieurs menés sur les mélanges PLA/PETG visant à concilier biodégradabilité, flexibilité et propriétés mémoire de forme, cette étude explore l'intégration de fibres de lin comme renfort naturel pour surmonter les limitations mécaniques de ces mélanges tout en conservant leurs capacités de récupération. L'objectif principal est de renforcer les propriétés mécaniques et thermiques des mélanges PLA/PETG à travers l'ajout de fibres de lin, tout en préservant une performance stable de mémoire de forme sur plusieurs cycles thermomécaniques, un aspect encore peu exploré dans le domaine des polymères à mémoire de forme imprimés en 4D.

Des composites PLA/PETG ont été formulés à trois ratios différents (25/75, 50/50, 75/25), chacun renforcé avec des fibres de lin à 5 %, 10 % et 15 %, puis traités par mélange thermocinétique pour assurer une bonne dispersion. Les matériaux ont été caractérisés mécaniquement, thermiquement (DSC), morphologiquement (SEM), et leur comportement en mémoire de forme a été évalué sur 10 cycles à 90 °C. Les résultats révèlent que la formulation PLA-75/PETG-25 avec 10 % de fibres de lin présente le meilleur équilibre entre résistance mécanique (44 MPa), rigidité (4 GPa) et capacité de récupération (92 % après 10 cycles). Les fibres de lin, agissant comme agents nucléants, ont amélioré la cristallinité et réduit le retrait après l'étude cyclique, bien que des concentrations plus élevées entraînent une perte de performance due à l'agglomération des fibres.

Grâce à leur comportement mécanique stable, leur réponse thermique fiable et leur bonne récupération dimensionnelle, ces composites s'avèrent particulièrement adaptés à des applications

avancées en impression 4D, notamment pour la fabrication de structures auxétiques adaptatives, où des déformations contrôlées et réversibles sont requises.

Advanced 4D Printing of Flax Fiber-Reinforced PLA/PETG Blends for Enhanced Mechanical, Thermal, and Shape Memory Properties

Karima Bouguermouh[1], Mohamed Habibi[1*], Luc Laperrière[1], Daniel Monplaisir[2], Zeshi Li[3], and Yasmine Abdin[3]

[1] *Department of Mechanical Engineering, Université du Québec à Trois-Rivières, Quebec, Canada.*
[2] *Department of Chemistry, Biochemistry and Physics, University of Quebec at Trois-Rivières, 3351 des Forges Boulevard, Trois-Rivières, Quebec, Canada*
[3] *Department of Materials Engineering, The University of British Columbia, Vancouver, BC V6T 1Z4, Canada*

5.1 Abstract

This study explores the development of flax fiber-reinforced PLA/PETG polymer blends for advanced 4D printing applications, aiming to enhance mechanical, thermal, and shape memory properties. This research bridges material innovation and environmental sustainability by combining the biodegradability of PLA with the flexibility and toughness of PETG and reinforcing with sustainable flax fibers.

PLA/PETG blends were prepared in varying ratios (25/75, 50/50, and 75/25) and reinforced with flax fibers at 5%, 10%, and 15% concentrations using a thermokinetic mixing process to ensure uniform fiber dispersion and enhanced material performance. Characterization techniques, including SEM, DSC, and tensile testing, were used to comprehensively analyze structural integrity, thermal stability, and shape memory behavior.

The optimized blend, PLA-75/PETG-25/F-10, exhibited exceptional performance, with a tensile strength of 44 MPa, a Young's modulus of 4 GPa, and approximately 92% shape recovery after 10 cycles at 90°C. Flax fiber reinforcement contributed significantly to dimensional stability, minimized shrinkage, and acted as a nucleating agent to enhance crystallinity, making these composites suitable for intricate auxetic designs and adaptive structures.

By leveraging sustainable materials and advanced fabrication techniques, this study not only advances the potential of 4D printing technologies but also sets a benchmark for eco-friendly materials in dynamic and multifunctional applications across automotive, aerospace, and biomedical sectors.

Keywords

Flax fiber-reinforced composites; PLA/PETG polymer blends; 4D printing; Shape memory properties; Sustainable materials.

5.2 Introduction

4D printing of reinforced polymer composites is an emerging frontier in additive manufacturing, blending smart material functionality with structural reinforcement to create dynamic and adaptive structures. By incorporating shape memory polymers (SMPs) with reinforcement fibers, these composites can achieve controlled shape changes in response to external stimuli, unlocking innovative applications in aerospace, biomedical devices, and flexible electronics [1-8].

Recent studies on 4D-printed PETG-based composites show significant mechanical and shape memory performance improvements through strategic reinforcement. Rahmatabadi et al. [9] reported that PETG reinforced with 1.5% short carbon fibers improved stress recovery by 22%, reaching 28% after annealing, with enhanced shape memory via print pattern optimization. In another study, Rahmatabadi et al. [10] showed that polylactic acid-polybutylene adipate terephthalate PLA-PBAT blends achieved up to 220% elongation and 93% shape recovery in seconds, offering high flexibility and fast response. In addition, Ali et al. [11] found that 3D printed polyethylene terephthalate glycol ethylene-vinyl acetate PETG–EVA blends are thermally stable with biphasic morphology and good compatibility, achieving tensile strengths of 20.14–25.38 MPa. The EVA30 blend showed the best mechanical performance and print quality. All blends exhibited excellent shape memory behavior, with over 90% recovery in 20 seconds, and faster recovery at higher EVA content. On the other hand, PETG–carbon black composites delivered over 97% recovery and better thermal response, with 1% carbon black yielding optimal strength [12]. Mirasadi et al. [13] observed that PETG–ABS–Fe_3O_4 nanocomposites enabled remote, magnetically triggered shape recovery, with improved strength but reduced print quality at higher filler loads. Finally, continuous fiber-reinforced PETG composites achieved dramatic modulus gains (up to 474%) and shape recovery of 94–98% even at room temperature, as described by Fallah et al. [14].

Incorporating natural fibers, such as flax, into polymer matrices offers a sustainable and environmentally friendly approach to enhancing mechanical properties like stiffness and shape

retention. Flax fiber reinforcement enables the creation of biocomposites with excellent adaptability and shape-changing properties, suitable for diverse applications ranging from biomedical devices to dynamic structural systems [15-18].

Thermokinetic mixing is an advanced pre-treatment technique used before extrusion processing. This method creates a highly homogeneous material blend by combining heat generation and mechanical shearing. Applying before extrusion allows for milder extrusion conditions, preserving the structural integrity of sensitive materials like fibers. Designed to address and overcome the challenges associated with extrusion, the Gelimat mixer excels at handling complex compounding and dispersion tasks often encountered in composite manufacturing [19, 20]. Its design principle is centered around the rapid heating, mixing, and compounding of materials, achieving these processes within minutes. This efficiency leads to a notably short thermal history for the compounded polymer, a significant advantage as it minimizes the risk of polymer degradation that could compromise the material's integrity and performance [20-23].

Operating on a unique mechanism, the Gelimat system propels particles at high velocities using blades attached to a rapidly rotating shaft. This rapid movement generates significant kinetic energy, which is then converted into thermal energy upon impact with the chamber walls. This energy transformation is at the core of the Gelimat's functionality, enabling it to quickly heat and mix the composite materials into a homogenous state. The swift and efficient mixing process ensures uniform dispersion of fibers and fillers within the polymer matrix and preserves the material's properties by preventing prolonged exposure to heat, a common issue in traditional extrusion methods [24].

Flax fiber-reinforced polymers significantly improve crystallinity and mechanical performance compared to the neat matrix. For example, Ming et al.[25] reported that composites with 30% flax fibers reinforced in polylactide stereocomplex (sc-PLA) achieved a crystallinity of 98.4%, a 32% increase compared to unreinforced sc-PLA, alongside mechanical enhancements such as a tensile strength of 52.9 MPa, Young’s modulus of 6.42 GPa, and an impact strength increase of 343%. Similarly, Nassiopoulos & Njuguna [26] study showed that unidirectional flax-reinforced composites achieved tensile strengths up to 72 MPa and stiffness values of 13 GPa, making them suitable for load-bearing applications. In polypropylene matrices, flax reinforcement improved

tensile strength by over 30%, with crystallinity levels correlating directly to improved modulus and load-bearing capacities [27]. These results underscore flax fibers' potential to enhance polymer matrices for applications requiring high performance and sustainability.

The exploration of multi-cycle performance in 3D-printed shape memory polymers (SMPs) and their composites remains limited, with most studies focusing on single-cycle behavior and initial shape recovery [28-31]. For example, Strutynski et al. [32] studies report shape recovery rates exceeding 98% in single-cycle tests for SMP composites. However, multi-cycle tests reveal significant degradation, with recovery dropping below 90% after 50 cycles, depending on the material composition. While 3D printing offers unparalleled precision in designing SMP structures and enables tailored actuation through intricate geometries, the durability of shape memory effects under repeated actuation remains insufficiently studied. Recent advancements in digital SMPs have demonstrated multi-shape transformations, with recovery rates close to 95% after 10 cycles, but their performance degrades substantially in subsequent cycles [33]. Similarly, multimaterial 4D-printed SMPs with customizable thermomechanical properties show promise for repeated activations but require further analysis to evaluate their long-term stability, as mechanical properties such as stiffness and tensile strength decrease by up to 15% after 20 cycles [34]. These findings highlight the urgent need for comprehensive investigations into the multi-cycle durability of 3D-printed SMPs to optimize their use in adaptive devices, robotics, and deployable systems, where consistent performance over numerous cycles is critical.

This study investigates the development and characterization of flax fiber-reinforced PLA/PETG polymer blends tailored for 4D printing applications, focusing on their mechanical, thermal, and shape memory properties. By leveraging the synergistic effects of PLA’s crystallinity, PETG’s flexibility, and flax fiber reinforcement, the objective is to create sustainable, high-performance materials suitable for adaptive and environmentally friendly applications. Specifically, the work explores three main aspects: mechanical performance, thermal and crystallization behavior, and shape memory properties. Mechanical testing evaluates tensile strength and stiffness to assess the load-bearing capabilities and structural stability of the composites. Thermal and crystallization behavior is analyzed to understand the role of flax fibers as nucleating agents, their impact on thermal transitions, and their ability to enhance crystallinity and stability. Shape memory

properties, including shape fixity, recovery, and dimensional stability, are assessed over multiple thermal cycles to establish the composites' suitability for dynamic and programmable applications.

PLA/PETG blends were prepared in three different ratios (25/75, 50/50, 75/25) and reinforced with flax fibers at concentrations of 5%, 10%, and 15%. The resulting composites underwent comprehensive characterization, including tensile testing, differential scanning calorimetry (DSC), and shape memory performance analysis across multiple thermal-mechanical cycles. Scanning Electron Microscopy (SEM) was employed to examine fractured surfaces, providing insights into interfacial bonding and fiber distribution within the polymer matrix. The findings aim to identify the optimal blend composition and fiber content for achieving balanced mechanical strength, thermal stability, and shape memory performance.

By presenting a detailed analysis of these properties, this work highlights the potential of flax fiber-reinforced PLA/PETG blends for diverse applications in fields such as automotive, aerospace, and biomedical engineering. These composites offer a sustainable and adaptable solution for 4D printing technologies, with the results underscoring their versatility and environmental benefits. The following sections describe the materials and methods, experimental findings, and detailed discussions, culminating in conclusions that emphasize the significance of this study in advancing sustainable materials for adaptive applications.

5.3 Materials and methods

5.3.1 Sample preparation

Materials

The flax fibers utilized in the study were obtained from Safilin (France, Poland) as a low-twist flax fiber yarn with a linear density of 5000 tex. The producer has reported some properties of a single flax fiber in the yarn: density of 1.45g/m^3, a diameter of fiber of about 20µm, elongation at break of 1.35%, a tensile strength of 738MPa, Young's modulus of 51.4GPa and specific Young's modulus of 35.4GPa/g/m^3 as reported by Safilin [35]. The surfaces of flax fiber yarns were untreated. Poly(lactic acid) (PLA) and polyethylene terephthalate glycol-modified (PETG) resin pellets were selected as the polymer matrices for developing the flax fiber-reinforced 4D printing blends. PLA pellets, with a density of 1.24 g/cm³, and PETG pellets, with a density of 1.27 g/cm³, were sourced from Push Plastics and served as the base materials for the composites.

Manufacturing

Figure 5.1 summarizes the complete manufacturing process, from raw material to 3D-printed sample, with four principal steps.

Step 1: Preparation of blends and composite pellets

To prepare the PLA, PETG, and flax for composite pellet fabrication, all components were pre-dried in a vacuum oven at 60°C for 24 hours to eliminate residual moisture.

Step 2: First, three binary combinations of PLA and PETG polymers were prepared in weight ratios of 25/75, 50/50, and 75/25 by mixing their pellets in a beaker immediately before the extrusion process. On the other hand, the preparation of PLA/PETG/Flax composites involved a two-step mixing process. Initially, flax fibers at concentrations of 5%, 10%, and 15% w/w, with PLA and PETG pellets, were blended in a DUSATEC Gelimat thermokinetic mixer (Model G Series), which was operated at a speed of 4500 rpm. The mixing continued until the material's temperature reached 200°C, with the melt state mixing duration lasting between 20 and 30 seconds. The solid masterbatch produced from this initial melt compounding was cooled and subsequently crushed into granules suitable for extrusion.

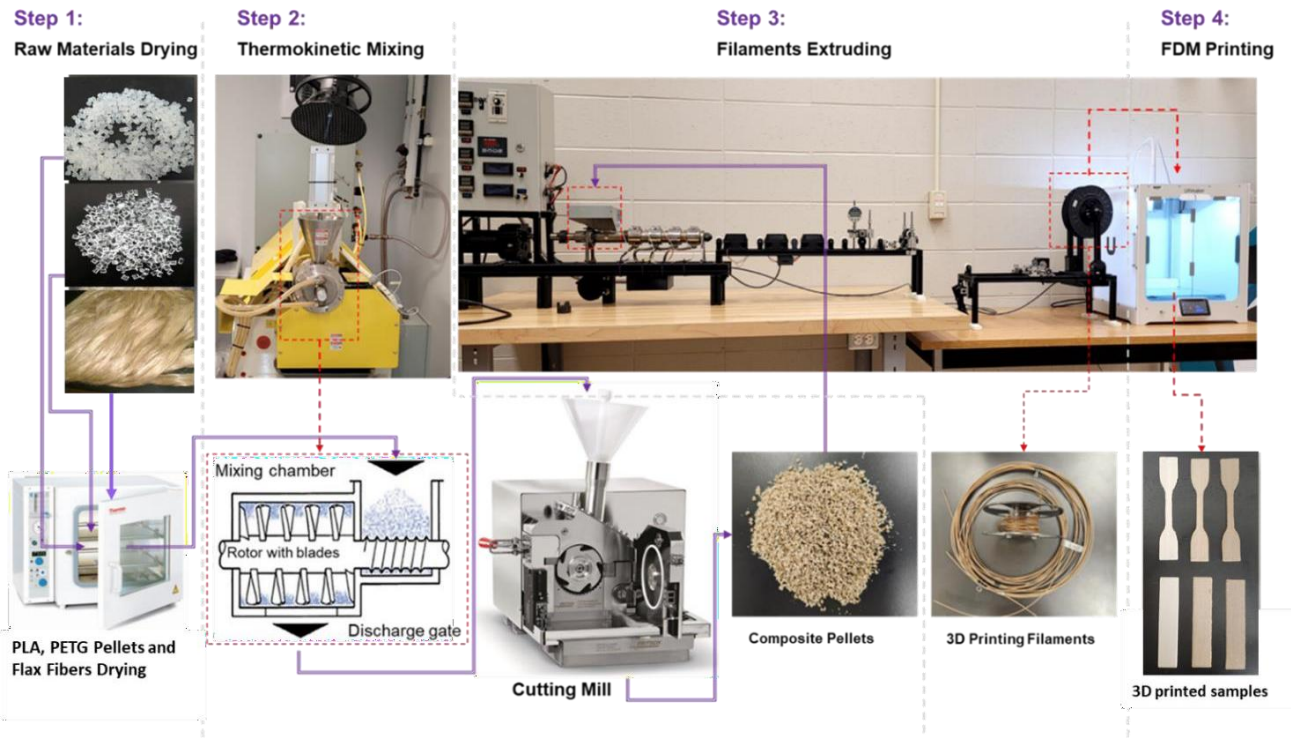

Figure 5.1: Process flow: From raw materials to final 3D printed samples.

Step 3: Extrusion of composite filaments

Granules were then fed into a single-screw extruder to create 3D printing filaments. Key processing parameters such as extrusion temperature, extrusion rate, line speed, and oven temperature were carefully optimized beforehand to ensure the filaments were of high quality, exhibiting minimal defects and consistent diameter. The extrusion temperatures were precisely controlled within the range of 197°C to 208°C, as reported in Table 5.1, to accommodate the distinct thermal and flow properties of each composition. Employing a nozzle with a diameter of 3 mm to produce 2.80 mm diameter filaments, as shown in Figure 5.2 (a) and b. Post-extrusion, the filaments were cooled and wound onto spools using a filament winding system, making them ready for 3D printing.

Step 4: 3D printing by Fused Filament Fabrication (FFF)

The PLA/PETG polymer blends and Flax Fibers-reinforced PLA/PETG blends composite filaments were used to print 100 mm x 20 mm x 1 mm samples for shape memory following the ASTM D638 Type IV, designed using CAD software. Five tensile specimens for each composition were printed using an Ultimaker S5 printer with the specified printing parameters: a BB and CC-nozzle with diameters of 0.4 and 0.6 mm, respectively, for PLA/PETG polymer blends and Flax Fibers-reinforced PLA/PETG blends composite. Printing parameters were optimized to ensure consistent performance across all samples, including layer heights of 0.2 mm and 0.3 mm, 100% infill density, infill line widths of 0.3 mm and 0.45 mm, and printing speeds of 30 mm/s and 20 mm/s [36, 37]. The nozzle and bed temperatures, which were tailored for each sample to optimize print quality, are listed in Table 5.1.

This systematic approach ensured uniform filament quality and reliable print performance for the PLA/PETG blends and the flax fiber-reinforced composites.

5.3.2 Structural and Visual Assessment of 3D-Printed PLA/PETG and Fiber Composites

The extruded PLA/PETG blend filaments exhibit uniform color and smooth surfaces, as illustrated in Figure 5.2 (a). In contrast, flax fiber-reinforced filaments display a natural, earthy tone resulting from the fiber incorporation (Figure 5.2 (b)).

Table 5.1: Compositions, extrusion temperatures, and 3D printing parameters of PLA/PETG blends and flax fiber reinforced PLA/PETG blends.

Samples	Nozzle Temperature (°C)	Build plate temperature (°C)	Print speed (mm/s)	Flow (%)	Layer height (mm)	Line width (mm)	Extrusion Temperatures (°C)	Mechanical properties	
								Tensile strength (MPa)	Young modulus (GPa)
PLA-25/PETG-75	255	100	30	100	0,2	0,3	197-197	56,01±3	2,99±0,22
PLA-50/PETG-50	255	100	30	100	0,2	0,3	197-177	48,49±2,5	2,97±0,3
PLA-75/PETG-25	255	100	30	100	0,2	0,3	197-197	60,03±1	3,11±0,12
PLA-25/PETG-75/F-5	255	100	20	100	0,3	0,45	202-205	32,89±2,5	2,29±0,23
PLA-25/PETG-75/F-10	260	100	20	95	0,3	0,45	205-208	26,32±2,4	2,14±0,2
PLA-25/PETG-75/F-15	260	100	20	95	0,3	0,45	205-208	25,65±2,1	2,23±0,25
PLA-50/PETG-50/F-5	260	100	20	100	0,3	0,45	202-205	30,75±2	2,81±0,28
PLA-50/PETG-50/F-10	260	100	20	105	0,3	0,45	198-200	26,61±2,2	3,04±0,24
PLA-50/PETG-50/F-15	260	100	20	100	0,3	0,45	185-190	28,55±1,9	3,75±0,26
PLA-75/PETG-25/F-5	255	100	20	102	0,3	0,45	190-195	35,20±1,3	3,15±0,15
PLA-75/PETG-25/F-10	255	100	20	105	0,3	0,45	190-195	43,96±1,26	4±0,13
PLA-75/PETG-25/F-15	260	100	20	105	0,3	0,45	200-205	34,14±1,4	3,4±0,14

The majority of the 3D-printed polymer blends and flax-reinforced specimens maintain a high-quality appearance characterized by smooth surfaces and strong layer adhesion, indicative of precise material flow during the printing process (Figure 5.2 (c and d)). These findings support the conclusion that advanced mixing processes like the Thermokinetic Mixer significantly enhance the quality and mechanical properties of 3D-printed polymer blends and flax-reinforced composites.

However, the PLA-75/PETG-25/F-15 blend exhibits more pronounced color variations and surface inconsistencies. These issues are likely attributable to the higher fiber content and lower PETG ratio, which could have influenced the homogeneity of the material. Overall, introducing flax fiber reinforcement imparts distinct aesthetic and structural modifications, with the printed specimens generally achieving high-quality results that are well-suited for subsequent testing and analysis.

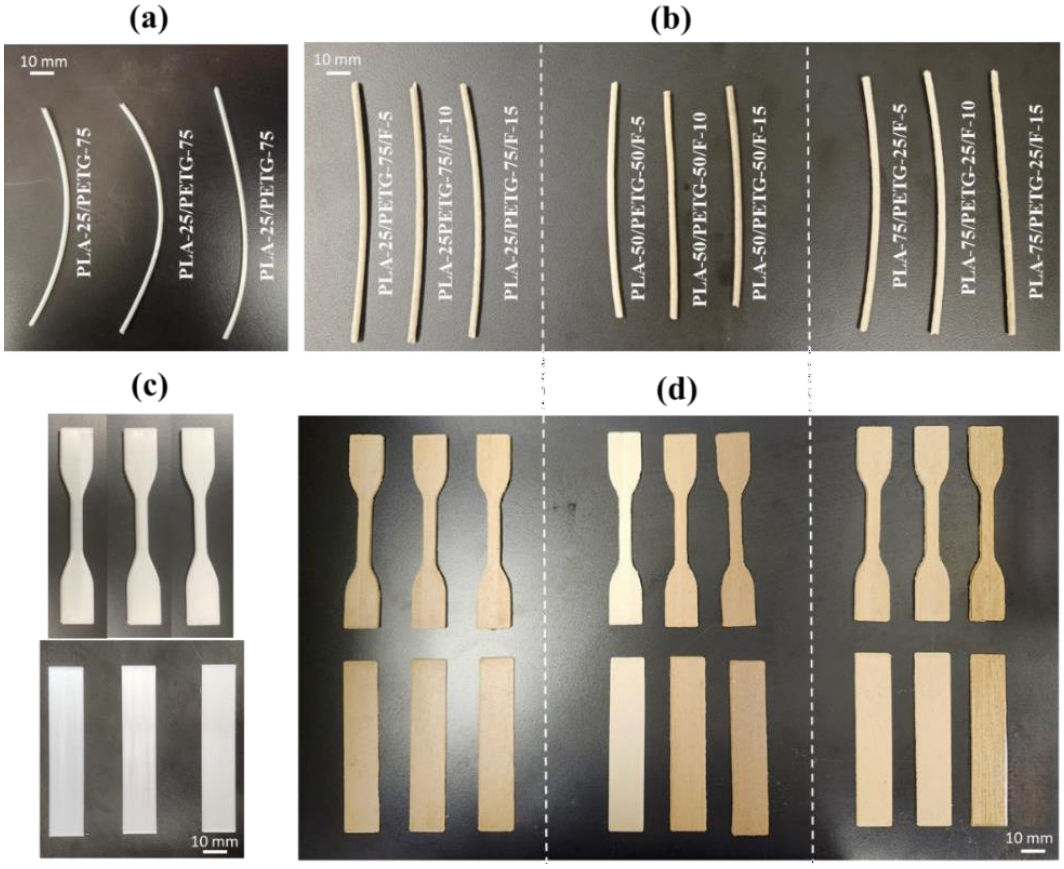

Figure 5.2: Illustration of (a) extruded PLA/PETG blend filaments, (b) flax fiber-reinforced PLA/PETG blend filaments, and (c) 3D printing of D638 Type IV specimens for tensile strength testing, as well as (d) 100 mm x 20 mm x 1 mm samples for shape memory testing, as well as (d) 100 mm x 20 mm x 1 mm samples for shape memory testing.

5.3.3 Characterization

5.3.3.1 Tensile test

Mechanical testing was conducted using an MTS machine with a 20 kN load cell under standard ambient conditions. Testing followed ASTM D638 guidelines, with Type IV specimens 3D-printed in 0° orientations. This setup allowed for a detailed analysis of the mechanical behavior, including tensile strength, Young's modulus, and elongation at break, providing key insights into the structural performance of the PLA/PETG blends and flax-reinforced composites.

5.3.3.2 Differential scanning calorimeter (DSC)

Thermal analyses were performed using a DSC Q800 (TA Instruments). For all mixtures, the heating process ranged from 30°C to 260°C, followed by a cooling process from 260°C to 30°C. Both heating and cooling cycles were conducted at a consistent rate of 10°C/min, with a holding time of 5 minutes at the maximum and minimum temperatures. This testing provided detailed thermal profiles of the blends, including glass transition, melting, and crystallization temperatures.

5.3.3.3 Scanning Electron Microscopy (SEM)

Surface morphology and microstructural analyses were conducted using scanning electron microscopy. Samples were sputter-coated with gold under argon plasma at approximately 20 mV for ~3.5 minutes. Images were captured under low vacuum conditions (50 Pa), with water as the chamber medium. The imaging employed a spot size of 5 μm at an accelerating voltage of 20 kV, ensuring high-resolution observations of fiber dispersion, polymer-fiber interfaces, and potential defects in the blends.

5.3.3.4 Shape Memory Test

U-shaped 3D-printed samples measuring 100 mm × 20 mm × 1 mm, oriented at 0°, were subjected to shape programming and recovery tests to evaluate the shape memory characteristics.

The samples were heated to a designated programming temperature (T_p) and then deformed to fit a mold 20 mm thick by applying sufficient force. While held in the mold, the samples were cooled to room temperature to stabilize their deformed shape. The fixed angle, referred to as θ_{fixed}, was recorded after mold removal.

The samples were reheated to a constant temperature for recovery evaluation, and the bending angle (θ_i) was carefully measured. Shape fixity (S_f) and shape recovery (S_r) were calculated using the following equations:

$$Shape\ fixity\ (S_f) = \frac{\theta_{fixed}}{\theta_{max}}\ X\ 100 \quad \text{(eq. 1)}$$

$$Shape\ recovery\ (S_r) = \frac{\theta_{\max} - \theta_i}{\theta_{\max}} X\ 100 \quad \text{(eq. 2)}$$

These metrics provided quantitative insights into the effectiveness of the shape memory behavior in the studied composites. Our earlier work [38] references detailed methodologies and previous results.

5.4 Results and discussions

5.4.1 Differential scanning calorimeter (DSC)

5.4.1.1 Glass transition temperature

Based on the DSC results presented in Figure 5.3 and Appendix 4, the PLA-25/PETG-75 blend exhibits two distinct glass transition temperatures, T_{g1} = 60.72°C and T_{g2} = 79.58°C, indicating the immiscibility of PLA and PETG as each phase retains its thermal characteristics. Similarly, PLA-50/PETG-50 displays T_{g1} = 59.97°C and T_{g2} = 80.13°C, confirming phase separation between the two polymers. In contrast, the PLA-75/PETG-25 blend exhibits two glass transitions at T_{g1} = 60.98 °C and T_{g2} = 80.66 °C. As shown in Figure 5.3 (a), the decreasing intensity of the PETG T_g signal at higher PLA content indicates that one phase becomes more dominant and continuous, suggesting improved miscibility [39]. This implies that as PLA content increases, phase separation diminishes, and the blend behaves more homogeneously.

The thermal behavior of the unreinforced PLA/PETG polymer blends observed in this study is consistent with previous findings reported in our earlier studies [38, 40]. Specifically, the dual glass transition temperatures (T_{g1} and T_{g2}) observed for PLA-25/PETG-75 and PLA-50/PETG-50 confirm the immiscibility between PLA and PETG, as reported in earlier DSC analyses on filament-based samples. The current T_g values obtained from 3D-printed specimens ranging from 59.97°C to 60.98°C for PLA-rich blends are comparable to those previously measured on extruded filaments, despite slight variations due to processing method differences.

The incorporation of flax fibers slightly reduces the T_g values in all blends. For example, PLA-25/PETG-75/F-5 shows T_{g1} = 58.83°C and T_{g2} = 77.68°C, reflecting a reduction compared to the unreinforced blend. A similar trend is observed in PLA-50/PETG-50/F-5, with T_{g1} = 59.69°C and T_{g2} = 78.80°C. This decrease can be attributed to the role of flax fibers in increasing free volume and chain mobility within the polymer matrix, effectively acting as a plasticizer. This enhanced mobility reduces the temperature required to transition from a glassy to a rubbery state [41].

On the other hand, the DSC thermograms for flax-reinforced PLA-75/PETG-25 samples (Figure 5.3 (c)) show a single glass transition temperature, even after fiber addition. This indicates that PLA and PETG remain miscible in this composition despite the presence of flax fibers. This suggests that the higher PLA content and fiber incorporation improve interfacial interactions, reducing phase separation.

As seen in Figure 5.4 (a), the melting temperature (T_m) of the PLA-50/PETG-50 blend is T_m=151.9°C, indicating that the crystalline structure of PLA is retained, but it is somewhat reduced due to the amorphous nature of PETG. In contrast, the PLA-75/PETG-25 blend shows a slightly higher melting temperature of T_m=154.38°C, as reported in Appendix 4, reflecting the higher crystalline content attributable to the higher PLA proportion.

5.4.1.2 Melting behavior

As shown in Figure 5.3 (a), the disappearance of the melting temperature (T_m) in the DSC thermogram of the PLA-25/PETG-75 blend can be attributed to the high PETG content, which significantly suppresses the crystallization behavior of PLA. Due to the predominantly amorphous nature of PETG, the formation of PLA crystalline regions is strongly inhibited, resulting in a blend that lacks a distinct melting transition. This observation is consistent with the crystallinity data presented in Section III.1.4, where the PLA-25/PETG-75 blend exhibits 0% crystallinity (X_c) and 0% cold crystallinity (X_{cc}), confirming its amorphous character. Similar findings have been reported in previous studies, indicating that the dominance of amorphous PETG in PLA/PETG systems disrupts the ordering of PLA chains and prevents the development of a crystalline phase [38, 42, 43].

The addition of flax fibers to PLA-25/PETG-75 blends significantly impacts the melting behavior, with fibers acting as nucleating agents [25]. This effect enhances the crystallization of PLA, broadening the melting temperature range. The nucleating effect of flax fibers introduces additional

crystallization sites, which not only influence the thermal transitions but also improve the thermal stability of the blend. These fibers interact with the polymer matrix, promoting better heat distribution across the composite and contributing to the observed thermal behavior [44].

Reinforcing the blend with 15 wt% flax fibers raises the melting temperature (T_m) to 154.73°C, similar to the unreinforced PLA-75/PETG-25 blend. This indicates that the flax fibers help maintain the crystalline structure of PLA, even when the blend is rich in PETG [45].

On the other hand, the melting temperature of the blends initially decreases by adding flax fibers up to 10%, as observed in both the PLA-50/PETG-50 and PLA-75/PETG-25 blends. This reduction suggests that flax fibers disrupt the crystalline structure of PLA, leading to a decrease in the thermal stability of the crystalline domains. However, at a higher flax fiber content of 15%, T_m increases again, indicating that the fibers, at higher concentrations, act as effective nucleating agents. This promotes crystallization and enhances the thermal stability of the crystalline regions [44]. The slightly reduced melting temperature observed in flax-reinforced blends demonstrates that flax fibers, while acting as reinforcements, slightly lower the energy required to melt the polymer matrix. This effect is attributed to the disruption of polymer crystallites by the flax fibers, which reduces the thermal stability of the crystalline domains [26].

The enthalpy of fusion (ΔH_m) reflects the energy required for melting and is directly related to the degree of crystallinity in the material. Figure 4 (b) shows that the ΔH_m of PLA-25/PETG-75 remains consistently low across different fiber content levels, indicating limited crystallization potential in PETG-rich blends. For PLA-50/PETG-50, ΔH_m increases slightly with fiber addition, peaking at 5% fiber content and stabilizing at higher levels. In contrast, PLA-75/PETG-25 shows a peak ΔH_m value at 10% fiber content, which signifies the highest degree of crystallinity before a sharp decline at 15%, as detailed in Appendix 4.

The peak ΔH_m value for PLA-75/PETG-25 at 10% fiber content highlights this concentration as optimal for enhancing crystallinity in PLA-rich blends. At this level, flax fibers effectively act as nucleating sites, facilitating the formation of crystallites. However, the fibers may agglomerate at higher fiber content (15%), reducing the overall crystallization efficiency and disrupting the polymer matrix [46]. In contrast, the consistently low ΔH_m values for PLA-25/PETG-75 indicate that PETG-rich blends are predominantly amorphous and exhibit minimal potential for crystallization, even with the addition of flax fibers.

5.4.1.3 Cold crystallization behavior

The addition of flax fibers also significantly influences cold crystallization behavior. As nucleating agents, flax fibers enhance the material's crystallization ability at higher temperatures. The cold crystallization temperature (T_{cc}) reflects the material's capacity to crystallize upon reheating after cooling in an amorphous state, further emphasizing the role of flax fibers in modifying the thermal properties of the blends [38, 47].

According to Figure 5.4 (c) PLA-25/PETG-75 exhibits relatively stable cold crystallization temperatures (T_{cc}), remaining around 134°C across the fiber content range (0 -15%). This consistency is due to the high PETG content, which is predominantly amorphous and inherently resistant to crystallization. PETG's amorphous nature limits the influence of flax fiber addition on the cold crystallization process until very high fiber concentrations are reached [44].

In contrast, PLA-50/PETG-50 demonstrates a slight increase in T_{cc} with fiber content up to 5%, followed by a decline at higher fiber contents (10% and 15%). This trend reflects an initial enhancement of nucleation and crystallization facilitated by the fibers, which later becomes less effective due to potential agglomeration.

For PLA-75/PETG-25, T_{cc} shows a notable decrease at 10% fiber content but rises again at 15%, as detailed in Appendix 4. The reduction at 10% fiber content suggests that flax fibers at this concentration temporarily disrupt the nucleation process of PLA, delaying crystallization. However, at 15% fiber content, the increase in T_{cc} indicates improved crystallization behavior. This recovery highlights the dual role of flax fibers: at optimized concentrations, they act as effective nucleating agents, enhancing crystallization, whereas at suboptimal levels, they may interfere with the polymer matrix's ability to crystallize efficiently [48].

Figure 4 (d) shows that the enthalpy of cold crystallization (ΔH_{cc}) for PLA-25/PETG-75 remains relatively stable across varying fiber contents, highlighting the low crystallization activity typical of PETG-rich blends. Since PETG is predominantly amorphous and not prone to crystallization, the addition of flax fibers does not significantly impact the cold crystallization behavior in this blend. In contrast, PLA-50/PETG-50 shows a gradual decrease in ΔH_{cc} with increasing fiber content, indicating that the flax fibers disrupt the matrix's ability to crystallize uniformly. For PLA-75/PETG-25, ΔH_{cc} peaks at 10% fiber content, reflecting the enhanced crystallization facilitated by the optimal nucleating effect of flax fibers. However, at 15% fiber content, ΔH_{cc} decreases

sharply, suggesting fiber agglomeration at higher concentrations disrupts uniform crystallization [46].

These enthalpy data underscore the significant role of flax fibers in promoting crystallization within PLA/PETG blends, particularly in PLA-rich compositions. The nucleating effect of flax fibers enhances the formation of crystalline structures within the polymer matrix, improving the overall crystallization behavior and thermal performance of the blends [49].

5.4.1.4 Crystallinity

As seen in Figure 5.4 (e and f), the PLA-25/PETG-75 blend exhibits 0% crystallinity (X_c) and cold crystallinity (X_{cc}), respectively, indicating a lack of substantial crystallization or cold crystallization activity. This result suggests that the high PETG content, characterized by its amorphous nature, significantly inhibits PLA's crystallization ability. In contrast, PLA-50/PETG-50 demonstrates moderate crystallinity, with X_c=3.78% and X_{cc}=1.48%. These values suggest that some degree of crystallization occurs, primarily during the melting process rather than cold crystallization. The more balanced ratio of PLA and PETG appears to enable limited crystallization, though the overall crystallinity remains relatively low due to PETG's influence.

Furthermore, the PLA-75/PETG-25 blend shows minimal crystallinity, with X_c=0.66% and X_{cc}=0.44%. This indicates that the higher PLA content slightly promotes cold crystallization, but the overall crystallization remains modest. These findings align with the literature, which highlights that increasing PLA content generally favors crystallization, but PETG's amorphous characteristics act as a strong inhibitor, limiting the overall degree of crystallinity in the blends [42].

Flax fiber-reinforced PLA-25/PETG-75 composites demonstrate a marked increase in crystallinity with higher fiber content. Specifically, the degree of crystallinity (X_c) for PLA-25/PETG-75/F-15 reaches 30.26%, while the degree of cold crystallization (X_{cc}) is 1.15%, as reported in Appendix 4. This significant enhancement suggests that flax fibers play a pivotal role in crystallization, particularly during the melting phase. Acting as nucleating agents, the fibers promote the formation of crystalline regions by providing sites where polymer chains can organize during heating. These findings align with previous research, which consistently indicates that fibers can increase the crystallinity of PLA-based blends by facilitating nucleation and improving the material's structural order during thermal transitions [43].

In the case of PLA-50/PETG-50/F-5, X_c is 9.37%, and X_{cc} is 4.52%, illustrating that flax fibers enhance the blend's cold crystallization ability. This result highlights the dual role of fibers in

improving the crystalline structure during both the melting and cooling processes. Enhanced cold crystallization reflects the material's ability to crystallize upon cooling from an amorphous state, further confirming the beneficial impact of fiber reinforcement on the thermal behavior and crystallization dynamics of PLA/PETG blends. For PLA-50/PETG-50 composites, increasing the flax fiber content beyond 5% results in a decline in the degree of X_c and X_{cc} compared to the PLA-50/PETG-50/F-5. Specifically, PLA-50/PETG-50/F-10 and PLA-50/PETG-50/F-15 exhibit lower X_c and X_{cc} values than PLA-50/PETG-50/F-5. This trend suggests that excessive fiber content hinders crystallization. At higher concentrations, fibers may restrict the mobility of polymer chains, which is essential for crystallization during both the melting and cooling phases. Similar findings have been reported by Nazari & Garmabi [47], who observed that higher fiber content can reduce polymer chain mobility, thereby limiting the crystallization potential of fiber-reinforced composites. In contrast, PLA-75/PETG-25/F-5 demonstrates notable enhancements in melting and cold crystallization, with X_c=13.99% and X_{cc}=10.68%. These values represent a significant improvement over the non-reinforced PLA-75/PETG-25 blend.

Table 5.2: Glass transition temperatures of polymer blends and flax fiber-reinforced polymer blends.

Samples	Glass transition temperature (T_g) (°C)	
	T_{g1}	T_{g2}
PLA-25/PETG-75	60.72	79.58
PLA-50/PETG-50	59.97	80.13
PLA-75/PETG-25	60.98	80,66
PLA-25/PETG-75/F-5	58.83	77.68
PLA-25/PETG-75/F-10	59.65	78.63
PLA-25/PETG-75/F-15	60.71	79.71
PLA-50/PETG-50/F-5	59.69	78.80
PLA-50/PETG-50/F-10	59.03	78.54
PLA-50/PETG-50/F-15	58.98	77.66
PLA-75/PETG-25/F-5	59.42	-
PLA-75/PETG-25/F-10	59.36	-
PLA-75/PETG-25/F-15	58.61	-

The substantial increase in cold crystallization highlights the role of flax fibers as effective nucleating agents, facilitating polymer chain alignment and crystallization even during the

cooling phase. This improvement underscores the importance of optimizing fiber content to achieve the best thermal and structural properties balance in fiber-reinforced PLA/PETG blends.

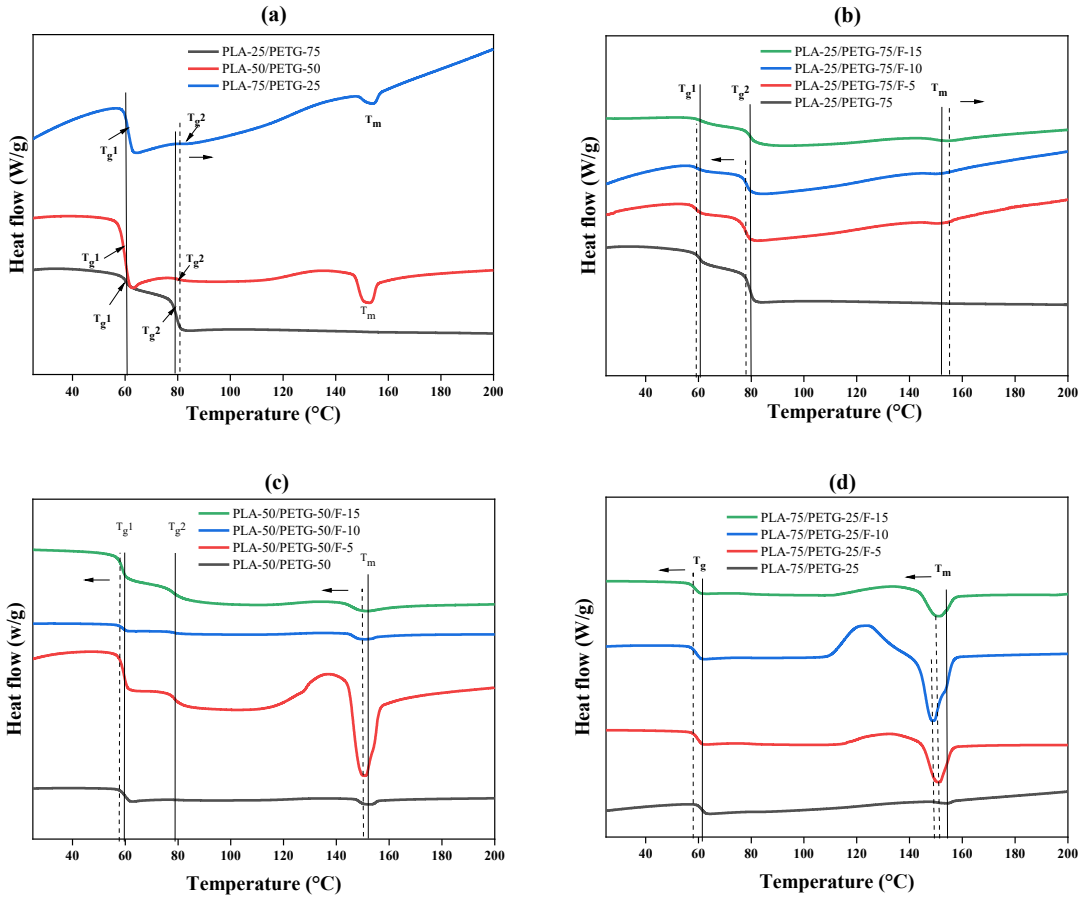

Figure 5.3: Differential Scanning Calorimetry of (a): PLA/PETG Polymer blends, (b): Flax Fiber-Reinforced PLA-25/PETG-75, (c): Flax fiber-Reinforced PLA-50/PETG-50, (d): Flax fiber-Reinforced PLA-75/PETG-25.

PLA-75/PETG-25/F-10 demonstrates the highest crystallinity among all samples, with a degree of X_c of 25.48% and X_{cc} of 30.64%. These results underline the significant influence of flax fibers in enhancing cold crystallization, enabling the polymer to reorganize into a more crystalline structure during the cooling phase. This behavior aligns with prior studies indicating fiber reinforcement effectively promotes crystal nucleation within polymer blends [50]. However, PLA-75/PETG-25/F-15 shows a marked decrease in melting and cold crystallization, with X_c reduced to 10.09% and X_{cc} to 10.83%. This decline suggests that excessive fiber content can negatively impact crystallization. The likely cause is steric hindrance introduced by the fibers, which restricts the

mobility of polymer chains, limiting their ability to align and form crystalline regions. This observation is consistent with the literature, highlighting that crystallization efficiency diminishes above a certain fiber loading threshold due to restricted chain mobility and increased fiber-polymer interactions [50].

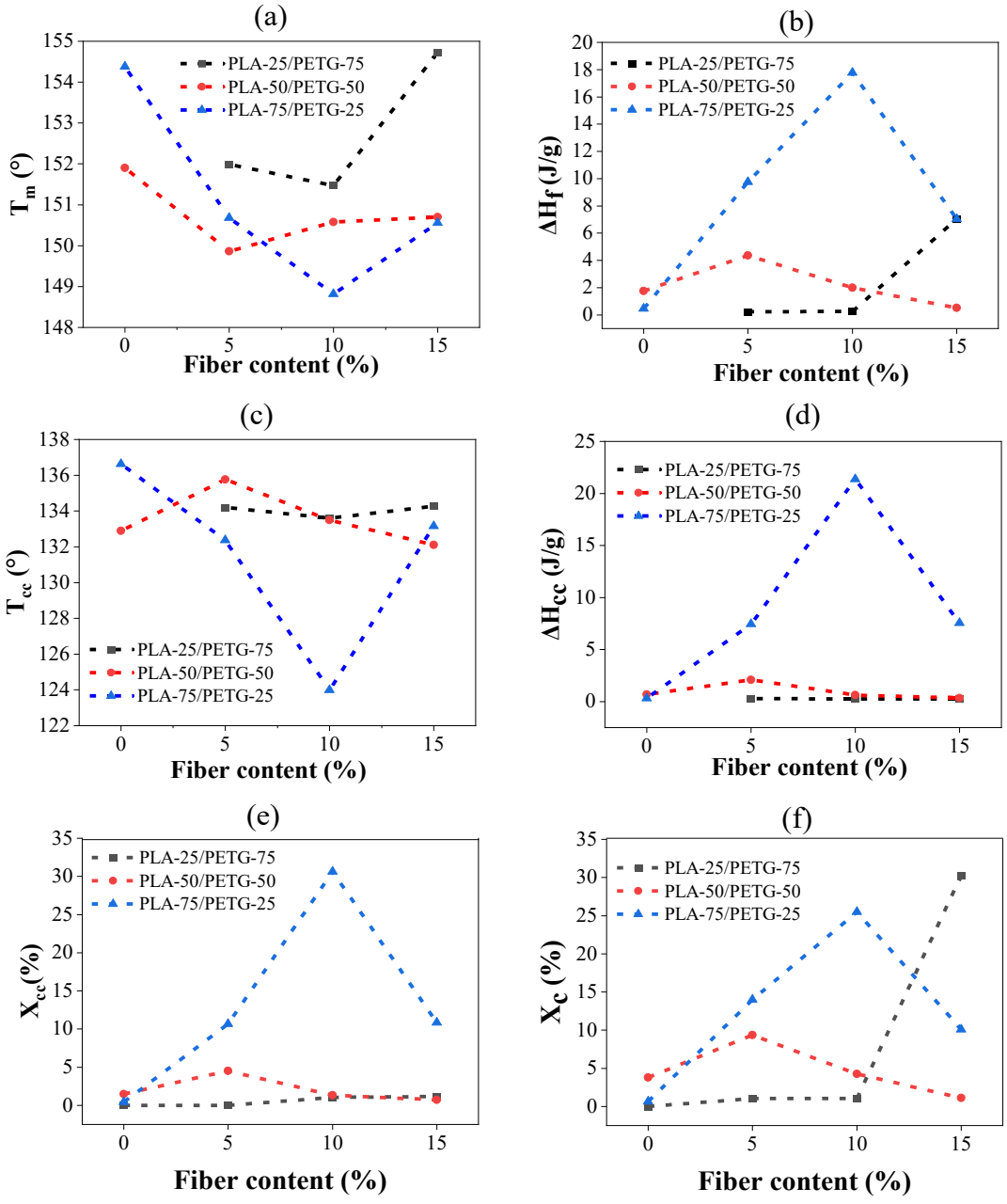

Figure 5.4: (a): Melting temperature T_m, (b): Enthalpy of fusion ΔH_m, (c): Cold crystallization temperature T_{cc}, and (d): Enthalpy of cold crystallization ΔH_{cc} , Cold crystallinity X_{cc} , Crystallinity X_c as a function of flax fiber content.

5.4.2 Shape memory performances

5.4.2.1 Overview of cycling performance

Several studies have demonstrated that fiber-reinforced shape memory polymer composites maintain excellent performance over multiple thermo-mechanical cycles. Quadrini et al. [51] reported that carbon fiber-reinforced laminates with SMP interlayers exhibited stable behavior over 10 successive cycles, achieving an average shape recovery of 98% with no signs of delamination or cracking. Similarly, Korotkov et al. [52] found that glass fiber-reinforced pultruded epoxy laminates maintained shape fixity ratios up to 99.7% and recovery ratios of 98.2% across 10 cycles, depending on fiber orientation.

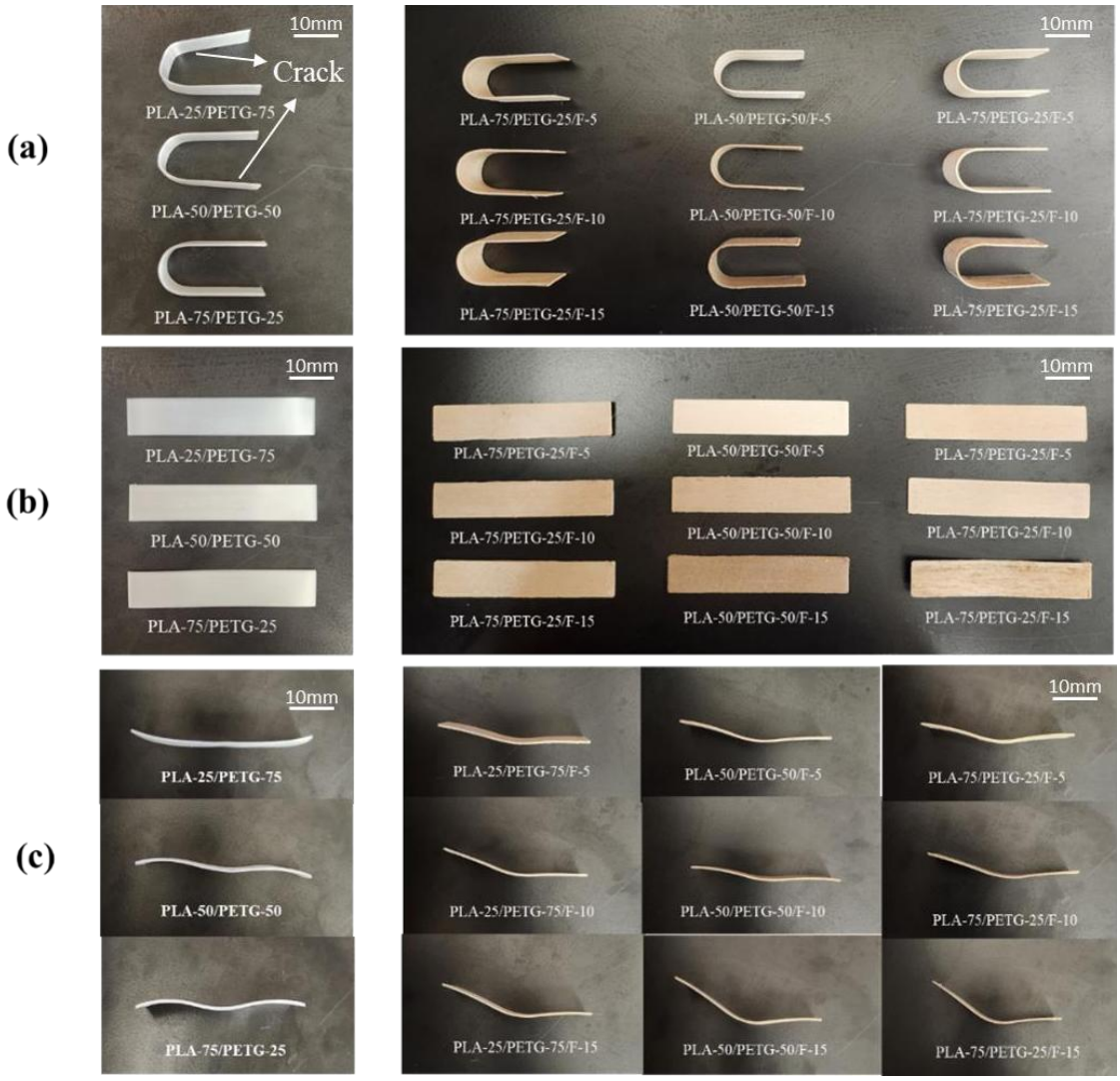

Figure 5.5: Illustrations of the shape memory performance of PLA/PETG polymer blends and flax fiber-reinforced PLA/PETG polymer blends, showing (a) Shape fixity, (b) Shape recovery after 1 cycle, and (c) Shape recovery after 10 cycles.

Woven fabric-reinforced composites also showed strong cyclic durability; Ming et al. [53] reported that these composites retained over 98% shape recovery and 90% fixity even under repeated actuation, with twill weaves offering the best balance of strength and recovery. In addition, Huang et al. [54] demonstrated that glass fiber-epoxy composites treated with silane coupling agents preserved excellent shape memory performance after 10 cycles, with faster recovery speeds and improved recovery forces due to enhanced interfacial bonding. These findings highlight the reliability and durability of fiber-reinforced SMP composites for repeated shape-changing applications. Inspired by these studies, we investigated the durability of 4D-printed flax fiber-reinforced PLA/PETG shape memory polymer blends, as no standardized evaluation has yet been conducted for these specific materials.

Figure 5.5 illustrates the shape memory performance of PLA/PETG blends and flax fiber-reinforced composites, focusing on shape fixity and recovery after one cycle and across multiple cycles. Among the blends, PLA-75/PETG-25 stands out for its superior shape fixity and recovery, demonstrating excellent performance even after repeated cycles, as reported in Figure 5.6. These characteristics make it suitable for applications requiring reliable and repeated shape memory functionality.

In contrast, PLA-25/PETG-75 and PLA-50/PETG-50 blends show good initial shape recovery at 90°C but are prone to crack formation during the temporary shape programming. This compromise in structural integrity may affect their durability under repeated use, limiting their suitability for high-cycle applications.

The incorporation of flax fibers significantly enhances shape retention due to the added rigidity they provide. However, this comes at the cost of slightly reduced shape recovery, particularly at higher fiber content levels and after multiple cycles. The reduced recovery is attributed to the fibers restricting the flexibility of the polymer matrix, which impairs the material's ability to return fully to its original shape. Despite this trade-off, PLA-rich, fiber-reinforced composites strike an effective balance between stability and partial shape memory recovery, making them ideal for applications where fixed shapes are prioritized over complete recovery. These results are explored in greater detail in subsequent sections.

Figure 5.6 presents the shape memory performance of three PLA/PETG blends, PLA-25/PETG-75, PLA-50/PETG-50, and PLA-75/PETG-25, and their composites over 10 successive cycles at 90°C. Key metrics include shape fixity (S_f %), shape recovery (S_r %), and the time required for shape

recovery. Additionally, Figure 5.6 (d) illustrates the percentage of shrinkage in length after 10 cycles, providing insights into the dimensional stability of the samples under repeated thermal cycling.

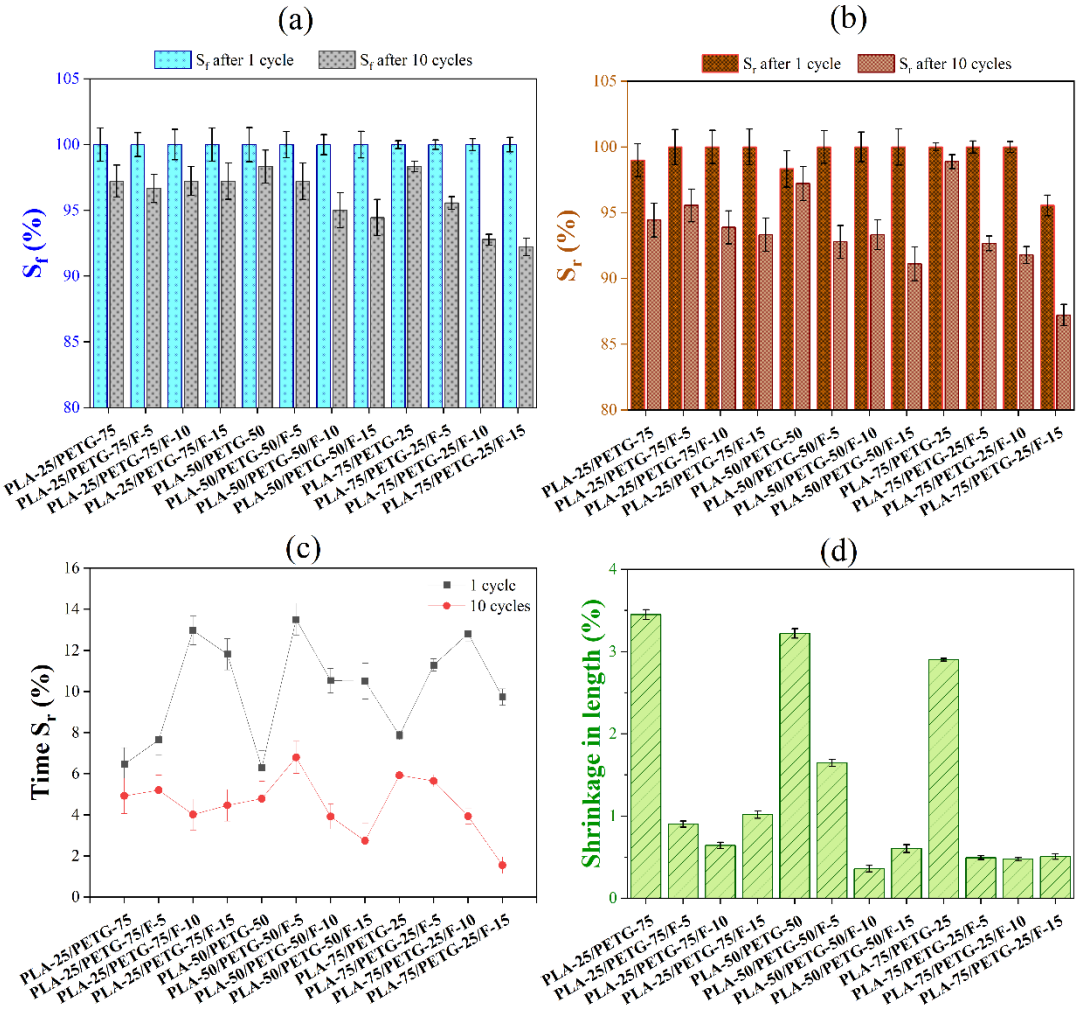

Figure 5.6: Shape Memory Performance of PLA/PETG Blends and Flax Fiber-Reinforced PLA/PETG Blends with (a): Shape fixity (S_f), (b): shape recovery (S_r), (c): Recovery time after 1 and 10 cycles of shape memory testing at 90°C. (d): Percentage shrinkage in length after 10 repeated cycles.

5.4.2.1.1 PLA-75/PETG-25 Polymer blend

As the PLA-25/PETG-75 blend shows a gradual decrease in shape fixity, declining from 100% in the first cycle to approximately 98.5% after 10 cycles, as depicted in Figure 5.6 (a). This decrease indicates a notable reduction in its ability to retain the programmed shape over repeated use. In

contrast, the PLA-50/PETG-50 blend demonstrates more stable shape fixity, fluctuating slightly around 99.5% over 10 cycles, reflecting better stability than PLA-25/PETG-75. Meanwhile, PLA-75/PETG-25 exhibits the highest shape fixity, maintaining close to 100% across all cycles, highlighting its superior ability to preserve the deformed shape consistently.

The superior performance of PLA-75/PETG-25 can be attributed to its higher PLA content, as PLA's semicrystalline nature enhances shape memory properties. The higher crystallinity of this blend, as evidenced by DSC results in Section III.1, enables better retention of the deformed shape over multiple cycles [35]. Conversely, the higher PETG content in PLA-25/PETG-75 increases amorphous regions within the blend, diminishing its capacity to maintain shape fixity under repeated thermal stress.

Regarding shape recovery, PLA-25/PETG-75 exhibits a noticeable decline from approximately 99% in the first cycle to below 96% by the 10th cycle. This decrease can be attributed to the high PETG content, which is amorphous and reduces the blend's ability to fully recover its original form. In comparison, PLA-50/PETG-50 demonstrates better shape recovery, maintaining around 98% for the first five cycles before gradually declining to 97% by the 10th cycle. The highest shape recovery is observed in the PLA-75/PETG-25 blend, which remains close to 100% across all 10 cycles, highlighting its superior resilience and ability to return to its original shape.

The excellent recovery performance of PLA-75/PETG-25 can be attributed to its higher PLA content, which promotes the formation of more crystalline regions critical for shape memory recovery. These crystalline domains act as "memory zones" that enable the material to revert to its original shape, even after repeated cycles. This finding aligns with existing studies, which consistently show that PLA-rich blends, such as PLA-75/PETG-25, exhibit superior shape memory performance due to their ability to maintain structural integrity and crystalline regions under repeated deformation [55].

The shape recovery time, a key parameter for evaluating the performance of shape memory polymers (SMPs), also varies among the blends. As shown in Figure 5.6 (c), PLA-75/PETG-25 demonstrates the slowest recovery times, particularly in the earlier cycles, ranging from 8s to 6s. While recovery time slightly decreases over subsequent cycles, it remains slower than the other blends throughout the 10 cycles.

The initial higher recovery time observed in the PLA-75/PETG-25 blend can be attributed to its higher crystallinity, which creates a more rigid structure that requires more time to recover from deformation. Over multiple cycles, repeated thermal-mechanical cycling likely results in a slight reduction in crystallinity or the release of internal stresses, leading to a marginal improvement in recovery time. This trend is consistent with findings in the literature, which indicate that blends with higher PLA content exhibit increased crystallinity and reduced chain mobility, contributing to slower shape recovery times [56]. In contrast, blends with higher PETG content, such as PLA-25/PETG-75, exhibit faster recovery times due to their greater elasticity and higher chain mobility, facilitating quicker deformation and recovery. The amorphous nature of PETG provides flexibility and a more responsive structure, allowing the material to recover its shape more rapidly. As demonstrated in our previous study, blends with higher PETG content show improved elasticity and an enhanced ability to respond to shape deformation [40].

Across all blends, the shape recovery time decreases slightly over the 10 cycles. This reduction suggests that repeated thermal cycling relaxes internal stresses or modifies the polymer microstructure, allowing faster recovery. This behavior is characteristic of shape memory polymers (SMPs), where repetitive thermal and mechanical activation can lead to microstructural adjustments, such as reduced crystallinity or changes in polymer chain alignment, thereby enhancing recovery performance over time [56].

Shrinkage in length after multiple cycles reflects the material's ability to maintain its original dimensions despite repeated deformation and recovery. In this study, PLA-25/PETG-75 shows the highest shrinkage after 10 cycles, at approximately 3.5%, as illustrated in Figure 5.7. This pronounced shrinkage can be attributed to the higher PETG content, which introduces more amorphous behavior into the blend. Amorphous materials are less structurally stable and more susceptible to dimensional changes under repeated thermal cycling. Prior research corroborates that shrinkage tends to be more significant in blends with lower crystallinity, as the absence of crystalline regions reduces structural support and increases the likelihood of permanent deformation [40].

The current shape memory results align with those reported in our previous study [38], confirming that PLA-rich PLA/PETG blends exhibit high shape fixity, excellent recovery, and low shrinkage due to increased crystallinity. Although slight differences exist due to processing conditions, the

overall performance trends are consistent, supporting the reliability of these materials for shape memory applications.

In contrast, PLA-50/PETG-50 demonstrates slightly less shrinkage at around 3.2%, indicating that the balance between amorphous and crystalline regions in this blend provides moderate dimensional stability. Meanwhile, PLA-75/PETG-25 exhibits the least shrinkage, with values slightly above 2.9%. The higher PLA content in this blend contributes to the formation of stable crystalline regions, which resist permanent deformation and enhance dimensional stability. This result aligns perfectly with the findings from DSC analysis, which demonstrated higher crystallinity in PLA-rich blends. The presence of these crystalline domains provides the structural integrity needed to minimize shrinkage during repeated thermal-mechanical cycles.

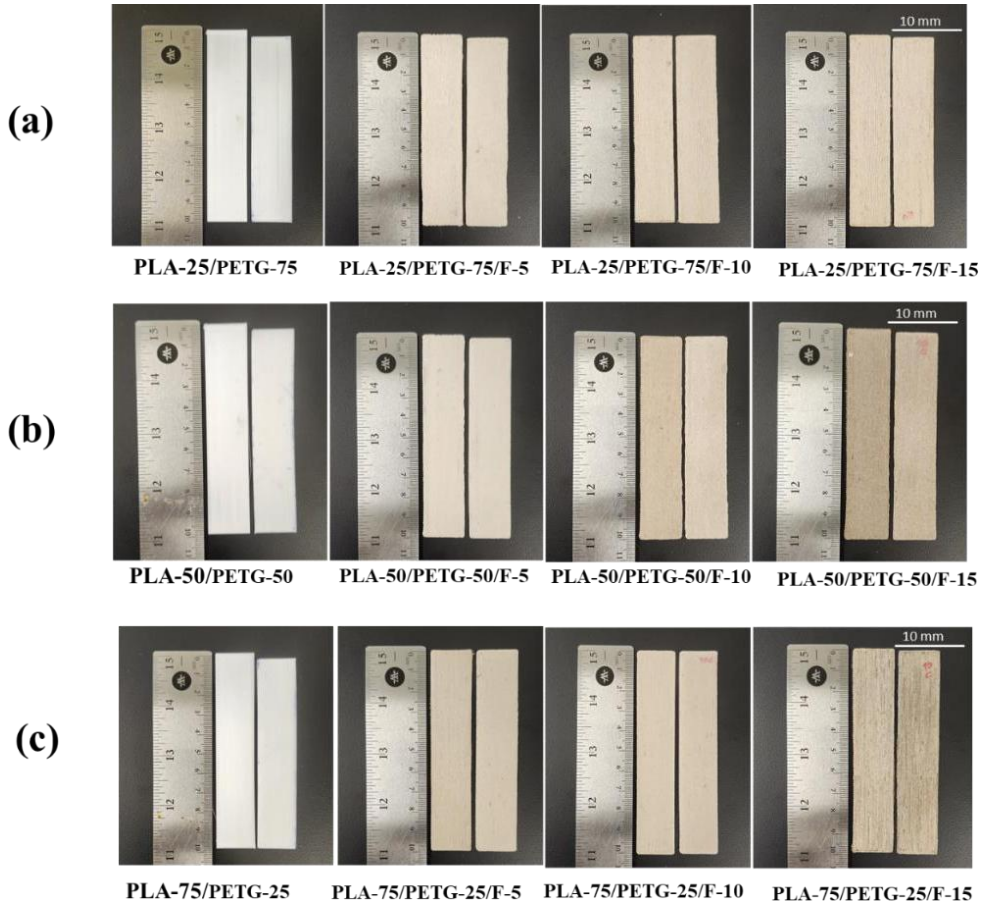

Figure 5.7: Illustration of length shrinkage in (a) PLA-25/PETG-75 polymer blend and its flax fiber-reinforced composites, (b) PLA-50/PETG-50 polymer blend and its flax fiber-reinforced composites, (c) PLA-75/PETG-25 polymer blend and its flax fiber-reinforced composites.

According to Mishra and Das [57], shrinkage occurs as a result of structural rearrangement within the sample. This rearrangement is brought about by the thermal release of this stored internal strain, which is stored in the polymer as orientational entropy and manifests itself as shrinkage.

5.4.2.1.2 Flax fiber-reinforced PLA-25/PETG-75 polymer blends

As depicted in Figure 5.6, the incorporation of flax fibers at 5% and 10% into the PLA-25/PETG-75 blend has a noticeable positive impact on shape fixity and recovery. At 5% flax fiber content, the blend achieves 100% shape fixity and recovery for the first seven cycles, outperforming the unreinforced PLA-25/PETG-75 polymer blend. This enhancement is attributed to the mechanical reinforcement provided by the flax fibers, which improve stress distribution and limit chain relaxation within the polymer matrix [58]. Additionally, flax fiber reinforcement at a lower concentration helps maintain elastic deformation, preventing excessive flow or permanent deformation of the polymer chains, thereby supporting better shape recovery. However, as the fiber content increases or the number of cycles increases, this improvement diminishes. Higher fiber content increases rigidity, limiting chain mobility and leading to mechanical fatigue over successive cycles.

Figure 5.6 (c) illustrates the effect of flax fiber reinforcement on the shape recovery time of PLA-25/PETG-75 blends over multiple cycles. The unreinforced PLA-25/PETG-75 blend demonstrates the shortest and most consistent recovery time, maintaining approximately 4-5 seconds across all cycles. In contrast, the PLA-25/PETG-75/F-5 blend starts with a slightly longer recovery time of about 8 seconds in the first cycle, gradually decreasing to approximately 5 seconds by the 10th cycle. This improvement suggests that the fibers may contribute to initial resistance but eventually allow better recovery performance as the material undergoes repeated thermal-mechanical cycling. For PLA-25/PETG-75/F-10, the initial recovery time is significantly higher at around 13 seconds but decreases to approximately 4 seconds by the 10th cycle. This trend may reflect a stabilization effect where the fiber reinforcement initially adds rigidity, but over successive cycles, the polymer-fiber matrix undergoes slight relaxation, leading to improved recovery times. Similarly, PLA-25/PETG-75/F-15 shows a high initial recovery time of about 12 seconds, which decreases slightly to around 5 seconds by the final cycle. This behavior aligns with findings in the literature that natural fiber reinforcement enhances mechanical stability but can restrict elastic recovery due to increased stiffness [59]. The gradual reduction in recovery time over cycles, particularly at higher

fiber contents, suggests that repeated cycling induces minor fatigue or relaxation at the fiber-polymer interface, allowing the material to recover more efficiently in later cycles. This highlights the complex interplay between fiber reinforcement, polymer matrix behavior, and shape memory performance over repeated use.

Based on Figure 5.6 (d), the addition of flax fibers significantly reduces shrinkage in the PLA-25/PETG-75 blend after 10 thermal cycles, with higher fiber content (10%) providing the most pronounced reduction. This decrease in shrinkage highlights the reinforcing role of flax fibers in stabilizing the polymer matrix. Flax fibers act as structural stabilizers, limiting the contraction and expansion of the polymer during thermal cycling. Their stiffness and inherent structural integrity help resist deformation, maintaining the composite's dimensional stability. These results align with findings in other studies, which have shown that natural fiber reinforcement reduces shrinkage in polymer composites by enhancing their resistance to thermal and mechanical deformation. By introducing flax fibers into the polymer matrix, the composite gains improved rigidity and reduced susceptibility to dimensional changes, making it more suitable for applications requiring long-term stability under repeated thermal cycling [60].

5.4.2.1.3 Flax fiber-reinforced PLA-50/PETG-50 polymer blends

For shape fixity, the 15% fiber-reinforced blend demonstrated superior performance during the first cycles, maintaining 100% fixity, while all fiber-reinforced samples displayed gradual declines over repeated cycles. Specifically, the 5% fiber blend decreased slightly from 100% to 97% by the 10th cycle, while the 10% fiber blend dropped from 100% to 94%. Similarly, the 15% fiber blend, despite its initial stability, also decreased from 100% to 94% over time. The initial advantage of 15% reinforcement suggests enhanced structural support provided by the increased stiffness of the matrix, although this benefit diminishes with repeated cycles as chain mobility becomes restricted. These findings align with previous studies indicating that natural fibers enhance mechanical properties early on but may impede flexibility with prolonged use [61].

In terms of shape recovery, as shown in Figure 5.6 (b), the unreinforced PLA-50/PETG-50 blend maintained nearly perfect recovery (~98%) across all cycles. In contrast, the addition of 5%, 10%, and 15% flax fibers initially improved recovery performance but exhibited gradual declines. Recovery values for the fiber-reinforced blends started at 97%, 96%, and 95%, respectively, but

decreased to 92%, 93%, and 91% by the 10th cycle. The early enhancement in recovery can be attributed to the flax fibers' ability to distribute stress uniformly within the matrix, promoting effective shape retention. However, as cycles progress, the increased rigidity associated with higher fiber content limits the polymer chains' ability to return fully to their original shape [62].

Recovery times, depicted in Figure 5.6 (c), were initially longer in fiber-reinforced blends due to the increased rigidity introduced by the flax fibers. During the first cycle, recovery times for PLA-50/PETG-50/F-5, PLA-50/PETG-50/F-10, and PLA-50/PETG-50/F-15 ranged between 14 s and 10 s. Over successive cycles, these recovery times decreased to 7 s, 4 s, and 3 s, respectively, by the 10th cycle. This reduction may be due to relaxation at the fiber-matrix interface or minor fatigue in the rigid structure, resulting in slight improvements in flexibility over time [63].

Regarding dimensional stability, as shown in Figure 5.6 (d), flax fiber reinforcement significantly reduced shrinkage after 10 cycles. The unreinforced blend exhibited approximately 3% shrinkage, while the addition of 5%, 10%, and 15% flax fibers reduced this to 1.6%, 0.4%, and 0.6%, respectively. The blend with 10% flax fibers achieved the most substantial reduction in shrinkage, suggesting that flax fibers enhance stability by resisting deformation and providing structural reinforcement to the polymer matrix.

5.4.2.1.4 Flax fiber-reinforced PLA-75/PETG-25 polymer blends

As illustrated in Figure 5.6, the lower variability in results observed in the PLA-75/PETG-25 blend and its composites indicates greater stability and homogeneity than the other compositions. On the other hand, the PLA-75/PETG-25 sample without flax fibers (0% flax) achieves the highest initial shape fixity, starting near 100% and decreasing marginally to approximately 98% by the 10th cycle. In comparison, samples reinforced with 5%, 10%, and 15% flax fibers also begin at 100% but experience more pronounced declines, reaching 96%, 93%, and 92%, respectively, after 10 cycles. These findings suggest that increasing flax fiber content diminishes shape fixity over repeated cycles. This reduction is likely attributed to the additional rigidity introduced by the fibers, which limits the polymer chain mobility required for effective shape fixation [63].

For shape recovery (S_r), as shown in Figure 5.6 (b), the neat PLA-75/PETG-25 sample exhibits exceptional performance, maintaining nearly 100% recovery throughout most cycles. With flax

fiber reinforcement, the samples containing 5% and 10% flax demonstrate complete recovery (100%) during the first cycles but gradually decline to 93% and 92%, respectively, by the 10th cycle. In contrast, the 15% flax-reinforced sample starts at a slightly lower initial recovery of 96%, which declines further to 88% after 10 cycles. These results indicate that while flax fibers improve recovery in the initial cycles, higher fiber content impacts long-term recovery performance, with lower flax content retaining better shape recovery properties.

Regarding shape recovery time, as depicted in Figure 5.6 (c), the 0% flax composite recovers most quickly, taking approximately 8 seconds in the first cycle. In comparison, flax-reinforced samples exhibit longer initial recovery times, with the 15%, 5%, and 10% flax composites requiring 10 seconds, 11 seconds, and 13 seconds, respectively, in the first cycle. Recovery times decrease consistently over successive cycles, reaching 6 seconds for PLA-75/PETG-25 and PLA-75/PETG-25/F-5, 4 seconds for PLA-75/PETG-25/F-10, and as low as 1 second for PLA-75/PETG-25/F-15 by the 10th cycle. The extended recovery time in fiber-reinforced samples during early cycles can be attributed to increased rigidity from fiber reinforcement. However, repeated cycles reduce recovery times slightly, possibly due to material adaptation to cyclic stress [60, 63].

In terms of shrinkage in length after 10 cycles, the 0% flax composite demonstrates the highest shrinkage, approximately 3%, indicating significant dimensional instability. Conversely, flax-reinforced samples show significantly reduced shrinkage, with values around 0.5%, highlighting their superior dimensional stability. This stabilization effect from flax fibers aligns with findings in Figure 5.6 (c) and can be attributed to the structural reinforcement provided by the fibers, which resist thermal and mechanical deformation.

Based on the above analysis, the shape memory performance observed in this study aligns well with previous research on fiber-reinforced shape memory polymer composites, which have demonstrated strong performance over multiple thermo-mechanical cycles. For example, the PLA-75/PETG-25 blend and its flax-reinforced counterparts achieved shape fixity and recovery levels exceeding 90% across 10 cycles, comparable to the 98–99.7% fixity and 98% recovery observed in carbon and glass fiber-reinforced SMPs reported by Quadrini et al. [51], Korotkov et al.[52], and Ming et al. [53]. In addition, the flax-reinforced blends showed a more pronounced trade-off between dimensional stability and recovery efficiency, particularly at higher fiber contents,

highlighting the unique behavior of natural fiber reinforcement. Despite this, the flax fiber-reinforced PLA/PETG blends maintained competitive performance and durability, underscoring their promise as sustainable alternatives for 4D-printed shape memory applications, where no standardized benchmarks yet exist for such biocomposite systems.

5.4.3 Mechanical properties

The mechanical performance of PLA/PETG blends is significantly influenced by both the matrix composition and the flax fiber content. As seen in Figure 5.8 (a), PETG-rich blends, particularly PLA-25/PETG-75, exhibit the most ductile behavior, as indicated by high elongation at break and smooth stress-strain profiles. This ductility is attributed to the inherent flexibility of PETG, which reduces the brittleness of PLA when blended [64]. However, when flax fibers are added, especially at 15%, the mechanical behavior becomes more brittle, with decreased strain and earlier fracture. This is due to the introduction of stress concentration sites by the fibers, which compromise ductility [65].

The unreinforced blend exhibits transitional behavior in balanced formulations like PLA-50/PETG-50, combining moderate strength and ductility. The addition of flax fibers at 5–10% slightly enhances stiffness while maintaining reasonable ductility. However, at 15% fiber content, these blends shift to a brittle failure mode, characterized by abrupt stress drops and reduced elongation. This transition is typical of immiscible or partially compatible systems, where fiber overload disrupts stress distribution [66].

PLA-rich blends, such as PLA-75/PETG-25, are inherently stiff and brittle, even though the addition of PETG slightly improves flexibility. This agrees with studies showing PLA's brittle nature and PETG's role in modifying it [67]. The addition of flax fibers to this matrix, particularly at 15%, further intensifies the brittleness, leading to early fracture and minimal strain. This is attributed to poor energy dissipation and increased crack propagation potential, as supported by fracture mechanics studies on PLA composites [68]. As illustrated in Figure 5.8 (b), the PLA-75/PETG-25 blend exhibits the highest tensile stress among the tested samples, reaching approximately 60 MPa. This superior stress resistance is attributed to the high PLA content, which is known for its higher tensile strength compared to PETG [38]. These results suggest that PLA-rich blends are particularly well-suited for applications demanding high tensile strength. The addition of flax fibers generally enhances stiffness due to their inherent rigidity. The PLA-75/PETG-25/F-10 composite achieves an optimal balance between stiffness and

flexibility, with a Young's modulus of approximately 4 GPa, making it suitable for load-bearing applications. This performance is consistent with findings from natural fiber-reinforced PLA composites, where tensile strengths range from 40–55 MPa and moduli from 3.5–6 GPa, depending on fiber loading and dispersion quality [69, 70]. The observed increase in crystallinity in PLA-75/PETG-25/F-10 (X_c = 25.48%, X_{cc} = 30.64%) as observed in the DSC results likely contributes to its improved tensile properties, as natural fibers are known to act as nucleating agents that enhance structural order [71].

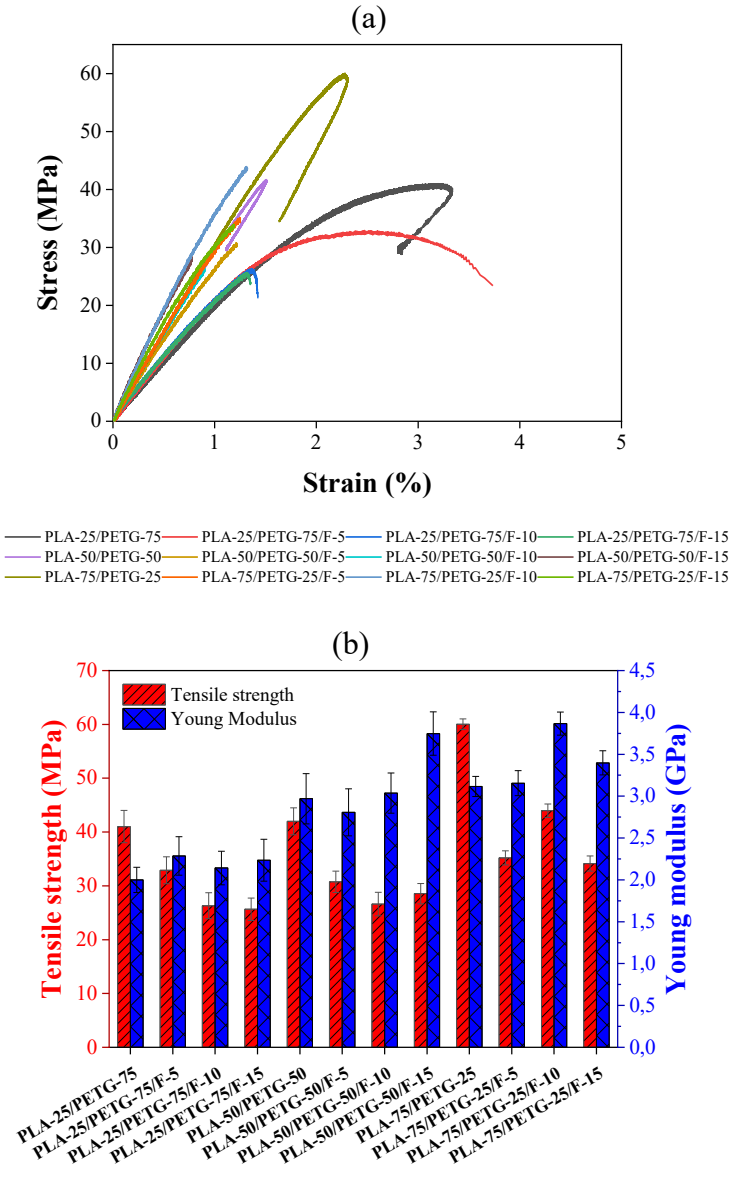

Figure 5.8: (a) Tensile performance of PLA/PETG blends and flax fiber-reinforced PLA/PETG composites, (b) Comparison of mechanical properties (stress and Young's modulus) for PLA/PETG blends and flax fiber-reinforced composites.

However, increasing fiber content to 15% slightly reduces tensile strength from 44 MPa to 34 MPa, likely due to interfacial bonding issues and poor fiber dispersion. These effects have been widely reported in the literature [72-74], where high fiber loadings lead to agglomeration, voids, and stress concentration zones, ultimately reducing mechanical performance [75-79]. In our case, flax fiber at 15% disrupted the polymer flow during thermokinetic mixing, causing inter-yarn voids, as will be further illustrated in the SEM analysis.

Conversely, the PLA-25/PETG-75 blend demonstrates lower mechanical properties, with a tensile stress of approximately 41 MPa and a Young's modulus of 2 GPa. While the higher PETG content improves ductility, it compromises overall strength and stiffness, which aligns with previous studies [80]. Adding flax fiber to this blend slightly increases Young's modulus (2.28 GPa for PLA-25/PETG-75/F-5), though it reduces tensile strength due to weak interfacial adhesion.

The PLA-50/PETG-50 blend achieves a moderate tensile stress of around 41 MPa and a Young's modulus of 3 GPa, offering a balanced compromise between PLA's rigidity and PETG's ductility. This composition is ideal for semi-structural applications requiring flexibility and mechanical integrity, as shown in existing literature [38]. Reinforcing this blend with flax fibers increases stiffness (up to 3.7 GPa at 15% fiber). However, tensile strength drops to approximately 28 MPa due to possible debonding and fiber pull-out under mechanical loading.

The mechanical properties of the unreinforced PLA/PETG blends obtained in this study, particularly the higher tensile strength and stiffness observed for PLA-75/PETG-25, are slightly improved compared to those reported in our previous work [38]. These enhancements are mainly attributed to using a different 3D printer (Ultimaker) and optimized printing parameters, resulting in better printing quality and improved mechanical performance.

Overall, the mechanical trends observed in this study strongly agree with prior work on natural fiber-reinforced polymer composites. Yet, they offer new insights into flax fiber-reinforced PLA/PETG blend materials for which standardized benchmarks are still lacking, particularly in the context of 4D printing and shape memory behavior.

5.4.4 Scanning Electron Microscopy observations

As illustrated in Figure 5.9 (a), the fracture surface of the PLA-75/PETG-25 polymer blend displays a relatively smooth structure with clear, deposited filaments. The continuous and uniform filament deposition suggests ductile behavior with some plastic deformation at the fracture site, aligning

with the earlier mechanical results. This behavior is typical of a neat polymer blend without reinforcement, where the absence of fibers or significant pores contributes to a more homogeneous fracture surface.

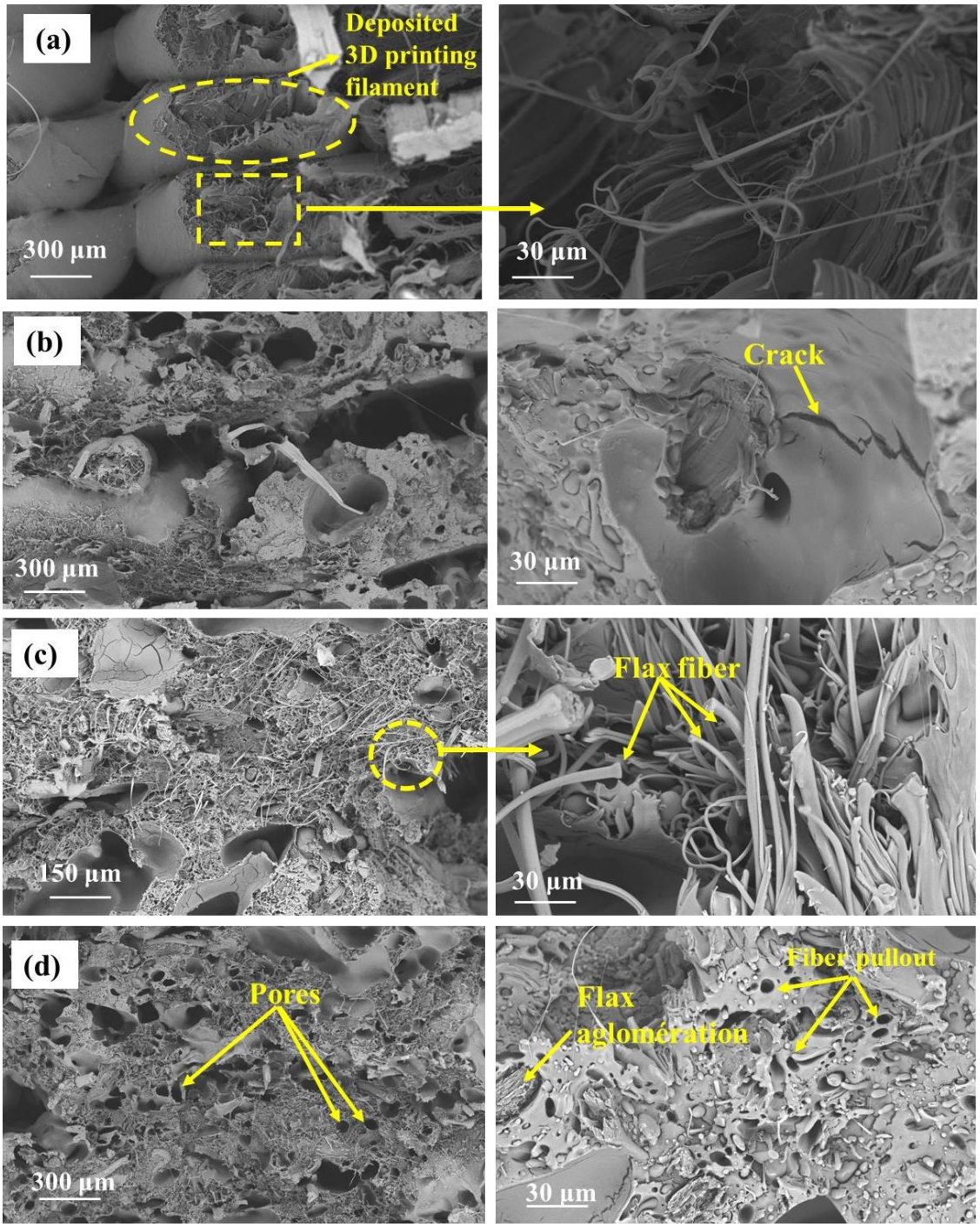

Figure 5.9: SEM images of tensile fractured surface of (a) PLA-75/PETG-25 polymer blend, (b) PLA-75/PETG-25/F-5, (c) PLA-75/PETG-25/F-10 and (d) PLA-75/PETG-25/F-15.

In contrast, irregularities such as cracks are visible on the fractured surface of the PLA-75/PETG-25/F-5 composite, as shown in Figure 5.9 (b). The presence of matrix cracks likely arises from stress concentration points introduced by the addition of flax fibers, which can create localized weak spots. The slightly increased brittleness compared to the neat polymer blend reflects the influence of flax fibers, which can reduce ductility in the polymer matrix, particularly at lower fiber content levels where fiber distribution may be less uniform. This aligns with typical behavior observed in fiber-reinforced composites, where reinforcement often improves stiffness but may compromise ductility.

The fractured surface of the PLA-75/PETG-25/F-10 composite, depicted in Figure 5.9 (c), reveals more prominent flax fibers embedded in the matrix. These fibers are partially exposed on the fracture surface, indicating fiber pull-out or fiber-matrix debonding occurrences. The heterogeneous structure, with regions containing visible fibers, reflects a balance between improved stiffness and strength due to fiber reinforcement and increased susceptibility to crack propagation. These findings are consistent with research by Kanakannavar & Pitchaimani [81], which demonstrated that higher fiber content enhances stiffness and leads to more brittle failure modes if the interfacial adhesion between fibers and the matrix is not optimized.

The fracture surface of the PLA-75/PETG-25/F-15 composite, illustrated in Figure 51 (d), exhibits the highest concentration of pores and fiber-related features. Flax fibers are visible in clusters, with signs of fiber pull-out indicating weak interfacial bonding. The presence of pores and fiber agglomerations suggests challenges in achieving uniform fiber dispersion and strong adhesion in the polymer matrix. These imperfections contribute to stress concentration points, increasing the composite's vulnerability to crack initiation and propagation under tensile stress. Similar observations were reported by Habibi et al. [17], who noted that voids in flax fiber composites were linked to reduced mechanical strength due to their role as stress concentrators.

In summary, the fracture surface analysis highlights the progressive impact of flax fiber reinforcement on the mechanical behavior and failure modes of PLA/PETG composites. While moderate fiber content (10%) balances reinforcement and structural integrity, higher fiber content (15%) introduces significant defects, including pores and agglomerations, compromising the composite's mechanical performance.

5.4.5 4D Printing of Anti-tri-chiral structures based on Flax fiber-reinforced PLA/PETG blend

Figure 5.10 highlights the potential of 4D-printed anti-tri-chiral auxetic structures made from flax fiber-reinforced PLA/PETG polymer blends. This structure offers significant advantages in weight reduction, dimensional stability, thermal adaptability, and environmental sustainability. The shape memory behavior observed in Figure 5.10 (a, b, and c) demonstrates the ability of these 4D-printed auxetic materials to revert to their original configurations after 55 % deformation at 93°C. Indeed, shape recovery rates of 99.27%, 91.32%, and 91.34% were reported for PLA-75/PETG-25, PLA-75/PETG-25/F-5, and PLA-75/PETG-25/F-10, respectively, highlighting their suitability for adaptive applications. This shape recovery property is critical for dynamic environments where materials must adapt to changing conditions, such as automotive interiors or aerospace components [82].

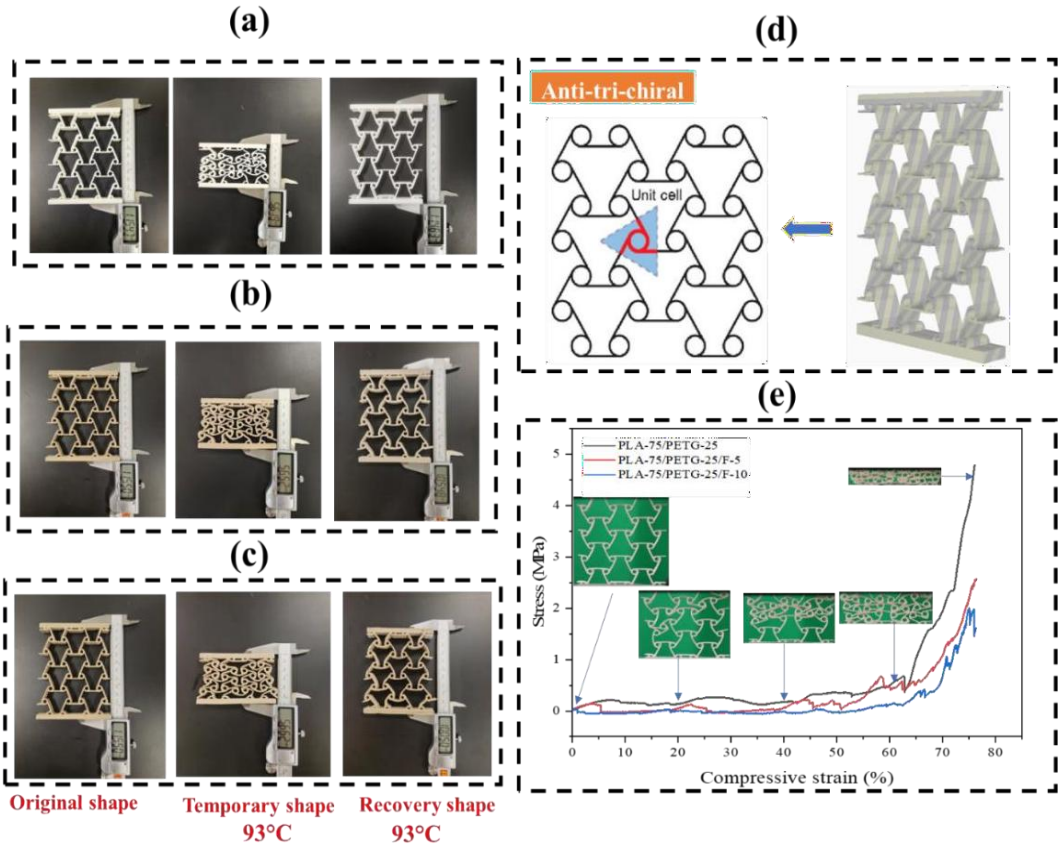

Figure 5.10: Images illustrating the shape memory behavior of anti-tri-chiral auxetic structures made from (a) PLA-75/PETG-25 blend, (b) PLA-75/PETG-25/F-5 and (c) PLA-75/PETG-25/F-10. (d) Schematic representation of the anti-tri-chiral unit cell. (e Mechanical properties of the different auxetic structures, comparing the PLA-75/PETG-25 polymer blend with fiber-reinforced PLA-75/PETG-25 composites.

As shown in Figure 5.10 (e), the compressive behavior of anti-tri-chiral auxetic structures with different fiber contents reveals distinct mechanical responses. In the initial linear elastic phase (0–10% strain), all samples exhibit a proportional increase in stress with strain. However, the stiffness varies with fiber content, with PLA-75/PETG-25 showing the highest initial modulus, while 5% and 10% fiber-reinforced polymer blends demonstrate slightly lower stiffness. The plateau phase (~10–50% strain) is characterized by progressive cell wall buckling, where fiber reinforcement helps stabilize deformation. The energy absorbed during compression, calculated as the area under the stress-strain curve, is 3.22 J/m^3 for PLA-75/PETG-25, 1.74 J/m^3 for PLA-75/PETG-25/F-5 and 1.12 J/m^3 for PLA-75/PETG-25/F-10, confirming that fiber reinforcement slightly decreases the energy dissipation and reduces peak stress resistance. The densification phase (~50–80% strain) shows a sharp increase in stress, where PLA-75/PETG-25 reaches a peak stress of ~5 MPa, whereas PLA-75/PETG-25/F-5 and PLA-75/PETG-25/F-10 reach lower peak stresses (~4 MPa and ~3.5 MPa, respectively), indicating that excessive fiber content weakens the structure. as reported by Hu et al. [83]. Indeed, excessive fiber content can lead to premature failure, leading to a 50% reduction in peak stress due to poor load transfer.

The integration of 4D printing technology enables the valorization of fiber-reinforced PLA/PETG polymer blend auxetic structures across diverse applications, despite the observed decrease in energy dissipation. The shape memory behavior of these materials allows them to recover their original form after deformation, enhancing their adaptability and longevity in dynamic environments. This capability makes them highly versatile for applications requiring shape adaptability, such as automotive interiors, aerospace components, and biomedical devices.

While fiber reinforcement slightly reduces energy dissipation and peak stress resistance, it provides dimensional stability, thermal adaptability, and lightweight structures. Additionally, the use of flax fibers as reinforcement promotes environmental sustainability, reducing reliance on synthetic materials while maintaining structural integrity.

The combination of auxetic properties, 4D shape recovery, and fiber reinforcement unlocks new possibilities for smart materials in energy-efficient transportation, medical supports, and protective gear. Therefore, the application of 4D-printed auxetic composites represents a promising advancement toward adaptive, lightweight, and eco-friendly engineering solutions.

5.5 Conclusions

This study demonstrates that flax fiber-reinforced PLA/PETG polymer blends, particularly the optimized formulation PLA-75/PETG-25 with 10% flax fiber, offer an effective combination of mechanical strength, thermal stability, and shape memory properties, making them ideal for advanced 4D printing applications. Key findings include:

1. **Enhanced Mechanical Performance**: Compared to other flax fiber composites, the PLA-75/PETG-25/F-10 blend exhibited the highest tensile strength (44 MPa) and Young's modulus (4 GPa). This improvement highlights flax fibers' ability to act as effective reinforcements, particularly by enhancing stiffness and load-bearing capacity. The fibers also served as nucleating agents within the PLA matrix, promoting crystallinity and improving thermal stability.

2. **Superior Shape Memory Behavior**: After multiple cycles, the flax fiber-reinforced PLA/PETG blends demonstrated excellent shape memory performance, achieving near-perfect shape fixity (close to 100%) and high shape recovery (~92%). Dimensional stability was significantly enhanced, with shrinkage reduced to below 0.5% after repeated thermal cycles, underlining their suitability for adaptive applications requiring repeated and precise shape transformations.

3. **Sustainability and Eco-friendliness**: Incorporating flax fibers, a biodegradable and renewable resource, reduces the environmental impact of these composites. Combined with PLA, an inherently biodegradable polymer, these materials present a sustainable alternative to conventional synthetic composites for 4D printing.

The lightweight, durable, and adaptable nature of these composites makes them suitable for diverse applications in industries such as automotive, aerospace, and biomedicine. Potential uses include adaptive interior panels, impact-resistant components, and medical devices like shape-transforming braces and bandages, where biodegradability and patient comfort are essential.

Despite these advantages, higher fiber content, such as 15%, was found to reduce shape recovery due to increased rigidity and potential challenges with fiber dispersion and interfacial bonding. Future research could focus on optimizing fiber-matrix interactions, possibly through surface treatments or advanced mixing techniques, to mitigate issues like fiber pull-out and pore formation.

Such advancements could further enhance the mechanical performance, structural integrity, and long-term durability of these composites, broadening their application potential across a broader range of industries.

5.6 Acknowledgement

The authors acknowledge the funding provided by the Natural Sciences and Engineering Research Council (NSERC) of Canada (grant number: CRSNG – RGPIN -2021-02846).

5.7 References

1. Miao, J.-T., et al., Dynamic imine bond-based shape memory polymers with permanent shape reconfigurability for 4D printing. ACS applied materials & interfaces, 2019. 11(43): p. 40642-40651.
2. Zhang, J., et al., Advances in 4D printed shape memory polymers: from 3D printing, smart excitation, and response to applications. Advanced Materials Technologies, 2022. 7(9): p. 2101568.
3. Subash, A. and B. Kandasubramanian, 4D printing of shape memory polymers. European Polymer Journal, 2020. 134: p. 109771.
4. Wang, L., et al., Photosensitive composite inks for digital light processing four-dimensional printing of shape memory capture devices. ACS Applied Materials & Interfaces, 2021. 13(15): p. 18110-18119.
5. Mahmood, A., et al., Revolutionizing manufacturing: A review of 4D printing materials, stimuli, and cutting-edge applications. Composites Part B: Engineering, 2023: p. 110952.
6. Zhou, X., et al., Advances in 3D/4D printing of mechanical metamaterials: From manufacturing to applications. Composites Part B: Engineering, 2023. 254: p. 110585.
7. Megdich, A., M. Habibi, and L. Laperrière, A review on 4D printing: material structures, stimuli and additive manufacturing techniques. Materials Letters, 2023. 337: p. 133977.
8. Megdich, A., et al., Advanced nanocomposites for 4D printing: High-performance electroactive shape memory polymers for smart applications. Applied Materials Today, 2025. 44: p. 102702.
9. Rahmatabadi, D., et al., 4D printing and annealing of PETG composites reinforced with short carbon fibers. Physica Scripta, 2024. 99(5): p. 055957.
10. Rahmatabadi, D., et al., Advancing sustainable shape memory polymers through 4D printing of polylactic acid-polybutylene adipate terephthalate blends. European Polymer Journal, 2024. 216: p. 113289.
11. Ali, S.J., et al., Experimental Evaluation of Mechanical Properties, Thermal Analysis, Morphology, Printability, and Shape Memory Performance of the Novel 3D Printed PETG-EVA Blends. Macromolecular Materials and Engineering, 2024. 309(10): p. 2400069.
12. Rahmatabadi, D., et al., Poly (ethylene terephthalate) glycol/carbon black composites for 4D printing. Materials Chemistry and Physics, 2024. 325: p. 129737.
13. Mirasadi, K., et al., 3D and 4D printing of PETG–ABS–Fe3O4 nanocomposites with supreme remotely driven magneto-thermal shape-memory performance. Polymers, 2024. 16(10): p. 1398.
14. Fallah, A., Q. Saleem, and B. Koc, Assessment of mechanical properties and shape memory behavior of 4D printed continuous fiber-reinforced PETG composites. Composites Part A: Applied Science and Manufacturing, 2024. 181: p. 108165.
15. Le Duigou, A., et al., A review of 3D and 4D printing of natural fibre biocomposites. Materials & Design, 2020. 194: p. 108911.
16. Elfaleh, I., et al., A comprehensive review of natural fibers and their composites: an eco-friendly alternative to conventional materials. Results in Engineering, 2023: p. 101271.
17. Habibi, M., G. Lebrun, and L. Laperrière, Experimental characterization of short flax fiber mat composites: tensile and flexural properties and damage analysis using acoustic emission. Journal of materials science, 2017. 52: p. 6567-6580.
18. Qiu, W., et al., Recent advances in 4D printing of fiber-reinforced polymer composites: A review and outlook. Composites Part B: Engineering, 2024. 283: p. 111645.

19. Sridhara, P.K. and F. Vilaseca, Assessment of fiber orientation on the mechanical properties of PA6/cellulose composite. Applied Sciences, 2020. 10(16): p. 5565.
20. Gopakumar, T. and D. Page, Compounding of nanocomposites by thermokinetic mixing. Journal of Applied Polymer Science, 2005. 96(5): p. 1557-1563.
21. Bischoff, E., et al., Influence of the dispersing agents to obtain polymer–clay nanocomposites processed in two-steps using thermokinetic mixer. Journal of Materials Science, 2020. 55(15): p. 6537-6550.
22. Özen, İ., et al., Comparison of melt extrusion and thermokinetic mixing methods in poly (ethylene terephthalate)/montmorillonite nanocomposites. Polymer Engineering & Science, 2012. 52(7): p. 1537-1547.
23. Lazarini, R.G. and J.M. Marconcini, Sugarcane bagasse fibers at high contents in thermoplastic composites: A novel approach using agro-industrial residue via thermokinetic mixing. Polymer Composites, 2021. 42(9): p. 4860-4871.
24. Costa, I.L., N.C. Zanini, and D.R. Mulinari, Thermal and mechanical properties of HDPE reinforced with Al2O3 nanoparticles processed by thermokinectic mixer. Journal of Inorganic and Organometallic Polymers and Materials, 2021. 31(1): p. 220-228.
25. Ming, R., et al., Flax fiber-reinforced polylactide stereocomplex composites with enhanced heat resistance and mechanical properties. Polymer Composites, 2017. 38(3): p. 472-478.
26. Nassiopoulos, E. and J. Njuguna, Thermo-mechanical performance of poly (lactic acid)/flax fibre-reinforced biocomposites. Materials & Design, 2015. 66: p. 473-485.
27. Lafranche, E., et al., Prediction of tensile properties of injection moulding flax fibre reinforced polypropylene from morphology analysis. Key Engineering Materials, 2013. 554: p. 1573-1582.
28. Basit, A., G. L'Hostis, and B. Durand, Multi-shape memory effect in shape memory polymer composites. Materials Letters, 2012. 74: p. 220-222.
29. Westbrook, K.K., et al., Two-way reversible shape memory effects in a free-standing polymer composite. Smart Materials and Structures, 2011. 20(6): p. 065010.
30. Mondal, S. and H.J. LIAN, Shape memory studies of functionalized MWNT-reinforced polyurethane copolymers. 2006.
31. Mao, Y., et al., Thermoviscoplastic behaviors of anisotropic shape memory elastomeric composites for cold programmed non-affine shape change. Journal of the Mechanics and Physics of Solids, 2015. 85: p. 219-244.
32. Strutynski, C., et al., 4D Optical fibers based on shape-memory polymers. Nature Communications, 2023. 14(1): p. 6561.
33. Wu, J., et al., Multi-shape active composites by 3D printing of digital shape memory polymers. Scientific reports, 2016. 6(1): p. 24224.
34. Ge, Q., et al., Thermomechanical behavior of a two-way shape memory composite actuator. Smart materials and structures, 2013. 22(5): p. 055009.
35. Habibi, M., et al., Combining short flax fiber mats and unidirectional flax yarns for composite applications: Effect of short flax fibers on biaxial mechanical properties and damage behaviour. Composites Part B: Engineering, 2017. 123: p. 165-178.
36. Ziadia, A., M. Habibi, and S. Kelouwani, Machine learning study of the effect of process parameters on tensile strength of FFF PLA and PLA-CF. Eng, 2023. 4(4): p. 2741-2763.
37. Abdelhamid, Z., H. Mohamed, and S. Kelouwani, The use of machine learning in process–structure–property modeling for material extrusion additive manufacturing: a state-of-the-art review. Journal of the Brazilian Society of Mechanical Sciences and Engineering, 2024. 46(2): p. 70.

38. Bouguermouh, K., et al., 4D-printed PLA-PETG polymer blends: comprehensive analysis of thermal, mechanical, and shape memory performances. Journal of Materials Science, 2024. 59(25): p. 11596-11613.
39. Paul, D. and J. Barlow, Polymer blends. Journal of Macromolecular Science—Reviews in Macromolecular Chemistry, 1980. 18(1): p. 109-168.
40. Bouguermouh, K., et al., Designing advanced 4D printing thermo-sensitive shape memory polymer blends for enhanced mechanical and shape memory performances. Progress in Additive Manufacturing, 2025: p. 1-20.
41. Bensadoun, F., et al., Impregnated fibre bundle test for natural fibres used in composites. Journal of Reinforced Plastics and Composites, 2017. 36(13): p. 942-957.
42. Park, J.Y., et al., Compatibility and physical properties of poly (lactic acid)/poly (ethylene terephthalate glycol) blends. Macromolecular Research, 2012. 20: p. 1300-1306.
43. Zhang, Z.-x., et al., Crystallization controlled shape memory behaviors of dynamically vulcanized poly (l-lactide)/poly (ethylene vinyl acetate) blends. Polymer Testing, 2016. 51: p. 82-92.
44. Sanivada, U.K., et al., PLA composites reinforced with flax and jute fibers—A review of recent trends, processing parameters and mechanical properties. Polymers, 2020. 12(10): p. 2373.
45. Kannan, T.G., et al., Effect of reinforcement on the mechanical and thermal properties of flax/polypropylene interwoven fabric composites. Journal of Industrial Textiles, 2013. 42(4): p. 417-433.
46. Guillou, E., et al., Use of a commingling process for innovative flax fibre reinforced unidirectional composites. Composites Part B: Engineering, 2024. 270: p. 111150.
47. Nazari, T. and H. Garmabi, Polylactic acid/polyethylene glycol blend fibres prepared via melt electrospinning: effect of polyethylene glycol content. Micro & Nano Letters, 2014. 9(10): p. 686-690.
48. Gupta, M., R. Srivastava, and H. Bisaria, Potential of jute fibre reinforced polymer composites: A review. Int. J. Fiber Text. Res, 2015. 5(3): p. 30-38.
49. Zhu, J., et al., Recent development of flax fibres and their reinforced composites based on different polymeric matrices. Materials, 2013. 6(11): p. 5171-5198.
50. Xia, X., et al., Effect of flax fiber content on polylactic acid (PLA) crystallization in Quadrini, F., et al., Durability of shape memory polymer composite laminates under thermo-mechanical cycling. Journal of Composites Science, 2022. 6(3): p. 91.
51. Korotkov, R., et al., Shape memory behavior of unidirectional pultruded laminate. Composites Part A: Applied Science and Manufacturing, 2021. 150: p. 106609.
52. Ming, G., et al., Shape memory cyclic behavior and mechanical durability of woven fabric reinforced shape memory polymer composites. Composites Science and Technology, 2024. 258: p. 110866.
53. Huang, Y., et al., Effect of silane coupling agent modification on shape memory behavior and mechanical properties of knitting fabric reinforced composites. Textile Research Journal, 2024. 94(9-10): p. 1012-1020.
54. Dogan, S., et al., Thermally induced shape memory behavior, enzymatic degradation and biocompatibility of PLA/TPU blends:“Effects of compatibilization”. Journal of the mechanical behavior of biomedical materials, 2017. 71: p. 349-361.
55. Hao, X., et al., Entanglement network formed in miscible PLA/PMMA blends and its role in rheological and thermo-mechanical properties of the blends. Polymer, 2015. 80: p. 38-45.

56. Mishra, J. and C. Das, Heat shrinkable polymer blends based on grafted low density polyethylene and polyurethane elastomer—part II. Journal of Elastomers & Plastics, 2001. 33(2): p. 137-153.
57. Bouguermouh, K., M. Habibi, and L. Laperrière, 4D printing of fiber-reinforced auxetic structures: the building blocks: A review. Smart Materials and Structures, 2024.
58. Wang, L., et al., Shape memory polymer fibers: materials, structures, and applications. Advanced Fiber Materials, 2022. 4(1): p. 5-23.
59. Gupta, R. and N. Banthia, Correlating plastic shrinkage cracking potential of fiber reinforced cement composites with its early-age constitutive response in tension. Materials and structures, 2016. 49: p. 1499-1509.
60. Farooq, A.S. and P. Zhang, Fundamentals, materials and strategies for personal thermal management by next-generation textiles. Composites Part A: Applied Science and Manufacturing, 2021. 142: p. 106249.
61. Malik, K., et al., A Review of flax fiber reinforced thermoset polymer composites: Thermal-physical properties, improvements and application. Journal of Natural Fibers, 2022. 19(15): p. 10412-10430.
62. Dezaki, M.L. and M. Bodaghi, 4D printing and programming of continuous fibre-reinforced shape memory polymer composites. European Polymer Journal, 2024. 210: p. 112988.
63. Bao, R.-Y., et al., Balanced strength and ductility improvement of in situ crosslinked polylactide/poly (ethylene terephthalate glycol) blends. RSC Advances, 2015. 5(44): p. 34821-34830.
64. Varsavas, S.D. and C. Kaynak, Effects of glass fiber reinforcement and thermoplastic elastomer blending on the mechanical performance of polylactide. Composites Communications, 2018. 8: p. 24-30.
65. Azizi Topkanlo, H., Z. Ahamadi, and F. Afshar Taromi. PET/PLA Blends Crystallization Kinetics. in Eco-friendly and Smart Polymer Systems 13. 2020. Springer.
66. McLauchlin, A.R. and O.R. Ghita, Studies on the thermal and mechanical behavior of PLA-PET blends. Journal of Applied Polymer Science, 2016. 133(43).
67. Afrifah, K.A., Fracture Mechanics and Statistical Modeling of Ternary Blends of Polylactide/ethylene-acrylate Copolymer/wood-flour Composites. 2012: Michigan State University. Forestry.
68. Goudenhooft, C., A. Bourmaud, and C. Baley, Flax (Linum usitatissimum L.) fibers for composite reinforcement: exploring the link between plant growth, cell walls development, and fiber properties. Frontiers in Plant Science, 2019. 10: p. 411.
69. Pickering, K.L., M.A. Efendy, and T.M. Le, A review of recent developments in natural fibre composites and their mechanical performance. Composites Part A: Applied Science and Manufacturing, 2016. 83: p. 98-112.
70. Singleton, A., et al., On the mechanical properties, deformation and fracture of a natural fibre/recycled polymer composite. Composites Part B: Engineering, 2003. 34(6): p. 519-526.
71. Malik, K., et al., A review of flax fiber reinforced thermoset polymer composites: Structure and mechanical performance. Journal of Natural Fibers, 2022. 19(14): p. 9656-9680.
72. Arbelaiz, A., et al., Mechanical properties of short flax fibre bundle/polypropylene composites: Influence of matrix/fibre modification, fibre content, water uptake and recycling. Composites science and technology, 2005. 65(10): p. 1582-1592.
73. Baley, C., et al., Variability of mechanical properties of flax fibres for composite

reinforcement. A review. Industrial crops and products, 2020. 145: p. 111984.
74. Madsen, B. and H. Lilholt, Physical and mechanical properties of unidirectional plant fibre composites—an evaluation of the influence of porosity. Composites Science and Technology, 2003. 63(9): p. 1265-1272.
75. Aslan, M., S. Mehmood, and B. Madsen, Effect of consolidation pressure on volumetric composition and stiffness of unidirectional flax fibre composites. Journal of Materials Science, 2013. 48: p. 3812-3824.
76. Kabir, H., et al., Investigation of physical and mechanical properties of bamboo fiber and PVC foam sheet composites. Universal Journal of Materials Science, 2014. 2(6): p. 119-124.
77. Munshi, M.R., et al., An experimental study of physical, mechanical, and thermal properties of rattan-bamboo fiber reinforced hybrid polyester laminated composite. Journal of Natural Fibers, 2022. 19(7): p. 2501-2515.
78. Khalil, H.A., et al., Natural fiber reinforced poly (vinyl chloride) composites: A review. Journal of Reinforced Plastics and Composites, 2013. 32(5): p. 330-356.
79. Martins, R.F., et al., Mechanical Properties of Additively Manufactured Polymeric Materials—PLA and PETG—For Biomechanical Applications. Polymers, 2024. 16(13): p. 1868.
80. Saadati, Y., et al., Study of translaminar fracture toughness of unidirectional flax/epoxy composite. Composites Part C: Open Access, 2020. 1: p. 100008.
81. Tripathi, N., M. Misra, and A.K. Mohanty, Durable polylactic acid (PLA)-based sustainable engineered blends and biocomposites: Recent developments, challenges, and opportunities. ACS Engineering Au, 2021. 1(1): p. 7-38.
82. Hu, C., et al., 3D printing of chiral carbon fiber reinforced polylactic acid composites with negative Poisson's ratios. Composites Part B: Engineering, 2020. 201: p. 108400.
83. PLA/flax fiber composites. Iranian Polymer Journal, 2017. 26: p. 693-702.

Chapitre 6 : Vieillissement en eau chaude : Effets sur les propriétés mécaniques et la mémoire de forme des composites PLA/PETG renforcés de fibres de lin et imprimés en 4D

Ce chapitre a fait l'objet d'un article :

Impact of Hot Water Aging on the Mechanical Performance and Shape Memory Behavior of 4D-Printed Flax Fiber-Reinforced PLA/PETG Composites. Bouguermouh Karima, Habibi Mohamed, Laperrière Luc and Daniel Monplaisir. Composite Part B : Engineering, 2026, p. 113477

Il peut être consulté en ligne à l'adresse suivante : https://doi.org/10.1016/j.compositesb.2026.113477

Poursuivant les travaux antérieurs ayant mis en évidence les performances mécaniques et la stabilité fonctionnelle du mélange PLA-75/PETG-25 renforcé par des fibres de lin, la présente étude explore la durabilité et la stabilité fonctionnelle de ces composites imprimés en 4D lorsqu'ils sont soumis à un vieillissement hydrothermique prolongé. L'objectif principal est d'évaluer de manière systématique l'effet de l'immersion dans l'eau chaude (45 °C) sur le comportement mécanique, structural, morphologique et mémoire de forme de composites PLA/PETG contenant 0, 5, 10 et 15 % massique de fibres de lin non traitées.

Les échantillons, élaborés par impression 4D via la technologie Fused Filament Fabrication (FFF), ont été immergés jusqu'à saturation puis ensuite caractérisés. Les essais de traction, les analyses spectroscopiques (FTIR), structurales (DRX) et morphologiques (MEB) ont été couplés à des tests fonctionnels de fixité (S_f) et de récupération de forme (S_r) afin de corréler la dégradation chimique et physique à l'évolution du comportement mémoire de forme.

Les résultats révèlent que le renfort par fibres de lin améliore la rigidité initiale du matériau, le module d'Young augmentant de 3,6 à 4,0 GPa pour 15 % de fibres, tout en induisant une forte sensibilité à l'humidité. Le taux d'absorption d'eau passe de moins de 2 % pour le mélange non renforcé à près de 20 % après 67 jours pour le composite le plus chargé. Cette absorption est directement liée à l'hydrophilie des fibres, entraînant un gonflement, un décollage interfacial et une dégradation hydrolytique de la matrice. Les spectres FTIR montrent un renforcement des bandes O–H et une diminution de l'intensité carbonyle (C=O), traduisant une hydrolyse des chaînes

esters, tandis que les diffractogrammes DRX révèlent une réorganisation cristalline et une recristallisation secondaire du PLA sous l'effet de la plastification aqueuse. Les micrographies MEB confirment ces phénomènes par la présence de fibres éclatées, de fissures longitudinales et d'une porosité accrue.

Sur le plan mécanique, la résistance à la traction diminue de 60,5 MPa à 40 MPa, tandis que le module chute de 44 % après vieillissement, avec des pertes maximales observées pour les composites à 15 % de fibres. Malgré ces dégradations, les performances mémoire de forme demeurent remarquables : la fixité de forme (S_f) passe de 100 % à 90 % et la récupération de forme (S_r) de 100 % à 93 %. De plus, le temps de récupération diminue après immersion, indiquant une plastification du réseau polymère qui accélère l'activation thermique.

En conclusion, cette étude met en évidence le potentiel des fibres naturelles dans la conception de composites 4D bio-sourcés combinant rigidité, réactivité et durabilité environnementale. Toutefois, la sensibilité accrue à l'eau souligne la nécessité de traitements de surface des fibres ou de revêtements barrière hydrophobes pour garantir la stabilité à long terme. Ces résultats offrent des perspectives prometteuses pour le développement de matériaux intelligents, durables et écoresponsables destinés aux applications adaptatives en environnements humides.

Impact of Hot Water Aging on the Mechanical Performance and Shape Memory Behavior of 4D-Printed Flax Fiber-Reinforced PLA/PETG Composites

Karima Bouguermouh[1], Mohamed Habibi[1*], Luc Laperrière[1], Daniel Monplaisir[2]

[1] Department of Mechanical Engineering, Université du Québec à Trois-Rivières, Quebec, Canada.

[2] Department of Chemistry, Biochemistry and Physics, Université du Québec à Trois-Rivières, Quebec, Canada.

6.1 Abstract

This work investigates how hot-water aging affects the mechanical and shape-memory properties of flax fibre-reinforced PLA/PETG composites for 4D printing. While flax reinforcement increases stiffness (Young's modulus from 3.6 GPa to ≈ 4.0 GPa at 15 wt%), it also markedly increases water uptake because of fibre hygroscopicity: the neat PLA/PETG absorbed < 2 % at saturation, whereas the 15 wt% composite reached ≈ 20 % after 67 days. Aging at 45 °C caused pronounced stiffness and strength losses (up to 44 % and 69 %, respectively), consistent with SEM evidence of fibre swelling, interfacial debonding, matrix fragmentation and increased porosity. FTIR revealed intensified O–H bands and XRD revealed structural reorganization, including secondary recrystallization in PLA, corroborating hydrolytic degradation. Despite these degradation phenomena, the shape-memory functionality remained largely preserved, with high initial performance (fixity ≈ 100 % and recovery ≈ 100 % for the neat blend) and only a moderate reduction in shape fixity (S_f ≈ 90 % at 15 wt%), accompanied by a slight decrease in shape recovery (S_r) after aging. These results demonstrate that shape-memory performance can be maintained even under severe hydrothermal exposure, addressing a critical knowledge gap in the functional durability of 4D-printed natural fiber–reinforced composites and providing a foundation for the development of more robust structures operating in humid environments.

Keywords: 4D printing, flax fiber-reinforced composites, PLA/PETG polymer blend, hydrothermal aging, mechanical properties, shape memory behavior.

6.2 Introduction

The advancement of 4D printing has revolutionized material design by enabling structures to

respond dynamically to external stimuli such as heat, moisture, and light [1] [2-6]. In recent years, natural fiber-reinforced polymer (NFRP) composites, such as flax, hemp, jute, and wood flour into these systems have gained considerable interest in this field due to their sustainability, biodegradability, and mechanical advantages [7-9]. This opened a sustainable pathway for 4D printing, particularly through Fused Deposition Modeling (FDM).

Natural fiber-reinforced polymers (NFRPs) not only enhance mechanical strength and biodegradability but also bring intrinsic hygroscopic behavior, which can be harnessed for moisture-responsive shape change. For instance, Le Duigou et al. [10] introduced "hygromorphic biocomposites," which use the hygro-expansive behavior of natural fibers to enable self-bending 4D-printed devices that react to humidity gradients. In another study, Duigou et al. [11] demonstrated that wood fiber-reinforced PLA composites printed via FDM could achieve faster and more pronounced bending under moisture exposure due to fiber anisotropy and porous microstructure, despite a relatively lower Young's modulus (~2.1 GPa) compared to compressed samples. Similarly, Kishore et al. [12] reviewed potential applications in agriculture and sustainable packaging, suggesting that 4D-printed natural fiber composites could serve as smart mulching films with programmable degradation and shape-memory behavior for eco-friendly deployment. These findings underline that incorporating natural fibers into FDM-based 4D printing not only improves the sustainability and functionality of the printed objects but also unlocks new bioinspired actuation mechanisms for fields such as soft robotics, adaptive building components, and environmentally responsive devices.

Natural fiber-reinforced polymer composites (NFRPCs) offer a great balance of strength and sustainability, making them an appealing choice for various applications. However, they face durability issues when exposed to heat and moisture. Research by Mayandi et al. [13] shows that long-term moisture exposure can weaken these materials by more than 25%, due to problems like fiber swelling, resin softening, and cracking at the points where fibers and matrix meet. Similarly, thermal stress can also take a toll. Sen et al. [14] found that composites made with fibers like sisal and jute lost up to 30% of their strength after being aged in high temperatures, mainly because the fibers degrade and the resin becomes brittle. Lately, flax fiber composites have gained interest in the 3D printing world because they're both strong and eco-friendly. Specifically, flax fiber-reinforced PLA/PETG composites show promise for structural and shape-changing applications

[15]. But there's a catch, these materials tend to absorb water easily, which causes the fibers to swell, weakens the bond between fiber and resin, and reduces overall performance [4, 16, 17]. This has led many researchers to closely study how moisture affects the strength and reliability of 3D-printed NFRP materials. Kesentini et al. [18] investigated the effects of water aging on 3D-printed poly-lactic acid (PLA) composites reinforced with flax fibers, revealed that moisture accumulation is a significant concern. The research demonstrated that water absorption led to notable changes in the mechanical properties of these bio-based composites, underscoring the need for strategies to mitigate moisture uptake. Habibi et al. [19] demonstrated that flax fiber mats improved the mechanical properties of composites but also increased their sensitivity to moisture, causing premature degradation. Athijayamani et al. [20] reported that natural fiber-reinforced composites exhibited a significant decline in tensile strength after prolonged water exposure due to hydrolytic degradation. Li and Xue [21] further confirmed that hydrothermal aging led to interfacial debonding and reduced mechanical performance in unidirectional flax fiber-reinforced composites. While various mitigation strategies such as fiber surface treatments and hydrophobic coatings have been proposed [22, 23], the long-term stability of NFRP composites under humid conditions remains a concern.

Hydrothermal aging commonly simulated by immersion in hot water is widely employed as an accelerated environmental conditioning method to reproduce the effects of moisture and temperature fluctuations encountered in service. For example, Thomason and Xypolias [24] investigated glass fiber–reinforced vinyl ester composites and emphasized the importance of hydrothermal exposure in elucidating degradation mechanisms under humid and marine-like environments. Similarly, Regazzi et al. [25] and Starkova et al. [26] studied PLA/flax and PBS/nanocellulose composites, respectively, employing immersion in hot water as an accelerated simulation of service moisture conditions. Both studies reported substantial reductions in stiffness and tensile strength up to 50% attributed to water diffusion, interfacial debonding, and matrix plasticization. Accordingly, hydrothermal conditioning remains an essential tool for evaluating the durability and long-term stability of 3D-printed bio-composites intended for use in humid or thermally variable environments.

Despite the extensive research on the mechanical and water absorption properties of NFRP composites, there is a significant gap in the literature regarding the effects of water absorption on

their shape memory performance. Previous studies have demonstrated that fiber reinforcement influences shape memory behavior by restricting polymer chain mobility [16, 27]. However, no comprehensive study has addressed how moisture absorption affects the shape fixity and shape recovery of 4D-printed fiber-reinforced composites. Given that water absorption leads to polymer plasticization, fiber swelling, and interfacial weakening, it is plausible that these factors could alter the deformation and recovery characteristics of 4D-printed structures [28].

In this context, the present work provides a comprehensive experimental investigation of the hydrothermal aging behavior of 4D-printed flax fiber–reinforced PLA/PETG composites. The originality of this study lies in a multi-scale, function-oriented approach that systematically correlates water diffusion, interfacial degradation, and matrix hydrolysis with the evolution of both mechanical properties and shape-memory performance. This analysis reveals the dual role of flax fibers, which simultaneously accelerate hydrothermal degradation while contributing to the preservation of geometric integrity during shape recovery. Importantly, this work demonstrates that shape-memory functionality can be partially preserved despite severe hydrothermal degradation, a behavior that cannot be inferred from mechanical property retention alone and has not been previously reported for 4D-printed natural fiber–reinforced composites. Collectively, these findings provide new mechanistic insights into degradation–function relationships and establish design-relevant guidelines for the development of durable, bio-based 4D-printed shape-memory systems.

6.3 Materials and methods

6.3.1 Sample preparation

Materials

The flax fibers utilized in the study were obtained from Safilin (France, Poland) as a low-twist flax fiber yarn with a linear density of 5000 tex. The producer has reported some properties of a single flax fiber in the yarn: density of ~1.5 g/cm³ a diameter of fiber diameter of about 20μm, elongation at break of 1.35%, a tensile strength of 738MPa, Young's modulus of 51.4 GPa, as reported by Habibi et al. [29]. The surfaces of flax fiber yarns were untreated. Poly(lactic acid) (PLA) and polyethylene terephthalate glycol-modified (PETG) resin pellets were selected as the polymer matrices for developing the flax fiber-reinforced 4D printing blends. PLA pellets, with a density of 1.24 g/cm³, and PETG pellets, with a density of 1.27 g/cm³, were sourced from Push Plastics and served as the base materials for the composites.

Preparation of blends and composite pellets

To prepare the PLA, PETG, and flax for composite pellet fabrication, all components were pre-dried in a vacuum oven at 60°C for 24 hours to eliminate residual moisture, as illustrated in Figure 6. 1. First, a binary combination of PLA and PETG polymers was prepared in weight ratios of 75/25 by mixing their pellets in a beaker immediately before the extrusion process. This specific composition was selected based on our previous studies, which demonstrated its superior shape memory properties [4, 16]. On the other hand, the preparation of PLA/PETG/Flax composites involved a two-step mixing process as reported in our recent study [15]. Initially, flax fibers at concentrations of 5%, 10%, and 15% w/w, with PLA and PETG pellets, were blended in a DUSATEC Gelimat thermokinetic mixer (Model G Series), which was operated at a speed of 4500 rpm. The mixing continued until the material's temperature reached 200°C, with the melt state mixing duration lasting between 20 and 30 seconds. The solid masterbatch produced from this initial melt compounding was cooled and subsequently crushed into granules suitable for extrusion.

Granules were then fed into a single-screw extruder to create 3D printing filaments. Key processing parameters such as extrusion temperature, extrusion rate, line speed, and oven temperature were carefully optimized beforehand to ensure the filaments were of high quality, exhibiting minimal defects and consistent diameter. The extrusion temperatures were precisely controlled within the range of 197-197°C to 200-205°C as reported in Table 6.1 to accommodate the distinct thermal and flow properties of each composition. Employing a nozzle with a diameter of 3 mm to produce 2.80 mm diameter filaments. Post-extrusion, the filaments were cooled and wound onto spools using a filament winding system, making them ready for 3D printing.

3D printing by Fused Filament Fabrication (FFF)

PLA/PETG polymer blends and flax fiber-reinforced PLA/PETG composite filaments were used to 3D print two types of samples: 100 × 20 × 1 mm specimens for shape memory testing, and ASTM D638 Type IV specimens for tensile testing, designed using CAD software. Five tensile specimens for each composition were printed using an Ultimaker S5 printer with the specified printing parameters: an AA and CC-nozzle with diameters of 0.4 and 0.6 mm, respectively, for PLA/PETG polymer blends and Flax Fibers-reinforced PLA/PETG blends composite. The printing parameters were selected based on our previously published work [15], in which the process conditions were systematically investigated and validated to achieve high-quality prints with excellent dimensional

accuracy. In the present study, the same parameters were adopted, including layer heights of 0.2 and 0.3 mm, an infill density of 100%, line widths of 0.3 and 0.45 mm, and printing speeds of 30 and 20 mm/s, consistent with established practices in the literature [2, 30]. The nozzle and bed temperatures were adjusted for each material according to the conditions defined in our prior study to ensure optimal flow behavior and interlayer adhesion, as summarized in Table 6.1. This approach ensured uniform filament deposition, dimensional stability, and reproducible print performance for both the PLA/PETG blends and the flax fiber-reinforced composite.

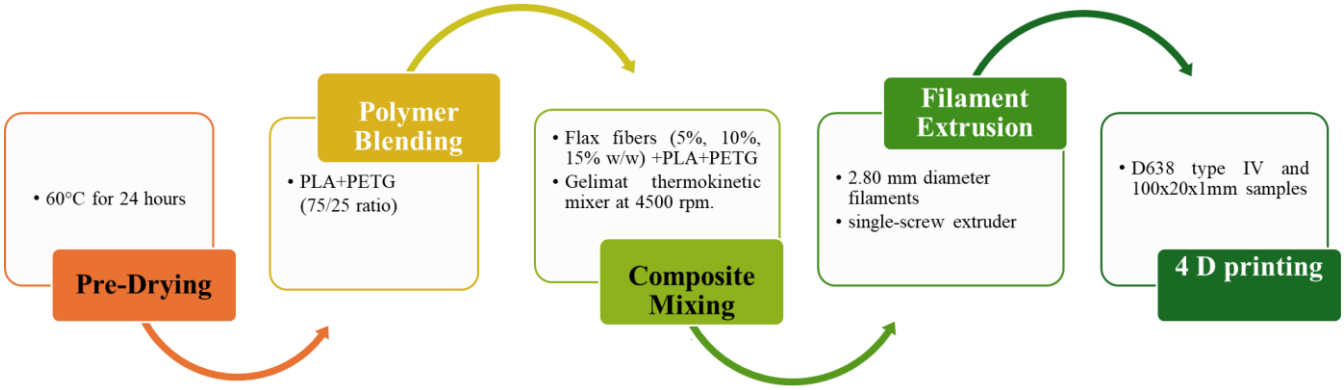

Figure 6. 1: Schematic representation of the preparation and processing of flax fiber-reinforced PLA/PETG composites for 4D printing.

Table 6.1: Compositions, extrusion temperatures, and 3D printing parameters of PLA/PETG blends and flax fiber reinforced PLA/PETG blends.

Samples	Extrusion Temperatures (°C)	Nozzle Temperatures (°C)	Plate temperatures (°C)	Print speed (mm/s)	Flow (%)	Layer height (mm)	Line width (mm)
PLA-75/PETG-25	197-197	255	100	30	100	0.2	0.3
PLA-75/PETG-25/F-5	190-195	255	100	20	102	0.3	0.45
PLA-75/PETG-25/F-10	190-195	255	100	20	105	0.3	0.45
PLA-75/PETG-25/F-15	200-205	260	100	20	105	0.3	0.45

6.3.2 Characterization

6.3.2.1 Water absorption

As shown in Figure 6.2, three tensile and shape-memory specimens of each material were first dried in an oven at 55 °C for 24 h and then weighed using an analytical balance (AB54-S/FACT). Subsequently, the specimens were immersed in distilled water at 45 °C in an adjustable hot-water bath (GRANT OLS200) until weight equilibrium was reached. The choice of 45 °C corresponds to a commonly used condition that accelerates moisture diffusion without inducing thermal degradation, while remaining below the glass transition temperature (T_g) of the PLA/PETG blends and flax fiber composites [15], thus ensuring realistic and thermally stable hydrothermal conditioning [31, 32]. During immersion, the specimens were periodically removed, gently dried with a lint-free cloth, and weighed to monitor water uptake until saturation.

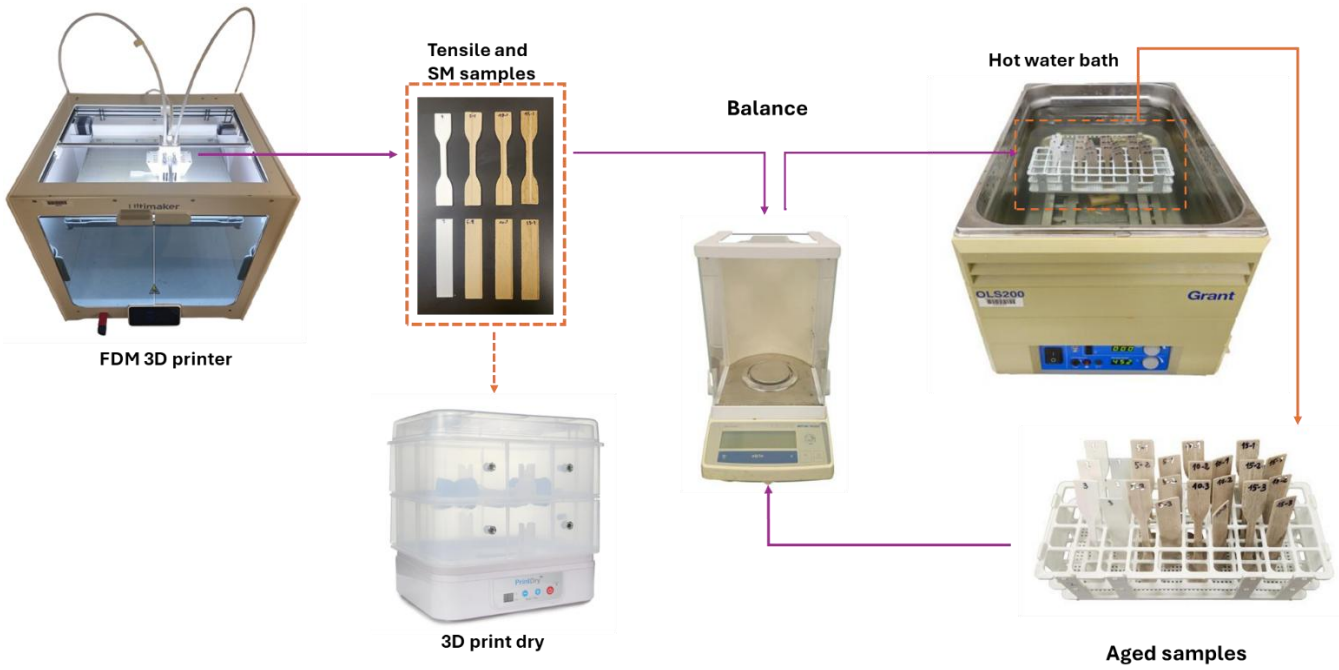

Figure 6.2: Schematic representation of the progressive aging stages in hot water for PLA/PETG polymer blends and flax-fiber reinforced polymer composites.

The initial dry mass of the samples is denoted as m_0, and the mass at a given immersion time (t) is represented by m_t. Water absorption behavior was assessed by plotting the moisture uptake per unit surface area as a function of the square root of immersion time ($\sqrt{t}$). These absorption curves were used to determine both the saturation content and the diffusion kinetics of water within the material. The maximum water uptake, Δm (t), expressed as a percentage of the dry mass, was calculated using Equation (1):

$$\Delta m(t) = 100 \times \frac{(m_t - m_0)}{m_0} \quad \text{(eq. 1)}$$

The initial diffusion coefficient D was estimated from the slope of the linear portion of the absorption curve at early times. Assuming Fickian diffusion through a plate of thickness L, the following analytical approximation was used (Equation 2):

$$\frac{M_t}{M_\infty} \approx \frac{4}{\sqrt{\pi}} \sqrt{\frac{Dt}{L^2}} \Rightarrow D = \frac{\pi}{16} (\text{ slope })^2 L^2 \quad \text{(eq. 2)}$$

Here, the slope refers to the gradient of the normalized moisture uptake (M_t/M_∞) versus $\sqrt{t}$ in the initial linear regime.

6.3.2.2 Tensile test

Mechanical testing was conducted using an MTS testing machine equipped with a 20 kN load cell under standard ambient conditions. Testing followed ASTM D638 guidelines, with Type IV specimens 3D-printed in 0° orientations. This setup allowed for a detailed analysis of the mechanical behavior, including tensile strength, Young's modulus providing key insights into the structural performance of the PLA/PETG blends and flax-reinforced composites before and after the aging test in hot water.

6.3.2.3 Infrared Spectroscopy (FTIR)

To evaluate water absorption during the aging process, Fourier Transform Infrared Spectroscopy (FTIR) was employed with a resolution of 4 cm^{-1}. Measurements were taken in Attenuated Total Reflectance (ATR) mode, covering key spectral bands across the 4000–400 cm^{-1} range.

6.3.2.4 X-Ray Diffraction (XRD)

X-ray diffraction (XRD) analysis was conducted using a diffractometer equipped with a Cu Kα radiation source (λ = 1.5406 Å). The operating conditions were set at 35 kV voltage and 30 mA current. Scans were performed over a 2θ range of 5° to 80°, with a step size of 0.02° and a scan

speed of 0.5°/min. These parameters ensured high-resolution diffraction patterns suitable for detailed crystallographic analysis.

6.3.2.5 Scanning Electron Microscopy (SEM)

Surface morphology and microstructural analyses of the different materials were conducted using scanning electron microscopy before and after aging in hot water. Samples were sputter-coated with palladium under argon plasma at approximately 20 mV for ~5 minutes. Images were captured under low vacuum conditions (50 Pa), with water used as the chamber medium. The imaging employed a spot size of 5 µm at an accelerating voltage of 5-20 kV*, ensuring high-resolution observations of fiber dispersion, polymer-fiber interfaces, and potential defects in the blends.

6.3.2.6 Shape Memory Test

To evaluate the shape memory characteristics, U-shaped 3D-printed samples measuring 100 mm × 20 mm × 1 mm, oriented at 0°, were subjected to shape programming and recovery tests. The samples were heated to a designated programming temperature (T_p) and then deformed to fit a mold 20 mm thick by applying sufficient force. While held in the mold, the samples were cooled to room temperature to stabilize their deformed shape. The fixed angle, referred to as θ_{fixed}, was recorded after mold removal.

For recovery evaluation, the samples were reheated to a constant temperature, and the bending angle (θ_i) was carefully measured. Shape fixity (S_f) and shape recovery (S_r) were calculated using the following equations:

$$Shape\ fixity\ (Sf) = 100 \times \frac{\theta fixed}{\theta max} \quad \text{(eq. 3)}$$

$$Shape\ recovery\ (Sr) = 100 \times \frac{\theta \max - \theta i}{\theta \max} \quad \text{(eq. 4)}$$

These metrics provided quantitative insights into the effectiveness of the shape memory behavior in the studied composites. Detailed methodologies and previous results can be referenced in our earlier work [16].

6.4 Results and discussions

6.4.1 Water absorption study

The water absorption behavior of 3D-printed PLA/PETG and fiber-reinforced composites was investigated by immersing the samples in hot water at 45°C. As shown in Figure 6.3 (a) and (b), the percentage of absorbed water increased progressively with immersion time, with fiber content playing a significant role in determining the absorption levels. The PLA-75/PETG-25 matrix exhibited the lowest absorption, stabilizing below 2%, indicating that the polymer blend itself resists moisture uptake.

A comparison between tensile and shape memory specimens revealed that both follow a similar absorption trend, although shape memory coupons tend to exhibit slightly higher absorption at higher fiber contents. This effect is further illustrated in Table 6.2, where water absorption increased steadily with fiber loading. For example, unreinforced tensile samples exhibited the lowest absorption (≈1.12%) after 450 h (18 days), whereas specimens containing 15 wt% flax fibers absorbed nearly 20% water after 1614 h (67 days). This clearly confirms that fiber reinforcement directly contributes to higher water uptake, since hydrophilic flax fibers inherently retain more moisture than the polymer matrix. The slight differences between tensile and shape memory samples may be attributed to microstructural variations such as fiber distribution, porosity, or fiber–matrix adhesion.

The diffusion analysis highlights the combined influence of geometry and printing strategy. Shape memory coupons (L = 0.5 mm) and tensile specimens (L = 1.2 mm) exhibited systematic differences in their Fickian diffusion parameters. At constant fiber content, tensile specimens consistently displayed higher diffusion coefficients (D) but lower equilibrium moisture uptake (M∞) compared to shape memory coupons as reported in Table 6.2. At 0% fibers (neat matrix), both geometries exhibited the highest diffusion coefficients ($D = 1.08\times10^{-6}$ mm²/s for tensile and $D = 9.76\times10^{-8}$ mm²/s for Shape memory), but very low saturation levels (M∞ = 1.12% and 1.26%, respectively). This indicates rapid but limited water uptake in neat PLA-75/PETG-25 polymer blend. With 5–15% fibers, diffusion coefficients decreased significantly in both geometries. For example, at 15% fiber content, tensile specimens reached $D = 1.03\times10^{-7}$ mm²/s with M∞ = 20.36%, while Shape memory coupons exhibited a slower diffusion rate ($D = 9.69\times10^{-9}$ mm²/s) but higher uptake (M∞ = 24.36%). These results confirm that flax fibers act as hydrophilic sites, enhancing equilibrium absorption, while the tortuous microstructure of the fiber network slows down diffusion kinetics [33].

Table 6.2: Equilibrium moisture uptake (M∞) and diffusion coefficients (D) of Shape memory and tensile specimens at different fiber contents.

Fiber content (wt%)	M∞ Shape Memory (%)	D Shape Shape Memory ($mm^2/s \times 10^{-8}$)	M∞ Tensile (%)	D Tensile ($mm^2/s \times 10^{-8}$)
0	1.26	9.76	1.12	108.41
5	16.88	0.58	7.53	4.42
10	19.09	0.73	16.20	6.59
15	24.36	0.97	20.36	10.34

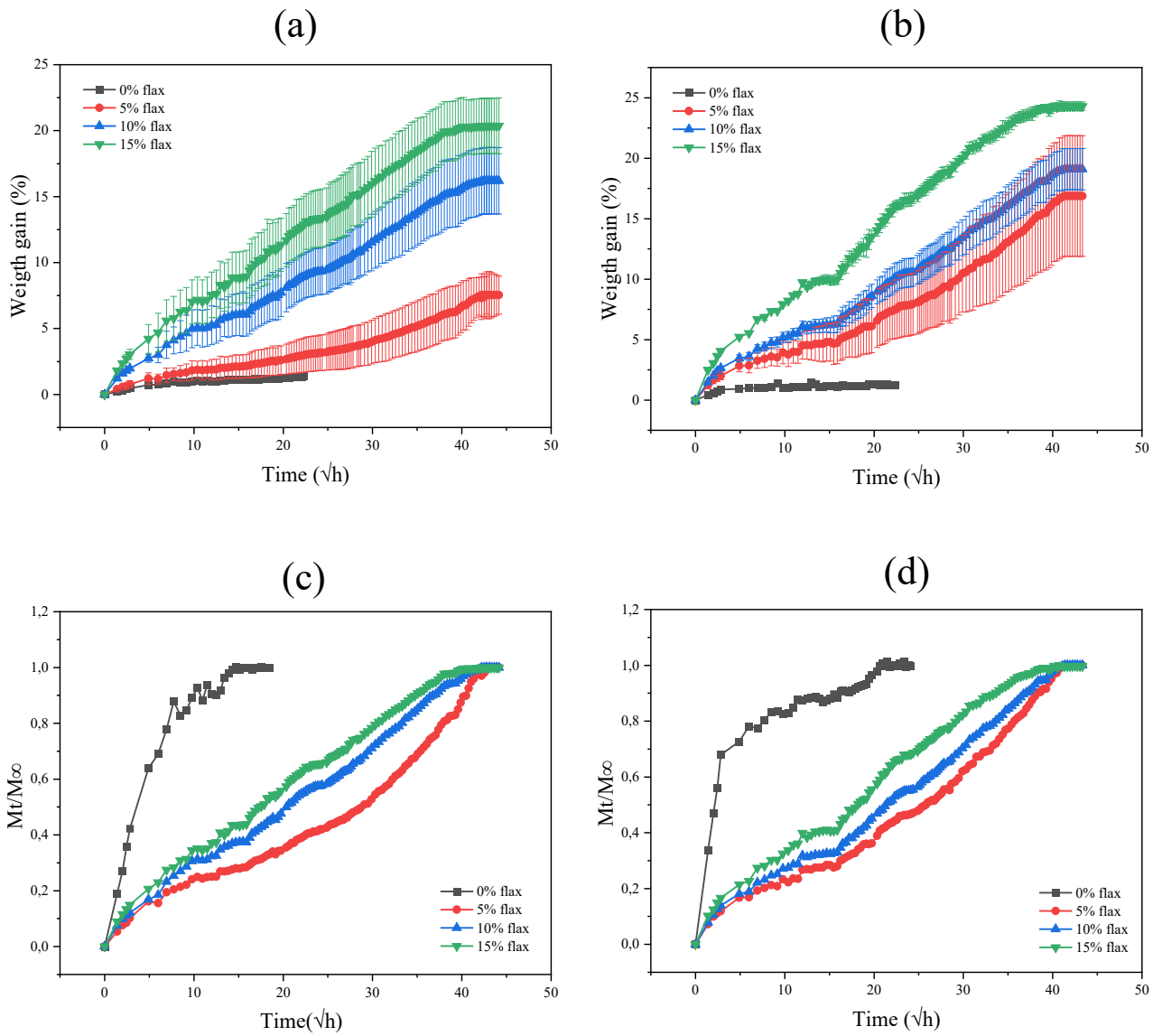

Figure 6.3: Water absorption percentage of (a) tensile samples, (b) Shape memory samples. Normalized absorption for tensile samples (c), and shape memory samples (d) as function of fiber content.

Overall, the findings underline the dual influence of fiber reinforcement and geometry. Indeed, thicker tensile specimens facilitate faster diffusion due to FDM-induced porosity and longer transport pathways, whereas thinner Shape memory coupons exhibit slower diffusion but higher overall uptake. On the other hand, when compared to the neat PLA/PETG matrix (0% fibers), fiber-reinforced composites consistently exhibit significantly lower diffusion coefficients (D) but markedly higher equilibrium moisture uptake (M∞), clearly reflecting the pronounced hydrophilic nature of flax fibers. These trends are consistent with previous studies, where specimen geometry and thickness were shown to strongly affect diffusion behavior [34]. Similarly, the increase of M∞ with fiber content despite slower initial kinetics agrees with earlier reports on natural fiber composites [35]. Finally, the higher diffusion coefficients observed in tensile specimens align with findings on FDM-induced porosity and filament orientation, which accelerate moisture transport compared to bulk polymers [36].

Aging effects due to immersion in hot water at 45°C were visually assessed in Figure 6.4 (a) and (b), where the condition of the samples before and after aging was compared. The pre-aged specimens appeared smooth and uniform in texture and color. However, after prolonged exposure, visible signs of material degradation, including surface roughening and discoloration apparent in fiber-reinforced composites. The extent of degradation was most noticeable in the PLA-75/PETG-25/F-15 sample, where fiber swelling and bending deformation could be observed as seen in Figure 6.4 (c). The PLA-75/PETG-25 sample, which does not contain fibers, maintained its structure and exhibited minimal changes, suggesting that the polymer matrix alone is more resistant to hydrolytic degradation.

The degradation effects seen in fiber-reinforced samples can be attributed to water absorption-induced swelling of fibers, which weakens the fiber-matrix interface over time. This phenomenon is consistent with prior findings on PLA-based composites, where prolonged water exposure leads to fiber swelling and polymer chain breakdown due to hydrolysis [22]. The increasing surface roughness and fiber exposure seen in this study are also reported in earlier research, where fiber-reinforced composites exhibited similar degradation patterns after water immersion [21].

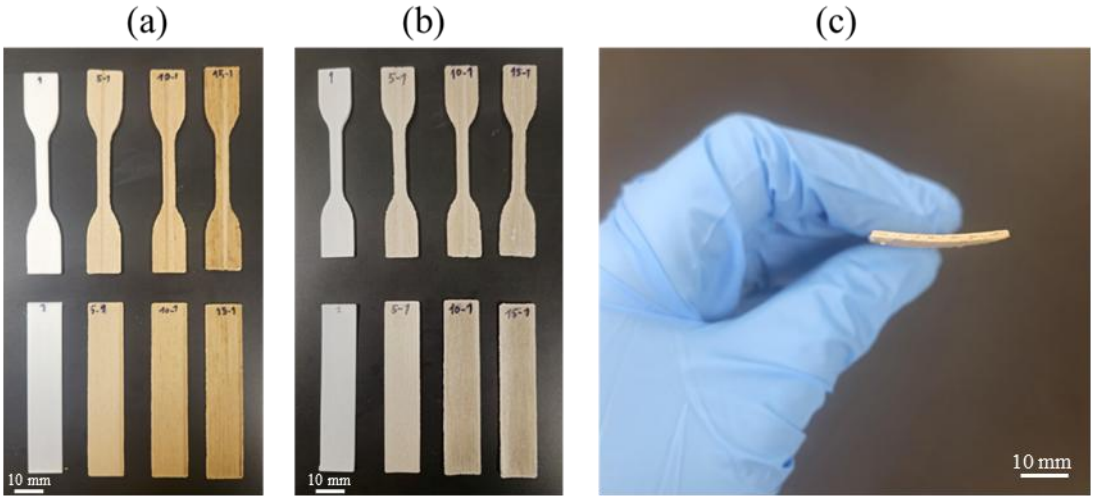

Figure 6.4: Visual assessment of 3D-printed PLA/PETG and fiber composites before (a) and after aging in hot water (b). Bending deformation of PLA-75/PETG-25/F-15 after saturation in hot water at 45°C (c).

6.4.2 Effect of aging on mechanical properties

The tensile stress-strain curves in Figure 6.5 (a) illustrate the mechanical performance of PLA/PETG polymer blends and fiber-reinforced composites before and after aging in hot water. Before aging, the mechanical properties of the PLA/PETG blend show a clear dependence on fiber content as seen in Figure 6.5 (b) and (c). The elastic modulus (E) increases with fiber addition, indicating enhanced stiffness. The PLA-75/PETG-25 blend without fibers has an elastic modulus of approximately 3.6 GPa, which rises as fiber content increases. The highest modulus, around 4 GPa, is observed at 15% fiber content (PLA-75/PETG-25-F15), confirming that fiber reinforcement improves rigidity. In contrast, tensile strength (σ) decreases with fiber addition. The PLA-75/PETG-25 blend without fibers exhibits the highest tensile strength (~60.5 MPa). However, as fiber content increases, tensile strength gradually declines, reaching approximately 40 MPa at 15% fiber content. This suggests that higher fiber loading weakens the material due to potential fiber-matrix interfacial defects, which create stress concentration points [37].

A noticeable decline in both tensile strength (σ) and elastic modulus (E) is observed post-aging, highlighting the detrimental effects of hydrolytic degradation and fiber-matrix debonding. Among the samples, PLA-75/PETG-25/F-15 initially exhibits the highest stiffness, followed by PLA-75/PETG-25/F-10 and PLA-75/PETG-25/F-5, but after aging, their performance significantly drops. The unreinforced PLA-75/PETG-25 retains better properties after aging compared to fiber-reinforced samples, suggesting that while fiber reinforcement initially enhances rigidity, it also

increases water absorption, accelerating degradation.

In terms of mechanical property retention, Figure 6.5 (d) quantifies the decline in elastic modulus and tensile strength before and after aging. The elastic modulus (E) of PLA-75/PETG-25/F-15 decreases from approximately 4 GPa to 2.26 GPa, representing a 44% reduction, as shown in Figure 6.5 (d). Similarly, its tensile strength (σ) drops from 40 MPa to 12.5 MPa, marking a 69% loss, indicating that higher fiber content increases water sensitivity and accelerates mechanical degradation. This trend aligns with previous research, which reports that natural fiber composites absorb 5–15% more moisture than pure polymer matrices, leading to faster degradation [37]. In contrast, the PLA-75/PETG-25 blend demonstrates better mechanical stability. After aging, its elastic modulus decreases from 3.6 GPa to 3.2 GPa, corresponding to a 10% reduction. Meanwhile, its tensile strength drops from 60.5 MPa to 32 MPa, reflecting a 47% decline in mechanical properties.

The visual analysis reveals clear differences between pre- and post-aging 3D printing specimens. Aged samples display surface roughness, discoloration, indicating structural weakening, which confirms that water exposure compromises the fiber-matrix adhesion. These observations align with studies indicating that moisture absorption in natural fiber composites leads to swelling and interfacial weakening, thereby reducing mechanical performances [38].

The two-way ANOVA analysis clearly demonstrated that both fiber content and water aging significantly influenced the tensile strength (σ_max) of the 3D-printed PLA/PETG composites, with p-values lower than 1.0×10^{-5} and 1.0×10^{-12}, respectively. However, the interaction term between these two factors was not statistically significant ($p = 9.68 \times 10^{-1}$), indicating that the reduction in strength due to aging occurred independently of fiber loading.

For Young's modulus (E), the ANOVA also confirmed a highly significant effect of water aging ($p < 1.0 \times 10^{-7}$). More importantly, a significant interaction between fiber content and aging was detected ($p = 1.65 \times 10^{-4}$), suggesting that the impact of fiber reinforcement on stiffness is dependent on the environmental exposure conditions. Although fiber content alone did not significantly affect the modulus ($p = 1.13 \times 10^{-1}$), its combination with aging led to more substantial reductions in stiffness.

These ANOVA results highlight the importance of assessing not only the main effects but also the interaction between composition and environmental factors when evaluating the mechanical performance of bio-based 3D-printed composites.

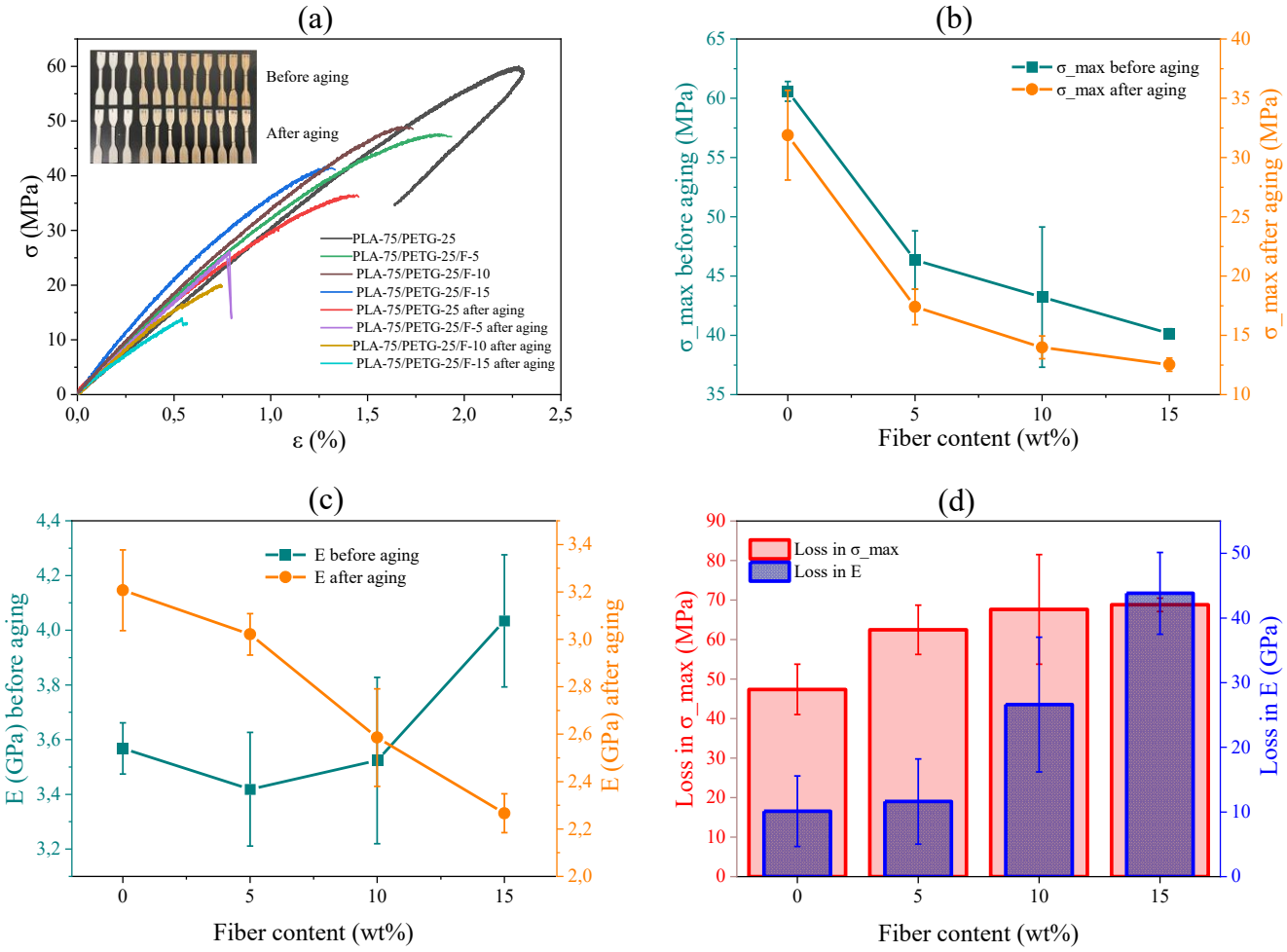

Figure 6.5: Mechanical performance of 3D-printed PLA-75/PETG-25 composites reinforced with 0–15 wt% flax fibers before and after water aging: (a) Stress–strain curves; (b) Maximum tensile strength (σmax) versus fiber content; (c) Young's modulus (E) versus fiber content; (d) Percentage losses in strength and modulus after aging.

6.4.3 Infrared Spectroscopy (FTIR) analysis

The FTIR spectra presented in Figure 6.6 reveal distinct differences between the PLA/PETG polymer blend and flax fiber-reinforced PLA-75/PETG-25 composites before and after the aging test in hot water. The unreinforced PLA-75/PETG-25 blend exhibits characteristic absorption peaks associated with its molecular structure, including a strong carbonyl (C=O) stretching peak at approximately 1750 cm^{-1}, C-O stretching between 1180-1100 cm^{-1}, and C-H stretching around 2900 cm^{-1} [4, 16]. These peaks provide a baseline for comparison with the flax fiber-reinforced composites.

Upon the addition of flax fibers (5wt%, 10wt%, 15wt%), new peaks emerge due to the presence of cellulose, hemicellulose, and lignin. Notably, the O-H stretching band around 3300-3400 cm^{-1}

becomes more prominent, indicating the presence of hydroxyl groups from cellulose. Additionally, the C-H stretching peak at ~2900 cm^{-1} and C-O-C stretching bands between 1030-1050 cm^{-1} confirm the presence of polysaccharides in flax fibers [39, 40]. These changes suggest enhanced hydrogen bonding interactions between the fiber and the polymer matrix.

After aging in hot water, the PLA-75/PETG-25 blend exhibits slight spectral modifications. The increased intensity and broadening of the O–H stretching region (~3300 cm^{-1}) reflect water absorption and stronger hydrogen bonding, while the reduction in the C=O peak (~1750 cm^{-1}) indicates partial ester hydrolysis in PLA. These findings are consistent with the known sensitivity of PLA to hydrolytic degradation in humid environments [41].

In flax fiber-reinforced composites, the changes are more pronounced. The broadening and intensification of the O–H band confirm greater water uptake, due to the hydrophilic nature of the natural fibers. A decrease in the C–O stretching band (~1050 cm^{-1}) is also observed, which is mainly attributed to increased hydrogen bonding and bound water of the fiber components [42]. Shifts and slight decreases in the C=O (~1750 cm^{-1}) and C–H (~2900 cm^{-1}) bands suggest chemical environment modifications at the matrix–fiber interface, possibly due to plasticisation and interfacial relaxation [23, 43].

The calculated absorbance ratios showed in Table 6. *3* further support these interpretations. Before aging, the A_{O–H}/A_{CH_3} ratio increases from 0.13 (0% fiber) to nearly 4.9 for all flax composites, while the A_{C=O}/A_{C–O} ratio rises from 0.48 to about 1.2, confirming that flax incorporation enhances hydrogen bonding and modifies the balance of functional groups. After aging, both ratios remain elevated, but a slight decrease is observed with increasing fiber content. This trend may be attributed to saturation of hydroxyl sites, restricted water diffusion in denser fiber networks, and matrix–fiber debonding during hydrothermal exposure. These effects collectively reduce the relative increase in hydrogen bonding and carbonyl interactions at higher fiber loadings.

The presence of lignin in flax fibers is identified by the C=C stretching vibration near 1530 cm^{-1}, associated with aromatic syringyl and guaiacyl units [44]. After aging, minor changes in this band may indicate subtle conformational or hydration-related alterations in lignin structure.

In conclusion, FTIR analysis confirms that flax fiber reinforcement introduces additional functional

groups and promotes hydrogen bonding within the composite. Aging in hot water increases moisture uptake and alters the chemical environment of both the polymer matrix and the fiber components. The observed evolution of absorbance ratios highlights that natural fiber composites are more prone to water-related plasticisation and interfacial modifications, which may ultimately compromise their long-term performance in humid environments.

Table 6. 3: Absorbance ratios (A_{O–H}/A_{CH₃} and A_{C=O}/A_{C–O}) of PLA-75/PETG-25 and flax fiber-reinforced composites before and after hydrothermal aging.

Fiber content (wt%)	Before aging		After aging	
	A_{O–H}/A_{CH₃}	A_{C=O}/A_{C–O}	A_{O–H}/A_{CH₃}	A_{C=O}/A_{C–O}
0	0.126	0.478	4.875	1.307
5	4.843	1.124	4.712	1.057
10	4.918	1.205	4.605	1.023
15	4.896	1.127	4.550	0.990

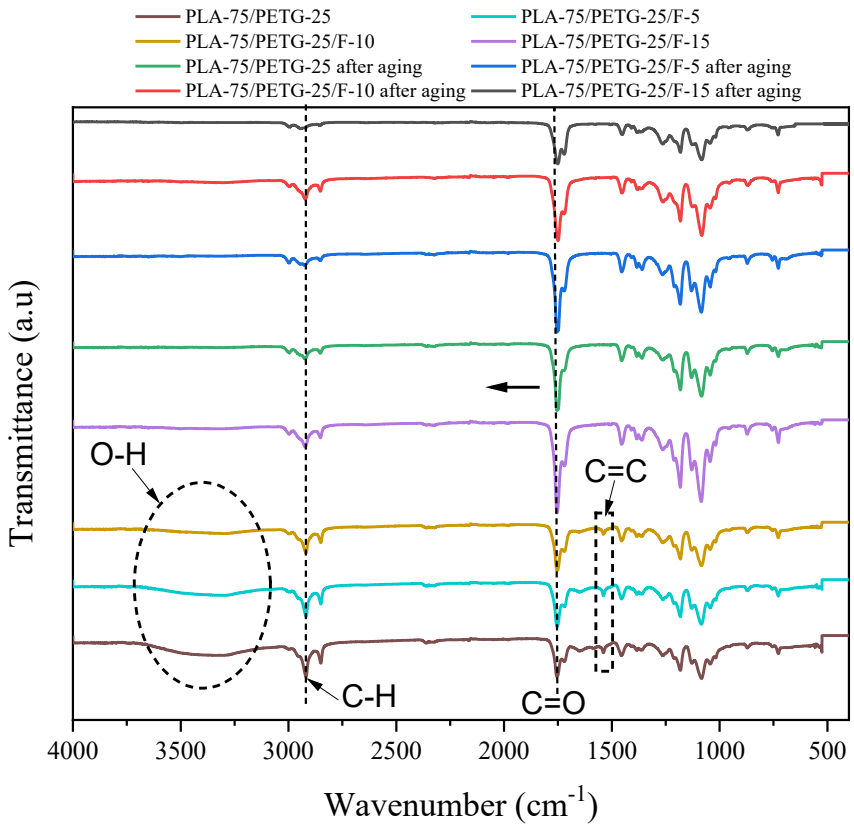

Figure 6.6: FTIR spectra of PLA-75/PETG-25 polymer blend and flax fiber reinforced polymer composites before and after aging in hot water.

6.4.4 X-Ray Diffraction analysis

The X-ray diffraction (XRD) patterns shown in Figure 6.7 provide insights into the structural organization of the PLA/PETG blend and its flax fiber-reinforced composites before and after hot water exposure.

The unreinforced PLA-75/PETG-25 blend exhibits a broad amorphous halo in the 15–25° 2θ range, indicating its predominantly amorphous nature. A minor diffraction peak is observed at approximately 16–20° 2θ, which corresponds to the semi-crystalline domains of PLA. This finding aligns with previous studies, which have reported that PLA exhibits low crystallinity due to its slow crystallization rate [45, 46]. Since PETG is inherently amorphous, its incorporation into the blend does not contribute to the formation of additional crystalline phases, thereby maintaining the overall semi-crystalline/amorphous structure.

Upon flax fiber addition (5, 10, 15 wt%), more pronounced peaks appear in the 16–22° 2θ region. These reflections can be attributed both to the crystalline phases of flax fibers, with characteristic signals at 16.5° (110) and 22.6° (200) [47], and to a nucleating effect that enhances PLA crystallization. Similar behavior has been reported in other natural fiber-reinforced biocomposites [15, 48, 49]. These observations are consistent with the FTIR results, where stronger O–H absorption indicated enhanced hydrogen bonding due to fiber incorporation.

After hot water aging, distinct changes are observed. The diffractograms of the unreinforced PLA/PETG blend, initially amorphous, show the appearance of sharper peaks in the 16–22° region. This can be explained by a secondary recrystallization of PLA induced by water plasticization: immersion at 45 °C increases chain mobility below glass transition temperature T_g, allowing shorter segments generated by hydrolysis to reorganize into crystalline domains [50, 51]. In the fiber-reinforced composites, peak broadening in the same region reflects structural reorganization, in line with FTIR evidence of stronger O–H signals and bound water interactions.

In conclusion, XRD results show that flax fibers introduce crystalline reflections and promote PLA nucleation in the composites, while hydrothermal exposure triggers secondary recrystallization in the neat PLA/PETG blend and structural reorganization in the composites. These findings,

consistent with FTIR observations, confirm that water aging simultaneously induces hydrolytic degradation and facilitates molecular rearrangement within the polymer matrix.

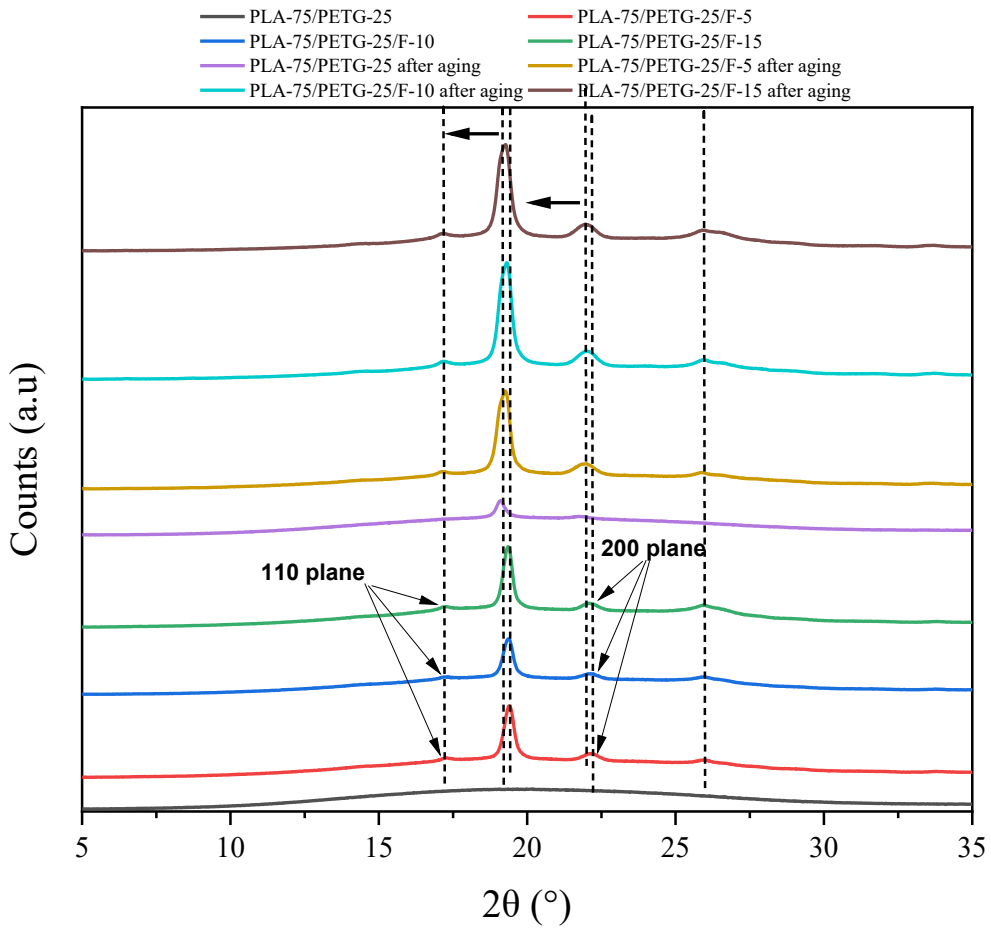

Figure 6.7: XRD patterns of PLA-75/PETG-25 polymer blend and flax fiber reinforced polymer composites before and after aging in hot water.

6.5 Effect of aging on shape memory performances

The shape memory performance of PLA/PETG polymer blends and flax fiber-reinforced PLA/PETG composites before and after aging in hot water is illustrated in Figure 6.8 and Figure 6.9. The results highlight the impact of fiber content on shape fixity, shape recovery, and recovery time, providing insights into the degradation mechanisms influencing shape memory behavior.

Before immersion in hot water (Figure 6.8 (a)), the PLA/PETG blend and its fiber-reinforced composites exhibited good shape memory behavior, with clear shape fixation and subsequent recovery upon reheating. However, after hot water aging (Figure 6.8 (b)), a noticeable decrease in shape fixity of all samples and post-recovery bending was observed in the PLA/PETG blend,

indicating a loss in mechanical integrity. This bending effect can be attributed to hydrolytic degradation, differential swelling, and plasticization effects, as discussed in previous studies [52-54]. The flax fiber-reinforced composites exhibited improved shape stability, suggesting that fiber reinforcement mitigates degradation effects by enhancing structural rigidity [55].

The quantitative evaluation of shape fixity (S_f) and shape recovery (S_r) in Figure 6.9 further supports these observations. Indeed, before aging (Figure 6.9 (a)), the shape fixity ratio of PLA/PETG composites remains relatively high across all fiber contents, maintaining values of 100%. This indicates that the addition of flax fibers does not significantly impact the material's ability to fix a temporary shape.

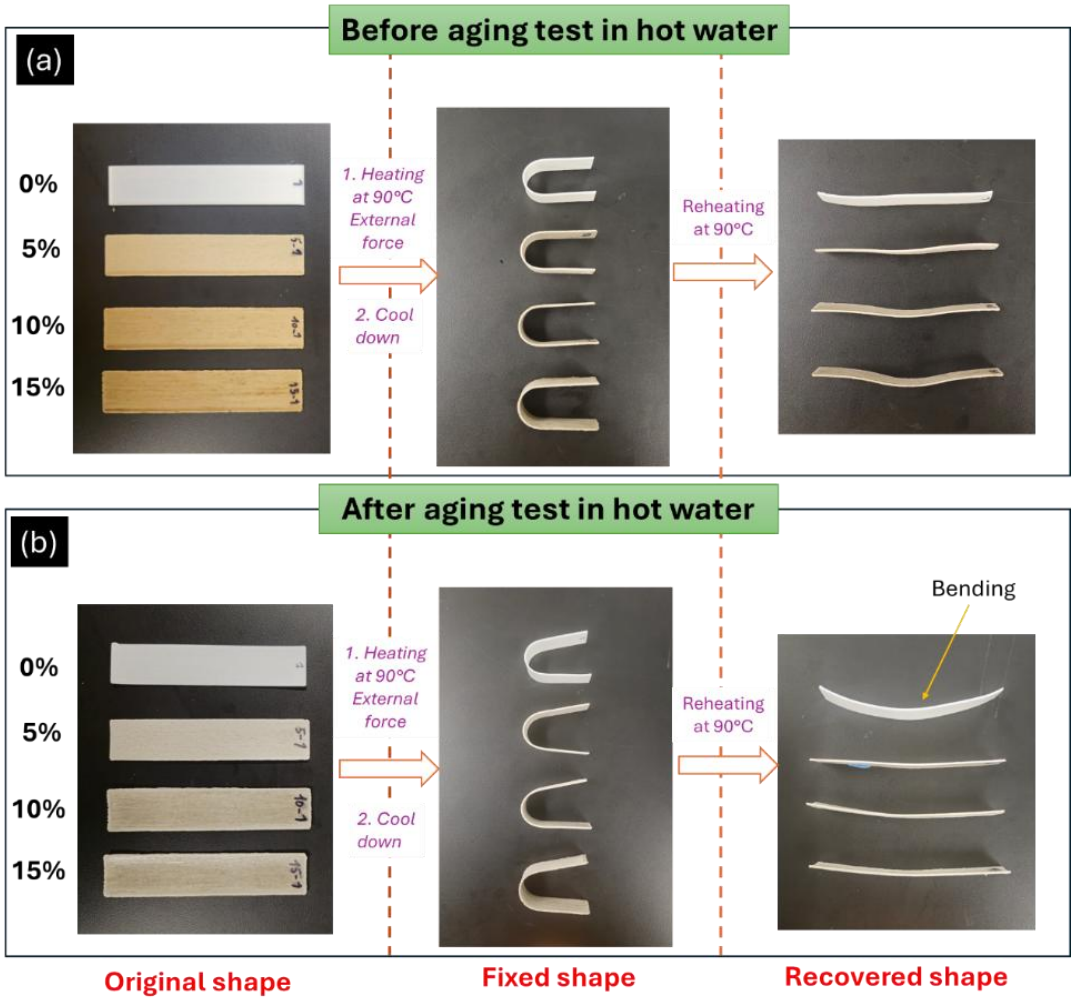

Figure 6.8: Shape memory performance of PLA/PETG polymer blend and flax fiber-reinforced PLA/PETG composite: (a) Before saturation in hot water and (b) After saturation in hot water.

However, after aging in hot water (Figure 6.9 (b)), a slight decrease in S_f is observed, particularly in fiber-reinforced composites. The reduction is more pronounced in higher fiber content samples, with the 15% fiber-reinforced composite showing a drop to approximately 90%. This decrease suggests that prolonged exposure to water at elevated temperatures affects the polymer-fiber interface, leading to increased plasticization and reduced structural integrity. Studies on hydrothermal aging of bio-composites have reported similar degradation effects, where moisture absorption weakens interfacial adhesion [56, 57], ultimately reducing shape fixity.

On the other hand, the shape recovery (S_r) before aging exhibits a small decreasing trend with increasing fiber content. While pure PLA/PETG shows a S_r of nearly 100%, composites with 15% fiber content demonstrate a reduced S_r of about 93%. The reduction can be attributed to the presence of rigid flax fibers, which restrict the mobility of polymer chains during shape recovery. Fiber reinforcement in shape memory polymers (SMPs) often leads to a trade-off between mechanical reinforcement and shape recovery efficiency, as previously discussed in studies on fiber-reinforced SMPs [27].

After aging in hot water, the recovered shape of the PLA/PETG polymer blend exhibited bending, which can be attributed to several key factors, including hydrolytic degradation, differential swelling, and plasticization of the polymer matrix [28]. Additionally, as a biodegradable polyester, PLA is particularly prone to hydrolytic degradation when exposed to moisture and elevated temperatures, leading to a loss of mechanical integrity [58]. This degradation induces non-uniform stress distribution during recovery, ultimately causing permanent deformation or bending. In contrast, no significant changes in S_r were observed in flax fiber-reinforced PLA/PETG polymer composites, aligning perfectly with previous studies [59, 60].

The recovery time, represented in Figure 6.9, shows an increasing trend with fiber content before aging, indicating that higher fiber reinforcement slows down the shape recovery process. The presence of fibers likely introduces mechanical constraints that hinder the molecular relaxation necessary for rapid shape recovery. However, after aging, the recovery time slightly decreases for some fiber-reinforced samples. This may be attributed to several interrelated factors. One primary reason is matrix softening due to water absorption, where water acts as a plasticizer, reducing intermolecular forces and increasing molecular mobility.

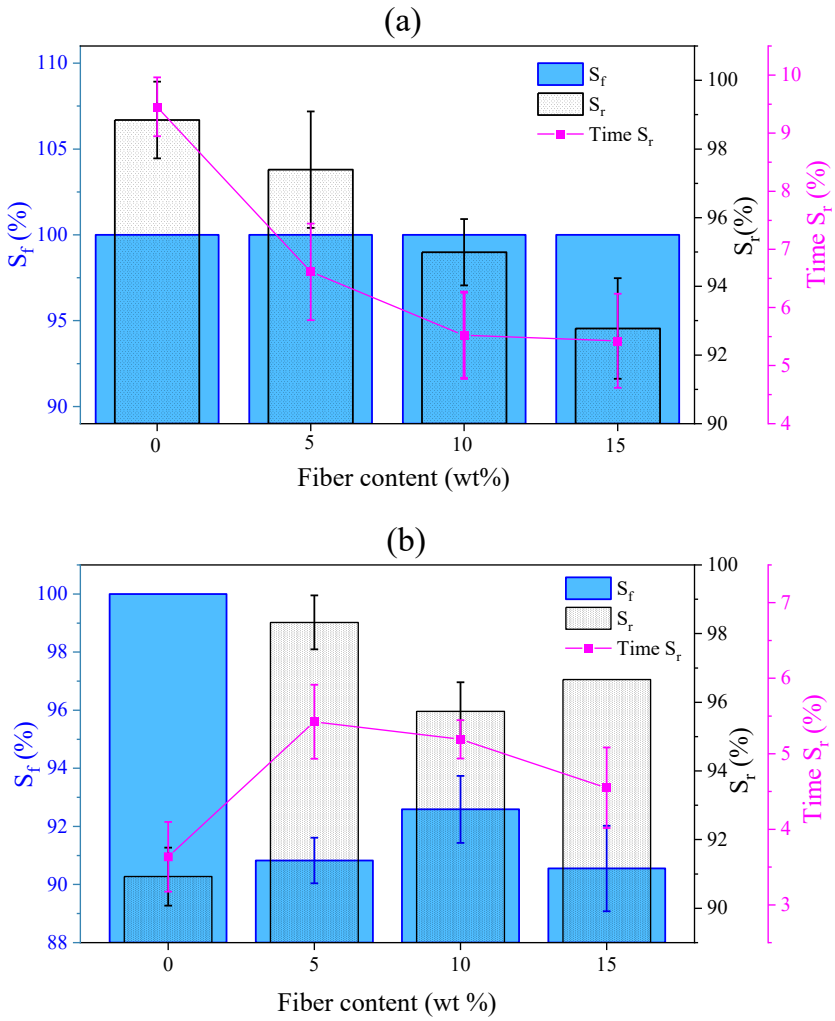

Figure 6.9: Influence of fiber content on shape fixity, shape recovery, and recovery time of PLA/PETG composites (a) before and (b) after aging in hot water.

This enhanced chain relaxation facilitates faster shape recovery despite potential degradation effects [61, 62]. Additionally, a reduction in interfacial adhesion between the fibers and polymer matrix occurs due to fiber swelling or hydrolytic degradation of bonding agents, which weakens the mechanical constraints imposed by the fibers, thereby accelerating the recovery process [63]. Another contributing factor is partial degradation of the polymer matrix, especially in biodegradable polymers like PLA, where hydrolysis leads to polymer chain scission and a consequent decrease in stiffness as reported in section 6.2, allowing for faster shape relaxation [64]. This was confirmed by FTIR and XRD analyses. Furthermore, the release of internal stresses accumulated during manufacturing or deformation can occur over time, reducing resistance to shape recovery. Finally, increased polymer mobility at elevated temperatures during hot water immersion may lower the glass transition temperature (T_g) of certain polymers, further softening the matrix and facilitating

shape recovery [28]. These combined effects explain the observed reduction in recovery time following exposure to hot water.

6.6 Scanning Electron Microscopy (SEM)

The SEM observations reveal key differences in the microstructure of 3D-printed PLA-75/PETG-25 samples before and after hot water immersion. Before immersion, the fracture surfaces (images a, b, c) show well-defined filament layers with strong interlayer adhesion, particularly attributed to the PLA-rich matrix. Figure 6.10 (a) exhibits a compact morphology with aligned deposition layers, characteristic of PLA's rigid and brittle nature, which promotes clean stacking during the printing process. In Figure 6.10 (b), a more heterogeneous internal structure is visible, reflecting partial miscibility between PLA and PETG phases as reported in our previous study [16]. PETG, being more ductile and amorphous, likely forms softer, embedded domains within the PLA matrix. At higher magnification Figure 6.10 (c) dispersed microspheres and voids are apparent, suggesting some degree of interfacial incompatibility and phase separation between the two polymers. This morphology is consistent with literature findings showing that PLA/PETG blends tend to form phase-separated structures with poor interfacial bonding [4].

After immersion in hot water, major degradation features are observed (Figure 6.10 (d–g)). In image (d), the macroscopic structure reveals delamination between printed layers and swelling of the overall sample. This degradation is primarily due to the hydrolysis of PLA, which is highly susceptible to moisture and elevated temperatures. The loss of mechanical integrity and increased porosity are consistent with the known behavior of PLA under hydrothermal aging [65]. Figure 6.10 (e) shows a mixture of brittle and ductile fracture zones: smooth, flat surfaces from brittle PLA rupture coexist with elongated, fibrillated PETG structures. This ductile fracture behavior from PETG is crucial for energy absorption and partially mitigates the embrittlement caused by PLA degradation. Similarly, Figure 6.10 (f) reveals broken and pulled-out fibers surrounded by a fractured matrix, confirming mixed-mode failure fragile in PLA regions and ductile in PETG-rich domains.

The high-magnification micrograph in Figure 6.10 (g) further supports this interpretation, displaying PETG filaments with rough and deformed fracture ends, indicating plastic deformation before rupture. Conversely, the PLA matrix appears fragmented and brittle, with no signs of yielding. These results align with previous studies, which demonstrate that immersion in hot water significantly

weakens the matrix/fiber interface and reduces interlaminar strength, especially in PLA-based composites [66]. Water-induced degradation leads to decreased glass transition temperature and storage modulus, accelerating microcrack propagation and fiber debonding under stress.

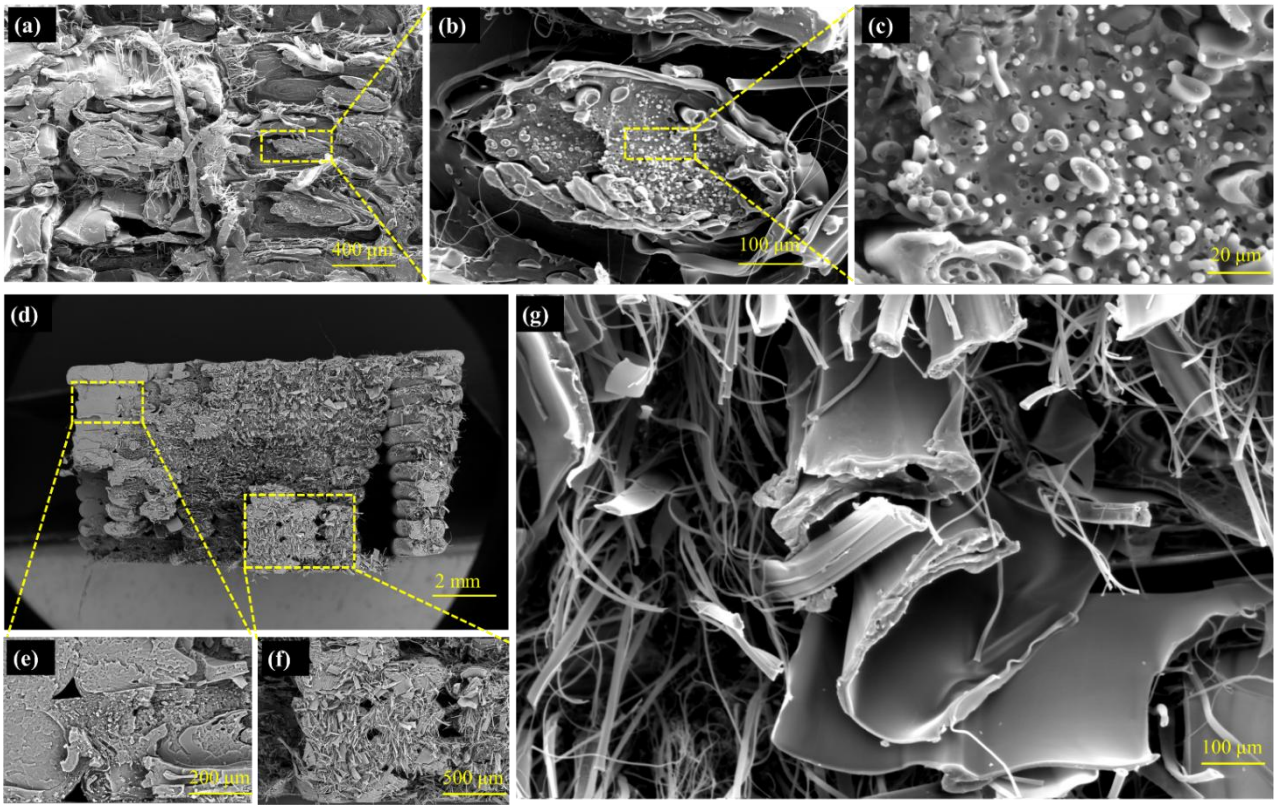

Figure 6.10: SEM micrographs of fractured 3D-printed tensile specimens made from PLA-75% / PETG-25% polymer blend before hot water aging (a, b, and c) and after hot water aging (d, e, f, g, and h).

Overall, SEM analysis highlights the detrimental effect of hot water immersion on the mechanical integrity of PLA/PETG composites. The PLA component undergoes hydrolysis and embrittlement, while PETG retains some ductility and contributes to ductile fracture mechanisms. The coexistence of brittle and ductile fracture features in the same fracture plane reflects the dual-phase behavior and underscores the importance of phase compatibility and moisture resistance in biopolymer blends [67].

The SEM micrographs clearly highlight substantial microstructural changes and variations in fiber–matrix interactions in the flax-reinforced PLA-75/PETG-25/F-5 composite before and after thermal aging. Before aging (Figure 6.11 (a-c)) partially bonded fibers surrounded by the PLA-rich matrix. However, gaps and interface discontinuities can already be seen, indicating limited interfacial compatibility between the hydrophilic flax fibers and the hydrophobic polymer matrix, a known

issue in natural fiber composites [68].

Figure 6.11 (b) and (c), higher magnification reveals relatively smooth fiber surfaces with minimal signs of damage or fibrillation. This suggests that before heat exposure, the flax fibers retain their structural integrity, and the polymer matrix (primarily PLA, with PETG providing minor ductility) remains mechanically stable. However, the clean fiber-matrix interface suggests a lack of strong adhesion, which can result in early debonding under stress.

After thermal aging, significant morphological changes are evident. Figure 6.11 (d) displays a macroscopic cross-section of the printed structure, where delamination between deposited filament layers is visible. This is likely due to the hydrolytic degradation of PLA, which is known to undergo molecular scission when exposed to heat and humidity, weakening interlayer bonding [69].

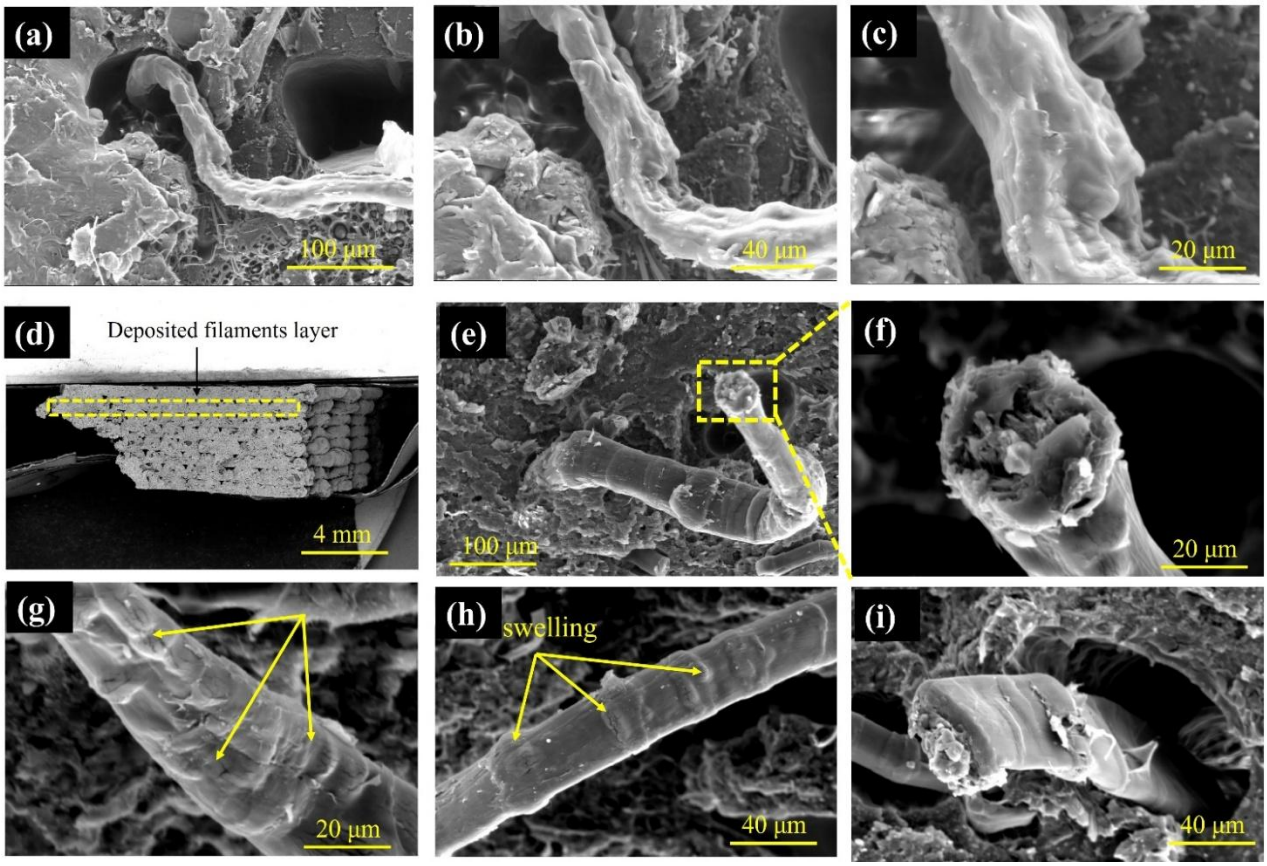

Figure 6.11: SEM micrographs of fractured 3D-printed tensile specimens made from PLA-75% / PETG-25%/F-5 reinforced polymer blend before hot water aging (a, b, and c) and after hot water aging (d, e, f, g, h, and i).

Figure 6.11 (e) captures a single flax fiber pulled out from the matrix, with the enlarged view (f)

showing a rough and damaged fiber end, indicative of fiber-matrix debonding. This highlights the mechanical weakening of the interface after aging, likely due to increased fiber swelling and matrix shrinkage, which reduces adhesion [70].

In Figure 6.11 (g), the fiber surface shows longitudinal cracks, evidence of brittle failure likely exacerbated by thermal-induced embrittlement of the PLA matrix.

Figure 6.11 (h) highlights localized swelling of the flax fiber, attributed to heat and moisture absorption, leading to internal fiber expansion and further interfacial stress. Swelling increases porosity and disrupts the continuity of the fiber-matrix interface, a behavior frequently documented in natural fiber-reinforced thermoplastics [71]. Finally, Figure 6.11 (i) shows a severely damaged flax fiber with visible delamination and separation from the surrounding matrix. This kind of morphology confirms a transition from initially intact bonding to complete mechanical failure, caused by hydrothermal aging effects such as hydrolysis, shrinkage, and loss of interfacial cohesion.

The microstructure of the composite with 10% flax fibers before immersion reveals a relatively dense fiber network with signs of porosity, but also zones of effective fiber-matrix bonding. In Figure 6.12 (a), although some pores and fiber pull-out regions are visible, the structure shows acceptable integrity, with no signs of large-scale delamination.

Figure 6.12 (b) highlights numerous embedded flax fibers, and the presence of microcracks in the surrounding matrix suggests localized stress during tensile loading. These cracks likely initiate at interfacial weaknesses or voids, which become more critical at higher fiber loading. However, Figure 6.12 (c) provides compelling evidence of good interfacial adhesion between the flax fiber and the polymer matrix. The fiber appears well-coated and tightly bonded to the surrounding material, with no visible interfacial gap or signs of early detachment. This strong adhesion helps transfer stress from the matrix to the fiber effectively, which contributes to mechanical reinforcement before aging. Compared to lower fiber content (e.g., 5%), this sample exhibits more visible contact and interlocking, despite the increased risk of porosity. This agrees with mechanical results that show a slight increase in stiffness and tensile strength before immersion for 10% flax composites.

After thermal aging, significant degradation is evident. In Figure 6.12 (d), slight layer separation and increased macroporosity are visible, indicating that hydrothermal exposure has compromised the interlayer cohesion, especially within the PLA-rich matrix. PLA is particularly prone to hydrolysis, and the presence of hydrophilic flax fibers amplifies water uptake. On the other hand,

Figure 6.12 (e) shows fiber debonding and partial pull-out, with a matrix that appears fractured and degraded. This marks a transition from good pre-immersion adhesion (as in image c) to interfacial failure post-aging. The degradation reduces stress transfer and mechanical efficiency of the fiber reinforcement. Figure 6.12 (f) further illustrates this with a swollen, cracked flax fiber, clearly affected by water-induced expansion. The surface shows longitudinal fissures, and the surrounding matrix seems detached and weakened. This degradation pathway aligns with mechanical test data that show a loss of tensile strength and ductility after immersion in high-humidity or thermal environments [68, 72].

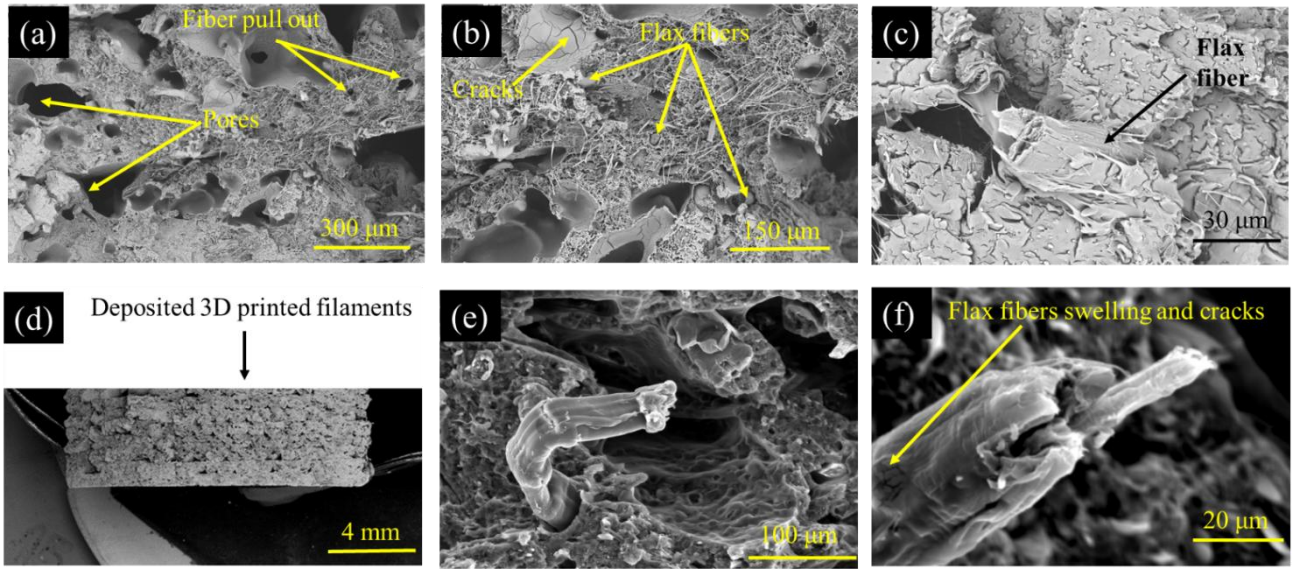

Figure 6.12: SEM micrographs of fractured 3D-printed tensile specimens made from PLA-75% / PETG-25%/F-10 reinforced polymer blend before hot water aging (a, b, and c) and after hot water aging (d, e, and f).

SEM micrographs of the PLA-75%/PETG-25% blend reinforced with 15% flax fibers show significant morphological changes associated with high fiber loading. Figure 6.13 (a) reveals numerous inter-filament voids and large pores, indicating a high porosity level due to fiber clustering and reduced matrix continuity. This is a direct result of excessive fiber content exceeding the polymer's wetting capability. Despite the porosity, the network of densely packed flax fibers observed in Figure 6.13 (b) contributes to increased stiffness; this is consistent with a higher Young's modulus reported in mechanical tests. The presence of a rigid, continuous fiber network enables better resistance to deformation. Furthermore, Figure 6.13 (c) highlights both embedded and partially debonded flax fibers. Although some fibers show good adhesion with the matrix, the abundance of voids and imperfect fiber dispersion results in stress concentrations and early crack

initiation, leading to brittle failure under tensile load before aging. These observations align with mechanical test results showing an increase in stiffness but a decrease in ultimate tensile strength before thermal aging compared to the unreinforced PLA-75/PETG-25 polymer blend.

Thermal aging in hot water significantly amplifies the degradation of the 15% flax fiber composite. Figure 6.13 (d) shows the macroscopic morphology of the 3D-printed tensile specimen after thermal aging. Although no clear signs of delamination between deposited layers are observed, the overall structure appears rougher and more porous. In addition, image (e) reveals severe porosity and fiber fragmentation, confirming that high fiber content facilitates water ingress and accelerates structural breakdown.

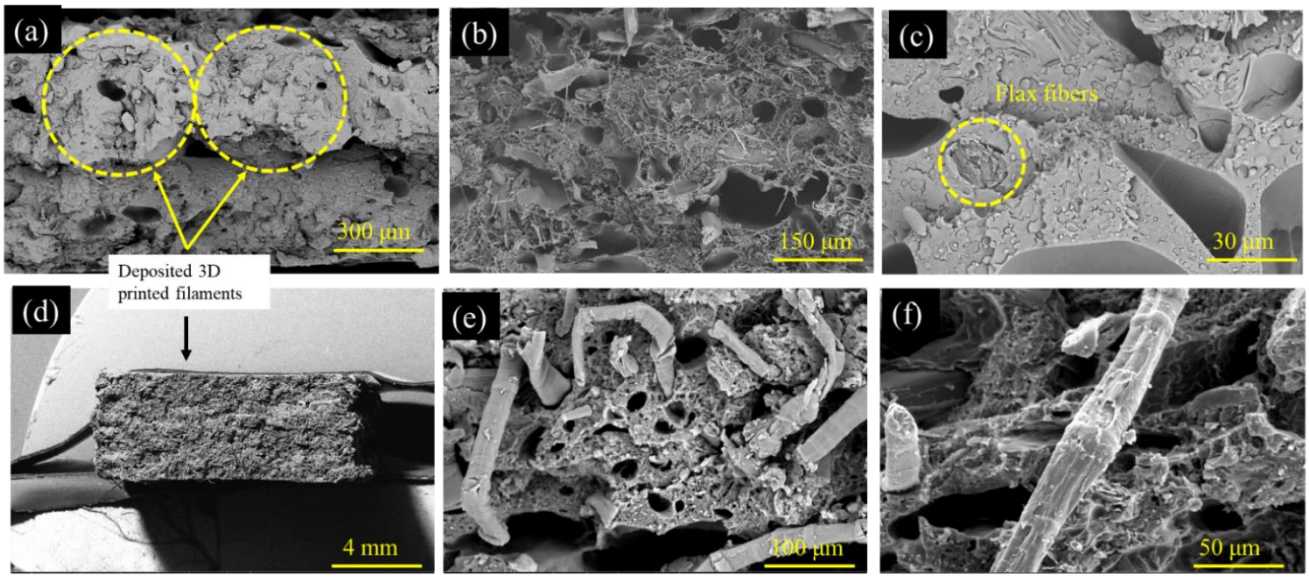

Figure 6.13: SEM micrographs of fractured 3D-printed tensile specimens made from PLA-75% / PETG-25%/F-15 reinforced polymer blend before hot water aging (a, b, and c) and after hot water aging (d, e, f, g, h, and i).

Compared to 5% and 10% fiber composites, the 15% sample exhibits the most intense microstructural damage after aging. Furthermore, Figure 6.13 (f) displays cracked and swollen flax fibers and a highly porous surrounding matrix. The fiber-matrix interface is visibly degraded, and fibers appear fractured or dislodged. These features explain the marked reduction in mechanical performance post-aging, especially in tensile strength and elongation at break.

The degradation phenomena discussed in this study are associated with hydrothermal aging in hot water at 45 °C, used as an accelerated aging environment. The results demonstrate the occurrence of PLA hydrolysis as part of the overall degradation process. This interpretation is supported by consistent experimental evidence: FTIR analysis (Figure 6.6) shows a reduction in the ester carbonyl

(C=O) band and an increase in hydroxyl (O–H) intensity, indicating ester bond cleavage; XRD patterns (Figure 6.7) reveal increased crystallinity after aging, consistent with chain scission and subsequent recrystallization; and SEM observations (Figure 6.10-13) highlight matrix embrittlement, interlayer delamination, and fiber–matrix debonding, which are characteristic features of hydrolytic degradation. These observations are in good agreement with previously reported studies on PLA degradation under humid and thermal conditions [50, 51, 54].

6.7 Conclusions

This study investigates the effects of hot-water aging on the mechanical properties and shape-memory behavior of flax fiber–reinforced PLA/PETG composites fabricated by 4D printing. It addresses the critical challenge of functional durability in natural fiber–reinforced systems exposed to humid environments. The novelty of this work lies in providing the first systematic demonstration of how hydrothermal aging influences shape-memory performance in flax fiber–reinforced PLA/PETG composites within the context of 4D printing, thereby filling an unaddressed gap in the current literature.

6.8 Key Findings:

- **Water Absorption:** Flax fiber addition markedly increases moisture uptake, rising from < 2 % for the neat PLA/PETG blend to ≈ 20 % for the 15 wt% composite after 67 days, due to fiber hygroscopicity, leading to fiber swelling, interfacial degradation, and increased porosity.
- **Mechanical Properties:** Fiber reinforcement enhances initial stiffness (Young's modulus from 3.6 to ≈ 4.0 GPa at 15 wt%) but reduces tensile strength (from 60.5 to 40 MPa) and results in severe losses after hydrothermal aging at 45 °C, with stiffness and strength decreasing by 44 % and 69 %, respectively.
- **Shape Memory Behavior:** Before aging, all composites exhibited 100% shape fixity, indicating excellent shape retention. After aging, the shape fixity of the 15 wt% fiber composite decreased to 90%, and shape recovery slightly reduced from 100% (unreinforced) to 93% (15% fiber content). Additionally, aging led to a reduction in recovery time, suggesting that water-induced plasticization affects actuation speed.
- **Material Degradation:** FTIR and XRD analyses showed that hot water aging causes important changes in PLA/PETG and flax fiber composites. FTIR revealed water uptake, stronger hydrogen bonding, and ester hydrolysis, while XRD indicated structural reorganization,

including secondary recrystallization in PLA and peak broadening in the composites.

Overall, this study demonstrates that shape-memory functionality can be partially preserved despite severe hydrothermal degradation, thereby establishing functional durability as a critical and independent design parameter for 4D-printed natural fibre–reinforced composites. These findings provide a robust basis for the rational design of bio-based 4D-printed structures intended to operate under humid environmental conditions.

6.9 References

1. Khalid, M.Y., et al., 4D printing of shape memory polymer composites: A review on fabrication techniques, applications, and future perspectives. Journal of Manufacturing Processes, 2022. 81: p. 759-797.
2. Abdelhamid, Z., H. Mohamed, and S. Kelouwani, The use of machine learning in process–structure–property modeling for material extrusion additive manufacturing: a state-of-the-art review. Journal of the Brazilian Society of Mechanical Sciences and Engineering, 2024. 46(2): p. 70.
3. Li, J., et al., A comprehensive review on 4D printing and applications of thermo-induced shape memory polymers. International Journal of Smart and Nano Materials, 2025: p. 1-60.
4. Bouguermouh, K., et al., Designing advanced 4D printing thermo-sensitive shape memory polymer blends for enhanced mechanical and shape memory performances. Progress in Additive Manufacturing, 2025: p. 1-20.
5. Kouka, M.A., et al., 4D printing of shape memory polymers, blends, and composites and their advanced applications: a comprehensive literature review. Advanced Engineering Materials, 2023. 25(4): p. 2200650.
6. Megdich, A., M. Habibi, and L. Laperrière, A review on 4D printing: material structures, stimuli and additive manufacturing techniques. Materials Letters, 2023. 337: p. 133977.
7. Prem Kumar, C., et al., Shape Memory Polymers, Blends, and Composites: Processing, Properties, and Applications. Polymer-Plastics Technology and Materials, 2025: p. 1-29.
8. Jamaludin, F.H., et al., Recent Advances in the Field of Shape-Memory Polymer from Bio-Based Precursors: Review and Perspective. Polymer Reviews, 2025. 65(1): p. 199-249.
9. Bouguermouh, K., M. Habibi, and L. Laperrière, 4D printing of fiber-reinforced auxetic structures: the building blocks: a review. Smart Materials and Structures, 2024.
10. Le Duigou, A., et al., A review of 3D and 4D printing of natural fibre biocomposites. Materials & Design, 2020. 194: p. 108911.
11. Le Duigou, A., et al., 3D printing of wood fibre biocomposites: From mechanical to actuation functionality. Materials & Design, 2016. 96: p. 106-114.
12. Ram Kishore, S., et al., Natural fiber biocomposites via 4D printing technologies: A review of possibilities for agricultural bio-mulching and related sustainable applications. Progress in Additive Manufacturing, 2024. 9(1): p. 37-67.
13. Mayandi, K., et al., Recent studies on durability of natural/synthetic fiber reinforced hybrid polymer composites, in Durability and life prediction in biocomposites, fibre-reinforced composites and hybrid composites. 2019, Elsevier. p. 1-13.
14. Dhakal, H., et al., Effects of water immersion ageing on the mechanical properties of flax and jute fibre biocomposites evaluated by nanoindentation and flexural testing. Journal of Composite Materials, 2014. 48(11): p. 1399-1406.
15. Bouguermouh, K., et al., Advanced 4D Printing of Flax Fiber-Reinforced PLA/PETG Blends for Enhanced Mechanical, Thermal, and Shape Memory Properties. Polymer, 2025: p. 128587.
16. Bouguermouh, K., et al., 4D-printed PLA-PETG polymer blends: comprehensive analysis of thermal, mechanical, and shape memory performances. Journal of Materials Science, 2024. 59(25): p. 11596-11613.
17. Thirugnanasambandam, A., et al., Development of 3D printed novel multi-polymer component based on blended filaments of polylactic acid and polyethylene terephthalate glycol. Progress in Additive Manufacturing, 2024: p. 1-14.

18. Kesentini, Z., et al., Effect of hydric aging on the static and vibration behavior of 3D printed bio-based flax fiber reinforced poly-lactic acid composites. Polymers and Polymer Composites, 2022. 30: p. 09673911221081826.
19. Habibi, M., L. Laperrière, and H.M. Hassanabadi, Effect of moisture absorption and temperature on quasi-static and fatigue behavior of nonwoven flax epoxy composite. Composites Part B: Engineering, 2019. 166: p. 31-40.
20. Athijayamani, A., et al., Effect of moisture absorption on the mechanical properties of randomly oriented natural fibers/polyester hybrid composite. Materials Science and Engineering: A, 2009. 517(1-2): p. 344-353.
21. Li, Y. and B. Xue, Hydrothermal ageing mechanisms of unidirectional flax fabric reinforced epoxy composites. Polymer degradation and stability, 2016. 126: p. 144-158.
22. Mohammed, M., et al., Challenges and advancement in water absorption of natural fiber-reinforced polymer composites. Polymer Testing, 2023. 124: p. 108083.
23. Van Schoors, L., et al., Effect of water on the characteristics of polyethylene/flax fibers composites. Academic Journal of Civil Engineering, 2017. 35(2): p. 440-444.
24. Thomason, J.L. and G. Xypolias, The effect of environmental ageing on the interphase in glass fibre–vinyl ester composites. Composite Interfaces, 2023. 30(4): p. 377-391.
25. Regazzi, A., et al., Modeling of hydrothermal aging of short flax fiber reinforced composites. Composites Part A: Applied Science and Manufacturing, 2016. 90: p. 559-566.
26. Starkova, O., et al., Hydrothermal ageing effect on reinforcement efficiency of nanofibrillated cellulose/biobased poly (butylene succinate) composites. Polymers, 2022. 14(2): p. 221.
27. Madbouly, S.A. and A. Lendlein, Shape-memory polymer composites. Shape-memory polymers, 2010: p. 41-95.
28. Garces, I.T., et al., Effect of moisture on shape memory polyurethane polymers for extrusion-based additive manufacturing. Materials, 2019. 12(2): p. 244.
29. Habibi, M., et al., Combining short flax fiber mats and unidirectional flax yarns for composite applications: Effect of short flax fibers on biaxial mechanical properties and damage behaviour. Composites Part B: Engineering, 2017. 123: p. 165-178.
30. Ziadia, A., M. Habibi, and S. Kelouwani, Machine learning study of the effect of process parameters on tensile strength of FFF PLA and PLA-CF. Eng, 2023. 4(4): p. 2741-2763.
31. Scida, D., et al., Influence of hygrothermal ageing on the damage mechanisms of flax-fibre reinforced epoxy composite. Composites Part B: Engineering, 2013. 48: p. 51-58.
32. Retegi, A., et al., Effects of hygrothermal ageing on mechanical properties of flax pulps and their polypropylene matrix composites. Journal of applied polymer science, 2006. 102(4): p. 3438-3445.
33. Moudood, A., et al., Flax fiber and its composites: An overview of water and moisture absorption impact on their performance. Journal of Reinforced Plastics and Composites, 2019. 38(7): p. 323-339.
34. Chilali, A., et al., Effect of geometric dimensions and fibre orientation on 3D moisture diffusion in flax fibre reinforced thermoplastic and thermosetting composites. Composites Part A: Applied Science and Manufacturing, 2017. 95: p. 75-86.
35. Karaduman, Y. and L. Onal, Water absorption behavior of carpet waste jute-reinforced polymer composites. Journal of Composite Materials, 2011. 45(15): p. 1559-1571.
36. Alam, S., et al., Comparative analysis of water-induced response in 3D-printed SCF/ABS composites under controlled diffusion. SAMPE Journal, 2024. 60(4): p. 16.

37. Sekar, S., et al., Evaluation of mechanical and water absorption behavior of natural fiber-reinforced hybrid biocomposites. Journal of Natural Fibers, 2022. 19(5): p. 1772-1782.
38. Ainin, F.N., et al., The influence of water absorption on the mechanical performance of 3D-printed sandwich composite structures made from PLA-based materials under quasi-static loading conditions. Polymer Composites.
39. Sathish, S., et al., Experimental investigation on volume fraction of mechanical and physical properties of flax and bamboo fibers reinforced hybrid epoxy composites. Polymers and Polymer Composites, 2017. 25(3): p. 229-236.
40. Mak, K. and A. Fam, The effect of wet-dry cycles on tensile properties of unidirectional flax fiber reinforced polymers. Composites Part B: Engineering, 2020. 183: p. 107645.
41. Pannico, M. and P. La Manna, Sorption of water vapor in poly (L-lactic acid): A time-resolved FTIR spectroscopy investigation. Frontiers in chemistry, 2019. 7: p. 275.
42. Dhakal, H.N., Z.a. Zhang, and M.O. Richardson, Effect of water absorption on the mechanical properties of hemp fibre reinforced unsaturated polyester composites. Composites science and technology, 2007. 67(7-8): p. 1674-1683.
43. Panigrahy, B., et al. Overview of flax fiber reinforced thermoplastic composites. in 2006 ASAE Annual Meeting. 2006. American Society of Agricultural and Biological Engineers.
44. Salmén, L., J.S. Stevanic, and A.-M. Olsson, Contribution of lignin to the strength properties in wood fibres studied by dynamic FTIR spectroscopy and dynamic mechanical analysis (DMA). Holzforschung, 2016. 70(12): p. 1155-1163.
45. Heo, Y.R., Blending PLA (Poly-lactic acid) with layered silicates. 2013.
46. Inkinen, S., et al., From lactic acid to poly (lactic acid)(PLA): characterization and analysis of PLA and its precursors. Biomacromolecules, 2011. 12(3): p. 523-532.
47. Moriana, R., et al., Improved thermo-mechanical properties by the addition of natural fibres in starch-based sustainable biocomposites. Composites Part A: Applied Science and Manufacturing, 2011. 42(1): p. 30-40.
48. Xia, X., et al., Effect of flax fiber content on polylactic acid (PLA) crystallization in PLA/flax fiber composites. Iranian Polymer Journal, 2017. 26: p. 693-702.
49. Wang, G., et al., Strong and thermal-resistance glass fiber-reinforced polylactic acid (PLA) composites enabled by heat treatment. International journal of biological macromolecules, 2019. 129: p. 448-459.
50. Cisar, J., et al., Changes in the Thermal and Structural Properties of Polylactide and Its Composites During a Long-Term Degradation Process. Polymers, 2025. 17(10): p. 1326.
51. Kobayashi, Y., et al., Changes in crystal structure and accelerated hydrolytic degradation of polylactic acid in high humidity. Polymers, 2021. 13(24): p. 4324.
52. Kaseem, M., et al., Material properties of polyethylene/wood composites: A review of recent works. Polymer Science Series A, 2015. 57: p. 689-703.
53. Sambha'a, E., A. Lallam, and A. Jada, Effect of hydrothermal polylactic acid degradation on polymer molecular weight and surface properties. Journal of Polymers and the Environment, 2010. 18(4): p. 532-538.
54. Kamau-Devers, K., Z. Kortum, and S.A. Miller, Hydrothermal aging of bio-based poly (lactic acid)(PLA) wood polymer composites: Studies on sorption behavior, morphology, and heat conductance. Construction and Building Materials, 2019. 214: p. 290-302.
55. Joseph, A., et al., Effects of Hygrothermal Aging on the Mechanical Properties of the Biocomposites, in Aging Effects on Natural Fiber-Reinforced Polymer Composites: Durability and Life Prediction. 2022, Springer. p. 63-83.

56. Radhakrishnan, S., et al., Deterioration of polymer composites after water ageing of chemically treated and untreated biomass. Biomass Conversion and Biorefinery, 2024. 14(17): p. 19985-20016.
57. Glaskova-Kuzmina, T., et al., Durability of biodegradable polymer nanocomposites. Polymers, 2021. 13(19): p. 3375.
58. Darabian, B., H. Bagheri, and S. Mohammadi, Improvement in mechanical properties and biodegradability of PLA using poly (ethylene glycol) and triacetin for antibacterial wound dressing applications. Progress in Biomaterials, 2020. 9: p. 45-64.
59. Alsaadi, M., et al., Viscoelastic, Shape Memory, and Fracture Characteristics of 3D-Printed Photosensitive Epoxy-Based Resin Under the Effect of Hydrothermal Ageing. Journal of Manufacturing and Materials Processing, 2025. 9(2): p. 46.
60. Shao, Y.-l., et al., Wood as a hydrothermally stimulated shape-memory material: mechanisms of shape-memory effect and molecular assembly structure networks. Holzforschung, 2023. 77(6): p. 426-436.
61. Gamstedt, E.K. Moisture induced softening and swelling of natural cellulose fibres in composite applications. in IOP Conference Series: Materials Science and Engineering. 2016. IOP Publishing.
62. Chandrasekar, M., et al., A review on the characterisation of natural fibres and their composites after alkali treatment and water absorption. Plastics, Rubber and Composites, 2017. 46(3): p. 119-136.
63. Bradley, W. and T. Grant, The effect of the moisture absorption on the interfacial strength of polymeric matrix composites. Journal of materials science, 1995. 30: p. 5537-5542.
64. Taourit, S., P.-Y. Le Gac, and B. Fayolle, Relationship between network structure and ultimate properties in polyurethane during a chain scission process. Polymer degradation and stability, 2022. 201: p. 109971.
65. Bergaliyeva, S., et al., Effect of thermal and hydrothermal accelerated aging on 3D printed polylactic acid. Polymers, 2022. 14(23): p. 5256.
66. Fang, X., et al., Improved interfacial performance of bamboo fibers/polylactic acid composites enabled by a self-supplied bio-coupling agent strategy. Journal of Cleaner Production, 2022. 380: p. 134719.
67. Wasti, S. and S. Adhikari, Use of biomaterials for 3D printing by fused deposition modeling technique: a review. Frontiers in chemistry, 2020. 8: p. 315.
68. Manral, A., et al., Effect of water ageing on mechanical performance of Kenaf/PLA bio-composites. Biomass Conversion and Biorefinery, 2025. 15(4): p. 6113-6130.
69. Lv, C., et al., Properties of 3D printing fiber-reinforced geopolymers based on interlayer bonding and anisotropy. Materials, 2022. 15(22): p. 8032.
70. Ecker, J.V., et al., Mechanical properties and water absorption behaviour of PLA and PLA/wood composites prepared by 3D printing and injection moulding. Rapid Prototyping Journal, 2019. 25(4): p. 672-678.
71. Takemura, K., S. Takai, and H. Katogi, Natural Filler and Fibre Composites: Development and Characterisation 145. Natural Filler and Fibre Composites: Development and Characterisation, 2015. 87: p. 145.
72. Liu, Z. and B.H. Tisserat, Coating applications to natural fiber composites to improve their physical, surface and water absorption characters. Industrial Crops and Products, 2018. 112: p. 196-199.

Chapitre 7: Impression 4D de structures auxétiques à base de mélanges PLA/PETG renforcés par de la nanocellulose

Ce chapitre a fait l'objet d'une publication :

4D Printing of Auxetic Structures Using Nanocellulose Reinforced PLA/PETG blends. Bouguermouh Karima, Habibi Mohamed, Laperrière Luc and Daniel Monplaisir. Journal of Composite Science, November 2025.

Il peut être consulté en ligne à l'adresse suivante : https://doi.org/10.3390/jcs9110637

L'intégration de renforts naturels, comme la nanocellulose, dans des matrices polymères biosourcées représente une stratégie prometteuse pour le développement de matériaux intelligents et durables. Grâce à sa structure cristalline, sa grande surface spécifique et sa capacité à former des liaisons hydrogène avec les chaînes polymériques, la nanocellulose agit à la fois comme agent de renforcement mécanique et comme nucléant, influençant favorablement la microstructure et les performances globales du matériau. Dans le contexte de l'impression 4D, l'enjeu est d'obtenir des composites capables de répondre à des stimuli externes tout en maintenant une bonne stabilité dimensionnelle, des propriétés mécaniques renforcées et un comportement morpho-adaptatif fiable.

Le présent travail vise à concevoir des structures auxétiques anti-chirales imprimées en 4D à partir d'un mélange PLA/PETG (75/25) renforcé par différentes teneurs en nanocellulose (0, 1, 2 et 3 % en masse). L'objectif principal est d'exploiter les propriétés uniques de la nanocellulose pour améliorer simultanément la rigidité, la résistance mécanique et la mémoire de forme de ces structures complexes. Les résultats expérimentaux montrent que l'ajout de 2 % de nanocellulose permet d'atteindre un module d'élasticité de 3,3 GPa et une résistance à la traction de 56 MPa, marquant une amélioration significative par rapport à la formulation non renforcée. Par ailleurs, les structures auxétiques imprimées présentent une capacité de récupération de forme atteignant 90,8 %, et un taux de fixité de forme passant de 98,1 % à plus de 99,8 %, grâce à la formation d'un réseau de liaisons hydrogène stabilisant la forme temporaire. À 3 % de renfort, une légère baisse de la récupération est observée, attribuée à une réduction de la mobilité des chaînes et à une agglomération locale du nanofiller.

Sous compression, les structures auxétiques présentent un comportement mécanique en trois phases : élasticité initiale, flambage auxétique, puis densification. L'ajout de nanocellulose, tout en réduisant légèrement la rigidité globale, améliore nettement la résistance à la compression, avec une valeur maximale de 0.22 MPa à 1 % de nanocellulose. Ce comportement est lié à une distribution plus homogène des contraintes et à une déformation plus progressive, retardant la rupture structurale. Toutefois, à 3 %, l'agglomération des charges limite cette flexibilité.

Ces résultats démontrent que l'incorporation contrôlée de nanocellulose permet une maîtrise fine des propriétés mécaniques et fonctionnelles des structures imprimées en 4D. Les architectures auxétiques développées allient adaptabilité de forme, absorption d'énergie et durabilité, ce qui les rend particulièrement adaptées à des applications avancées telles que la robotique souple, les dispositifs portables, les échafaudages biomédicaux ou encore la protection contre les impacts. Leur porosité contrôlée et leur composition biosourcée ouvrent également des perspectives pour des usages environnementaux comme la purification de l'eau. Ainsi, ce travail constitue une avancée à l'intersection de la science des matériaux, de la fabrication additive et de l'ingénierie verte, posant les bases de systèmes imprimés en 4D, intelligents, programmables et respectueux de l'environnement.

4D Printing of Auxetic Structures Using Nanocellulose Reinforced PLA/PETG blends

Karima Bouguermouh[1], Mohamed Habibi[1*], Amal Meghdich[1], Luc Laperrière[1], Daniel Monplaisir[2]

[1] Department of Mechanical Engineering, Université du Québec à Trois-Rivières, Québec, Canada.
[2] Department of Chemistry, Biochemistry and Physics, Université du Québec à Trois-Rivières, Québec, Canada

7.1 Abstract

This study explores the development of 4D-printed smart structures based on PLA/PETG (75/25) polymer blends reinforced with nanocellulose (0–3 wt%), processed using fused filament fabrication (FFF). Both conventional U-shaped specimens and anti-tri-chiral auxetic architectures were fabricated to evaluate the effects of nanocellulose on mechanical performance and shape memory behavior. Tensile tests demonstrated that nanocellulose reinforcement enhanced both strength and stiffness, with the highest values observed at 2 wt% (tensile strength of 56 MPa and Young's modulus of 3.3 GPa). In standard U-shaped samples, all compositions showed excellent shape fixity and recovery (100%). For auxetic structures, shape memory behavior and deformation response varied with nanocellulose content. Notably, 2 wt% nanocellulose yielded the highest shape recovery ratio (90.8%) and fixity (99.8%), indicating improved elasticity and structural responsiveness. Meanwhile, 1 wt% nanocellulose resulted in the highest compressive strength and more controlled deformation under compression, suggesting enhanced energy dissipation and stress distribution. A slight decrease in performance at 3 wt% is attributed to nanocellulose agglomeration and reduced polymer chain mobility. These findings highlight nanocellulose as a multifunctional additive that enables fine-tuning of mechanical and functional properties in 4D-printed structures. Depending on the intended application whether focused on energy absorption, mechanical strength, or shape recovery nanocellulose content can be strategically adjusted. This approach opens pathways for designing responsive materials suited for biomedical engineering, adaptive devices, and advanced environmental technologies.

Keywords: 4D printing, nanocellulose, PLA/PETG polymer blend, auxetic structures, shape memory materials, mechanical reinforcement, smart materials.

7.2 Introduction

The consideration of time as a fourth dimension in additive manufacturing resulted in the introduction of 4D printing, a type of technology by which the printed objects can be programmed to change shape or property upon exposure to environmental stimuli like heat, light, or water [1-9]. This type of dynamic behavior is extremely attractive for smart materials and responsive structures [10, 11]. Although shape memory polymers (SMPs) are already the basis material for this application, they have poor mechanical properties and are currently receiving considerable attention as targets for reinforcement using high performance fillers such as nanocellulose, a renewable material with high mechanical performance, high surface area to volume ratio, and capacity to form strong hydrogen-bonded networks. It has become a promising reinforcement filler in polymer matrix [12].

Recent developments in the 3D printing of nanocellulose polymer-based composites show notable enhancements in mechanical property, printed resolution and biocompatibility. For instance, Latif et al. [13] also showed that resin-infused nanocellulose architectures had more than 40% higher bending strength and higher thermal stability than unmodified epoxy composites. Similarly, Ma et al. [14] grafted nanocellulose with PLA and PCL to get PLA/PCL NCC based bionanocomposites suitable for 3D printing and exhibiting tensile strength over 50 MPa, high shape retention of printed objects. Zhou et al. [15] reported gelatin–oxidized nanocellulose hydrogels with compression strength of 20–35 kPa, yet they were verified to be biocompatible for biomedical applications. In SLA printing, Barkane et al. [16] has demonstrated that the incorporation of nanocellulose as low as 0.1 wt% into a bio-based acrylate resin raised the modulus to 160 MPa and increased glass transition temperature by 15°C, highlighting the functional impact of nanocellulose at ultra-low concentrations. When comparing bacterial and pulp-derived nanocellulose in cartilage bioprinting, Jovic et al. [17] demonstrated that formulations including bacterial nanocellulose had better print fidelity and higher cell survival (>90%). The production of high-performance, sustainable, and bioactive composite materials for structural, biomedical, and environmental applications is made possible by the versatility and functional advantages of nanocellulose in 3D printing, as demonstrated by these works taken together.

The potential of nanocellulose-reinforced polymer composites in intelligent and adaptable systems is demonstrated by recent developments in 4D printing of these materials. For example, Gu et al.

[18] used PCL/PBAT reinforced with cellulose nanofibers (CNFs) to create thermally sensitive shape memory composites, which resulted in stable deformation and great printability for soft grippers. Like this, Zhang et al. [19] showed that PVA/CNC composites' mechanical strength, thermal stability, and water resistance were greatly increased by hydrogen bonding and coordination interactions, opening the door to direct ink writing 3D/4D printing. These results demonstrate that nanocellulose is a crucial enabler for high-performance, sustainable, and programmable 4D-printed structures because it can improve mechanical performance, shape memory behavior, and interfacial bonding in thermally or photothermally sensitive composite systems.

Superior mechanical flexibility and energy absorption qualities are provided by auxetic structures, which are distinguished by a negative Poisson's ratio. These qualities are further improved by 4D printing and the use of intelligent reinforcements such as nanocellulose. According to a recent assessment, fiber-reinforced auxetic structures made with 4D printing have the potential to be used in robotics and aerospace because they can produce scalable, controllable form changes in response to stimuli [20]. Although there are currently no direct studies on nanocellulose in auxetic 4D-printed structures, related research on cellulose nanofiber (CNF)-reinforced shape memory polymers has demonstrated that minor additions of 1 part per hundred (phr) of polymer mass improve printability and mechanical performance while permitting dependable self-deforming behaviors like winding in soft grippers inspired by plants [18]. A further study that used $La_{0.7}Sr_{0.3}MnO_3$ nanoparticles in shape memory polymers for auxetic structures showed that the shape recovery rate was improved (179.5%/min compared to 124.3%/min baseline) although fixity remained at about 100% and the recovery ratio only slightly decreased (from 88% to 81%) [21]. According to these results, nanocellulose can also improve the actuation efficiency, thermal responsiveness, and structural integrity of auxetic 4D-printed materials due to its natural hydrogen-bonding potential and mechanical reinforcement ability. This could lead to new applications in biomedical scaffolds, adaptive wearables, and responsive filtration systems.

This study examines the mechanical and shape memory properties of nanocellulose-reinforced PLA/PETG polymer composites that are 4D printed into auxetic anti-tri-chiral structures. The goal of the research is to develop smart materials with reversible transformations and structural flexibility by utilizing the reinforcing qualities of nanocellulose and the distinct deformation

behavior of auxetic geometries. Biomedical devices, adaptive actuators, and environmental systems are just a few of the many possible uses for these materials. In particular the natural adsorption ability of nanocellulose and the porosity of auxetic structures can be used in concert for filtration and heavy metal adsorption applications.

7.3 Materials and methods

7.3.1 Samples preparation

7.3.1.1 Materials

The nanocellulose utilized in this study were obtained from CelluForce. The producer has reported some properties: It appears white to off-white, with a moisture content ≤ 6 %, bulk density of 0.5–0.8 g/cm³, and powder particle size ranging from 1 µm to 50 µm. When dispersed at 2 wt %, the NC exhibits nanoparticle dimensions below 150 nm, a pH between 5 and 8, conductivity under 350 µS/cm, and viscosity greater than 5 cP. The material shows 70–90 % crystallinity. Some researchers had studied the NCC from the same sources [22-24]. Polylactic acid (PLA) and polyethylene terephthalate glycol-modified (PETG) resin pellets from Push Plastic were selected as the polymer matrices for developing the Naanocellulose-reinforced 4D printing blends. PLA pellets, with a density of 1. 24 g/cm³, and PETG pellets, with a density of 1.27 g/cm³, were sourced from Push plastics and served as the base materials for the composites.

7.3.1.2 Preparation of blends and nanocomposite

To prepare PLA, PETG, and nanocellulose for nanocomposite fabrication, all components were pre-dried in a vacuum oven at 60°C for 24 hours to remove residual moisture, as illustrated in Figure 7.1.

First, a binary polymer blend of PLA and PETG was prepared at a 75/25 weight ratio by mixing their pellets in a beaker immediately before extrusion. This specific composition was selected based on our previous studies, which demonstrated its superior shape memory properties [3, 25]. Nanocellulose powder was then incorporated at concentrations of 0%, 1%, 2%, and 3% w/w by blending it with the PLA-PETG pellets.

The resulting mixtures were fed into a single-screw extruder to produce 3D printing filaments. Key processing parameters, including extrusion temperature, extrusion rate, line speed, and oven temperature, were carefully optimized to ensure high filament quality with minimal defects and

consistent diameter. Extrusion temperatures were precisely maintained between 180°C and 185°C, as detailed in Table 7.1, to accommodate the distinct thermal and flow properties of each composition. A 3 mm nozzle was used to extrude filaments with a target diameter of 2.80 mm. Following extrusion, the filaments were cooled and wound onto spools using a filament winding system, preparing them for 3D printing.

7.3.1.3 3D printing by Fused Filament Fabrication (FFF)

PLA/PETG polymer blend and nanocomposite filaments were 4D-printed into three geometries according to the targeted evaluation: U-shaped specimens (100 mm × 20 mm × 1 mm) for shape-memory assessment, ASTM D638 Type IV specimens for tensile testing, and anti-tri-chiral auxetic structures for compression analysis. The specimens were designed using CAD software and printed using an Ultimaker S5 printer.

For the PLA/PETG polymer blend and nanocellulose-reinforced polymer blend, a 0.4 mm AA nozzle was used. Printing parameters were optimized to ensure consistent performance across all samples, including a layer height of 0.2 mm, 100% infill density, an infill line width of 0.45 mm, and a printing speed of 20 mm/s. The bed temperature was maintained at 100°C [26, 27].

The nozzle temperature was tailored for each sample to optimize print quality, with specific values listed in Table 7.1. This systematic approach ensured uniform filament quality and reliable print performance for both the PLA/PETG blends and nanocellulose-based nanocomposites.

Table 7.1: Compositions, extrusion temperatures, and 3D printing parameters of PLA/PETG blend and nanocellulose-reinforced PLA/PETG nanocomposites.

Samples	Nozzle Temperature (°C)	Plate temperature (°C)	Print speed (mm/s)	Flow (%)	Layer height (mm)	Line width (mm)	Extrusion Temperatures (°C)
PLA-75/PETG-25	245	100	20	110	0.2	0.45	180-185
PLA-75/PETG-25/NC-1	245	100	20	110	0.2	0.45	180-185
PLA-75/PETG-25/NC-2	240	100	20	110	0.2	0.45	180-185
PLA-75/PETG-25/NC-3	240	100	20	110	0.2	0.45	180-185

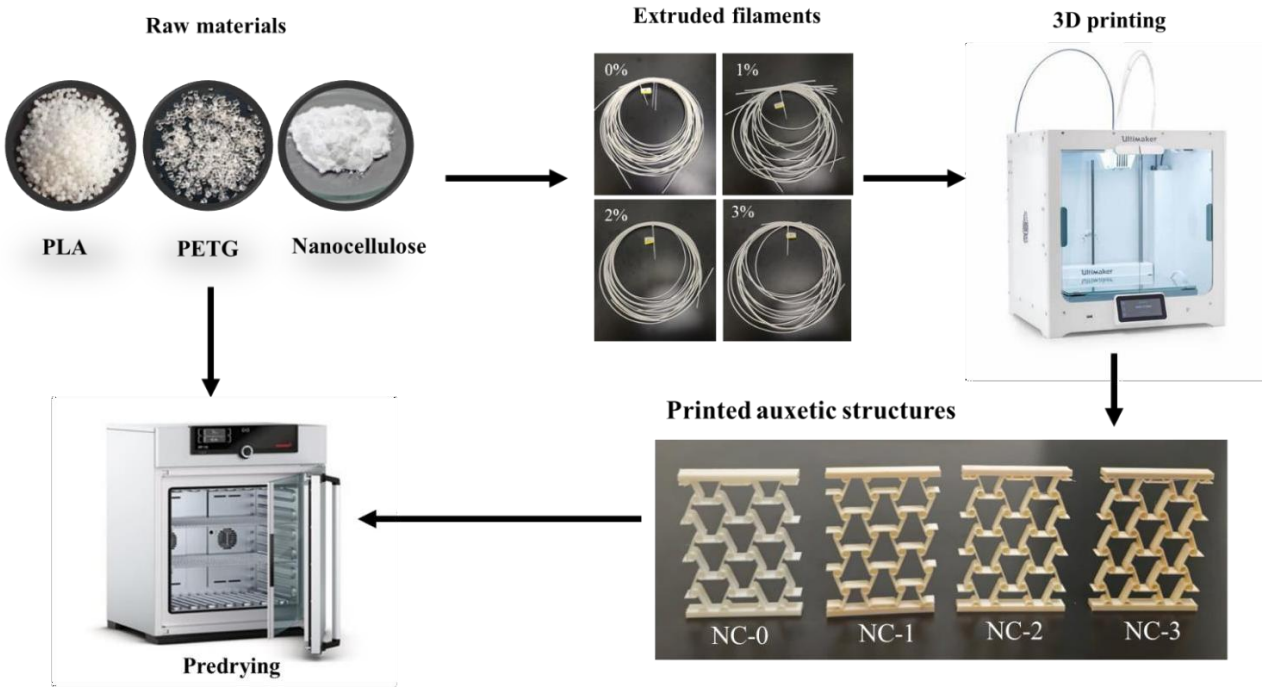

Figure 7.1: Schematic representation of the preparation and processing of nanocellulose-reinforced PLA/PETG nanocomposites for 3D Printing.

7.3.2 Characterization

7.3.2.1 Tensile test

Mechanical testing was performed under standard ambient conditions using an MTS universal testing machine equipped with a 20 kN load cell. Five specimens per composition, conforming to ASTM D638 Type IV standards, were 3D-printed with a 0° raster orientation to ensure consistency in loading direction. This setup enabled a comprehensive evaluation of the tensile behavior of the materials, including the determination of ultimate tensile strength (*UTS*) and Young's modulus (*E*). The obtained data provide valuable insights into the influence of nanocellulose reinforcement on the structural integrity and mechanical performance of the PLA-75/PETG-25 polymer blends.

7.3.2.2 Compression of auxetic anti-trichiral structures

Mechanical compression tests were performed on three 3D-printed anti-tri-chiral auxetic specimens fabricated from a PLA/PETG (75/25) blend with different nanocellulose reinforcements. The tests were carried out using an MTS universal testing machine under standard ambient conditions, with a constant crosshead speed of 5 mm/min. Each specimen was designed

based on a repeating anti-tri-chiral unit cell geometry consisting of circular ligaments with a radius of 2.5 mm connected by straight beams 10 mm wide as reported in Table 7.2, forming a triangular lattice pattern as seen in Figure 7.2 (a). The full 3D-printed structures measured 105 mm in height, 85 mm in width, and had a thickness of 15 mm, as shown in the Figure 7.2 (b, c).

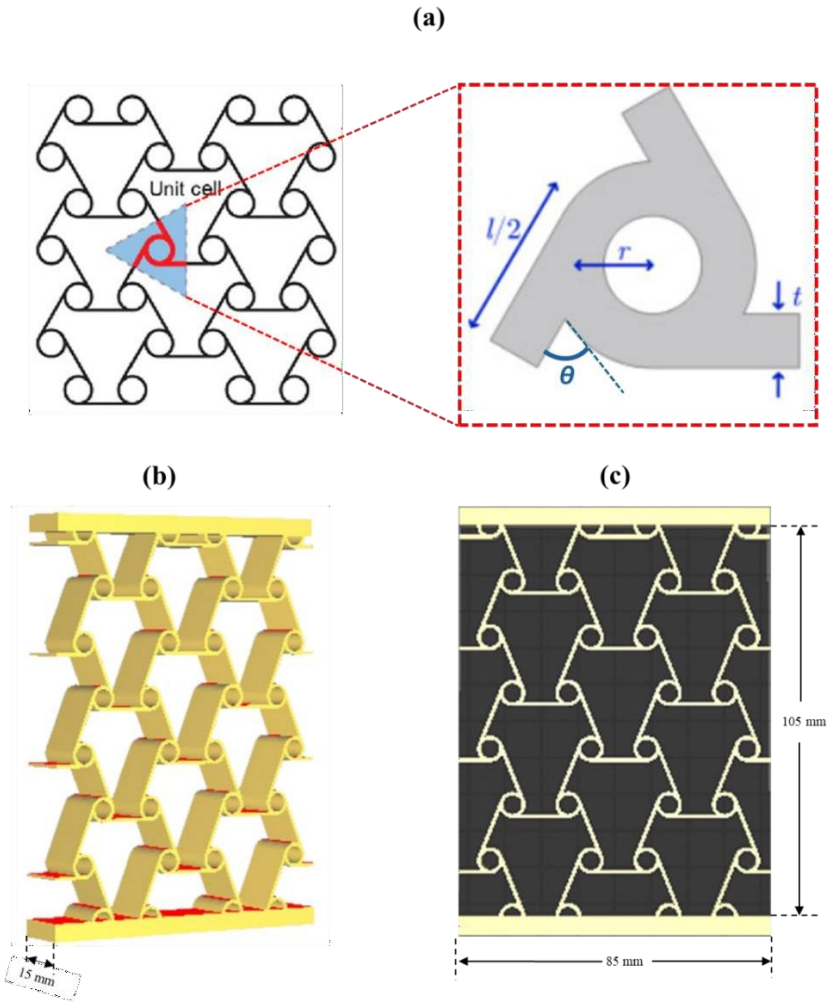

Figure 7.2: Schematic sketch of the unit cells for the anti-trichiral auxetic structure, illustrating the geometric parameters. The parameter r represents the mean radius of the circular node, l/2 denotes half the ligament length, and t indicates the ligament thickness (a) 3D design (b), and dimensions of the anti-trichiral auxetic structure specimen (c).

Table 7.2: Geometic parameters of anti-tri-chiral unit cell.

Auxetic structure	r (mm)	l (mm)	t (mm)	θ (°)
Anti-trichiral	2.5	15	1	60

7.3.2.3 Infrared Spectroscopy (FTIR)

Fourier Transform Infrared Spectroscopy (FTIR) was performed in Attenuated Total Reflectance (ATR) mode with a resolution of 4 cm^{-1}, covering the spectral range of 4000–400 cm^{-1}.

7.3.2.4 X-Ray Diffraction (XRD)

X-ray diffraction (XRD) analysis was performed to examine the structural characteristics of the PLA/PETG nanocomposites. The measurements were carried out using a diffractometer with a Cu Kα radiation source (λ = 1.5406 Å), operating at 30 kV and 30 mA. Scans were recorded over a 2θ range of 5°–40°, with a step size of 0.02° and a counting time of 1 to 2 seconds per point. These conditions provided clear and detailed diffraction patterns suitable for evaluating the effect of nanocellulose on the material structure.

7.3.2.5 Shape Memory Test

Three U-shaped 3D-printed samples per composition measuring 100 mm × 20 mm × 1 mm and printed at a 0° orientation were subjected to shape programming and recovery tests to evaluate their shape memory properties. The samples were first heated to the designated programming temperature (T_p) and then deformed to fit a 20 mm-thick mold. While held in the mold, they were cooled to room temperature to stabilize the temporary shape. After cooling, the mold was removed, and the fixed angle (θ_{fixed}) was measured to quantify the shape fixation stage.

For recovery evaluation, the samples were reheated to a constant temperature, and the bending angle (θ_i) was carefully measured. Shape fixity (S_f) and shape recovery (S_r) were calculated using the following equations:

$$Shape\ fixity\ (Sf) = \frac{\theta fixed}{\theta max}\ X\ 100 \qquad \text{(eq. 1)}$$

$$Shape\ recovery\ (Sr) = \frac{\theta \max - \theta i}{\theta \max}\ X\ 100 \qquad \text{(eq. 2)}$$

These measurements provided quantitative insights into the efficiency of the shape memory behavior in the studied composites. Detailed experimental procedures and previous results can be found in our earlier work [28].

7.4 Results and discussions

7.4.1 Infrared Spectroscopy (FTIR)

The structural features and chemical interactions of PLA/PETG blends with different amounts of nanocellulose (NC) are depicted in the FTIR spectrum shown in Figure 7.3. Key functional groups that correspond to the polymer matrix and nanocellulose are visible in the spectrum data, which sheds light on how they interact.

The spectrum clearly shows the distinctive peaks of PETG and PLA. The C=O stretching vibration from ester bonds, a characteristic that distinguishes both PLA and PETG, is represented by the prominent absorption peak at about 1750 cm^{-1}. C–O stretching vibrations also show up between 1200 and 1100 cm^{-1}, which supports the polyester structure even more.

The presence of aromatic groups is indicated by the benzene ring vibrations from PETG, which emerge around 1600 cm^{-1} and 1500 cm^{-1}, whereas the CH_3 asymmetric and symmetric stretching vibrations of PLA are seen in the range of 2995–2945 cm^{-1} [3, 29, 30].

New spectrum characteristics are introduced by the addition of nanocellulose, which are mostly linked to hydroxyl (-OH) groups. The development of hydrogen bonds between nanocellulose and the polymer matrix is suggested by a broad band in the 3300–3400 cm^{-1} range that corresponds to O–H stretching vibrations. These vibrations become more noticeable as the NC concentration increases. Furthermore, cellulose's C–O–C stretching vibrations occur between 1100 and 1000 cm^{-1} and frequently coincide with PLA/PETG's ester groups [31, 32].

The spectra show that nanocellulose significantly affects the structure of the polymer. Peak intensity variations and broadening in the O-H stretching region suggest improved intermolecular interactions, which could result in better adhesion and dispersion in the composite.

Hydrogen bonding between PLA and nanocellulose has been demonstrated to improve structural stability and mechanical qualities [33, 34]. Strong interfacial adhesion between nanocellulose and polymers is indicated by the expansion of the O–H stretching peak, which has been widely documented [35].

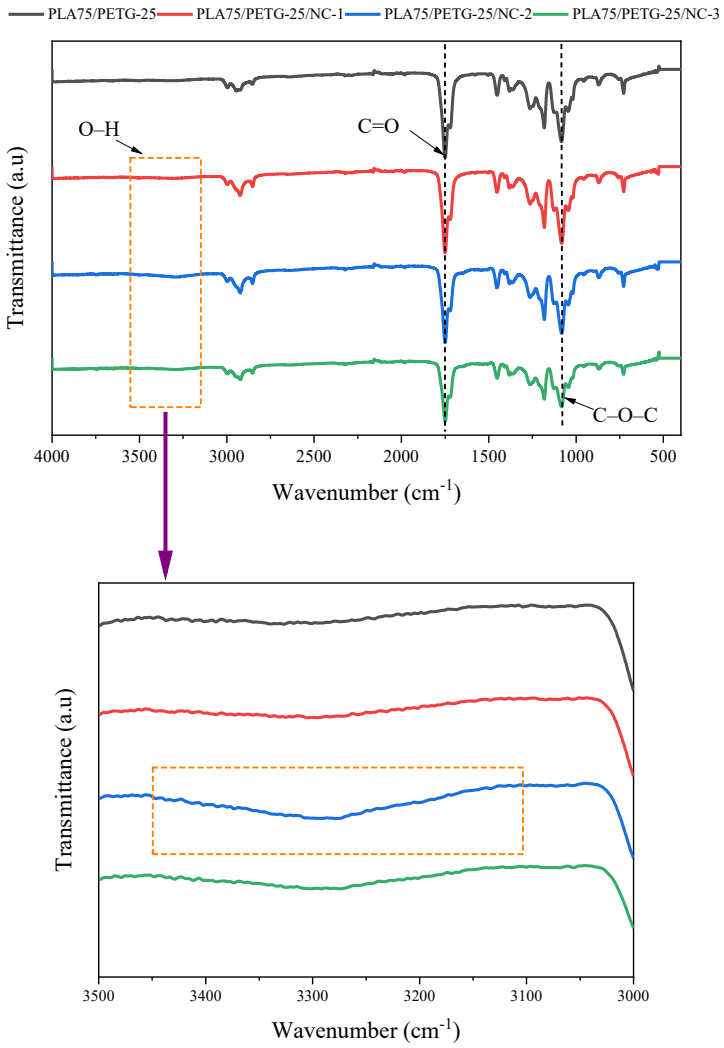

Figure 7.3: FTIR analysis of PLA/PETG nanocomposites with increasing nanocellulose content.

Finally, with discernible interactions between the constituents, the FTIR measurement validates the effective incorporation of nanocellulose into the PLA/PETG matrix. Improved compatibility and structural alterations within the composite are indicated by changes in peak intensity and position, especially in the O–H and C=O stretching areas. These results demonstrate nanocellulose's potential to improve polymer characteristics and are consistent with earlier research on nanocellulose-reinforced polymer systems.

7.4.2 X-Ray Diffraction (XRD)

The X-ray diffraction (XRD) patterns of PLA-75/PETG-25 composites reinforced with varying nanocellulose contents (0%, 1%, 2%, and 3%) seen in Figure 7.4 reveal characteristic amorphous

halos centered around 2θ° ≈ 16–25°, indicating a predominantly amorphous microstructure across all samples [36]. This broad diffraction band is typical of PLA and PETG blends, which are known to exhibit low crystallinity due to their molecular structure and the thermal history imposed by the 3D printing process [37].

Upon incorporation of NC at 1%, 2%, and 3%, the overall intensity of the diffraction pattern gradually increases without the appearance of sharp crystalline peaks. This indicates that NC enhances local ordering within the matrix but does not induce new crystalline phases or change the fundamental amorphous character of the system. These results align well with the FTIR analysis, which showed no new characteristic absorption bands attributable to crystalline structures, but rather an intensification of existing peaks particularly in the hydroxyl (–OH) and carbonyl (C=O) regions suggesting enhanced hydrogen bonding and polymer chain interactions.

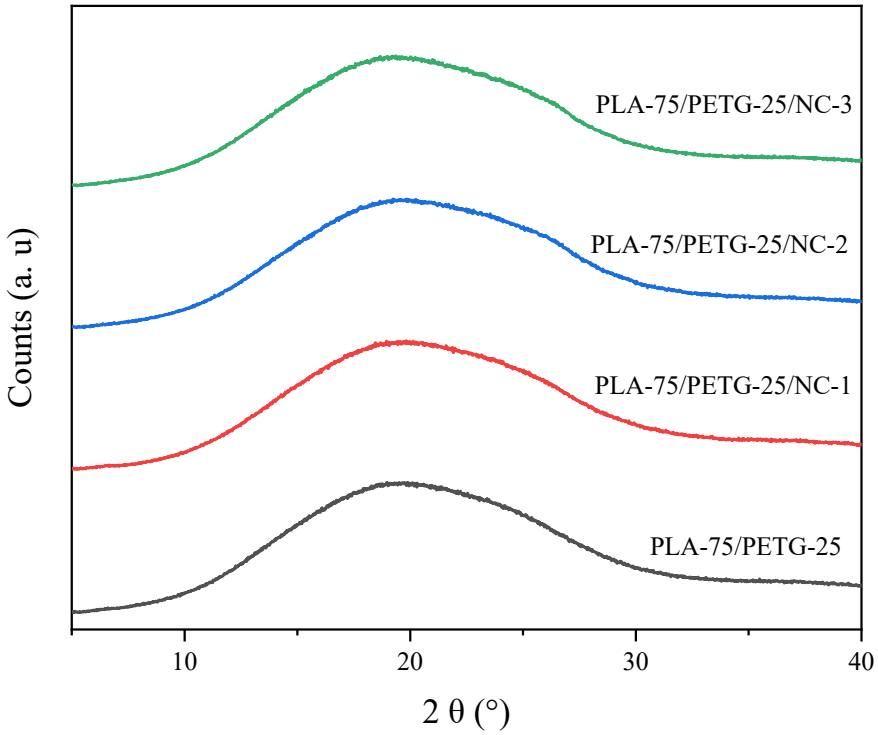

Figure 7.4: XRD of 3D printing of PLA-75/PETG-25 polymer blend and Nanocellulose reinforced polymer composites.

FTIR and XRD findings suggests that nanocellulose may exhibit a weak nucleation effect not detectable as bulk crystallinity at the molecular level, promoting intermolecular interactions and possible local ordering, but not to the extent of forming detectable crystalline domains. Similar

behavior has been reported in previous studies where NCC led to improved molecular packing and hydrogen bonding in PLA-based systems without significantly modifying the bulk crystalline structure [36, 38, 39].

In summary, the XRD analysis demonstrates that while nanocellulose marginally enhances structural organization in PLA/PETG blends, it does not change their amorphous nature or introduce new crystalline phases, consistent with previous findings in PLA/NC nanocomposites.

7.4.3 Mechanical properties

Fused Deposition Modeling (FDM) 3D-printed samples were utilized to assess the mechanical characteristics of PLA/PETG mixes with nanocellulose (NC) reinforcement. All samples show similar elastic behavior at low strain levels (<1%), according to the stress-strain curves (Figure 7.5 (a)), indicating that the addition of NC slightly increases the stiffness, with a clear optimum at 2 wt%. With varying NC concentrations, however, differences in ultimate tensile strength (*UTS*) are noted. With a strength of above 55 MPa, the PLA-75/PETG-25/NC-2 sample exhibits the maximum strength, with a little drop at 3 wt% NC. This pattern suggests that enhanced interfacial bonding and stress transmission increase mechanical performance at an ideal NC concentration of 2 wt%. At 3 wt% NC, however, potential nanocellulose agglomeration might serve as stress concentrators, decreasing efficacy [26].

The change in UTS (σ, in MPa) and elastic modulus (E, in GPa) with NC concentration is quantified by the bar chart in Figure 70 (b). The average UTS and E of the control sample (0 wt% NC) are approximately 52 MPa and ~3±0.3 GPa, respectively. At 2 wt% NC, the strength reaches its maximum (~56 MPa), and at 3 wt% NC, it slightly decreases to ~54 MPa. The elastic modulus has a similar trend, peaking at around 3,3±0.6 GPa for 2 wt%, suggesting increased stiffness as a result of NC reinforcement [40]. The bar chart's error bars indicate mechanical property variability, which is probably caused by irregular layer deposition and the intrinsic anisotropy of FDM-printed parts [41].

The FDM process has a significant impact on mechanical performance. Local weak regions of FDM-printed objects are introduced by the layering process, especially when subjected to tensile pressure. Strength and stiffness are increased by improved layer adhesion, which is facilitated by nanocellulose. However, excess NC might cause nozzle blockage or uneven dispersion at higher

NC loadings (3 wt%), which would impair mechanical performance [42]. Previous studies have demonstrated that nanocellulose reinforcement enhances the characteristics of the polymer matrix at low concentrations; however, excessive filler might result in flaws, diminishing the mechanical benefits [43].

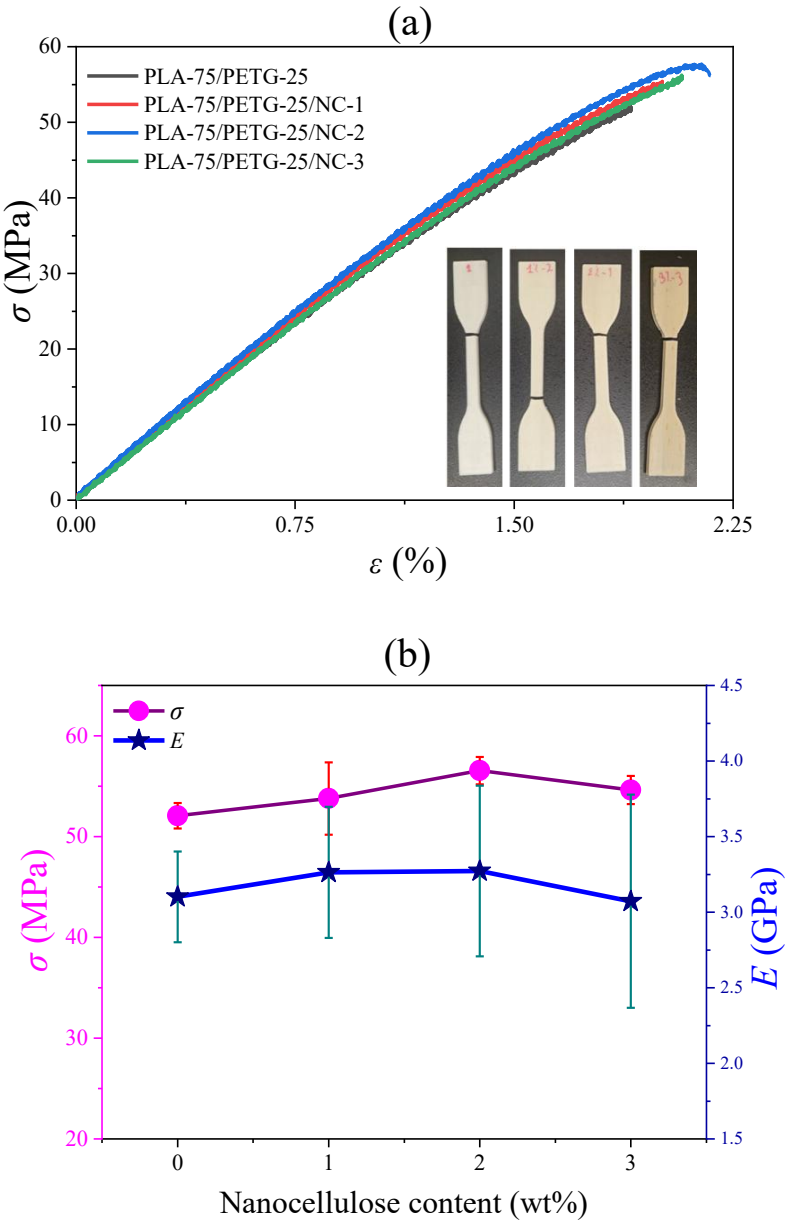

Figure 7.5: Mechanical properties of PLA/PETG nanocomposite with different nanocellulose content (a) stress-strain curves and (b) comparison of ultimate tensile strength (σ) and elastic modulus (E) for PLA-75/PETG-25 blends with varying nanocellulose (NC) content

In summary, PLA-75/PETG-25 used in FDM 3D printing showed a maximum tensile strength (~56 MPa) and stiffness (~3.3 GPa) when the NC content is 2 wt%. Although it exhibits declining results at increasing concentrations, nanocellulose reinforcement improves mechanical characteristics by strengthening polymer connections. To maximize the mechanical performance of printed items, the intrinsic limits of FDM, such as interlayer adhesion and NC dispersion, must be adjusted.

7.4.4 U-Shape memory performances

The shape memory behavior of 3D-printed PLA/PETG nanocomposite samples with various levels of nanocellulose (0%, 1%, 2%, and 3%) is shown in Figure 7.6. There is a discernible color shift, with an opaquer look resulting from a higher nanocellulose concentration. The images additionally illustrate excellent printing quality, with smooth surfaces and distinct shapes. The as-printed flat state, deformation into a U-shape following heating over the glass transition temperature (T_g = 90°C) with an applied external force, and subsequent chilling to maintain the temporary shape are the three primary steps in the shape memory process. Regardless of the amount of nanocellulose present, all samples completely regain their initial flat shape when heated to 90°C. This suggests that while adding nanocellulose may affect other mechanical properties, it does not impair the shape memory effect. These findings demonstrate the potential of PLA/PETG composites reinforced with nanocellulose for use in biomedical devices, smart actuators, and self-healing materials. Additional quantitative research may shed more light on how nanocellulose affects mechanical performance and recovery kinetics.

The impact of nanocellulose content on form fixity (S_f), shape recovery (S_r), and shape recovery time can be observed in Figure 7.7. Nanocellulose content has no detrimental effect on the material's capacity to hold and regain its shape because shape fixity and recovery are always 100%. This implies that for all evaluated compositions, the polymer matrix offers adequate structural integrity and flexibility. The small difference in shape recovery time, however, suggests that the concentration of nanocellulose affects recovery speed but has no effect on recovery capabilities. This pattern may be explained by how nanocellulose alters the matrix's viscoelastic characteristics, which in turn alters how responsive it is to outside stimuli.

Strong hydrogen bonds seen in nanocellulose, as shown by FTIR data, may be one reason. These bonds increase network rigidity and limit polymer chain mobility, which may impede shape recovery. Furthermore, the presence of nanocellulose may change the material's thermal

conductivity as reported by Uetani et al. [44], which indicates that nanocellulose exhibits higher intrinsic thermal conductivity than most polymer matrices. This facilitates faster heat distribution during thermal triggering, promoting faster transition through the glass transition temperature of PLA. These changes could impact heat distribution and shape recovery kinetics. Additionally, nanocellulose may function as a plasticizer, changing the mechanisms of stress transmission, or as a reinforcement, increasing stiffness and viscosity, depending on how it is dispersed. While too much nanocellulose could limit polymer mobility and slow recovery, the trend in the time recovery curve might suggest an ideal concentration of nanocellulose at which the fastest recovery occurs.

According to previous studies on nanocellulose-reinforced shape-memory polymers (SMPs), although nanocellulose improves mechanical characteristics, its higher crystallinity and intermolecular interactions may also have an impact on recovery speed [31]. Based to this research, a low concentration of nanocellulose can speed up recovery by enhancing stress transfer and heat conductivity [44], while a higher concentration could hinder recovery by decreasing polymer mobility. Because poor dispersion can result in heterogeneous structures that either delay or localize form recovery, the degree of filler-matrix interaction is crucial [45].

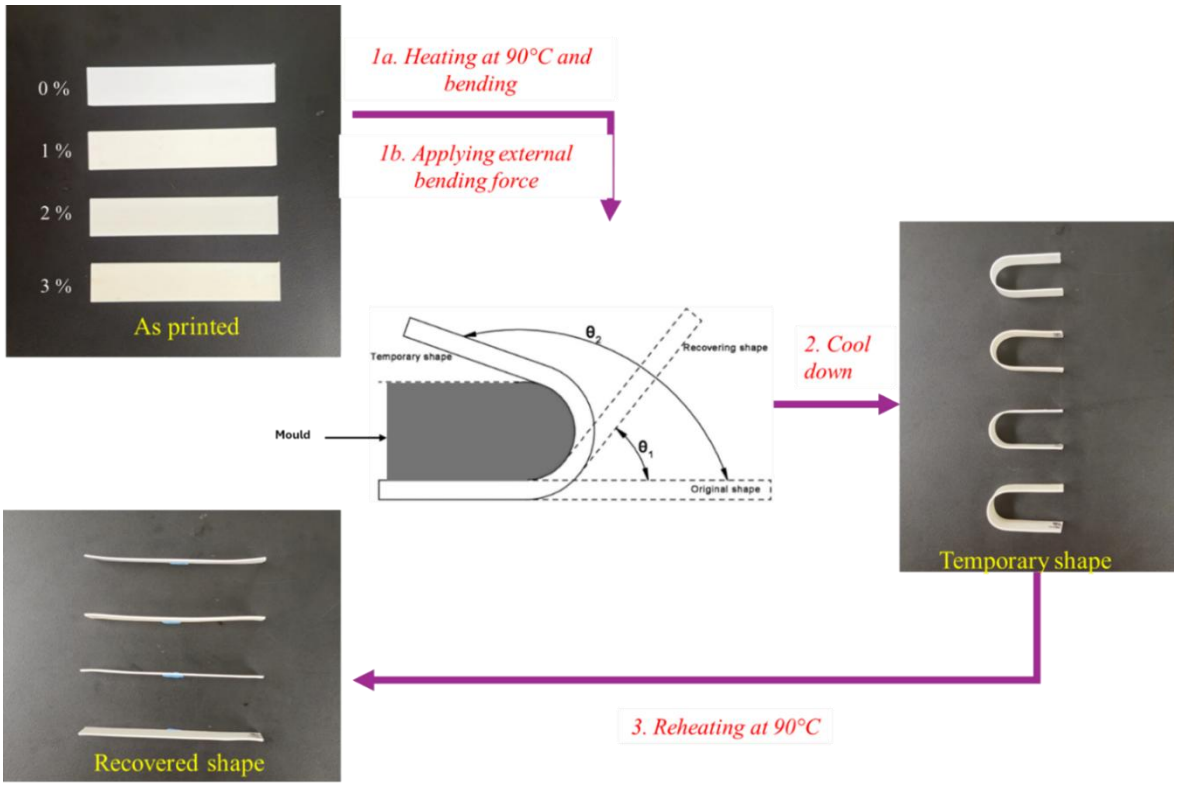

Figure 7.6: Shape memory behavior of 3D-Printed PLA/PETG nanocomposite with different nanocellulose contents.

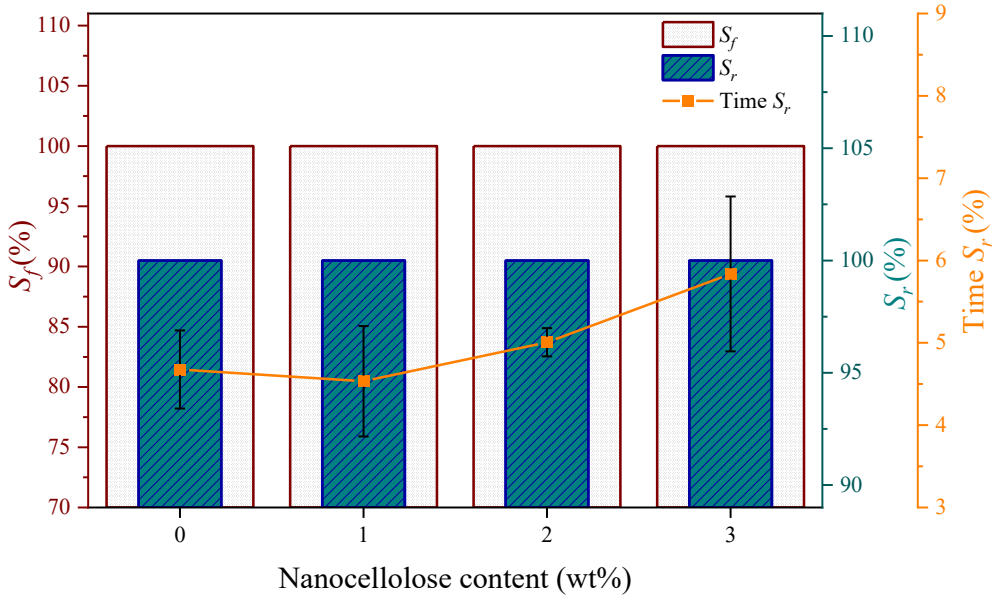

Figure 7.7: Shape memory performance of PLA/PETG composites as a function of nanocellulose content.

In summary, nanocellulose amount has a slight impact on recovery time but has no effect on shape fixity or recovery % in standard U-shape memory test. The significance of striking a balance between reinforcement and flexibility to maximize recovery speed is highlighted by this behavior, which is probably caused by variations in matrix stiffness, thermal conductivity, and viscoelastic behavior.

7.5 Anti-tri-chiral auxetic structures

7.5.1 Mechanical performance under compression

The compression tests performed on the anti-trichiral auxetic structures based on PLA-75/PETG-25 reinforced with varying nanocellulose contents revealed a distinct mechanical evolution as seen in Figure 7.8. The compressive strength slightly increased with the incorporation of 1 wt.% nanocellulose (0.22 MPa) and subsequently decreased for higher concentrations (2–3 wt.%) as reported on Figure 7.9. This trend indicates the presence of an optimal reinforcement concentration, at which the nanocellulose is sufficiently dispersed to enhance interfacial load transfer between the polymer phases without forming aggregates. Beyond this threshold, excessive nanocellulose leads to stress concentration zones and structural heterogeneity, which explain the decline in both maximum

stress and modulus. Similar trends have been reported by Kothavade et al. [46] and Zhang et al. [12], who observed that optimal reinforcement in PLA/nanocellulose composites typically occurs between 0.5–2 wt.%, whereas higher loadings cause a deterioration of mechanical properties due to poor dispersion and reduced interfacial compatibility.

The progressive decrease of the Young's modulus (from 0.78 to 0.66 MPa for 0–3 wt.% nanocellulose) suggests a global softening effect in the auxetic structure. This can be attributed to the anti-trichiral geometry, which promotes rotational and radial deformation during compression. Comparable results were reported by Hamzehei et al. [47], who found that polymeric auxetic structures exhibited reduced apparent stiffness due to the flexibility of their cellular geometry, while maintaining excellent energy absorption capacity [48]. The observed decrease in stiffness, combined with the moderate strength improvement at low filler content, indicates that nanocellulose acts more as an energy dissipating agent than as a rigid load-bearing phase at the macroscopic scale.

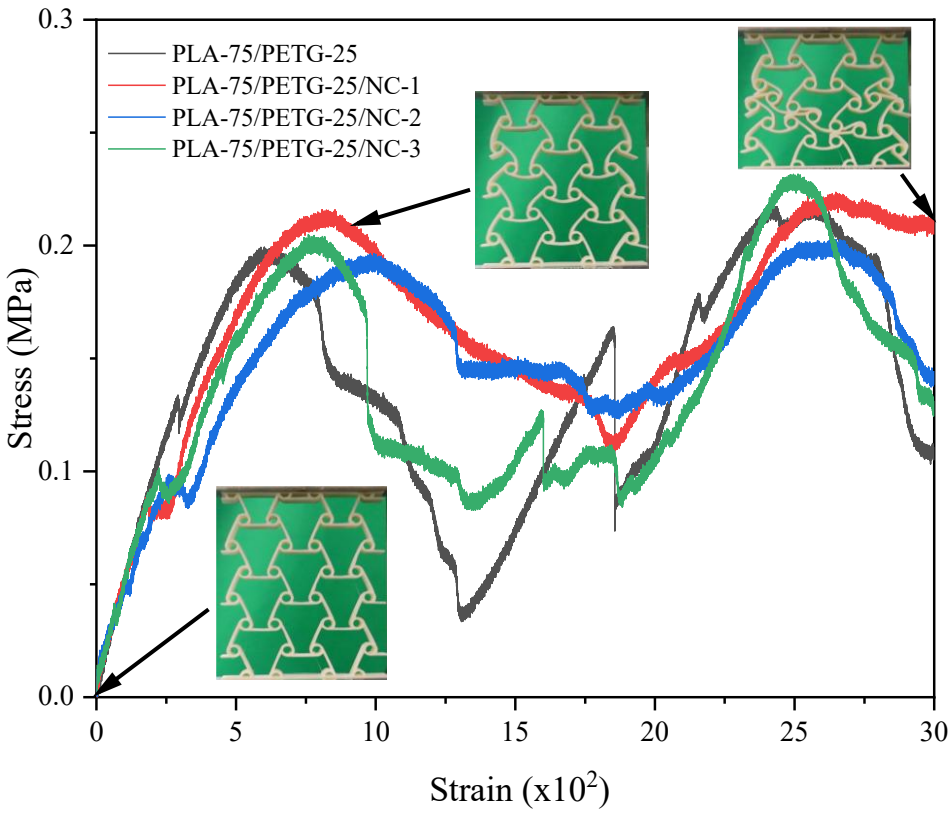

Figure 7.8: Compression behavior of anti-tri-chiral auxetic structures based on PLA-75/PETG-25 blend reinforced with nanocellulose.

The multiple oscillations identified in the stress–strain curves indicate a progressive deformation mechanism typical of auxetic materials. These fluctuations, corresponding to successive load–unload cycles, reflect cellular rearrangements and rotational motion of anti-trichiral nodes throughout compression. Similar behavior was reported by Hu et al. [49], who demonstrated that the anti-trichiral topology combines high flexibility with excellent energy absorption, attributed to localized kinematic deformation.

The optimal performance achieved for the PLA-75/PETG-25/NC-1 formulation aligns with the findings of Li et al. [50], who showed that a small nanocellulose addition (~1 wt.%) in PLA/PETG composites enhances both strength and stability due to improved interfacial adhesion and homogeneous filler dispersion. Overall, these findings confirm that the synergistic interaction between auxetic topology and nanocellulosic reinforcement can yield lightweight, energy-absorbing, and mechanically stable structures suitable for impact mitigation and biomechanical applications.

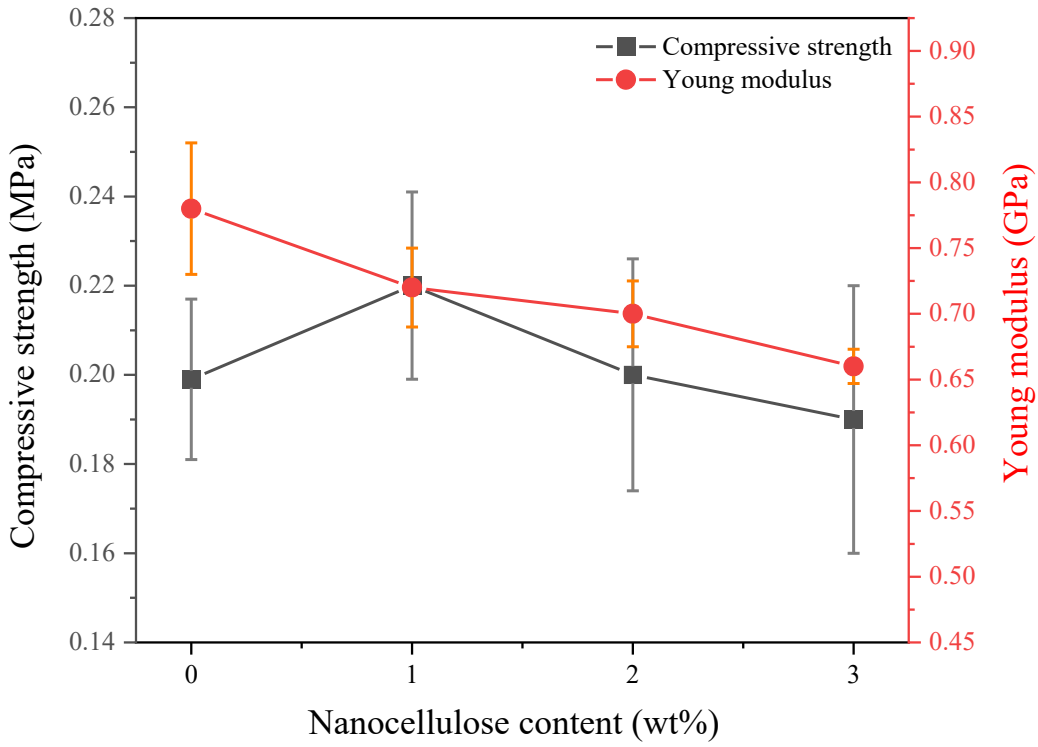

Figure 7.9: Effect of nanocellulose content on compressive strength and elastic modulus in the elastic deformation stage.

7.5.2 Shape Memory Behavior Process

The 3D-printed auxetic structures in Figure 7.10 (a) are of the highest quality because they can display the negative Poisson's ratio behavior that is typical of auxetic materials. High deformation capacity and better energy absorption are made possible by this special characteristic as it demonstrated in the above section, which improves structural performance. The improved shape memory and mechanical performance is a result of careful material selection and printing.

Following external stimuli or deformation, Figure 7.10 (b) illustrates the final fixation of the temporary shape, demonstrating the stability and dependability of the 3D-printed structure. A key feature of shape memory polymers is fixing, in which the structure maintains its transient state even after being exposed to different mechanical or environmental stresses.

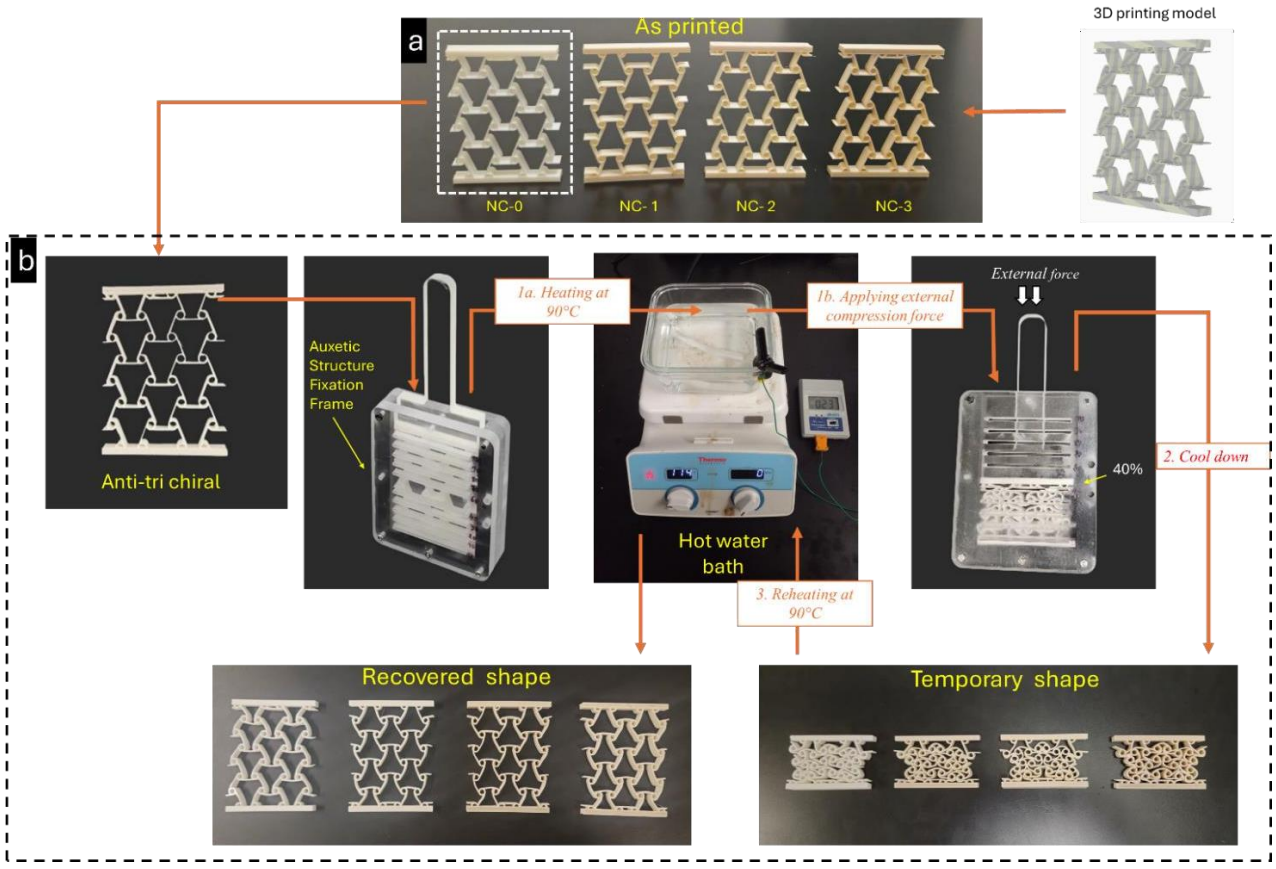

Figure 7.10: Shape memory process of Tri-Chiral auxetic structures reinforced with nanocellulose. (a) 3D printed Tri-chiral auxetic structures based on PLA-75/PETG-25 polymer blend reinforced with 1, 2, and 3 wt% of nanocellulose. (b) Shape memory programming and recovery process: The auxetic structure is placed in an Auxetic Structure Fixation Frame and heated above the glass transition temperature (T > Tg, 90°C) in a hot water bath while an external force is applied to deform the structure. After cooling, the temporary shape is maintained. Upon reheating at 90°C, the structure recovers its original form, demonstrating its shape memory behavior.

The figure clearly demonstrates the printed material's superior functional performance, highlighting its appropriateness for applications needing regulated shape transitions and the maintenance of a programmed form.

As illustrated in Figure 7.11, the performance of shape memory is much improved by the addition of nanocellulose to anti-tri-chiral PLA/PETG auxetic structures. According to the figure, the shape recovery ratio (S_r) peaks at 90.8% with 2% nanocellulose before somewhat declining to 90.4% at 3%, while the shape fixity ratio (Sf) grows from 98.1% to over 99.8% as the nanocellulose content increases to 3%. According to FTIR studies, this enhancement is attributed to nanocellulose's capacity to create a hydrogen-bonded network inside the polymer matrix, improving crystallinity and fostering mechanical and thermal stability. Higher concentrations, however, may cause nanocellulose agglomeration to impair soft segments' elasticity, which would lessen form recovery. These trends are in line with the findings of Gorbunova et al. [51], who emphasized the role of nanocellulose as a thermal trigger in shape memory materials, Fu & Tian [52], who highlighted its contribution to temporary phase stabilization and enhanced shape memory performance, and Auad et al. [53], who reported recovery rates above 95% with only 1–2% nanocellulose in TPU composites. The usefulness of nanocellulose as a functional additive in 4D-printed polymer systems for intelligent applications is supported by these findings.

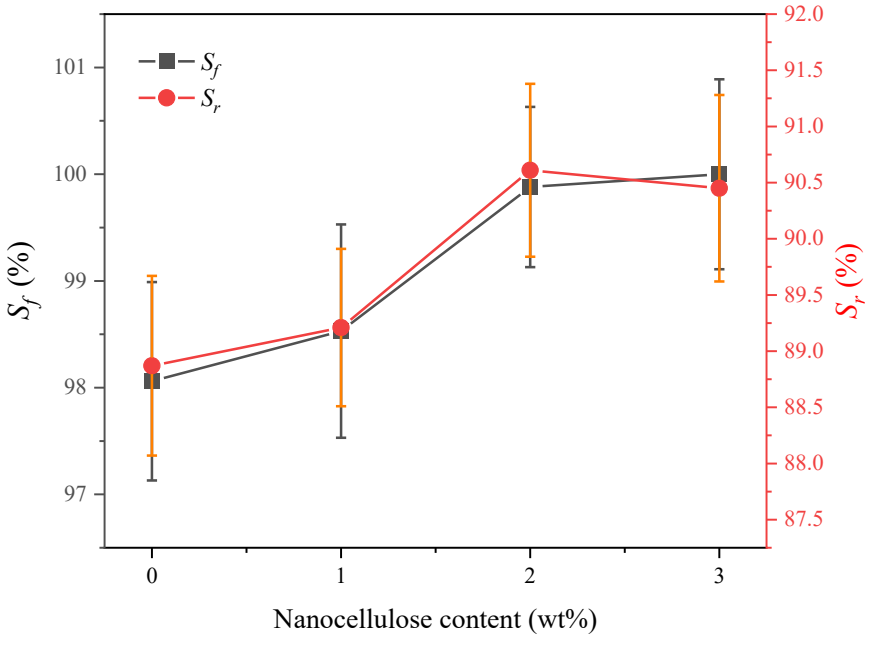

Figure 7.11: Evolution of the shape fixity ratio (Sf) and the shape recovery ratio (Sr) as a function of nanocellulose content (0–3 wt%) in PLA/PETG-based anti-tri-chiral auxetic structures.

A strong correlation was observed between the shape-memory performance and the compressive response of the anti-tri-chiral PLA/PETG structures reinforced with nanocellulose. The shape-fixity ratio (S_f) increased steadily with NC content, from 98.1 % (0 wt%) to 99.8 % (3 wt%), reflecting the stabilizing effect of the temporary configuration. The shape-recovery ratio (Sr) reached an optimum of 90.8 % at 2 wt%, indicating the presence of an ideal balance at this concentration. This enhancement is attributed to the development of a hydrogen-bonded interfacial network between CNCs and the polymer chains (confirmed by FTIR), which promotes elastic energy storage during programming while ensuring sufficient segmental mobility above T_g for recovery.

In contrast, compressive properties exhibit a moderate decline with increasing CNC loading in the quasi-elastic region. The reference structure (0 wt% NC) demonstrates the highest initial stiffness (Young's modulus ≈ 0.78 GPa), whereas the addition of CNC progressively decreases these values due to localized mobility restriction and stress concentrations. At 1 wt%, the structure retains competitive strength (≈ 0.22 MPa) and a modulus of ~0.72 GPa, suggesting uniform dispersion and efficient interfacial stress transfer. Beyond this concentration, the mechanical response degrades, with compressive strength dropping to 0.20 MPa (2 wt%) and 0.19 MPa (3 wt%), along with a reduction in modulus down to 0.66 GPa.

7.6 Conclusion

This study aimed to develop intelligent, responsive 4D-printed anti-tri-chiral auxetic structures using PLA-75/PETG-25 blends reinforced with nanocellulose. By leveraging the reinforcing capability of this sustainable nanofiller, both tensile strength and stiffness were improved. The highest performance was achieved at 2 wt% nanocellulose, with an elastic modulus of 3.3 GPa and a tensile strength of 56 MPa.

The addition of nanocellulose notably enhanced the shape memory performance of the auxetic structures, achieving a maximum recovery ratio of 90.8% and a fixity ratio exceeding 99.8% at 2 wt%. This improvement results from hydrogen bonding between nanocellulose and the polymer matrix, which strengthens the internal network and stabilizes the temporary shape. A slight decrease at 3 wt% was attributed to reduced chain mobility and filler agglomeration, indicating that a moderate nanocellulose content allows precise tuning of the material's mechanical and functional behavior.

Under compression, the incorporation of nanocellulose slightly decreases the stiffness of the structures but improves stress distribution and promotes smoother deformation behavior, particularly at 1 wt%, where the material demonstrates the most stable compressive response. However, at 3 wt%, the formation of nanocellulose agglomerates leads to reduced flexibility and local stress concentration, resulting in a gradual decline in mechanical performance.

These auxetic structures offer shape adaptability, energy absorption, and durability, making them suitable for soft robotics, biomedical, and protective applications. Their porosity and nanocellulose content also support environmental uses such as water purification. Overall, this work unites materials science, additive manufacturing, and sustainability to develop bio-based, programmable 4D-printed structures with intelligent and adaptive performance.

7.7 Acknowledgements

The authors gratefully acknowledge the financial support provided by the Natural Sciences and Engineering Research Council of Canada (NSERC), the University of British Columbia, and the Department of Materials Engineering.

7.8 References

1. Ding, A., F. Tang, and E. Alsberg, 4D printing: A comprehensive review of technologies, materials, stimuli, design, and emerging applications. Chemical Reviews, 2025. 125(7): p. 3663-3771.
2. Wang, Z., et al., 4D printing polymeric biomaterials for adaptive tissue regeneration. Bioactive Materials, 2025. 48: p. 370-399.
3. Bouguermouh, K., et al., Designing advanced 4D printing thermo-sensitive shape memory polymer blends for enhanced mechanical and shape memory performances. Progress in Additive Manufacturing, 2025: p. 1-20.
4. Bouguermouh, K., et al., Advanced 4D Printing of Flax Fiber-Reinforced PLA/PETG Blends for Enhanced Mechanical, Thermal, and Shape Memory Properties. Polymer, 2025: p. 128587.
5. Kouka, M.A., et al., 4D printing of shape memory polymers, blends, and composites and their advanced applications: a comprehensive literature review. Advanced Engineering Materials, 2023. 25(4): p. 2200650.
6. Megdich, A., M. Habibi, and L. Laperrière, A review on 4D printing: material structures, stimuli and additive manufacturing techniques. Materials Letters, 2023. 337: p. 133977.
7. Megdich, A., et al., Advanced nanocomposites for 4D printing: High-performance electroactive shape memory polymers for smart applications. Applied Materials Today, 2025. 44: p. 102702.
8. Saska, S., et al., Bioresorbable polymers: advanced materials and 4D printing for tissue engineering. Polymers, 2021. 13(4): p. 563.
9. Kafle, A., et al., 3D/4D printing of polymers: fused deposition modelling (FDM), selective laser sintering (SLS), and stereolithography (SLA). Polymers, 2021. 13(18): p. 3101.
10. Franco Urquiza, E.A., Advances in additive manufacturing of polymer-fused deposition modeling on textiles: From 3D printing to innovative 4D printing—A review. Polymers, 2024. 16(5): p. 700.
11. Sajjad, R., et al., A review of 4D printing–technologies, shape shifting, smart polymer based materials, and biomedical applications. Advanced Industrial and Engineering Polymer Research, 2024. 7(1): p. 20-36.
12. Shen, Z., et al., Nanocellulose-based composite phase change materials for thermal energy storage: status and challenges. Energy & Environmental Science, 2023. 16(3): p. 830-861.
13. Latif, M., et al. 3D printing of nanocellulose structures infused Epofix resin with improved mechanical properties. in 2022 2nd International Conference on Digital Futures and Transformative Technologies (ICoDT2). 2022. IEEE.
14. Ma, R., et al., One-pot cellulose nanofibrillation, surface-modification and grafting by deep eutectic solvent towards high performance 3D printing nanocellulose-enriched bionanocomposites. Industrial Crops and Products, 2024. 210: p. 118134.
15. Zhou, S., et al., Gelatin-oxidized nanocellulose hydrogels suitable for extrusion-based 3D bioprinting. Processes, 2022. 10(11): p. 2216.
16. Barkane, A., et al., Biobased resin for sustainable stereolithography: 3D printed vegetable oil acrylate reinforced with ultra-low content of nanocellulose for fossil resin substitution. 3D Printing and Additive Manufacturing, 2023. 10(6): p. 1272-1286.
17. Jovic, T.H., et al., A comparative analysis of pulp-derived nanocelluloses for 3D bioprinting facial cartilages. Carbohydrate Polymers, 2023. 321: p. 121261.
18. Gu, T., et al., Design and development of 4D-printed cellulose nanofibers reinforced shape

memory polymer composites: Application for self-deforming plant bionic soft grippers. Additive Manufacturing, 2023. 70: p. 103544.
19. Bai, H., et al., Photo-crosslinkable poly (vinyl alcohol)/nanocrystalline cellulose composites with controllable performance and exceptional water vapor barrier property for packaging application. Cellulose, 2022. 29(14): p. 7721-7734.
20. Karima, B., M. Habibi, and L. Laperrière, 4D printing of fiber-reinforced auxetic structures: the building blocks: a review. Smart Materials and Structures, 2024. 33(6): p. 063001.
21. Yousuf, M.H., W. Abuzaid, and M. Egilmez, 4D Printing of Magnetic Shape Memory Polymer—La0. 7Sr0. 3MnO3 Nanocomposite. Advanced Engineering Materials, 2025. 27(5): p. 2402423.
22. Wojno, S., et al., Percolation and phase behavior in cellulose nanocrystal suspensions from nonlinear rheological analysis. Carbohydrate Polymers, 2023. 308: p. 120622.
23. Wojno, S., et al., Phase transitions of cellulose nanocrystal suspensions from nonlinear oscillatory shear. Cellulose, 2022. 29(7): p. 3655-3673.
24. Gupta, A. and T.H. Mekonnen, Cellulose nanocrystals enabled sustainable polycaprolactone based shape memory polyurethane bionanocomposites. Journal of Colloid and Interface Science, 2022. 611: p. 726-738.
25. Bouguermouh, K., et al., 4D-printed PLA-PETG polymer blends: comprehensive analysis of thermal, mechanical, and shape memory performances. Journal of Materials Science, 2024. 59(25): p. 11596-11613.
26. Abdelhamid, Z., H. Mohamed, and S. Kelouwani, The use of machine learning in process–structure–property modeling for material extrusion additive manufacturing: a state-of-the-art review. Journal of the Brazilian Society of Mechanical Sciences and Engineering, 2024. 46(2): p. 70.
27. Ziadia, A., M. Habibi, and S. Kelouwani, Machine learning study of the effect of process parameters on tensile strength of FFF PLA and PLA-CF. Eng, 2023. 4(4): p. 2741-2763.
28. Bouguermouh, K., et al., 4D-printed PLA-PETG polymer blends: comprehensive analysis of thermal, mechanical, and shape memory performances. Journal of Materials Science, 2024: p. 1-18.
29. Vinyas, M., et al., Mechanical characterization of the Poly lactic acid (PLA) composites prepared through the Fused Deposition Modelling process. Materials Research Express, 2019. 6(10): p. 105359.
30. Thirugnanasambandam, A., et al., Development of 3D printed novel multi-polymer component based on blended filaments of polylactic acid and polyethylene terephthalate glycol. Progress in Additive Manufacturing, 2024: p. 1-14.
31. Zhou, Y., et al., 3D printing of polyurethane/nanocellulose shape memory composites with tunable glass transition temperature. Industrial Crops and Products, 2022. 182: p. 114831.
32. Zain, N.M., S.M. Yusop, and I. Ahmad, Preparation and characterization of cellulose and nanocellulose from pomelo (Citrus grandis) albedo. J Nutr Food Sci, 2014. 5(1): p. 334.
33. Yakkan, E., et al., Nanocellulose-polypropylene nanocomposites enhanced with coupling agent. Bartın Orman Fakültesi Dergisi, 2018. 20(3): p. 491-502.
34. Wei, L., et al., Preparation and Characterization of the Nanocomposites from Chemically Modified Nanocellulose and Poly (lactic acid). Journal of Renewable Materials, 2017. 5(5): p. 410-422.
35. Mukherjee, T., et al., Chemically imaging the interaction of acetylated nanocrystalline cellulose (NCC) with a polylactic acid (PLA) polymer matrix. Cellulose, 2017. 24: p. 1717-1729.

36. Lu, J., et al., Properties of polylactic acid reinforced by hydroxyapatite modified nanocellulose. Polymers, 2019. 11(6): p. 1009.
37. Park, J.Y., et al., Compatibility and physical properties of poly (lactic acid)/poly (ethylene terephthalate glycol) blends. Macromolecular Research, 2012. 20(12): p. 1300-1306.
38. Chi, K. and J.M. Catchmark, Enhanced dispersion and interface compatibilization of crystalline nanocellulose in polylactide by surfactant adsorption. Cellulose, 2017. 24(11): p. 4845-4860.
39. Wang, Q., et al., Structure and properties of polylactic acid biocomposite films reinforced with cellulose nanofibrils. Molecules, 2020. 25(14): p. 3306.
40. Ambone, T., A. Torris, and K. Shanmuganathan, Enhancing the mechanical properties of 3D printed polylactic acid using nanocellulose. Polymer Engineering & Science, 2020. 60(8): p. 1842-1855.
41. Popescu, D., et al., FDM process parameters influence over the mechanical properties of polymer specimens: A review. Polymer Testing, 2018. 69: p. 157-166.
42. Tian, C., et al., Multi-material 3D-printing nozzle design based on the theory of inventive problem solving and knowledge graph. Designs, 2023. 7(5): p. 103.
43. Sztorch, B., et al., Natural and synthetic polymer fillers for applications in 3D printing—FDM technology area. Solids, 2022. 3(3): p. 508-548.
44. Uetani, K. and K. Hatori, Thermal conductivity analysis and applications of nanocellulose Markandan, K. and C.Q. Lai, Fabrication, properties and applications of polymer composites additively manufactured with filler alignment control: A review. Composites Part B: Engineering, 2023. 256: p. 110661.
45. Kothavade, P.A. and K. Shanmuganathan, Mechanical Properties of PLA/Nanocellulose Composites, in Polylactic Acid-Based Nanocellulose and Cellulose Composites. 2022, CRC Press. p. 181-206.
46. Hamzehei, R., et al., 2D triangular anti-trichiral structures and auxetic stents with symmetric shrinkage behavior and high energy absorption. Mechanics of Materials, 2020. 142: p. 103291.
47. Meng, L., et al., The energy absorption and bearing capacity of light-weight bio-inspired structures produced by selective laser melting. Journal of the mechanical behavior of biomedical materials, 2019. 93: p. 170-182.
48. Hu, L., Z. Wu, and M. Fu, Mechanical behavior of anti-trichiral honeycombs under lateral crushing. international journal of mechanical sciences, 2018. 140: p. 537-546.
49. Benini, K.C.C.d.C., A.S.C.d. Bomfim, and H.J.C. Voorwald, Cellulose-reinforced polylactic acid composites for three-dimensional printing using polyethylene glycol as an additive: a comprehensive review. Polymers, 2023. 15(19): p. 3960.
50. Gorbunova, M., et al., Nanocellulose-based thermoplastic polyurethane biocomposites with shape memory effect. Journal of Composites Science, 2023. 7(4): p. 168.
51. Fu, S. and C. Tian, Nanocellulose and its application for shape-memory materials. Eco-friendly polymer nanocomposites: Chemistry and applications, 2015: p. 101-135.
52. Auad, M.L., et al., Characterization of nanocellulose-reinforced shape memory polyurethanes. Polymer International, 2008. 57(4): p. 651-659.
53. materials. Science and Technology of advanced MaTerialS, 2017. 18(1): p. 877-892.

Chapitre 8: Conclusions et perspectives

8.1 Conclusions

Cette thèse s'inscrit dans le champ émergent de l'impression 4D appliquée aux matériaux intelligents, avec un accent particulier sur le développement de structures auxétiques renforcées par des fibres naturelles. Elle a permis de démontrer que l'impression 4D, combinée à des polymères à mémoire de forme (PMF) optimisés et à des géométries auxétiques, peut produire des structures programmables capables de répondre à des stimuli externes tout en conservant des propriétés mécaniques robustes et stables.

Dans une première phase, des mélanges polymériques à mémoire de forme ont été conçus en combinant différentes matrices (PLA, ABS, PETG, PMMA), dans le but de surmonter les limites des PMF classiques en termes de complexité de mise en œuvre et de sensibilité environnementale. L'approche par mélanges polymériques s'est révélée efficace pour obtenir des températures de transition multiples, ouvrant la voie à des effets mémoire séquentiels, essentiels dans les applications avancées comme la robotique souple. Les essais mécaniques et thermiques réalisés ont permis d'identifier des formulations optimales qui assurent à la fois rigidité, flexibilité et performance mémoire sur plusieurs cycles.

La deuxième phase a porté sur l'incorporation de renforts naturels, en particulier des fibres de lin, dans ces mélanges polymériques, pour former des composites imprimables par dépôt de fil fondu (FDM). Ces renforts ont significativement amélioré la rigidité, la résistance mécanique et la stabilité dimensionnelle sans compromettre l'effet mémoire, à condition de maîtriser finement leur pourcentage dans la matrice. L'étude a également exploré le comportement de ces composites sous vieillissement thermohydrique (immersion en eau chaude). Les résultats montrent que, malgré une certaine dégradation des interfaces fibres/matrice, des performances stables peuvent être maintenues avec des formulations bien choisies, répondant ainsi à des exigences de durabilité dans des environnements humides ou médicaux.

La troisième phase a approfondi l'intégration de nanocellulose comme renfort biosourcé. Grâce à sa haute surface spécifique et à ses propriétés mécaniques remarquables, la nanocellulose a permis d'augmenter la rigidité des composites, tout en renforçant dans certains cas l'effet mémoire de

forme. Ce double avantage, performance et durabilité positionne la nanocellulose comme un matériau clé pour les futures générations de composites multifonctionnels imprimés en 4D.

Enfin, la dernière partie de la recherche a permis de concevoir et fabriquer expérimentalement des structures auxétiques à base des matériaux développés. Ces structures, grâce à leur géométrie à rapport de Poisson négatif, ont montré une capacité remarquable d'absorption d'énergie, de flexibilité et de déformation programmable. Les tests de compression et de mémoire de forme ont confirmé leur potentiel pour des applications où les propriétés adaptatives sont cruciales, comme les dispositifs déployables, les implants médicaux ou les composants souples de robots.

En somme, cette recherche propose une méthodologie complète pour concevoir des matériaux 4D à la fois intelligents, biodégradables, mécaniquement performants et adaptatifs. Elle contribue à combler plusieurs lacunes identifiées dans la littérature, notamment en ce qui concerne la durabilité des composites à base de fibres naturelles, l'effet mémoire sous sollicitations prolongées, et la mise en forme de structures auxétiques fonctionnelles par fabrication additive. Les résultats obtenus ouvrent la voie à une nouvelle génération de matériaux imprimables, adaptés aux défis technologiques actuels en ingénierie, biomécanique et robotique.

8.2 Perspectives

Les travaux réalisés dans cette thèse ont permis de poser les bases solides pour le développement de matériaux intelligents imprimés en 4D, combinant polymères à mémoire de forme, fibres naturelles et géométries auxétiques. Plusieurs pistes prometteuses peuvent désormais être envisagées pour prolonger et enrichir ces résultats :

- ***Optimisation des formulations à mémoire de forme pour stimuli multiples***

Bien que l'étude ait principalement ciblé la mémoire thermique, une perspective majeure serait d'explorer des formulations sensibles à d'autres stimuli, tels que la lumière, l'humidité, les champs électriques ou magnétiques. Le développement de matériaux multi-stimuli permettrait d'envisager des comportements encore plus complexes et programmables, adaptés à des environnements dynamiques ou des systèmes embarqués intelligents.

- ***Fonctionnalisation des interfaces fibres/matrice***

La performance à long terme des composites dépend fortement de l'adhésion entre la matrice polymère et les renforts naturels. Une perspective pertinente serait d'explorer des traitements de surface ou des agents de couplage (biosourcés si possible) afin d'améliorer la compatibilité interfaciale, notamment dans des conditions de vieillissement accéléré (humidité, température, cycles thermiques).

- ***Exploration de nouvelles fibres naturelles et hybrides***

Le lin et la nanocellulose ont montré un bon potentiel dans cette thèse, mais d'autres fibres naturelles telles que le chanvre, le jute, ou encore les fibres issues de résidus agricoles pourraient être testées pour améliorer la durabilité environnementale. Par ailleurs, le développement de systèmes hybrides (naturel/synthétique ou naturel/nanoparticules fonctionnelles) permettrait d'atteindre des compromis optimaux entre performance mécanique, mémoire de forme et coût.

- ***Miniaturisation et impression multi-matériaux***

Le passage à l'échelle micro ou nano des structures auxétiques représente une avancée importante, notamment pour les applications biomédicales (stents, implants intelligents). L'intégration d'imprimantes multi-buses pour l'impression simultanée de plusieurs matériaux (matrices, renforts, agents conducteurs, etc.) offrirait un niveau de complexité et de fonctionnalité supérieur, par exemple pour la fabrication de capteurs embarqués ou de systèmes de morphing autonome.

- ***Modélisation numérique avancée***

Des outils de modélisation plus fins, basés sur des approches multi-échelles et intégrant des lois de comportement viscoélastiques couplées à la mémoire de forme, pourraient être développés. Cela permettrait d'optimiser les géométries auxétiques de manière plus prédictive et de réduire les itérations expérimentales.

- ***Applications industrielles et prototypage fonctionnel***

Une suite logique à ces travaux serait la mise en œuvre de prototypes fonctionnels pour des domaines d'application concrets : dispositifs biomédicaux, éléments de robots souples, structures de protection ou d'absorption d'énergie (automobile, aéronautique), textiles techniques

morphables, etc. L'étude de leur comportement en conditions réelles constituerait une étape essentielle vers la valorisation industrielle.

- ***Durabilité environnementale et analyse du cycle de vie***

Étant donné l'enjeu croissant de la durabilité, une analyse du cycle de vie des matériaux développés, depuis la production des fibres jusqu'à la fin de vie des objets imprimés, permettrait de positionner ces solutions dans une logique d'éco-conception. L'intégration de matériaux entièrement compostables ou recyclables serait une voie complémentaire à explorer.

ANNEXE 1

Supporting Information

Designing advanced 4D printing thermo-sensitive shape memory polymer blends for enhanced mechanical and shape memory performances

Appendix 1: Tensile strength of polymers and blends in 0° printing orientation.

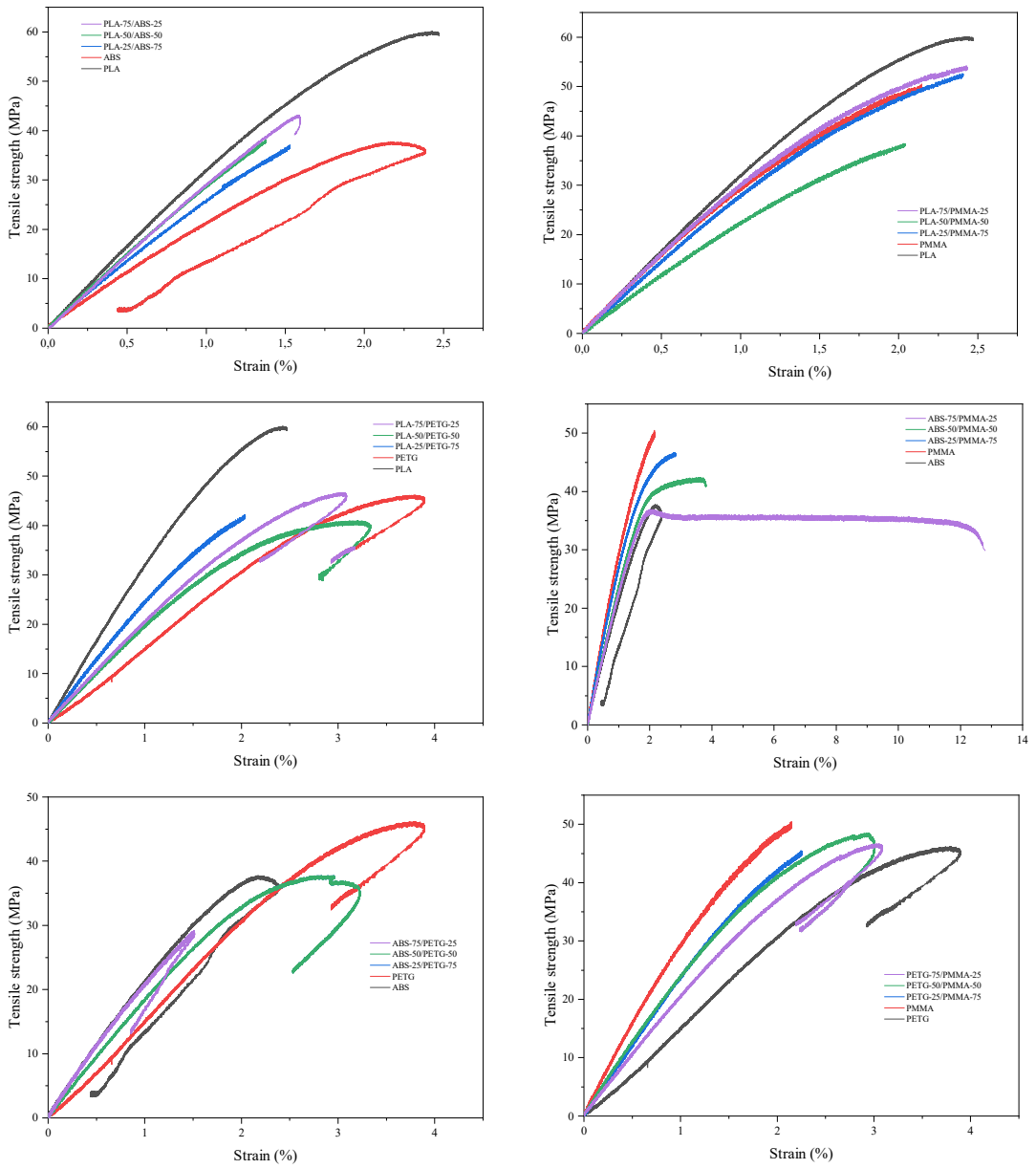

Appendix 2: Tensile strength of polymers and blends in ±45° printing orientation.

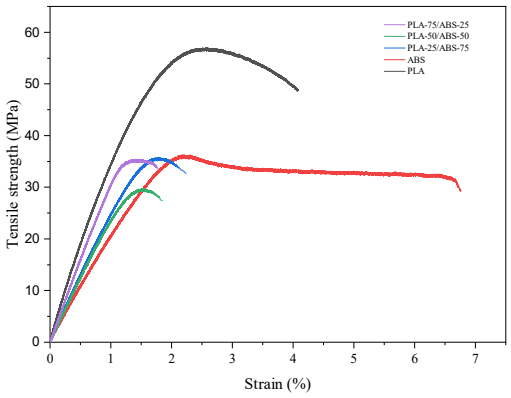

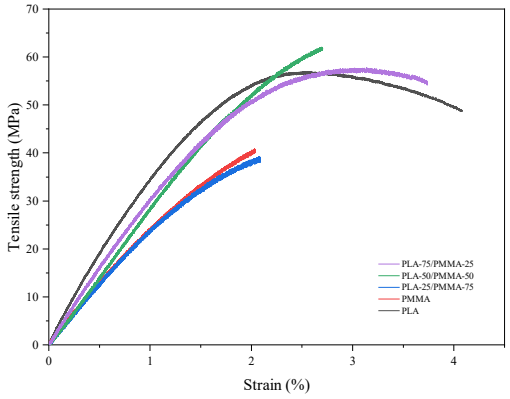

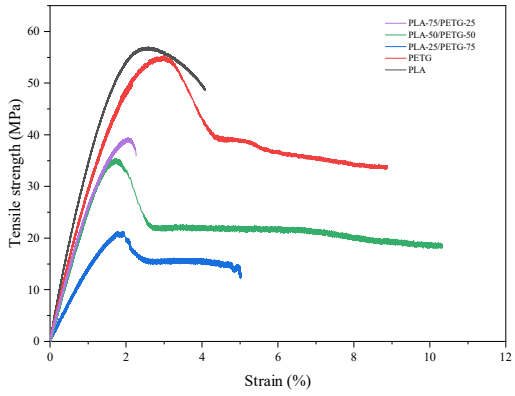

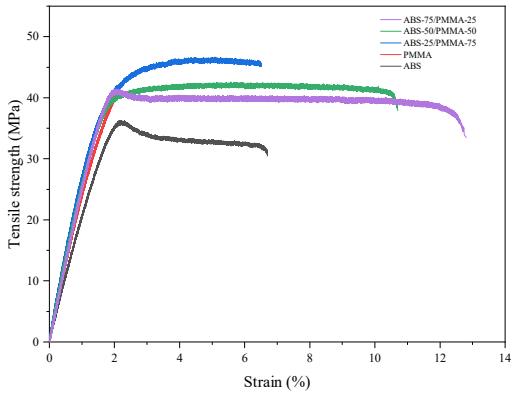

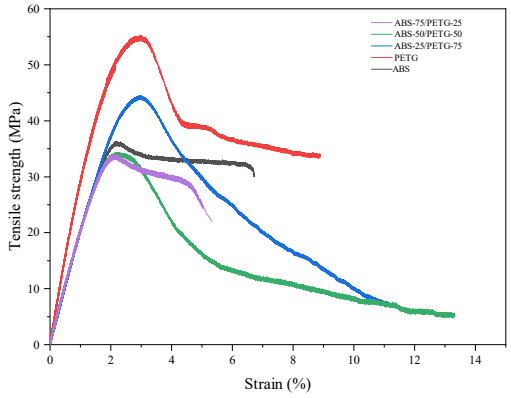

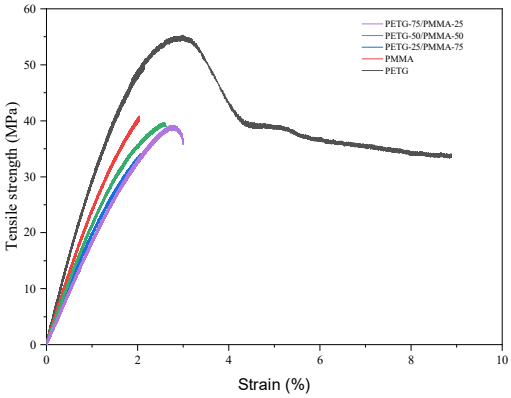

Appendix 3: Tensile strength of polymers and blends in 90° printing orientation.

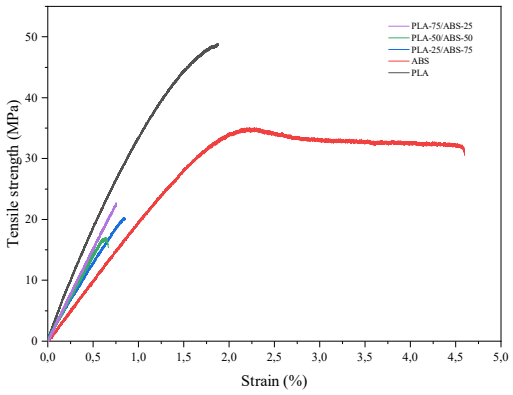

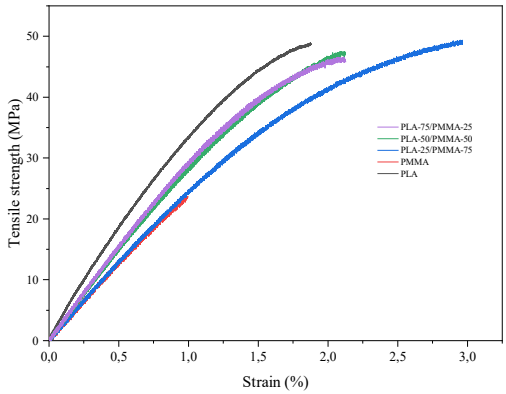

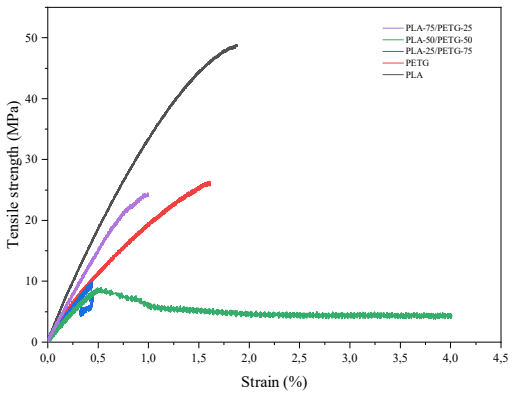

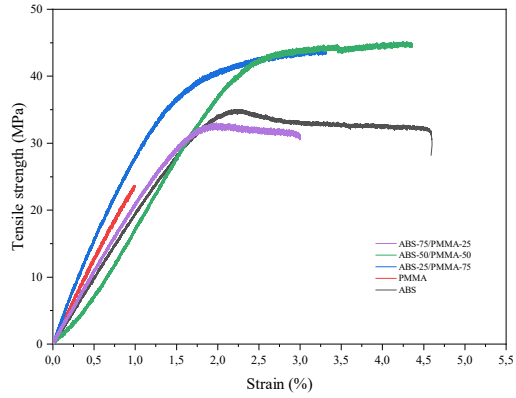

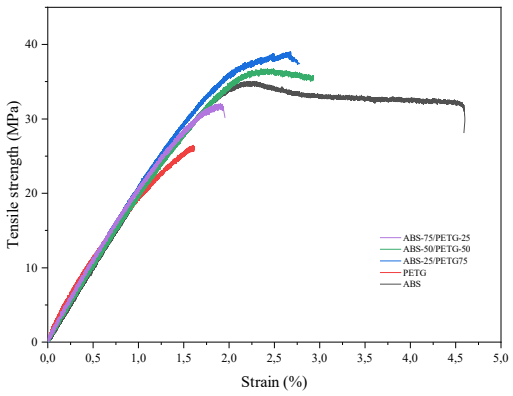

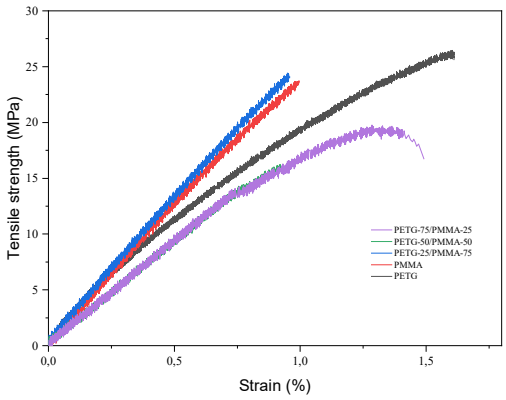

ANNEXE 2

Supporting Information

Advanced 4D Printing of Flax Fiber-Reinforced PLA/PETG Blends for Enhanced Mechanical, Thermal, and Shape Memory Properties

Appendix 4. Thermal properties of PLA/PETG polymer blends and Flax fiber-reinforced polymer blends.

Samples	Glass transition temperature (T_g) (°C)		Melting temperature (T_m)(°C)	Cold crystallization temperature (T_{cc}) (°C)	Enthalpy of fusion (ΔHf) (J/g)	Enthalpy of cold crystallization (ΔH_{cc}) (J/g)	X_{cc} (%)	X_c (%)
	T_g1	T_g2						
PLA-25/PETG-75	60,72	79,58	-	-	-	-	0.00	0.00
PLA-50/PETG-50	59,97	80,13	151,90	132.89	1.76	0.69	1.48	3.78
PLA-75/PETG-25	60.98	80,66	154.38	136.62	0.46	0.31	0.44	0.66
PLA-25/PETG-75/F-5	58.83	77.68	151.99	134.20	0.24	0.28	0.01	1.05
PLA-25/PETG-75/F-10	59.65	78.63	151.47	133.61	0.25	0.25	1.06	1.06
PLA-25/PETG-75/F-15	60.71	79.71	154.73	134.26	7.04	0.27	1.15	30.26
PLA-50/PETG-50/F-5	59.69	78.80	149.86	135.77	4.36	2.10	4.52	9.37
PLA-50/PETG-50/F-10	59.03	78.54	150.58	133.49	1.99	0.62	1.33	4.28
PLA-50/PETG-50/F-15	58.98	77.66	150.70	132.11	0.52	0.33	0.71	1.12
PLA-75/PETG-25/F-5	59.42	-	150.68	132.37	9.76	7.45	10.68	13.99
PLA-75/PETG-25/F-10	59.36	-	148.82	123.99	17.77	21.37	30.64	25.48
PLA-75/PETG-25/F-15	58.61	-	150.56	133.16	704	7.56	10.83	10.09